Mechanisms of instabilities of high-frequency combustion and application in engines-rockets

Yoann Méry

Ecole Centrale Paris

THESE

présentée par

Yoann Méry

pour l'obtention du

GRADE de DOCTEUR

Formation doctorale : Energétique

Laboratoire d'accueil : Laboratoire d'Énergétique Moléculaire et Macroscopique, Combustion (EM2C) du CNRS et de l'ECP

Mécanismes d'instabilités de combustion haute-fréquence et application aux moteurs-fusées.

Soutenue le 27 mai 2010

Jury :	Françoise	Baillot	(Rapporteur)
	Sébastien	Candel	(Directeur de thèse)
	Carlos	Cruz	
	Michel	Champion	(Président)
	Sébastien	Ducruix	
	Geoff	Searby	(Rapporteur)
	Marie	Théron	

Ecole Centrale des Arts et Manufactures
Grand Établissement sous tutelle
du Ministère de l'Éducation Nationale
Grande Voie des Vignes
92295 Châtenay-Malabry Cedex
Tél : 33 (1) 41 13 10 00
Télex : 634 991 F EC PARIS

Laboratoire d'Énergétique Moléculaire et Macroscopique, Combustion (E.M2.C.)
UPR 288, CNRS et Ecole Centrale Paris
Tél : 33 (1) 41 13 10 31
Fax : 33 (1) 47 02 80 35

2010ECAP0012

Remerciements

Le travail présenté dans ce document a été possible grâce à la participation de nombreuses personnes que je tiens à remercier chaleureusement. Sébastien Candel et Sébastien Ducruix sont les personnes avec qui j'ai eu la chance d'interagir le plus durant mon séjour au laboratoire EM2C. Je leur suis reconnaissant pour la grande qualité de leur encadrement, leur disponibilité et leurs qualités humaines. En particulier, la confiance qu'ils m'ont accordée et l'ambiance générale du groupe, équilibre entre camaraderie et émulation, ont participé à faire de ces années de thèse une période particulièrement enrichissante. Je remercie également Philippe Scouflaire pour l'aide qu'il m'a apportée pendant les essais, parfois délicats, que nous avons entrepris. Son savoir faire a été grandement utile à l'obtention des résultats.
Je remercie Françoise Baillot et Geoff Searby, qui ont bien voulu faire parti du jury de la thèse et d'en être rapporteurs - ce qu'ils ont fait très consciencieusement - ainsi que Michel Champion, qui m'a fait l'honneur de présider la soutenance. Je remercie Marie Théron, représentante du CNES, qui a suivi tout le processus de conception et les campagnes, et qui a contribué à faire commencer les expériences dans un délai raisonnable. Je remercie Carlos Cruz, de Snecma Vernon, qui a suivi de très près mon travail. L'intérêt qu'il a porté a mes recherches a été très motivant.
Je remercie les collaborateurs de l'Onera. Tout d'abord, l'équipe de conception, Pierre Hervat et Patrice Marquès, qui a dessiné la partie stratégique de nos expériences qui s'est avérée un succès. Ensuite l'équipe du DEFA et en particulier du banc Mascotte, constituée de Gérard Ordonneau, Lucien Vingert et Franck Vannier, qui, malgré un effectif réduit et des conditions expérimentales très sollicitantes, nous a permis de mener cette campagne jusqu'au bout et de ramener toutes les données dont nous avions besoin.
J'ai eu l'opportunité de bénéficier de la compétence d'enseignants-chercheurs de grande qualité au laboratoire EM2C : Marc Massot, Olivier Gicquel, Denis Veynante, Laurent Zimmer, Franck Richecoeur, Benoît Fiorina, Thierry Schuller... Avoir une telle équipe autour de sois est précieux, et je remercie chacun d'eux pour le temps qu'ils ont bien voulu m'accorder. Je remercie également Thomas Schmitt, pour l'aide qu'il m'a apporté sur la simulation numérique et pour son enthousiasme communicatif. Ce travail aurait été probablement différent sans

les interminables discussions passionnées que j'ai eu avec Ronan Vicquelin, sur la combustion, la science et le reste. Son amitié a contribué à faire passer ces trois années de thèse très vite.
L'équipe technique du laboratoire a également été disponible et amicale, et je tiens à remercier particulièrement Jérôme Beaunier et Samira El Ghazi pour leur aide pendant la préparation de mes essais. Je remercie également le personnel administratif, le secrétariat ainsi que les directeurs successifs du laboratoire, d'abord Nasser Darabiha puis Estelle Iacona, pour l'accueil qui m'a été fait. Mon séjour au laboratoire a été agréable également grâce à la présence des doctorants et post-doctorants.
Je remercie ma famille qui m'a porté jusqu'à la thèse, puis jusqu'à sa fin, avec un amour inaltérable et un soutien inconditionnel. Enfin, je remercie mes amis, grâce auxquels j'ai pu travaillé à exprimer mes idées simplement, m'aidant à les avoir claires, et qui m'ont même, pour certain(e)s, aidé à améliorer la qualité de mon anglais.

Abstract

This thesis presents a study of high frequency instabilities in rocket engines. This issue, which has plagued many engine development programs, is approached by three complementary viewpoints: experimental, theoretical, and numerical. First, experiments are carried out to identify the main processes involved and bring forth mechanisms taking place when an engine becomes unstable. To achieve this stage, a new modulator (the VHAM), capable of creating acoustic waves representative of what occurs in an actual engine, is designed. It is demonstrated that it generates very strong acoustic fields at the 1T, 1T1L and 1T2L modes of the chamber.
This device is then used to study the impact of acoustics on cryogenic jets. High speed diagnostics show that primary and secondary atomizations are dramatically modified by the velocity field. The liquid core length is strongly reduced and an alternate pattern of liquid oxygen appears in the chamber. An oscillation of the oxygen distribution in the transverse direction of the chamber is observed.
These characteristics have an important effect on the flame pattern, as it is shown in the next step of the study. The modification of atomization induces different flames' shapes, which are strongly dependent of the acoustic wave spatial distribution. When the acoustic wave amplitude is important near the injection plane - particularly when the 1T2L mode is excited - primary atomization is enhanced and the combustion area becomes compact, near the injector plane. In this case, the acoustic response reaches nearly 30% of the chamber mean pressure. In parallel, asymmetry is observed on the flame pattern. This phenomenon is attributed notably to non-linear acoustics and is thought to have an additional impact on the acoustic response.
The second part of this thesis concern theoretical analysis. Two models are developed following the main conclusions of the experimental campaign: heat release oscillations are due to the transverse flames' motion, and the phenomenon is triggered when droplets become small enough to be convected by the acoustic field.
Using these models as a baseline, a numerical code (STAHF) is presented. Its purpose is to account for mechanisms identified previously for little computational cost. It is based on the standard decomposition of Lores and Zinn (1973)

and Culick (1976). This code is validated on particularly responding situations observed during experiments. It is then shown that it can be used to study real scale rocket engines.
The third point of view adopted to address the problem is numerical simulation. Full compressible LES is chosen to study the interaction between acoustics and combustion. A new combustion model for non-premixed flames with infinitely fast chemistry is presented and validated on a well documented flame (H3). It is then used to study the interaction between a transverse acoustic wave and the H3 flame. A comparison between the Rayleigh source term computed from the simulation and the one predicted by the theoretical model FAME is conducted eventually.

Résumé

Cette thèse présente une étude des instabilités haute fréquence dans les moteurs de fusée. Ce phénomène, qui a posé de nombreux problèmes dans les programmes de développement de moteur, est abordé par trois points de vue complémentaires : expérimental, théorique et numérique. Premièrement, des expériences sont menées afin d'identifier les principaux processus et d'apporter les mécanismes ayant lieu lorsque le moteur devient instable. Pour parvenir à ce stade, un nouveau modulateur (VHAM), capable de créer des ondes acoustiques représentatives de ce qui se produit dans un moteur réel, est conçu. Il est démontré qu'il génère de très forts champs acoustiques aux modes 1T, 1T1L et 1T2L de la chambre.

Cet appareil est alors utilisé pour étudier l'impact de l'acoustique sur les jets cryogéniques. Des diagnostiques haute vitesse montrent que les atomisations primaire et secondaire sont considérablement modifiées par le champ de vitesse. La longueur du cœur liquide est fortement réduite et un motif d'oxygène liquide apparaît dans la chambre. Une oscillation de la distribution d'oxygène dans la direction transverse de la chambre est observée.

Ces caractéristiques ont un effet important sur la structure de flamme, comme c'est montré dans l'étape suivante de l'étude. La modification de l'atomisation induit des formes de flamme différentes, qui sont fortement tributaires de la répartition spatiale de l'onde acoustique. Lorsque l'amplitude de l'onde est importante à proximité du plan d'injection - en particulier lorsque le mode 1T2L est excité - l'atomisation primaire est augmentée et la zone de combustion devient plus compacte, près du plan d'injection. Dans ce cas, la réponse acoustique atteint près de 30% de la chambre de pression moyenne. En parallèle, on observe sur les flammes une dissymétrie. Ce phénomène est attribuable notamment à l'acoustique non-linéaire et est supposé avoir un impact supplémentaire sur la réponse acoustique.

La deuxième partie de cette thèse concerne l'analyse théorique. Deux modèles (FAME, SDM) sont développés en suivant les principales conclusions de la campagne expérimentale : les oscillations de dégagement de chaleur sont dues au mouvement transverse des flammes, et le phénomène est déclenché lorsque des gouttelettes deviennent suffisamment petites pour être convectées par le champ acoustique.

En utilisant ces modèles comme base de référence, un code numérique (STAHF) est présenté. Son but est de rendre compte des mécanismes déjà identifiés pour un coût de calcul faible. Il est basé sur la décomposition introduite notamment pas Lores and Zinn (1973) et Culick (1976). Ce code est validé sur les cas pour lesquels la réponse était particulièrement forte lors des expériences. Il est ensuite montré qu'il peut être utilisé pour étudier des moteurs-fusées grandeur nature.
Le troisième point de vue adopté pour résoudre le problème est la simulation numérique. La LES compressible est choisi pour étudier l'interaction entre l'acoustique et la combustion. Un nouveau modèle de combustion pour flammes non-prémélangées basé sur une hypothèse de chimie infiniment rapide est présenté et validé sur une flamme bien documentée (H3). Il est ensuite utilisé pour étudier l'interaction entre une onde acoustique transverse et la flamme H3. Une comparaison entre le terme source de Rayleigh calculé à partir de la simulation et celui prédit par le modèle théorique FAME est finalement menée.

Contents

Introduction

The early development of liquid rocket engines (LRE) during the twentieth century was plagued by combustion instabilities. This was experienced, for example, in the Ariane developement program in which the second launcher was destroyed after a few seconds of flight because of high frequency instabilities in the propulsion system of the first stage. Oscillations associated to unsteady heat release led in many cases to a rapid intensification of heat fluxes to the thrust chamber walls, causing fatal damage and a spectacular destruction of the propulsion system. A typical consequence of this process is shown in Fig. 1 where the chamber and nozzle have exploded during such a high frequency instability.

Figure 1: *Damaged combustion chamber after a high frequency combustion instability.*

The powerful instabilities appearing in these high performance engines are usually identified in terms of their characteristic frequencies (see (Barrère and Williams 1969) and (Harrje and Reardon 1972)). One generally distinguishes intrinsic instabilities linked to the combustion process itself, low (LF) instabilities involving a coupling of the full system including the feed manifold and thrust chamber and high frequency (HF) instabilities which are mainly coupled

by the chamber acoustic eigenmodes.
There is in fact no clear division between the low and high frequency ranges because the resonant frequency depends on the system geometry and scale. It might then be useful to improve the classification by indicating the physical cause of the process. But again, this is not easy. For example, low-frequency instability, also designated as *chugging*, can result from several mechanisms. The range of frequency is below a few hundred Hz, and the common feature of chugging is that the wavelength is much larger than the characteristic dimensions of the thrust chamber and of the feed system. The coupling is often independent from acoustics but the chamber length may be important, and longitudinal acoustic modes may intervene.
The driving mechanism of low-frequency instabilities is essentially related to the time lag between injection of propellants and their chemical conversion in the thrust chamber. The existence of such a time lag and its importance for combustion instability analysis is well underlined in early studies of this process. This has led to the sensitive time lag model explored in great detail in Crocco and Cheng (1956). Chugging instabilities can be handled analytically with this type of modeling, though it remains important to include dynamical descriptions of the feeding manifold. In practice, chugging can be removed by augmenting the pressure drop in the injection units. This decouples the feed lines from the chamber and, in most cases, eliminates the low frequency oscillations. While this is effective during steady state operation, some chugging is observed during transients because the injector head loss is reduced when the flow is not fully established in the system giving rise to a transient coupling. Low-frequency instabilities are also caused by other types of coupling. One very low frequency oscillation (around a few Hz) is due to a combination between the elastic response of the feed lines and propellant tanks with thrust oscillations. In this so called *pogo* instability, the propellant flow rate is modulated by the structural elasticity generating thrust oscillations, which in turn act on the launcher structure. This feedback process may lead to a rapid destruction of the launcher system.

High frequency instabilities, also designated as *screaming*, mainly observed in liquid rocket engines, correspond to shorter wavelengths. As the wavelength is reduced the coupling may involve a higher order mode of the thrust chamber. Both longitudinal and transverse (radial, azimuthal and rotating) modes are concerned by this process. The oscillation frequency is generally close to the modal eigenfrequencies. Rocket engine hot fire tests indicate that transverse modes are the most destructive because they are less susceptible to damping by the nozzle and their amplitude may reach very high levels. The acoustic mode enhances the combustion process, shortening the flame, augmenting the heat flux to the chamber walls and injection plane. This can lead to a rapid

melting of injectors, as shown in Fig. 2.

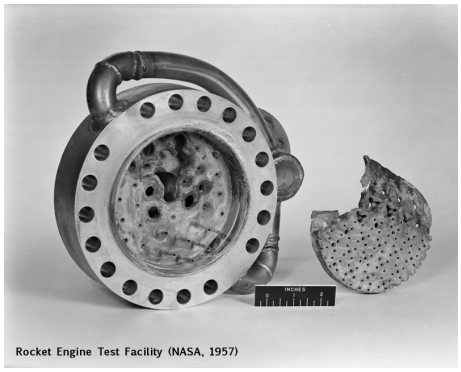

Figure 2: *Typical consequence of a high frequency instability in a liquid rocket engine.*

The coupling between combustion, the resonant modes of the chamber and fluid dynamics is illustrated in Fig. 3 which provides another piece of information. There is a wide variety of processes involved in the high frequency combustion instabilities mechanism. Some of these processes are (atomization, spray dynamics, turbulent combustion, flame/acoustic interactions, nonlinear acoustics) are the subject of active research.

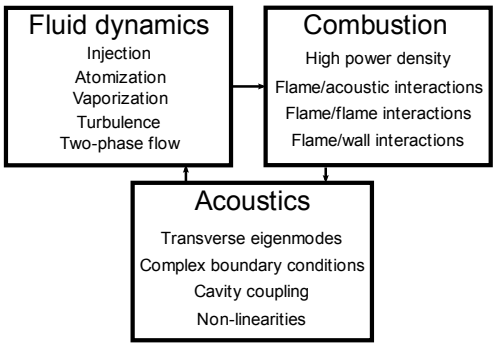

Figure 3: *Schematic diagram of the high frequency combustion mechanism. Some of the processes involved are included in this diagram.*

The present investigation is focused on high-frequency instabilities coupled by transverse modes. One central objective of this research is to observe and understand the physical processes involved in transverse high-frequency combustion/acoustic coupling. This is used to identify the fundamental processes and derive a realistic mechanism explaining the coupling between acoustic and combustion, providing elements on the growth rate of such instabilities.

While low frequency instabilities coupled by longitudinal modes are well documented, this is not the case for instabilities in the high frequency range. These

tests mainly provide pressure records obtained from a limited number of sensors. Most of the HF instability tests were carried out during the development of new engines. An experimental test program was needed for each new development. Large scale efforts were necessary in each case to deal with instabilities and modify the initial design by adding baffles, resonators or cavities to reduce the level of oscillation and check that the system could operate in a stable manner. The story of the costly trial and error process followed to suppress instabilities in the F1 engine is synthesized in a comprehensive article by Oefelein and Yang (1993). The combustion process was not visualized in the full scale tests for practical reasons, and because the objective was to find solutions to the problem and not to advance the scientific knwoledge. This did not allow detailed analysis of the driving mechanisms.
A limited number of experiments were carried out on smaller scale engines to understand the driving processes and serve to guide modeling effort. However much of this work was developed in blind systems providing no optical access to the combustion chamber with the consequence that little could be learned about the driving mechanisms and the associated flame dynamics. Some experiments were, however, developed in transparent systems or in systems comprising of a thin slit, which provided limited access to the combustion process. High speed films were used to obtain streak images of the light emitted by the flame. These films indicated that the combustion process is fundamentally modified when the chamber becomes unstable. This is exemplified in the experiments of Tischler and Male (1956), Lawhead (1961) and Barrère and Corbeau (1963). The streak film method provided interesting but limited information on the space time distribution of heat release in unstable rocket engines. All the available material obtained during the 1960s and early 1970s, an intense period of research on the subject, is gathered in a classical report SP-194 due to Harrje and Reardon (1972).

Correlatively there has been less work on high frequency instabilities in liquid rocket engines (LRE) but problems have continued to occur causing some failures. High frequency instabilities constitute a major obstacle in the development of new systems but the level of research in this area had generally diminished. The state of the art in the early 1990's is summarized in an edited book by Yang and Anderson (1995).
During the 1990s, much progress was accomplished in the understanding of the fundamental mechanisms controlling cryogenic propellant combustion used in high performance LREs, intoducing a new perspective on the problem of combustion instabilities. A recent article (Candel et al. 2006) contains a review of innovative advances in this domain.
A new program aiming at the understanding of high frequency combustion instabilities was initiated in 2001 by a consortium industrial partners, agencies

and research laboratories. The second phase of this program designated as REST ("Rocket Engine Stability") is currently underway. It was apparent at the beginning of this project that advances could be made by a combination of new knowledge, advanced optical diagnostics, combustion experiments on transparent test chambers and modern computational methods. It was also considered that laboratory experiments could provide the missing elements on the mechanisms driving instabilities. The Common Research Chamber (CRC) was developed on this basis and implemented at IRPHE (Cheuret 2005) and at DLR while the Multiple Injector Combustor (MIC), featuring three injectors representative of a LRE, was conceived at EM2C (Rey 2004), designed by ONERA and operated on the Mascotte facility of ONERA. Work at EM2C was reported in various conference papers and articles (Rey et al. 2002), (Rey et al. 2002), (Rey et al. 2004) and (Rey et al. 2005). A program on LRE combustion instabilities was also initiated in the United-States, during the same period involving universities and governmental laboratories in a collaborative experimental and numerical effort.
Studies were pursued by Richecoeur (Richecoeur et al. 2006; Richecoeur et al. 2008) on the multiple injector configuration used by Rey (2004). A new experimental geometry was designed as a logical development of the multiple injector system, including a new backplane featuring five injectors and an improved modulator. The system was operated with liquid and transcritical oxygen but methane replaced hydrogen injection used in the initial experiments carried out by Rey.

The present investigation exploits the MIC system and pursues experimental and theoretical work initiated by Rey and Richecoeur. To obtain higher levels of modulation and come closer to amplitudes existing in unstable real scale rocket engines during sustained oscillations, a new system designated as Very High Amplitude Modulator (VHAM, see Fig. 4), was imagined at EM2C and adapted to the MIC. Various studies have been carried out to specify the geometry that would provide the highest possible response. Some aspects of this research effort are reported in chapter 1. High speed PIV and pressure measurements, compared to acoustic numerical calculations, provide elements to understand the behavior of the system, validate the use of a low order model in such conditions, and give insight in the key parameters in order to optimize the chamber response.

Combustion instability investigations are complicated by the number of physical processes involved. The approach followed in the present research consists of decoupling the different processes to understand the respective roles of each in the full mechanism. In this framework, results reported in chapter 2 intend to give insight to the process of coupling between subcritical or transcritical

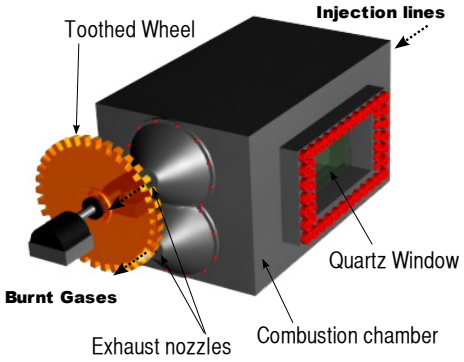

Figure 4: *Scheme of the Very High Amplitude Modulator (VHAM).*

cryogenic jets and high amplitude acoustic fields. Combustion is eliminated from the study to only focus on the effect on the liquid and transcritical jets. It is thought that the processes linked to the liquid or transcritical phase may have an important impact on the instability mechanism. Jet break-up, atomization, mixing, and motion of the dense phase are investigated using the MIC equipped with the VHAM. It is shown that a powerful acoustic field changes the oxygen distribution in the chamber and enhances sensibly atomization and mixing (Fig. 5). This provides useful information to tackle the combustion coupling problem, the focus of the next chapter.

Figure 5: *Acoustically modulated cryogenic jets.*

Hot fire experiments, reported in chapter 3, describe most of the processes present in a real unstable rocket engines. Subcritical and transcritical cryogenic jets are injected in the multiple injector combustion chamber (MIC). Five powerful methane/LOx flames are established in this system. These flames are modulated by an acoustic wave with an amplitude of several bars (Fig. 6). The frequency range (1000 Hz - 3500 Hz) and the strength of the acoustic field are

consistent with rocket instability observations. One - albeit essential - difference with a real rocket combustion chamber is the power density. The MIC features five flames to represent the several hundred flames of typical engines. Conditions where a feedback of the flame on the acoustic field are obtained. In these conditions, the flame motion is investigated in detail using high speed imaging. From this material, compiled with the conclusions of chapter 2, a scenario is derived to explain the coupling between the acoustic field and the flames.

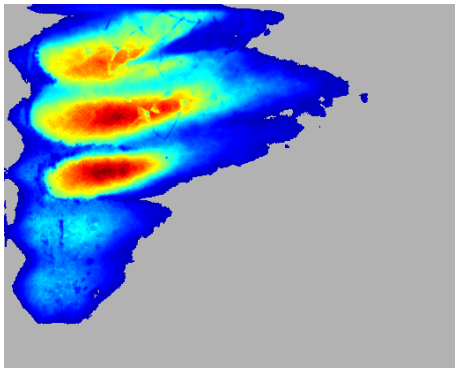

Figure 6: *Acoustically modulated flames.*

The next chapter (chapter 4) is concerned with the low order modeling of combustion instabilities. This chapter focuses on a quantitative estimation of mechanisms involved in the process. Two models are developed using conclusions obtained from experimental observations. The objective is to account for the combustion feedback on the acoustic energy balance equation. It is shown that flame motion observed in the experiment is responsible for the growth of modal amplitudes.

Other models are required to complete the description of a rocket thrust chamber. An accurate model for the chamber acoustics, injector and feed line response is needed. Several complementary methods are presented. The study is based on the normal mode expansion introduced by Lores and Zinn (1973) and extensively used by Culick (1976), in the nonlinear analysis of acoustic modes in combustor cavities. It is here used to predict the evolution of pressure for each mode. To compare the numerical results with experimental data, it is necessary to represent the acoustic source term imposed by the VHAM. One also has to estimate the damping in the cavity. This important parameter defines the amplitude of the limit cycles in the system. A method is proposed to evaluate this quantity under the complex conditions prevailing in the MIC. These elements are reported in chapter 5. The various models are implemented in a

code, designated as STAHF (STAbility HF) and comparisons with experimental data are carried out. It is shown that the model derived for the combustion response accounts for the increase of the acoustic amplitude in the chamber, and that this corresponds to the order of magnitude observed experimentally. A rocket thrust chamber geometry combined with a LOx dome is also considered to get an estimate of the possible impact of the modeled source term proposed under conditions of a realistic configuration (Fig. 7).

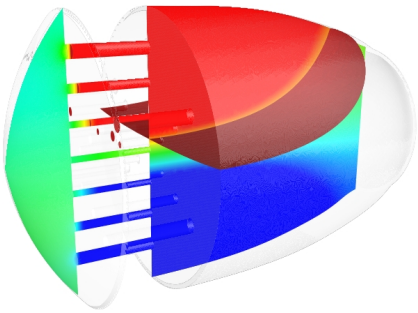

Figure 7: *Screenshot of a real scale rocket engine simulation using STAHF.*

The last chapter (6) focuses on multidimensional numerical simulation of interest in combustion dynamics. The purpose of this section is to improve the current techniques which can be used to simulate non-premixed flames in a large eddy simulation framework. A model, based on the infinitely fast chemistry limit, is presented, embedded in the AVBP code and validated on a well documented experiment (H3). The “H3" flame is then used to demonstrate the possibility of calculating the interaction between an acoustic wave and a non-premixed flame. This is obtained by imposing oscillations at the boundaries of the domain. This generates an acoustic wave which modifies the dynamics of the flame. These calculations show that the flame, as also observed in the experiments, oscillates following the acoustic field. It is possible to numerically integrate the Rayleigh source term over a couple of cycles and it is shown that this source term is close to that predicted by theory in chapter 4.

Part I

High Frequency Instability Experiments

Chapter 1

Very High Amplitude Modulator

In this chapter a new actuator, designed to create powerful transverse acoustic waves, is presented. The principle of the Very High Amplitude Modulator (VHAM) is to modulate the total mass flow rate injected in the chamber using two exit nozzles, one located on the top of the chamber, another on the bottom. These nozzles are alternatively closed by a toothed wheel which creates an intense transverse excitation in the chamber. The VHAM is tested on the Transparent Pressurized Cavity (TPC), into which cold compressed air is injected. This simple experimental set up, combined with high frequency diagnostics (high speed PIV, pressure transducers), allows for comprehension of the structure of the acoustic field created by the VHAM, in particular the link between the pressure and velocity fields. The response of the jet to acoustic perturbations is also investigated. Eventually the ability of the acoustic code AVSP to predict the spatial distribution of acoustic pressure in a chamber equipped with a VHAM is validated. Agreement is reached between the experimental and numerical fields obtained, even near the nozzles where flow conditions are harsh.

1.1 Introduction

Combustion dynamics affecting many practical systems often involve very high acoustic levels. To understand, predict, and control such phenomena, one wishes to reproduce these high amplitudes with an external modulator. This raises difficult issues because the system has to operate under extreme conditions prevailing in combustors. In most cases, the use of loudspeakers is not possible because the driver unit is in contact with high temperature gaseous streams at a very high mean pressure. These harsh conditions are typical of the model scale experiments carried out to study acoustic coupling with cryogenic

jet flames (Richecoeur 2006). One possible solution which is commonly adopted in propulsion applications consists in using fluidic actuator systems relying on rotating toothed wheels.
The present study concerns one such device which is specifically designed to examine interactions between transverse acoustic oscillations and cryogenic combustion. The modulator comprises a rotating toothed wheel periodically blocking the flow through a couple of nozzles. This device was initially installed on the lateral side of the Multiple Injector Combustor (MIC) and the wheel was used to block the flow through an auxiliary nozzle. Fig. 1.1 (a) shows the principle of this initial set up. Propellants were injected through three or five coaxial injectors (liquid oxygen - gaseous/transcritical methane), and are ejected by the main exhaust nozzle. A secondary nozzle, located at the top of the chamber, is periodically blocked or set open by the toothed wheel inducing pressure oscillations in the chamber. This device was used to establish interactions between the flames and the transverse motion as described for example in (Richecoeur 2006). Unfortunately, the level of oscillation of a few percent of the chamber pressure was too weak to trigger self-sustained instabilities. It also did not quite reproduce conditions which typically prevail in rocket engines when a transverse acoustic instability occurs.

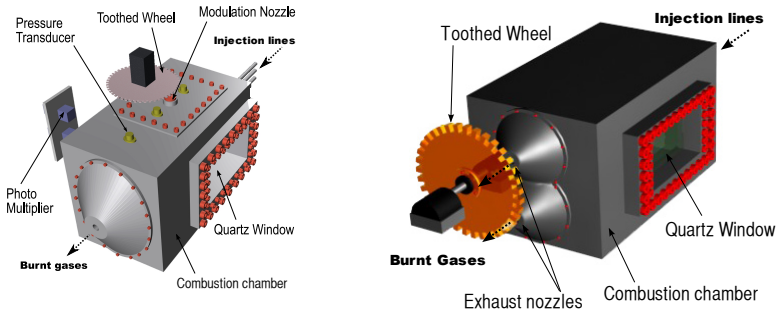

Figure 1.1: *(a) MIC equipped with a lateral toothed wheel modulator and diagnostics - (b) VHAM geometry.*

It was assumed that higher levels of modulation could be obtained by modulating the total mass flow rate. The Very High Amplitude Modulator (VHAM) exploits this idea by making use of an arrangement in which the total mass flow rate injected in the chamber escapes through two nozzles blocked alternately by a toothed wheel (Fig. 1.1 (b)). Propellants are still introduced in the chamber through five coaxial injectors. The wheel is designed so that one nozzle is shut when the other nozzle is open. Gases are exhausted from the chamber through one nozzle at a time. Since the wheel is turning, the gas stream is ejected successively from the top and from the bottom of the chamber. This

induces a pressure drop at the operating nozzle and an acoustic wave is created by this process. The excitation of upper and lower regions of the chamber will favor transverse modes, providing strong resonances at the 1T and 1T1L eigenfrequencies which are typical of the transverse motion under combustion instability. Because the system operates on the total flow rate, it may be possible to generate much higher levels of modulation eventually reaching 20% of the mean pressure, levels which are typically observed in self-sustained liquid rocket instabilities.
The detailed design and manufacturing of the VHAM has been carried out at ONERA and the system has become operational in the fall of 2008. To assist this process, it was decided to develop experiments on a cold flow chamber pressurized with air at a moderate value of 2.5 - 3 bar, and equipped with a VHAM. The objective was to examine the effect of operating parameters and to optimize their value in order to maximize the acoustic response in the chamber. Some geometrical parameters defining the VHAM (wheel diameter, thickness, materials, etc.) were selected on the basis of theoretical and numerical studies (Méry et al. 2007). Other parameters have been defined experimentally with another laboratory system which focused on the understanding of the influence of nozzle length and exit diameter as well as on the influence of mean pressure. This provided useful indications that helped define the full scale VHAM. Some comparisons between experiments and numerical simulation were also carried out previously (Richecoeur 2006).

The objective of the present cold flow system designated as the Transparent Pressurized Cavity (TPC) is to allow an experimental analysis of the unsteady velocity and pressure fields induced by the VHAM. The chamber is transparent with Plexiglas lateral walls providing complete optical access (see Fig. 1.2). This configuration can be used to perform time resolved PIV[1] measurements inside the cavity, using a procedure described by Barbosa et al. (2009).
The TPC can be used to examine various questions. One first wishes to get a better understanding of the transfer of convective energy into acoustic energy and to examine effects of some geometrical parameters (such as nozzle exit diameters). Second, it is interesting to confirm that the velocity field is that corresponding to acoustic eigenmodes identified by the wall mounted pressure sensors. Third, it is instructive to see if the flow field compares well with numerical simulations, especially when some characteristics are neglected (mean velocity, central jet, open/closed nozzles). Experiments on the TPC constitute an excellent test bench for validation of numerical acoustic codes.
Another aspect which can be investigated is the sensitivity of confined jets to external modulations. It is known that free jets are quite susceptible to external acoustic perturbations (Birbaud et al. 2007) but much less is known about

[1]Particle Image Velocimetry

confined jets submitted to transverse excitation. The jet Strouhal number corresponding to the most amplified perturbations is typically controlled by a Strouhal number scaling rule: St $\simeq 0.3$. It is then interesting to examine the coupling between the jet and the transverse motion when the most amplified frequency coincides with that of the acoustic motion.

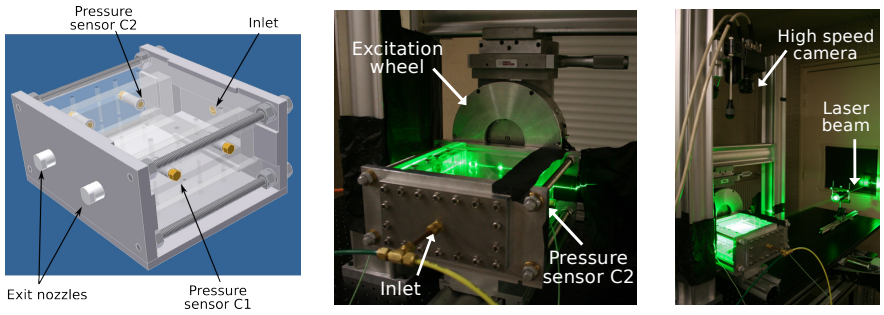

(a) (b) (c)

Figure 1.2: *General view of the experimental test bench - (a) Details of the transparent pressurized cavity - (b) View of the TPC equipped with the VHAM modulator - (c) Optical arrangement for PIV measurements.*

1.2 Experimental methods

Experiments are carried out in the setup shown in Fig. 1.2. The chamber is equipped with a single air injector and operates at a nominal pressure $p_c = 2.5$ bar. The unsteady pressure is recorded by pressure sensors C1 and C2 located on the two sides of the TPC. The unsteady flowfield is deduced from high speed PIV measurements described in the next subsection. The modal identification method is examined subsequently.

1.2.1 Particle Image Velocimetry

Particle Image Velocimetry (PIV) is used in the present investigation to determine the acoustic velocity field induced by the VHAM (Adrian 1991; Adrian 2004). The PIV arrangement is shown in Fig. 1.2 (c). A horizontal laser sheet is transmitted into the TPC from the side. The flow is seeded with small oil droplets and illuminated by this light sheet. A CCD camera collects light scattered by the droplets. Two images of the flow are recorded at two instants in time separated by a short delay Δt. The droplet velocity can then be determined by measuring its displacement vector, $\Delta \boldsymbol{x}$, between the two instants t and $t + \Delta t$. The local droplet velocity will coincide with the local flow velocity if the droplet size is sufficiently small and the droplets follow the flow and

its fluctuations with a negligible time lag. The local velocity of a droplet and consequently the local velocity of the flow is then given by $\boldsymbol{v}(\boldsymbol{x}, t) = \Delta\boldsymbol{x}/\Delta t$. In processing the successive droplet images by cross correlation it is assumed that the statistical droplet displacement is proportional to the average local flow velocity.

The chamber lateral walls are transparent so that the laser sheet can cross the cavity horizontally. The light sheet is generated by a system consisting of two Nd:YAG lasers (*Quantronix*), a laser beam recombining device and a set of cylindrical lenses (*Melles Griot*). Both lasers emit a pulse at a wavelength of 532 nm. The pulse energy and temporal width are 6 mJ and 160 ns respectively. Optics are used to combine both beams along the same trajectory. A set of lenses is used to transform the laser beam into a planar light sheet 90 mm wide and 0.3 mm thick. The Photron Fastcam APX camera can record 1024×1024 pixel images at a rate of 2000 frames per second. It is equipped with a 105 mm F/1.8 Nikon Nikkor objective and placed perpendicularly to the TPC axis.
The two lasers operating at 12 kHz and the camera operating at 24 kHz are synchronized by a pulse delay generator (*BNC* 555 pulse/delay Generator), as shown in the time trace diagram displayed in Fig. 1.3 (a). In addition, tomographic experiments have been performed with a single laser pulsing at 12.5 kHz and the camera operating at the same rate.

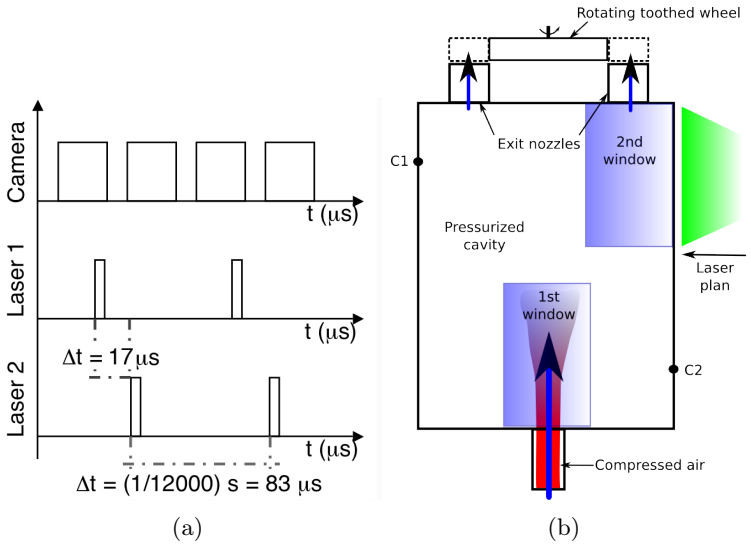

(a) (b)

Figure 1.3: *(a) Time diagram for the time resolved PIV - (b) Zones of interest in the cavity.*

At the rate of 24 kHz (for the camera), the image size must be reduced to 128×512 pixels, a limited size which will be improved using new generation

systems. At a lower frequency of 12.5 kHz images have twice as many pixels (256×512). The airflow is seeded with oil droplets with a nominal diameter $d = 1\,\mu$m. According to Adrian (1991), one can estimate that the error introduced by the droplet time delay due to drag forces is less than 2%. From an estimation of the maximum velocity, one deduces the time delay between the two pulses $\Delta t = 17\,\mu$s at the camera framing rate of 24 kHz.
At 12.5 kHz, with only one laser operating, PIV processing can still be used, but the time lapse (which is then $1/12.5 \times 10^3 \simeq 83\mu$s) is too large to cope with the highest velocities in the chamber. This mode of operation yields the same number of velocity fields than the 24 kHz tests but provides a double-sized window.
The raw image pairs are exported and an off-line image processing is performed with an adaptive cross-correlation code ("Flow-Manager" from *Dantec*) using Fast Fourier Transform algorithms. The raw image pairs are divided into square interrogation windows having final dimensions of 8×8 pixels with an overlap of 25 %. The PIV analysis is optimized to deal with high velocity and density gradients, providing a peak finding error of less than 0.1 pixel in classical applications (Westerweel, Dabiri, and Gharib 1997). Parameters used for the time resolved PIV treatments are gathered in table 1.1.

Sampling				
Field-of-view	Image size	Camera pitch	Frequency	Images nb
x = 48 mm or 24 mm; y = 95 mm	[128 × 512] pixels or [256 × 512]	0.017 mm/px	12 kHz or 24 kHz	24000 or 12000
Processing				
Sub-pixel scheme	Initial window size	Final window size	Overlap	Nb of vectors
Gaussian	[32 × 32]	[8 × 8]	25%	[21 × 85] or [42 × 85]

Table 1.1: *PIV sampling and processing parameters. There are two image sizes and the region observed in the TPC can be modified.*

To get a suitable resolution, the camera has to be focused on specific regions of interest. Two domains identified as most representative of the flow dynamics are shown in Fig. 1.3 (b):
(1) The chamber head region, is used to observe the injected air stream and the acoustic field around the axial pressure node. (2) The flow field in the nozzle vicinity provides indications on the region where the acoustic field is generated. It is interesting to examine this region and see if and how a gas element changes its trajectory when a tooth blocks the nozzle.
The influence of several parameters has been studied (nozzle exit diameters, mean pressure and backplane shape), and for each of these parameters, five tests have been carried out (1) Flow without acoustic modulation, (2) Linear

frequency sweep to find the eigenfrequencies, (3) Continuous wave operation at the 1L eigenfrequency, (4) Continuous wave operation at the 1T eigenfrequency, (5) Continuous wave operation at the 1T1L eigenfrequency. In each of these tests, three camera frequencies and two domains were explored. From the systematic tests carried out with this setup (3 parameters $\times$ 5 types of modulation $\times$ 2 camera frame rates $\times$ 2 domains = 60), we only discuss the most relevant results. The data confirms that the mass flow rate, controlled by the nozzle diameters, is the parameter with the most critical influence on the level of modulation. Results discussed in the next section were obtained with the largest nozzle diameter.

1.2.2 Acoustic mode identification

The modal eigenfrequencies are determined by imposing a constant acceleration to the wheel. The frequency is swept linearly from 0 to 2600 Hz. Signals recorded by the pressure transducers are then processed to determine the short time spectral density and identify the eigenmodes. Continuous Wave (CW) modulation tests are then carried out to excite the 1T and 1T1L eigenmodes. Fig. 1.4 (a) shows results of a linear frequency modulation. Four resonance peaks emerge above the background noise. The two highest peaks respectively correspond to the 1T mode ($t \simeq 7000$ ms) and to the 1T1L mode ($t \simeq 8500$ ms). To identify the eigenmodes, one can use a short time Fourier analysis as exemplified in Fig. 1.4 (b). This figure displays the spectral content of the signal as a function of time. The horizontal and vertical axis correspond to time and frequency respectively while the color contours represent the amplitude of the short time Fourier transform of the signal recorded by a pressure transducer. Hence, the main straight line in the graph is the linear modulation, and the red areas correspond to frequencies where the chamber resonates.
High speed PIV provides a large number of instantaneous velocity fields. The data presented in this article are obtained by digital processing of more than 6000 instantaneous velocity fields for each case. To observe the 1T mode, for example, the wheel is turned on and brought to a fixed angular velocity corresponding to the frequency of the 1T mode of the cavity (here, f_{1T} =1215 Hz). The high speed camera coupled with the laser records a specified number M of periods.
For a frame rate of 24000 images per second one obtains 12000 velocity fields per second. For the 1T mode one gets 12000/1215 $\simeq$ 10 fields per period. Since each instantaneous field also includes effects of turbulent fluctuations and some noise, it is interesting to use conditional sampling and add up images corresponding to the same phase in the cycle. This extracts the acoustic velocity field from the background noise and eliminates the turbulent fluctuations. The phase conditioned results are smooth and easier to interpret as exemplified in Figs. 1.6 (a) and (b). Formally, the velocity field can be cast in the form:

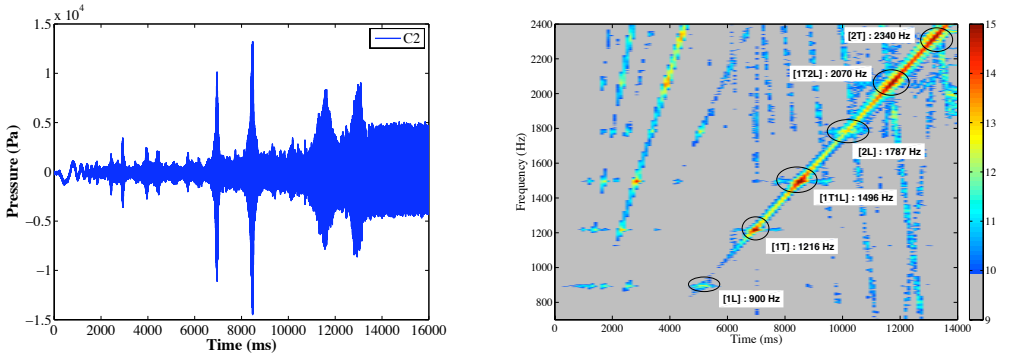

(a) (b)

Figure 1.4: *(a) Time trace of the signal recorded by a side mounted pressure transducer - (b) Short time power spectral density. The frequency is swept linearly from 0 to 2600 Hz.*

$$\begin{aligned} \boldsymbol{v}(t) &= \boldsymbol{v}_a + \boldsymbol{v}_t + \boldsymbol{v}_c + \boldsymbol{n}, \\ \overline{\boldsymbol{v}} &= \overline{\boldsymbol{v}_a} + \overline{\boldsymbol{v}_c} + \overline{\boldsymbol{n}}, \end{aligned}$$

where $\boldsymbol{v}_a$, $\boldsymbol{v}_t$ and $\boldsymbol{v}_c$ respectively correspond to acoustic, turbulent, mean flow velocities while $\boldsymbol{n}$ represents measurement noise. One expects that phase-averaging will reduce the noise component while the turbulent fluctuations will be averaged out. Thus $\overline{\boldsymbol{v}}$ will essentially contain the mean flow velocity which is quite small in most of the domain and the average of the acoustic velocity over a small phase interval $[\phi_1\ \phi_2]$ around the phase used to record each instantaneous image:

$$\overline{\boldsymbol{v}}(\phi) \simeq \frac{1}{N} \sum_{\phi \in [\phi_1\ \phi_2]} \boldsymbol{v}(\phi),$$

where N is the total number of fields having a phase in the range $[\phi_1\ \phi_2]$. One expects to find $\overline{\boldsymbol{n}} = 0$ but the bias introduced by the measurement technique is not arbitrary and the corresponding error can grow when N becomes very large. If the experiment is done correctly, this phenomenon only occurs in limited regions which can be easily identified and eliminated manually.

1.3 Flow configuration in the jet vicinity

1.3.1 Velocity fields

The jet neighborhood is examined in this section by aiming the camera at the first window (see Fig. 1.5 (a)). The velocity field represented in Fig. 1.5 (b)

defines the nominal operating conditions. The mean pressure is $p \simeq 2.5$ bar, the diameter of the exhaust nozzles is $\phi = 1.8$ mm. First, the jet without modulation is studied. One of the exhaust nozzles is closed so that the mass flow rate has the same order of magnitude as that obtained when the wheel is rotating (the wheel shuts one nozzle after the other). The jet spreading angle is relatively small and the maximum velocity on the jet axis is about 16 m.s^{-1}. Note that axis x* and y* represents mm in the reference of each window.

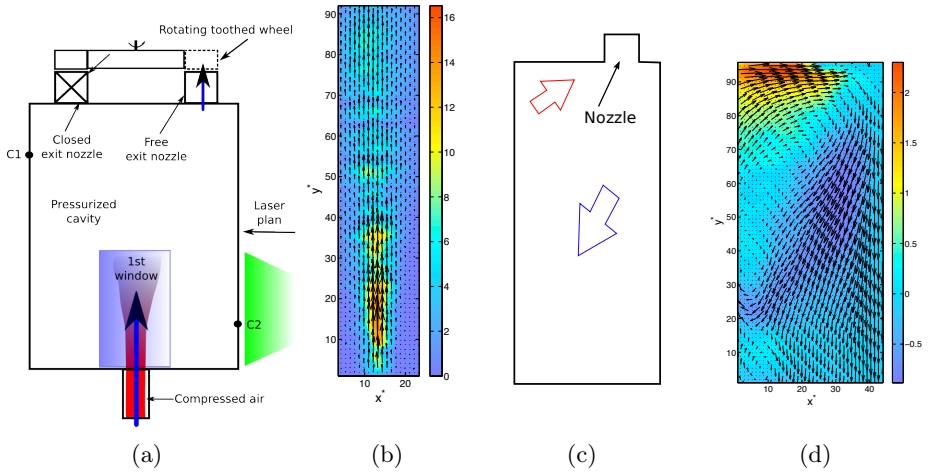

Figure 1.5: *(a) Experimental configuration for a steady flow test - (b) Contour plot of the axial flow velocity in the jet (m.s^{-1})- (c) Schematic representation of the PIV window near the nozzle - (d) Mean flow field without excitation colored by transverse velocity near the nozzle (m.s^{-1}).*

Figs. 1.6 (a) and (b) display velocity distributions at two instants of a period for the 1T and 1T1L modes respectively. Arrows show the direction of the flow, the background color represents the local transverse velocity. This component oscillates between -3 and 6 m.s^{-1} for the 1T mode and between -3.5 and 5 m.s^{-1} for the 1T1L mode (the bias of the velocity vectors towards the right direction is due to a slight dissymmetry of the wheel mounting with respect to the nozzles). These values are relatively important compared to the mean injection velocity of 16 m.s^{-1}. The plots indicate that the flow oscillates from left to right in both cases, which confirms that the motion corresponds to transverse modes. The most important difference between the two unsteady flow fields is that, for the 1T mode, the transverse velocity is always rather constant in the whole domain whereas for the 1T1L mode the velocity amplitude is close to zero at the top of the domain. These differences can be understood by examining numerical simulations, which will be described in section 1.5.

It is also interesting to consider the shape of the jet injected into the TPC. Compared with Fig. 1.5 (b), the angle is larger and the jet spreads more rapidly. This finding is discussed in section 1.3.2.

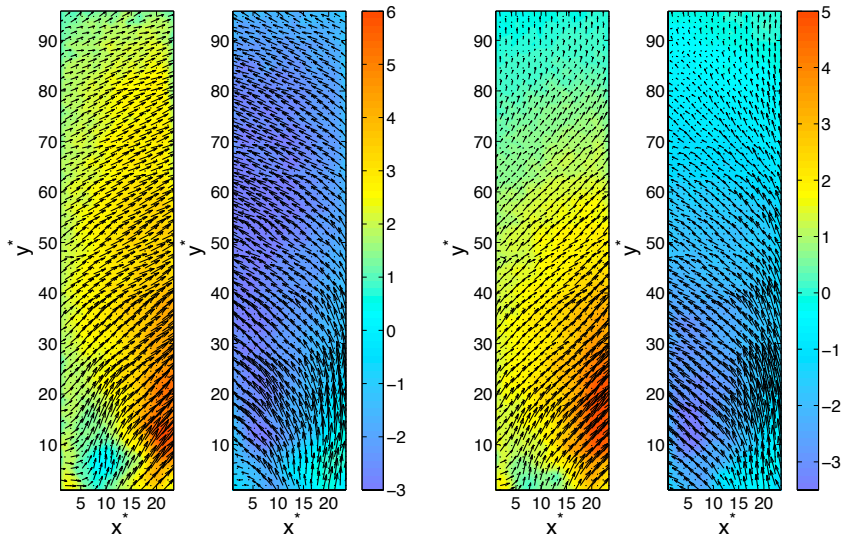

Figure 1.6: *Velocity field in the jet vicinity at two phases in a cycle. The transverse velocity is shown on a color scale ($m.s^{-1}$) - (a) Modulation at 1215 Hz (1T mode) - (b) Modulation at 1453 Hz (1T1L mode)*

1.3.2 Hydrodynamic instabilities

It is natural to examine the possible coupling between the jet hydrodynamic instabilities and the external acoustic modulation. It is known that the initial velocity difference between the jet and the surrounding environment creates a shear region in which the inflectional velocity profile gives rise to instabilities. This phenomenon may intervene in the mechanism of combustion instability. There are fundamental experiments on this topic (Crow and Champagn 1971) and this issue is reviewed in Ho and Huerre (1984) and Ongoren and Rockwell (1988). It is then logical to see if a resonant coupling is possible between transverse acoustic modes and hydrodynamic instabilities.
The growth rate of hydrodynamic instabilities is controlled by a Strouhal number St= fD/U, where f is the frequency, D is the jet diameter, U is the jet velocity and St is the Strouhal number. Experiments on air jets at moderate Reynolds numbers between 100 and 10^4 (Crow and Champagn 1971), indicate that the growth rate of hydrodynamic instabilities reaches its highest value for

a Strouhal number of 0.3. This defines the preferred mode of instability of a free jet. For a diameter $D = 4$ mm, an injection velocity $U \simeq 16$ m.s^{-1} and taking $St = 0.3$ one obtains a preferred frequency of $f = 1200$ Hz which nearly coincides with the 1T eigenfrequency. The spreading angle at the injector exhaust has been measured and is much larger than that corresponding to a naturally developing jet. The jet instability mode is clearly excited. When the excitation frequency is shifted from the eigenfrequency of the cavity, the amplitude of modulation is weaker and the jet spreads as if it were not submitted to an external forcing. The amplitude of modulation has the greatest influence on the spreading angle.
The 1T1L mode ($f = 1453$ Hz) features a very high amplitude of modulation. At this frequency the spreading angle is as important as that corresponding to the 1T mode, indicating that the jet is also receptive over a range of Strouhal numbers surrounding $St = 0.3$. The receptivity of the system is broad and the jet spreading angle remains high even when the modulation frequency differs from the preferred jet frequency.
This short analysis gives some useful information on the coupling between hydrodynamics and acoustics. The interaction modifies the jet shape even when the acoustic frequency does not exactly coincide with the preferred hydrodynamic frequency, as long as the wave amplitude is important enough.

1.4 Flow configuration in the nozzle vicinity

The nozzle area plays a key role in the VHAM operation. The toothed wheel closes the nozzle exit periodically, creating a source in the nozzle convergent which generates an acoustic field in the chamber. This process is now characterized by determining the velocity distribution near the nozzle entrance.

1.4.1 Velocity fields

Velocity distributions were recorded at a regular frame rate of 12.5 kHz because the maximum velocity is lower and can be accurately resolved by using successive couples of images in the sequence. The window size is in this case twice that used previously.
The mean flow field is shown in Fig. 1.5 (d). Since the cavity pressure is around 3 bar and the ambient pressure is 1 bar near the nozzle exit, the flow is naturally oriented outwards (and the nozzle throat is sonic). The mean field indicates that the nozzle acts like a sink and that most of the flow is recirculating. An instantaneous velocity field shows that there are many vortices in the cavity.
Figs. 1.7 (a) and (b) show the velocity field at two instants of a cycle for the two modulation frequencies. The field is organized by the acoustic perturbation, and the vortices have been averaged out by the phase lock averaging technique.

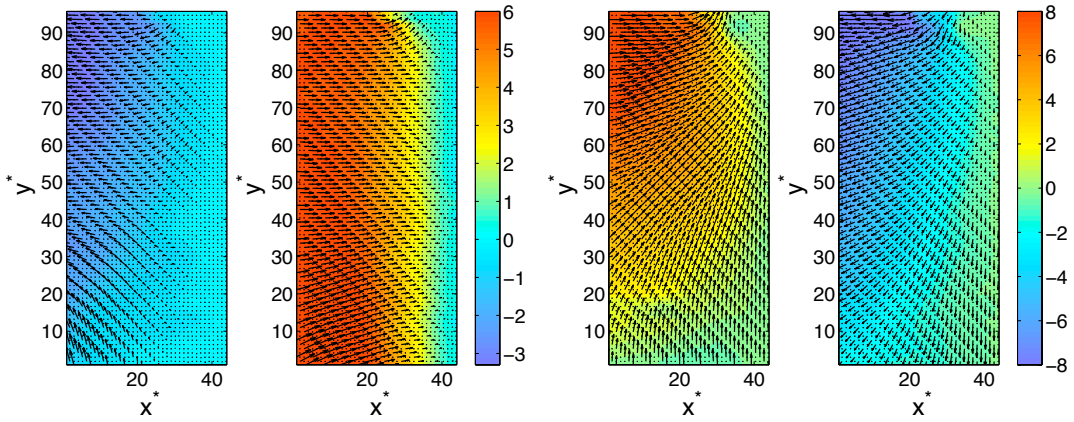

(a) (b)

Figure 1.7: *Velocity field in the vicinity of the nozzle at two phases in a cycle. The transverse velocity is shown on a color scale ($m.s^{-1}$) - (a) Modulation at 1225 Hz (1T mode). In the first field the velocity vectors point away from the nozzle - (b) Modulation at 1461 Hz (1T1L mode). In the second field the velocity vectors point away from the nozzle.*

These figures indicate that close to the nozzle, the velocity changes its direction and the flow field is directed inwards during one half period and outwards during the following half period. The velocity levels reached in this oscillation are quite significant with a maximum of 8 $m.s^{-1}$ for the 1T1L mode. This inversion of velocity direction corresponds to the presence of a tooth which creates a local pressure increase propagating inwards and an oscillatory velocity field.
Spatial features of the velocity fields for the two modes are similar to what was already observed in the injection region. For the 1T mode, the acoustic velocity is essentially transverse. The velocity node is located at the lateral sides of the rectangular cavity. For the 1T1L mode, velocity vectors originate from the left and bottom of the window, which suggests that the node of the velocity field is the corner of the cavity. This explains why this mode is particularly well excited since the excitation point is close to the velocity node and the pressure antinode.

1.4.2 Pressure and velocity consistency

The pressure signals displayed in Fig. 1.8 are measured at the wall of the cavity by two sensors C_1 and C_2 at locations shown in Fig. 1.2 (a). The transverse velocity signal is measured at a point located at $x^* = 13$ mm and $y^* = 77.8$

mm in the window defined in the nozzle vicinity. This velocity component is multiplied by $\rho_0 c$ to allow direct comparisons with the pressure waveform. For the 1T excitation, the signals detected by C_1 and C_2 are out of phase. As expected the velocity signal is in quadrature with the pressure signal detected by sensor C2. It is interesting to note that the various signals have the same level indicating that $\rho_0 c$ suitably represents the scaling between pressure and velocity. This also indicates that pressure measured by wall transducers and velocity determined by PIV are consistent.

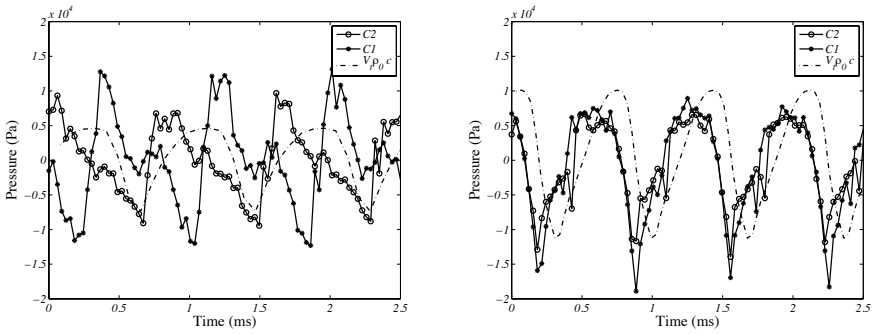

(a) (b)

Figure 1.8: *Pressure evolution recorded by the C_1 and C_2 transducers plotted with the velocity evolution at point $x^* = 13$ mm and $y^* = 75.8$ mm of the field - (a) 1T mode, $f = 1225$ Hz - (b) 1T1L mode, $f = 1461$ Hz.*

1.5 Comparison with numerical results

It is now worth checking wether the experimental data gathered in the TPC can be retrieved from numerical calculations based on an acoustic solver. AVSP is used to this purpose in the VHAM geometry with the aim of calculating the pressure and velocity fields associated with the TPC eigenmodes. AVSP is an acoustic code developed by CERFACS that solves Helmholtz equation. More information on this software can be found in a recent article (Nicoud et al. 2007).

The mesh used for the present calculations comprises $\simeq$ 90000 cells. Rigid walls are used as boundary conditions. The nozzle walls also define velocity nodes but the exhausts are treated by imposing a reduced acoustic admittance: $\beta_* = (\gamma - 1)/2$, where $\beta_* = (u'/\overline{u})/(p'/\overline{p})$ (Marble and Candel 1977). This expression describes the response of a compact choked nozzle to longitudinal pressure waves. The temperature is fixed at 300 K, the mean pressure equals 2.5 bar, and $\gamma = 1.4$.

The fields are determined with AVSP for the different eigenmodes. Fig. 1.9

shows the spatial structure of the transverse velocity for the 1T and 1T1L modes. An important feature of these modes is the antinode locations. For the 1T mode, velocity is maximum on the chamber symmetry axis and the transverse velocity is nearly the same in each constant y section. The 1T1L mode does not show this property. The transverse velocity is stronger near the cavity head and backplane and vanishes near the cavity center.

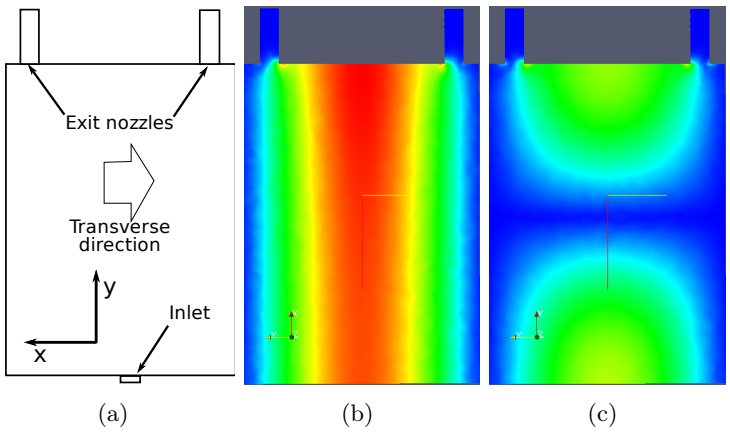

Figure 1.9: *Transverse velocity field for the 1T mode (b) and the 1T1L mode (c) computed with AVSP (blue: velocity node, red: velocity antinode - arbitrary units).*

A comparison with experimental results displayed in Figs. 1.6 (a) (mode 1T) and (b) (mode 1T1L) indicates that these spatial characteristics are well retrieved. For the 1T mode (Fig. 1.6 (a)), the transverse velocity represented by the color levels is almost uniform over the whole window. In contrast, in Fig. 1.6 (b), the horizontal velocity is not only non-uniform, but it also features the patterns observed in the computations: the highest velocity is near the injection plane and the velocity near the center of the cavity (corresponding to the top of the window), is constant and nearly vanishes.
Considering the second observation window located near the nozzle, the comparison between computation and experiment gives complementary elements and a good agreement is also observed. In addition, Fig. 1.7 (a) (phase 2) shows that the transverse velocity is clearly uniform and does not depend on y, in distinction with what is observed in Fig. 1.7 (b) for which, once again, the velocity field distribution depends on the two spatial coordinates.
Finally, in the close vicinity of the exit nozzle, comparison with computational results is not straightforward (Fig. 1.10). Physical phenomena in the nozzle region are difficult to describe only in acoustics terms. The compact nozzle impedance boundary condition used in the calculations does not reflect the complex processes induced by the rotating wheel. An exchange of energy takes place inside the nozzle giving rise to the pressure and velocity fields in the

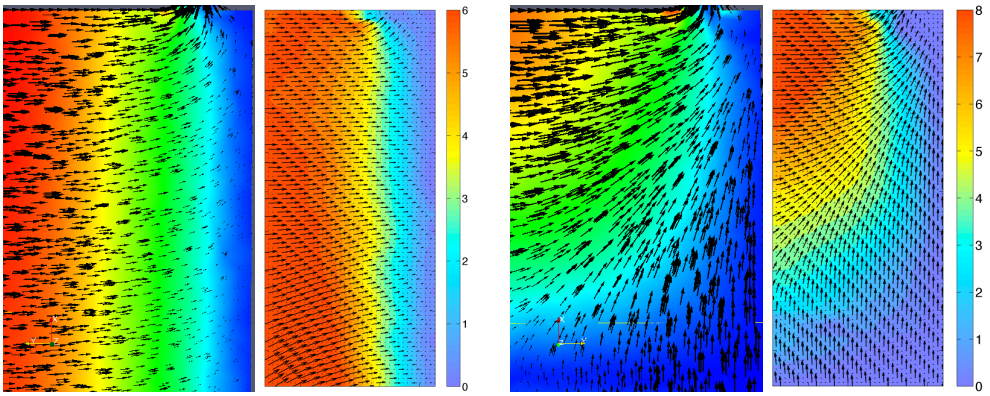

(a) (b) (c) (d)

Figure 1.10: *Comparisons between experimental and numerical results for the window located in the vicinity of the exhaust nozzle. The transverse velocity field is displayed on a color scale. Arrows show the velocity vectors. (a) Calculated field corresponding to the 1T mode - (b) Measured field corresponding to the 1T mode ($m.s^{-1}$) - (c) Calculated field corresponding to the 1T1L mode - (d) Measured field corresponding to the 1T1L mode ($m.s^{-1}$).*

chamber. One should not expect a perfect match between simulation and experiments. However, the calculated velocity patterns in Fig.1.10 (a) and (c) are very close to the measured ones displayed in Fig.1.10 (b) and (d) for the 1T and 1T1L modes respectively.

1.6 Conclusion

This chapter has focused on the structure of pressure and velocity fields generated by the Very High Amplitude Modulator (VHAM). This actuator was designed to generate large amplitude oscillations to allow detailed investigations of high-frequency coupling between transverse acoustic modes and cryogenic flames. The VHAM system is here mounted on a Transparent Pressurized Cavity (TPC) allowing measurements of the velocity field with high speed PIV and providing pressure records at the walls. It is shown that acoustic waves can reach high amplitudes when the system is brought to resonance at the 1T and 1T1L eigenfrequencies. The flow induced by the VHAM has the expected structure and features large velocity fluctuations. It is shown that modulation close to the most amplified jet hydrodynamic frequency augments the jet spreading angle. Velocity distributions are determined numerically with an acoustic solver together with a compact nozzle impedance condition. While transfer of energy taking place in the nozzles is quite complex, it is found that the calculated and experimental velocity patterns are in good agreement.

Chapter 2

Dynamics of cryogenic jets submitted to high amplitude acoustic waves

The VHAM is mounted at a significantly more powerful test facility, the Mascotte bench at ONERA, and the effect of high amplitude oscillations on liquid and transcritical jets is investigated. Five coaxial injectors are distributed in the inlet plane. Dense oxygen is injected in the center while gaseous nitrogen is injected in the coflow. Five pressure sensors set to dynamic mode, while two high speed cameras are used to determine the spatial structure of the pressure modes and their effect on the jets. The acoustic code AVSP is used to predict the spatial structure and frequency of the resonant modes of the cavity in the range of interest. Resonant frequencies are determined by making use of the frequency sweep technique. Modes are identified by comparing numerical results and the phase characteristic of pressure signals. A continuous wave modulation is then carried out on the first transverse mode which demonstrates the dramatic effect of acoustic velocity on the jet structure. The atomization process is enhanced, decreasing core length. Jets oscillate in the transverse direction, creating a non-homogenous distribution of oxygen between the top and bottom of the chamber. The pressure oscillation amplitude reaches 20% of the mean pressure, close to that observed in unstable engines.

2.1 Introduction

Once the Very High Amplitude Modulator (VHAM) is characterized and the acoustic tool is validated, the study can focus on a more realistic configuration. The VHAM is used here to examine the dynamics of cold jets formed by shear

coaxial injectors. Results presented in this chapter concern the mechanism of jet break-up, spray formation and dispersion under strong transverse perturbations. It is generally admitted that these processes are of importance in combustion instabilities but most experiments have been carried out at relatively low levels using loudspeakers (Boisdron et al. 2006) These driver units also have the drawback of limiting experiments to atmospheric pressure. The present experiments were carried out under high pressure conditions (7.5 to 55 bar) with acoustic levels reaching several bar under resonant conditions, which are representative of real engine conditions.
This chapter begins with a description of the experimental set-up (section 2.2). Resonant frequencies and eigenmodes are determined in section 2.3 by solving the Helmholtz equation by assuming a uniform temperature and composition. Experimental results obtained under subcritical and transcritical pressure conditions are described in sections 2.4 and 2.5 respectively.

Remark
In this chapter and in chapter 3, exact chamber dimensions and injector parameters are not given due to confidentiality.

2.2 Experimental set-up

2.2.1 Presentation of the Very High Amplitude Modulator

In the set of experiments carried out by Richecoeur (Richecoeur et al. 2006; Richecoeur et al. 2008) on the Multiple Injector Combustor (MIC) a toothed wheel was used to periodically block the flow exhausted through an auxiliary nozzle (Fig. 1.1 (a)). This induced pressure oscillations in the chamber creating interactions between the flames and the transverse motion. Unfortunately, the level of oscillation was too weak to trigger self-sustained instabilities. It also did not reproduce conditions which typically prevail in rocket engines when an instability arises.
It was reasoned that higher levels of modulation could be obtained by modulating the total mass flow rate, and the VHAM was designed to exploit this idea. Propellants are still introduced in the chamber through five coaxial injectors. The excitation of upper and lower regions of the chamber will favor transverse modes providing strong resonances at the 1T and 1T1L eigenfrequencies which are typical of the transverse motion under combustion instability. Because the system operates on the total flow rate, it was considered that it would provide much higher levels of modulation eventually reaching 20% of the mean pressure, levels which are typically observed in self-sustained liquid rocket instabilities. The objective is to obtain the coupling conditions found in real engines when oscillations have reached a limit cycle.

The detailed design and fabrication of the VHAM has been carried out by ONERA. To assist this process, it was decided to develop experiments at EM2C lab on a pressurized cold flow chamber, which are the subject of the previous chapter (see also Méry et al. (2009))
The geometry of the MIC equipped with the VHAM is represented in Fig. 2.1 (a).

2.2.2 Diagnostics

The MIC shown in Fig. 2.1 (a) is equipped with five pressure sensors located on the top and on the bottom of the chamber. The signals detected by these sensors can be used for modal identification. For example, the first transverse eigenmode of the cavity is obtained when the three sensors placed at the upper wall HF1, HF3 and HF5 are in phase, and when the lower wall sensors HF2 and HF4 are also in phase but when these two groups are out of phase. Two other pressure sensors give the mean pressure in the chamber. Other sensors are located in the injection element to study the coupling between the chamber and the liquid oxygen injection dome, but they will not be examined in what follows.

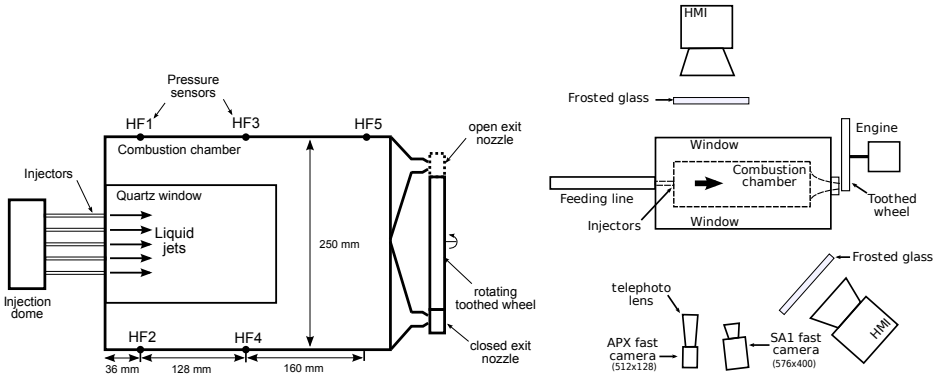

Figure 2.1: *(a) Combustion chamber equipped with the VHAM actuator and five pressure transducers - (b) Arrangement of the optical diagnostics.*

Fig. 2.1 (b) gives a top view of the experimental setup showing the optical diagnostics arrangement. The ICCD camera and the photomultiplier, detecting OH* emission produced by the flames, are not used during the cold flow experiments. Results shown in this chapter are mainly based on data gathered by the two high speed cameras operating in a backlighting mode.
Light is emitted by an HMI spot located in front of the cameras (Fig. 2.1 (b)). The light emitted by the spot is transmitted by the first quartz window, crosses the dense parts of the flow (liquid/transcritical oxygen), passes through the sec-

ond quartz window and is finally detected by the cameras. Light transmission is reduced when it passes through the liquid or transcritical core and through the droplet spray, providing a qualitative information on the jet break-up and atomization process. Images obtained in this way may be difficult to interpret quantitatively because the effect of the dense fluid on the light intensity is integrated over the line of sight. The transmitted light is recorded by Photron Fastcam APX and SA1 cameras synchronized and operating at a frame rate of 24 kHz. The SA1 camera provides a view of the complete combustion chamber with an image size of 576×400 and a resolution of 263 μm/pixel (38 pixel/cm). It is equipped with a Nikkor lens of 105 mm, the aperture is set at F/2.8 and the exposure time is 1/362000 s. The APX camera focuses on the jet located in the middle of the injection plane. The image size is 512×128 and the resolution is 204 μm/pixel (49 pixel/cm), it has a Nikkor telephoto lens (80-200 mm, set at 200 mm), the aperture is fixed at F/5.6 and the shutter exposure is 1/150000 s.
A second HMI spot has also been added, to illuminate the front side of the jets (see Fig. 2.1 (b)). The first part of the jets which are in the shadow is now made visible by this spot thus extending the domain of visualization. Another effect of this secondary HMI light is that it adds a perspective effect, allowing a better understanding of the jet structure.

2.2.3 Experimental parameters

Experiments are carried out under conditions summarized in table 2.1 for three different types of acoustic modulations. In a first test operated without modulation (**OWM**) the modulator is removed and the flow is ejected by the two exhaust nozzles but with a modified throat area to obtain the same chamber pressure. Images gathered in this case are meant to provide a perspective on the atomization of cryogenic oxygen surrounded by a nitrogen coflow and will be used as a reference to understand in what way strong transverse modulation can affect the atomization process.
The modal eigenfrequencies are determined in a second test by imposing a constant acceleration to the wheel (**LFM** for linear frequency modulation). The frequency is swept linearly from 600 to 2000 Hz at a rate of 93 Hz/s. Signals recorded by the pressure transducers are then processed to determine the short time spectral content and identify the eigenmodes.
A third test is carried out by imposing a continuous wave modulation (**CWM**) at one of the frequencies identified in the second step.

	P_{mean}	$\dot{m}_{N_2}$ (g/s)	$\dot{m}_{LOx}$ (g/s)	$\dot{m}_{He}$ (g/s)
OP1	7.5 bar	80	100	15
OP2	55 bar	170	80	30

Table 2.1: *Parameters chosen for the cold flow tests.*

2.3 Numerical simulation

The eigenmode analysis of the chamber is an important step in the analysis of experimental results. A short description of eigenmodes, based on numerical simulation, is carried out in this section. The calculations are based on the AVSP software, which is further described in chapter 5. AVSP solves the classical Helmholtz equations for complex 3D geometries. A realistic mesh is first generated to closely follow the Multiple Injector Combustor geometry. Fig. 2.2 (a), shows from left to right: the LOx dome, filled with liquid oxygen at temperature $T = 80$ K and density $\overline{\rho} = 1190$ kg m^{-3}, the five LOx injectors, the combustion chamber, filled with gases the composition of which is determined in the next subsection, and the two exit nozzles used to operate the VHAM. The mesh is divided in 336208 tetrahedral cells (68121 nodes). A planar cut through the mesh is shown in Fig. 2.2 (b).

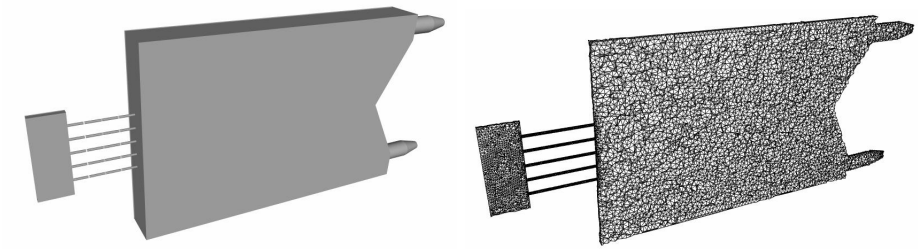

(a) (b)

Figure 2.2: *(a) Geometry of the MIC used to carry out eigenmode calculations - (b) Cut of the corresponding mesh.*

2.3.1 Thermodynamic conditions in the chamber

The sound velocity is given by $c = \sqrt{\gamma(R/W)T}$, with γ the specific heat, R the perfect gas constant, W the mean molar mass of the mixture and T the mean temperature.
Constants γ, W and T are calculated using mass flow rates specified in table 2.1 by assuming that the final mixture is homogeneous. As it will be seen in the

following images of the flow field, this hypothesis is an approximation, since there is a non negligible amount of oxygen which has not been vaporized at the chamber exit. Following experiments also show that the proportion of liquid oxygen vaporized depends on the excitation level. These problems introduce an uncertainty on the sound velocities inside the cavity.
Liquid oxygen is injected at 80 K, helium and nitrogen are injected at 300 K. NIST databases are used to evaluate enthalpies of each species at various temperatures. Conservation of enthalpy provides the final temperature for the two operating points. The characteristic values are given in table 2.2.

	T (K)	γ	W (g mol^{-1})	$\overline{\rho}$ (kg m^{-3})	c (m s^{-1})
OP1	137	1.491	20	14	294
OP2	218	1.497	17.4	53.4	394

Table 2.2: *Chosen parameters for the cold flow tests.*

Remark
In the calculations described in the next section, it is assumed that only 75% of the liquid oxygen is vaporized, which corresponds to $c = 360$ m s^{-1}for OP1 and $c = 430$ m s^{-1}for OP2. This simple hypothesis allows a better comparison between experiments and simulation. This also highlights one limitation of the comparison. It is useful to list other characteristics of the configuration which may intervene in this comparison:

- There are three different gases in the mixture: oxygen, nitrogen, and helium.
- Helium has a low molar mass and its sound speed is quite large. A small change in helium concentration has a large effect on the mean sound velocity in the mixture.
- Oxygen is injected in liquid form, and it needs to be evaporated to be part of the mixture. It is not easy to evaluate the proportion of oxygen which actually evaporates inside the chamber, because it depends on the quality of atomization and external excitation.
- When a mode is excited, the modulation amplitude increases and mixing is enhanced. This affects the mixing of oxygen but also the mixing of helium, which is injected along the lateral boundaries of the domain.

2.3.2 Modal frequencies and spatial distributions

This analysis provides eigenfrequencies given in table 3.4. Only the first transverse mode and the coupled longitudinal and first transverse modes are included

in this table, because other modes (pure longitudinal modes, second transverse modes, etc...), are not excited by the VHAM actuator.

mode	1T	1T1L	1T2L	1T3L	1T4L
OP1	652 Hz	819 Hz	1093 Hz	1296 Hz	1557 Hz
OP2	778 Hz	971 Hz	1299 Hz	1545 Hz	2037 Hz

Table 2.3: *Calculated eigenfrequencies for a uniform temperature distribution. For OP1 (7.5 bar), the sound velocity is* $c = 360\ ms^{-1}$*, while for OP2 the sound velocity* $c = 430\ ms^{-1}$

Eigenfrequencies appearing in table 2.3 correspond to the spatial pressure distributions shown in Fig. 2.3 (the spatial distributions are the same for the two operating points).

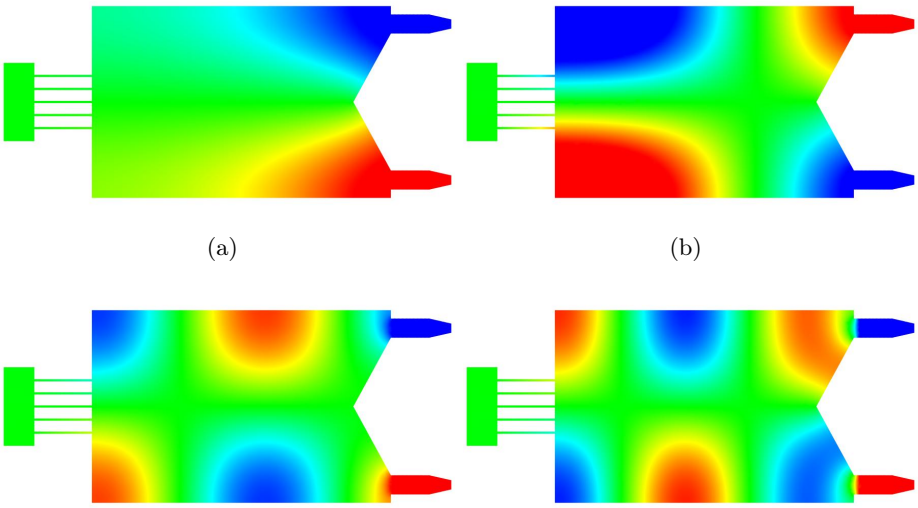

Figure 2.3: *Pressure distribution of the chamber eigenmodes (blue:* $p' = -p_{max}$*, red:* $p' = p_{max}$*) - (a) 1T mode - (b) 1T1L mode - (c) 1T2L mode - (d) 1T3L mode*

Some features can be deduced from the previous calculations.

- For the first transverse mode (1T), in Fig. 2.3, the pressure amplitude is significantly larger near the backplane than in the vicinity of the injection plane. This is indeed observed in the experiments.
- For the 1T1L mode, the amplitude is more important near the injection plane. In the axial direction, the pressure antinode is shifted towards

the chamber endplane. As a consequence, one expects that the pressure transducers HF1 and HF3 will be in phase and HF2, HF4 and HF5 will also be in phase but these two groups will be out of phase.

- For the higher frequency transverse modes, it will be more difficult to predict the pressure transducers phase pattern. Pressure antinodes approach each other as frequency increases and the uncertainty in the relative position of the pressure transducers with respect to the modal distribution is augmented.

2.4 Experimental results under subcritical conditions

Results obtained for the first operating point (OP1) appearing in table 2.1 are examined in this section. The mean pressure of 7.5 bar is well below the critical pressure of oxygen and this substance is injected as a liquid. Mass flow rates of nitrogen, liquid oxygen and helium are respectively 80 g/s, 100 g/s and 15 g/s. The quality of break-up and primary atomization in shear coaxial injectors is commonly characterized by the gas to liquid momentum flux ratio $J = \rho_g v_g^2/\rho_l v_l^2$. For this operating point, $J = 4.1$, which corresponds to a relatively poor atomization process.

2.4.1 Operation Without Modulation (OWM)

It is logical to first examine experiments without external modulation (OWM) in which the actuator is removed. In this test, the shutter speed for the SA1 and the APX cameras were respectively of 1/120000 s and 1/70000 s (smaller than the values used later on). Because of this choice, one cannot distinguish droplets and the liquid inclusions are slightly blurred.
Due to the low value of the momentum flux ratio J, the intact core length is important and the visualization window is too short to observe the complete atomization process. Droplets are extracted out of the jet (Fig. 2.4) but the jet itself is only destabilized at a distance of approximately 17 diameters from the liquid injector exhaust.

2.4.2 Linear Frequency Modulation (LFM)

During the linear frequency sweep (LFM), the pressure amplitude signals are highly variable as shown in Fig. 2.5 (a). To identify the eigenfrequencies, one uses a short time Fourier analysis as already proposed in chapter 1 and exemplified in Fig. 2.5 (b). This figure displays the spectral content of the signal detected by the HF2 sensor as a function of time. The horizontal and vertical axis correspond to time and frequency respectively while the color contours represent the amplitude of the short time Fourier transform of the signal recorded

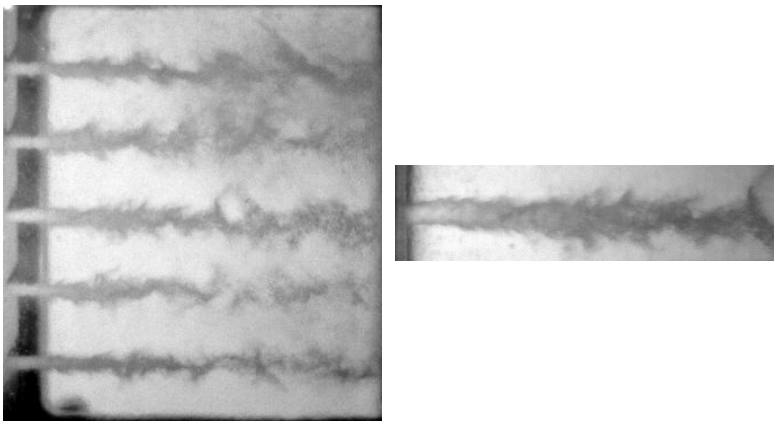

Figure 2.4: *Backlighting images of the five jets without modulation - (left) Fastcam SA1 camera - (right) Fastcam APX camera.*

by a pressure transducer. In this graph the main straight line defines the linear frequency sweep, and the red areas correspond to frequencies where the chamber resonates. Six peaks emerge well above the background noise.

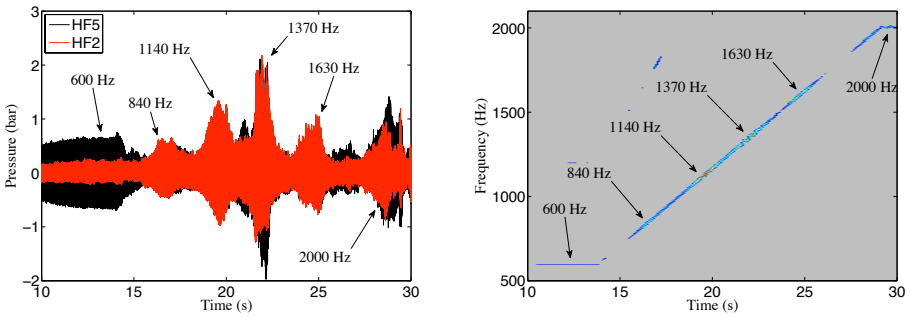

(a) (b)

Figure 2.5: *(a) Time recording of the LFM test - (b) Periodogram obtained by post-processing the HF2 response during the LFM.*

Modal identification then relies on an examination of the phase difference between the pressure transducers. Signals displayed in Fig. 2.6 (a) correspond to a frequency of 600 Hz. Pressure transducers HF1, HF3 and HF5 are in phase, HF2 and HF4 are also in phase and their phase is opposed to that of HF1, HF3 and HF5. This behavior is expected from the first transverse mode (1T). Numerical calculations, reported in section 3, indicate that the frequency of the 1T mode at operating point 1 (OP1) should be 699 Hz (see table 3.4), which is

in reasonable agreement with the value obtained here, given the uncertainty on the speed of sound, geometry and boundary conditions used in the simulation. It is interesting to examine the relative amplitudes recorded by the pressure sensors. The level at HF5, near the chamber endplane, is much more important than that detected by the other transducers. The amplitudes at HF3 and HF4 are also more important than those prevailing at HF1 and HF2. These features give an idea on the mode shape which is in good agreement with the numerical distribution of the 1T mode displayed in Fig. 3.3 (a).
Fig. 2.6 (b) displays signals recorded at 840 Hz. HF1 and HF3 are in phase, HF2, HF4 and HF5 are in phase and the two groups are out of phase. Considering the modes plotted in Fig. 2.3, this configuration corresponds to the 1T1L mode (Fig. 2.3 (b)). The predicted frequency was 813 Hz, which is close to the eigenfrequency deduced from the short time Fourier analysis thus confirming that this peak corresponds to the 1T1L mode.
Identification based on the phase difference of the transducers becomes more difficult for higher order modes, because the uncertainty on the sensor positions with respect to the nodal lines of the pressure distribution corresponding to the 1T2L, 1T3L and 1T4L modes increases. For example, in Fig. 2.6 (c), the signal recorded by HF5 barely oscillates, indicating that this transducer is located near a pressure node. It is still possible to verify that the phase differences are consistent, but it is more convenient to base the modal identification on the calculated eigenfrequencies. Table 2.3 gives $f_{1T2L} = 1093$ Hz, $f_{1T3L} = 1415$ Hz and $f_{1T4L} = 1706$ Hz. Signals plotted in Fig. 2.6 (c), (d) and (e) are recorded at $f = 1140$ Hz, 1370 Hz and 1630 Hz, which are close to the calculated frequency values. Table 2.4 allows a direct comparison between experimental frequencies and values estimated with AVSP.

mode	1T	1T1L	1T2L	1T3L	1T4L
Num	652 Hz	819 Hz	1093 Hz	1296 Hz	1557 Hz
Exp	600 Hz	840 Hz	1140 Hz	1370 Hz	1630 Hz

Table 2.4: *Comparison between experimental and numerical eigenfrequencies obtained for operating point OP1.*

The amplitude of the eigenmodes, displayed in Fig. 2.6, varies from 0.6 bar to 1.7 bar depending on the eigenmode and on the transducer. This corresponds to an intense acoustic fields (1.7 bar of amplitude corresponds to 195.6 dB). This last value, compared to the mean pressure of the chamber (7.5 bar) yields a relative modulation amplitude of 22.7% , which is of the same order of magnitude as levels observed in rocket engines undergoing combustion instability.

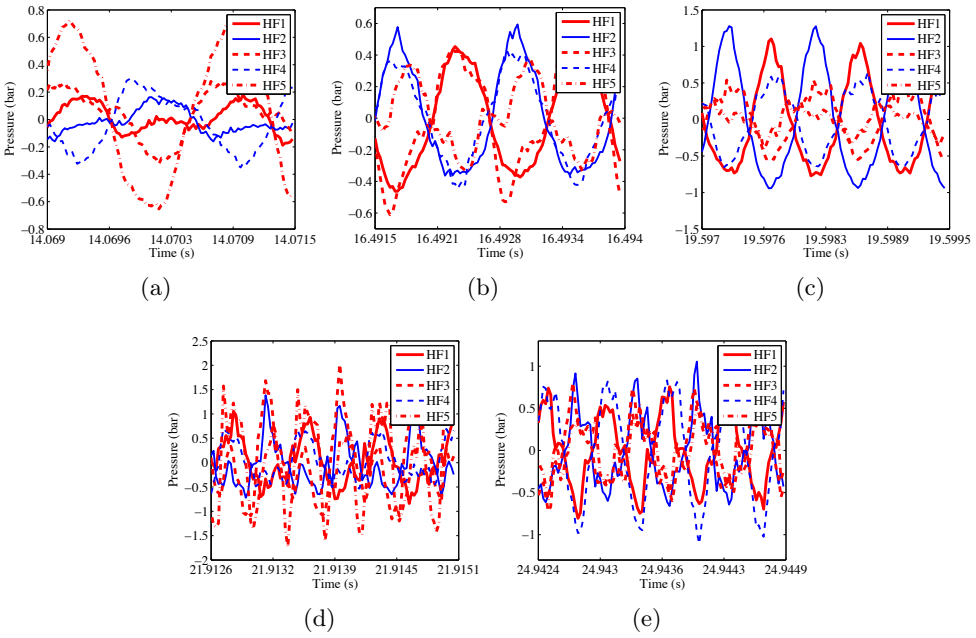

Figure 2.6: *Records of the five pressure sensors obtained by zooming on the peaks determined in the LFM test - (a) 600 Hz (1T mode)- (b) 840 Hz (1T1L mode) - (c) 1140 Hz (1T2L mode) - (d) 1370 Hz (1T3L mode) - (e) 1630 Hz (1T4L mode).*

2.4.3 Continuous Wave Modulation (CWM)

The continuous wave modulation test case described below corresponds to the 1T1L mode (840 Hz). The response is not as important as that of other modes identified previously, but its spatial structure is well defined. The backlighting results for the SA1 camera are shown in Fig. 2.7. Fig. 2.8 provides a close-up view of the central jet for the same instants. These last data have been obtained with the APX camera. The jet motion is cyclic. Since the cameras operate at 24 kHz, they record more than 28 images per period, which is more than sufficient to describe the motion.

Each jet behaves like a “flag", flapping in space with an increasing amplitude. The amplitude of oscillations measured from these images reaches approximately six liquid jet diameters (6 d_{LOx}). Droplets formed at the end of the core are distributed sideways with great momentum, enhancing mixing, and reducing the core length to about forteen liquid jet diameters (14 d_{LOx}). This produces a nonuniform pattern of droplets in the chamber. Since the jets are parallel, when they are all submitted to a velocity directed towards the top of the chamber (Fig. 2.7 (a) and 2.8 (a)), an amount of oxygen is accumulated

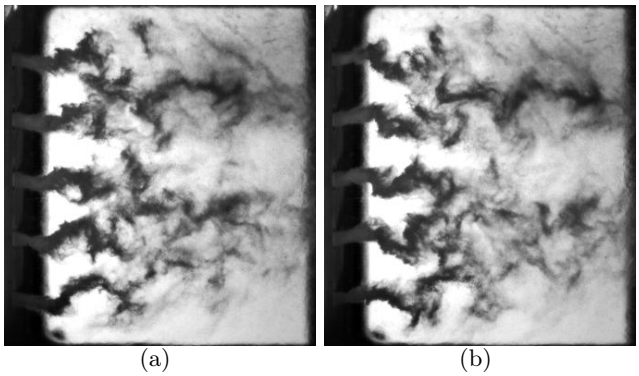

(a) (b)

Figure 2.7: *Backlighting images of the five jets submitted to a 1T1L mode (840 Hz) at two instants of a period, obtained with the Fastcam SA1 camera - (a) $\phi = 0$ - (b) $\phi = \pi/2$.*

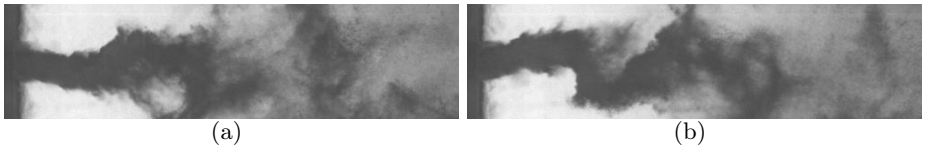

(a) (b)

Figure 2.8: *Backlighting images of the central jet submitted to a 1T1L mode (840 Hz) at two instants of a period, obtained with the Fastcam APX camera - (a) $\phi = 0$ - (b) $\phi = \pi/2$.*

in this region while less oxygen is available in the bottom part. The organized motion associated with the transverse acoustic modulation is best visualized by forming phase average images (Fig. 2.9). These images clearly exhibit the nonuniform pattern of liquid droplets formed by the transverse modulation. Since oxygen is the limiting reactant in a rocket engine, this dissymmetry in the oxygen density field may be of great importance in the instability process.

2.5 Experimental results under transcritical conditions

It is interesting to examine the same processes under transcritical injection conditions (operating point OP2 in table 2.1). The chamber pressure is set at 55 bar and exceeds the critical pressure of oxygen ($p_c(O_2) = 50.4$bar) while the injection temperature of oxygen is below the critical value $T_c(O_2) = 151.4$ K). Mass flow rates of nitrogen, liquid oxygen and helium are respectively 170 g.s^{-1}, 80 g.s^{-1}and 30 g.s^{-1}.

2.5.1 Operation Without Modulation (OWM)

For this set of parameters, the gas to liquid momentum flux ratio is $J = 5.1$, which is slightly above the value for the previous operating point. While the two values of momentum flux ratio are close, Fig. 2.10 indicates that the dense jets have a different appearance. As the liquid oxygen is injected in a transcritical state there is no liquid gas interface and the surface tension has vanished. Atomization is replaced by mass transfer from the dense oxygen core at low temperature to the surrounding stream at a higher temperature. The rate of transfer is governed by the amount of surface separating the dense and lighter fluid and by the local strain rates. The length of the dense core is reduced in this case indicating that the transfer process is more intense than in the subcritical case.

2.5.2 Linear Frequency Modulation (LFM)

The linear frequency modulation test is used to determine the resonant frequencies of the system. The temporal response is plotted in Fig. 2.11 (a), and the short time spectral analysis of the HF5 transducer is displayed in Fig. 2.11 (b). Four spectral peaks emerge from the background noise.
These peaks can be associated to the chamber eigenmodes by considering the phase and amplitude differences between the pressure sensors located on the upper and lower walls as done previously. The signals in Fig. 2.12 - (a-d) respectively correspond to the 1T, 1T1L, 1T2L and 1T3L modes. The corresponding frequencies are (720, 970, 1340 and 1640 Hz) which are close to values predicted

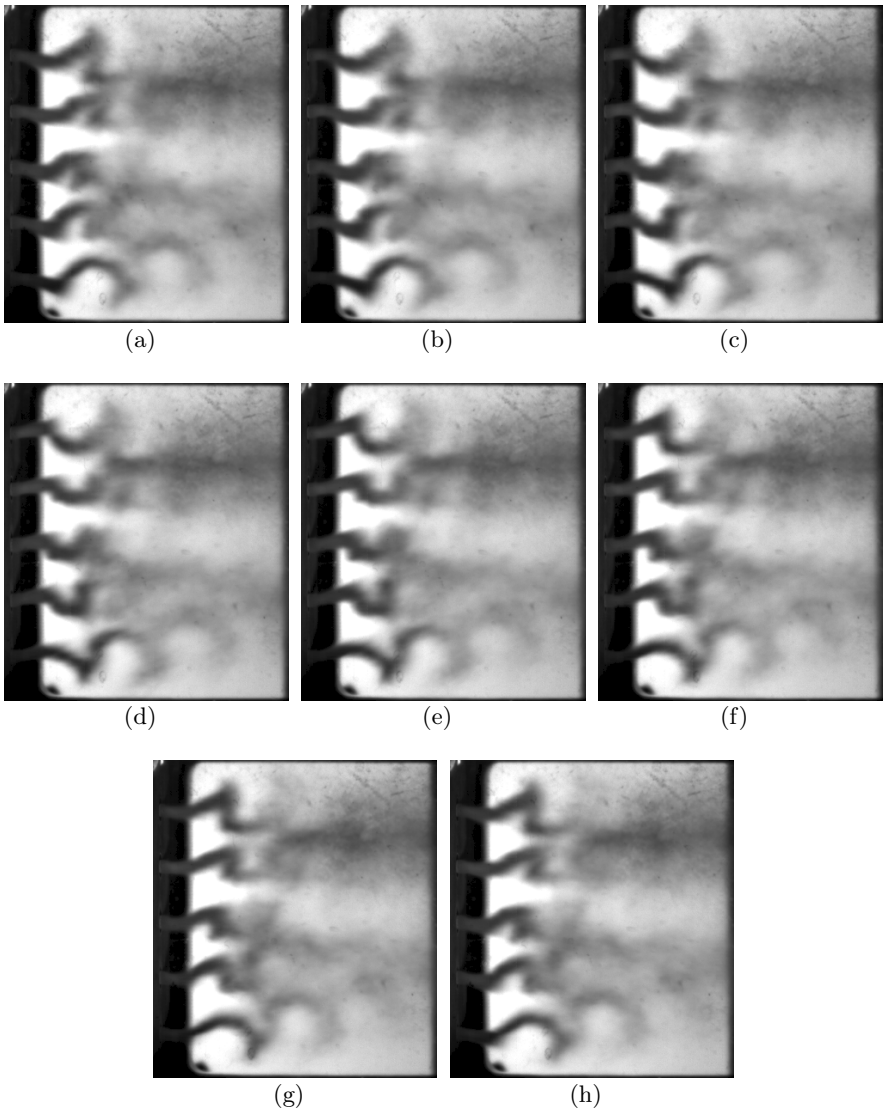

Figure 2.9: *Phase conditioned average backlighting images of the five jets submitted to a 1T1L mode (840 Hz) at eight instants of a period, obtained with the Fastcam SA1 camera. Approximately 100 images are summed to form each each phase conditioned image - (a)* $\phi = 0$ *- (b)* $\phi = \pi/4$ *- (b)* $\phi = \pi/2$ *- (b)* $\phi = 3\pi/4$ *- (b)* $\phi = \pi$ *- (b)* $\phi = 5\pi/4$ *- (b)* $\phi = 3\pi/2$ *- (b)* $\phi = 7\pi/4$.

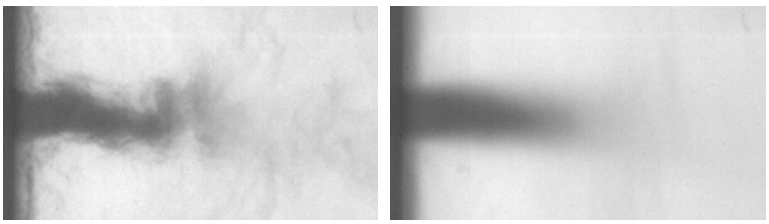

(a) (b)

Figure 2.10: *Backlighting image of the non-modulated jet (OWM) at operating point OP2 - (a) Instantaneous image. Oxygen is injected in a transcritical state, there are no droplets - (b) Average image.*

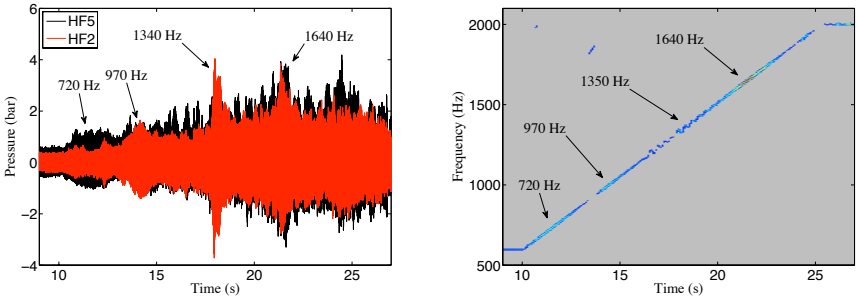

(a) (b)

Figure 2.11: *(a) Time recording of the LFM test - (b) Periodogram obtained by post-processing the LFM data.*

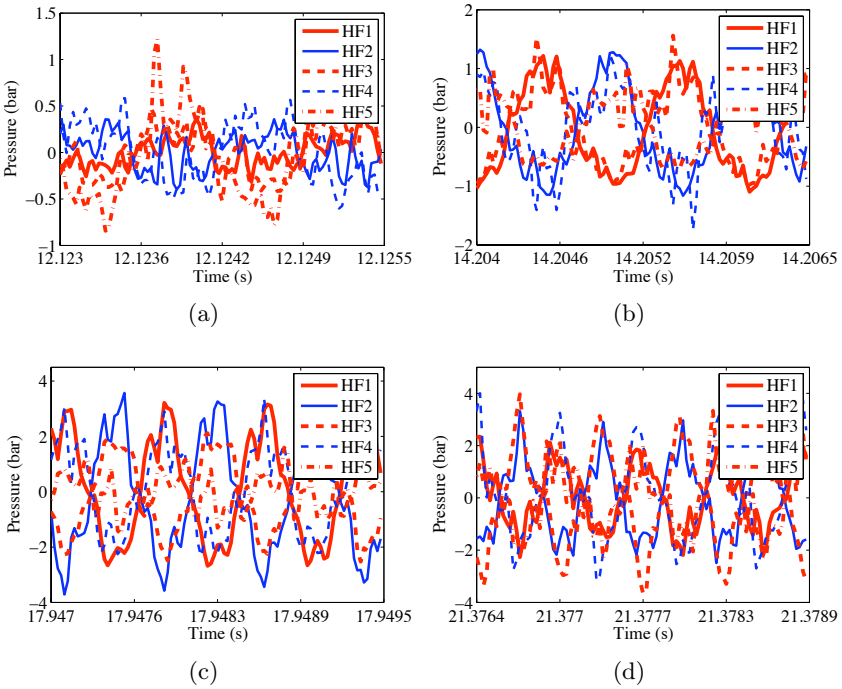

Figure 2.12: *Recording of the five pressure sensors obtained by zooming on the peaks of the LFM test - (a) 720 Hz (1T mode)- (b) 970 Hz (1T1L mode) - (c) 1340 Hz (1T2L mode) - (d) 1640 Hz (1T3L mode).*

numerically (778, 971, 1299 and 1545). The comparison between experimental and numerical results is shown in table 2.5.

mode	1T	1T1L	1T2L	1T3L
Num	778 Hz	971 Hz	1299 Hz	1545 Hz
Exp	720 Hz	970 Hz	1340 Hz	1640 Hz

Table 2.5: *Comparison between experimental and numerical eigenfrequencies obtained for operating point OP2.*

In Fig. 2.12 (a), the signals are similar to those observed at 7.5 bar. The level of the HF5 transducer is more important than that detected by the other sensors, indicating that the acoustic amplitude near the endplane is stronger than near the injection plane, which is in agreement with numerical results. A difference with previous measurements is that the broadband noise level is augmented. This is due to the higher mass flow rates used in the present case. The structure of the 1T1L mode is well identified in Fig. 2.12 (b), with a phase pattern in

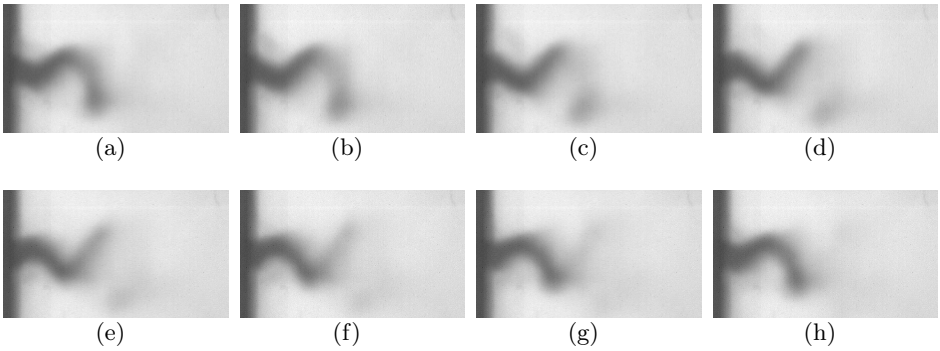

Figure 2.13: *Phase average backlighting images of the five jets submitted to a 1T1L mode (970 Hz) at eight instants of a period, obtained with the Fastcam APX camera. Approximately 100 images are used to form each phase conditioned image - (a) $\phi = 0$ - (b) $\phi = \pi/4$ - (b) $\phi = \pi/2$ - (b) $\phi = 3\pi/4$ - (b) $\phi = \pi$ - (b) $\phi = 5\pi/4$ - (b) $\phi = 3\pi/2$ - (b) $\phi = 7\pi/4$.*

which HF1 and HF3 are out phase with respect to HF2, HF4 and HF5.
The response reaches 4 bar in amplitude, corresponding to extremely high acoustic levels. However, this is less than 20% of the mean chamber pressure. It is found that the amplitude of the acoustic perturbation does not scale like the mean pressure in the chamber but rather as a function of the mass flow rate which is being modulated. For OP2, the mass flow rate is only multiplied by 2 compared to OP1. The acoustic response is also multiplied by a similar factor.

2.5.3 Continuous Wave Modulation (CWM)

The continuous wave modulation test corresponds to the resonant frequency of the 1T1L mode (970 Hz). The effect of acoustics on the jet is visualized by taking phase averages of the high speed camera images. The averaged cycle of oscillation is shown in Fig. 2.13. Compared to the mean shape of the jet in the absence of modulation (Fig. 2.10), the dense core length is not much modified. However, the jet oscillates in the transverse direction, which changes the oxygen distribution. One can see that the jet shape is modified by the stresses imposed by acoustic velocity and that dense pockets of oxygen are shed away from the jet (images (c), (d) and (e)).
In the case of a mixing layer between two fluids of very different densities, it is known (Villermaux 1998) that the group velocity of flow perturbations can be estimated by:

$$v_c = \frac{\sqrt{\rho_g} v_g + \sqrt{\rho_l} v_l}{\sqrt{\rho_g} + \sqrt{\rho_l}}. \tag{2.1}$$

Together with the frequency of modulation (970 Hz), this gives a typical wavelength for the jet motion induced by the acoustic field of $\lambda = v_c/f \approx 5$ mm. In the frames shown in Fig. 2.13, the first wavelength can be measure and one finds $\lambda \approx 8$ mm, which is close to the expected value. Downstream, near the end of the core, the wavelength increases due to the gaseous jet influence.

2.6 Conclusions and perspectives

Experiments have been carried out to study the influence of high amplitude acoustic perturbations on cryogenic jets formed by shear coaxial injectors. The configuration includes five jets formed in a rectangular chamber equipped with quartz windows and pressure transducers. A novel modulator (VHAM) designed to create intense acoustic fields, is employed to generate relative pressure fluctuations $p'/\overline{p}$ of the order of those found in real engines when instabilities occur. Results are reported for cold flow injection and two operating pressures, the first (7.5 bar) is well below the critical value of oxygen while the second (55 bar) is above that value. The dynamics of flow is examined by first running the facility without modulation. A linear frequency sweep (LFM) is then used to determine the resonant frequencies and identify the excited modes. The third case is carried out by imposing a continuous wave modulation at one of the eigenfrequencies determined in the second step. Wave amplitudes created by the VHAM reach expected values ($p'/\overline{p} > 20\%$). The structure of the acoustic field in the chamber determined experimentally corresponds to that calculated by solving the Helmholtz equation for a uniform speed of sound. The comparison between experimental signals and predictions allows a reliable identification of the successive modes and improves the signal interpretation. The dense jet break-up and atomization is modified by the acoustic field as deduced from backlighting technique and two high speed cameras. It is found that the core length is reduced by a large amount and that the jets are set in a large scale group motion imposed by the acoustic velocity field. This produces a periodic nonuniformity of the oxygen content in the chamber. This can be considered as one of the mechanisms driving combustion instabilities. These cold flow tests also indicate that the VHAM will give valuable information on the coupling between cryogenic flames and transverse modes under hot fire conditions. This is investigated in the next chapter.

Chapter 3

Dynamics of cryogenic flames submitted to high amplitude acoustic waves

In this chapter, cryogenic (liquid and transcritical) flames are submitted to high amplitude transverse waves, leading a step closer to real engine conditions. Two high speed cameras are used to study time resolved dynamics of the dense oxygen (backlight) and heat release (CH^* emission) in the chamber. Acoustic modes are determined numerically and experimentally using the same procedure as the one described in chapter 2. During most responding test cases, extreme acoustic amplitudes are reached (9 bar for a mean pressure of 26 bar). This response goes along with a modification of the flames' shape, as the flames become significantly shorter. The wall temperature increases, and flames oscillate in the transverse direction. An asymmetry of the combustion area and of the acoustic mode is also observed. These features are thought to be consistent with what occurs when a rocket engine becomes unstable. Using these observations, a mechanism involving the effect of acoustics on atomization and the flame transverse motion is built. Its relevance in the representation of combustion instabilities is discussed in subsequent chapters.

3.1 Introduction

Experiments reported in this chapter were carried out on the cryogenic combustion test facility “Mascotte" of ONERA, already described in the previous chapter. Nitrogen injected for the previous experiments is now replaced by gaseous methane.

The Multiple Injector Combustor (MIC) is used to gather information on high frequency combustion dynamics and combustion acoustic coupling. Previous work (Richecoeur 2006) has already shown an influence of acoustic modes on flame structure, but the oscillation level, which reached in one case about 8% of the chamber pressure, was too weak to represent conditions prevailing in rocket engine thrust chambers undergoing high frequency instability conditions. This led to the development of the Very High Amplitude Modulator (VHAM), a new modulation system which could generate higher acoustic amplitudes under resonant conditions. The concept and some applications of the VHAM under cold flow conditions are described in previous chapters. The VHAM is now used under hot fire conditions to generate transverse modes and analyze their impact on flame dynamics.
The influence of several parameters is investigated, by varying the mean pressure and momentum flux ratio, and by scanning different eigenmodes. The first objective is to link the flame dynamics to the acoustic modes. This is accomplished by examining pressure sensor signals, photo-multiplier signals and images recorded by two high speed cameras. These data are complemented by images of the mean flame shape under acoustic modulation as observed with an intensified ICCD camera operating at a low frame rate. It is shown that combustion dynamics are linked to the break-up and atomization processes when the mean pressure is below the critical value ($p < p_c(O_2)$) and to the mass transfer process from the high density oxygen jets when the mean pressure exceeds the critical value.

3.2 Diagnostics and experimental procedure

The study of high frequency combustion dynamics requires a combination of sensors and imaging methods discussed in the next subsection. These tools are exploited in an experimental procedure including linear frequency sweep experiments which are mainly used to identify the eigenmodes of the system and continuous wave modulation tests at the various resonant frequencies. This procedure is explained next.

3.2.1 Diagnostics

The Multiple Injector Combustor (MIC) shown in Fig. 3.1 (a) is equipped with five pressure sensors located on the top and bottom walls of the chamber. These sensors operate in the dynamic mode to record the unsteady variations of pressure. The signals detected by the wall sensors can be used for modal identification. One pressure sensor, set in steady mode, provides the mean pressure in the chamber. Another one, located in the liquid oxygen injection dome, aims at identifying the possible coupling between the chamber and the

LOx dome. The mean temperature in the chamber is measured by a type K thermocouple inserted in the bottom wall of the chamber. All the dynamic pressure sensors are sampled at a rate of 40 kHz. The mean pressure sensor and the thermocouple are recorded at 10 kHz.

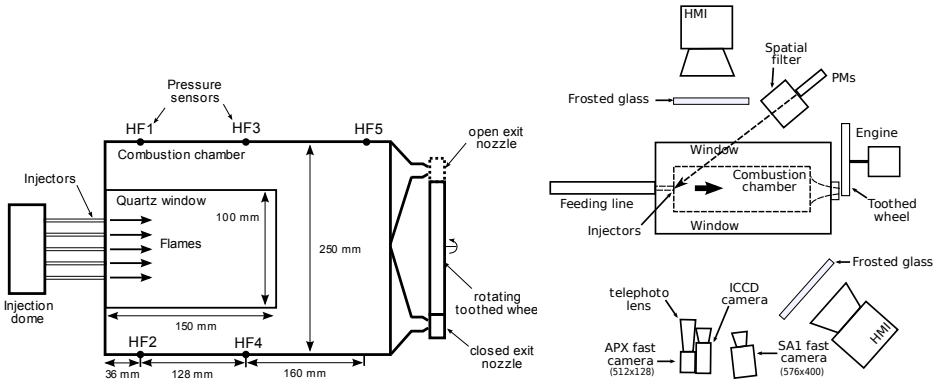

Figure 3.1: *(a) Combustion chamber equipped with the VHAM actuator and five pressure transducers. HF1, HF3 and HF5 (odd numbered sensors) are placed on the upper wall. HF2 and HF4 (even numbered sensors) are located on the lower wall - (b) Top view of the optical diagnostics arrangement. HMI designate continuous light spots. The photomultipliers PM1 and PM2 (PMs on the scheme) are located on a vertical line and point towards the injection plane.*

Fig. 3.1 (b) shows a top view of the optical diagnostics arrangement. This includes three cameras and two photo-multipliers. The Photron Fastcam SA1 camera operates at a frame rate of 24 kHz. This camera provides a view of the complete combustion chamber with an image size of 576×400 and a resolution of 263 μm/pixel (38 pixel/cm). It is equipped with a Nikkor lens of 105mm and a CH* filter. It is known that the filtered signal can be linked to heat release rate but the relationship is less well established than in the premixed case. The other high speed camera, the Photron Fastcam APX, also operates at 24 kHz and is synchronized with the Fastcam SA1. It focuses on the central jet. The image size is 512×128 and the resolution is 204 μm/pixel (49 pixel/cm). This camera is equipped with a Nikkor telephoto lens ($80 - 200$mm, set at 200mm), and operates in a backlighting mode to locate the position and dynamics of the dense oxygen jet, droplets or packets. Light is emitted by the HMI spot located in front of the cameras (Fig. 3.1 (b)). As already mentioned in chapter 1, images obtained in this way may be difficult to interpret quantitatively because the effect of the dense fluid on the light intensity is integrated along the line of sight. It should be noted that the SA1 camera detects a part of the white light

emitted by the spot, even when a filter is used to isolate the light emitted by CH* radicals. To avoid an important bias, a careful setting of the imaging diagnostic is needed and requires a trade-off between two opposing goals. On one hand, when the spot light is intense, the backlighting results are suitably contrasted but the CH* emission recorded by the SA1 camera is perturbed by the contribution of the white light near the CH* wave length. On the other hand, when the spot light is weaker, the flame contrast recorded by the SA1 camera is good, yet the liquid jet can barely be distinguished in images obtained by the APX camera. A trade-off, involving the intensity of the HMI spot, exposure time and aperture of the cameras, must be found. Since this trade-off strongly depends on the mean light emitted by the flame, which is difficult to predict, it is necessary to adjust the light level by a trial and error process, which depends on the operating point characteristics.
Considering the important flux of data when the cameras are operating at 24 kHz, the recording time is limited, at a typical value of 1 s (which corresponds to 24000 images).
An intensified camera (ICCD), providing a high dynamic range (16 bit), is also used. The field of view contains major parts of the chamber. It is equipped with a Nikkor UV lens of 105 mm and with an OH* filter (88SA). The OH* emission of a flame can also be linked with the heat release. In the present case, the critical benefit of the OH* peak compared with the CH* peak is that its wavelength is located in the near UV of the light spectrum. The white light created by the HMI has a negligible contribution in the UV range of the spectrum, and no interferences are observed between the two diagnostics. The ICCD camera operates at a low rate (approximately 15 Hz) and cannot be used to study the dynamics of the process. Because this camera operates during the entire test case it provides interesting information on the mean shape of the flame during the linear sweep tests.

At this point it is interesting to see if the different optical diagnostics yield consistent data. This is done by comparing the high dynamic range OH* images obtained with the ICCD camera and the high speed CH* data obtained with the SA1 camera (Fig. 3.2). In general, images obtained at the same instant are quite similar, with only minor differences. There is a slight difference in axial size due to the fact that the ICCD camera is perpendicular to the combustor axial plane, whereas the SA1 observes the chamber with a finite angle. The injector near field is less well observed by the SA1 camera. The perspective is also modified and the flames seem shorter in the SA1 images. Except for these differences, results are in agreement. The OH* and the CH* emission regions have similar structures.
In addition to high speed images it is interesting to record time resolved signals corresponding to free radicals emitted from the flames. This is accomplished

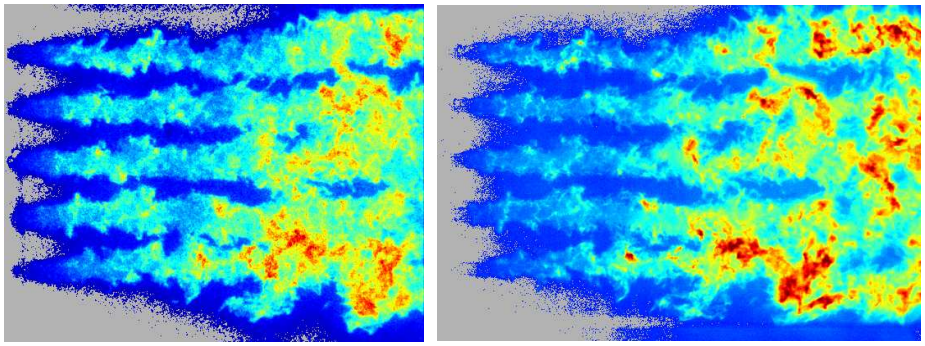

(a) (b)

Figure 3.2: *ICCD (a) and SA1 (b) images taken at the same instant. The flame structure is similar, which establishes consistency between the two diagnostics. (PF4 operating point, in the absence of external modulation (OWM).*

with two photo-multipliers (PM), equipped with OH* filters: PM1 detects OH* radiation from the upper part of the chamber while PM2 records OH* radiation from the bottom part. This arrangement is used to obtain the time evolution of heat release in the transverse direction of the chamber, which plays a key role in the understanding of HF coupling between combustion and transverse modulations. A spatial filter, reducing the solid angle, is set so that the upper PM does not detect light emitted from the bottom of the chamber, and vice versa. In Fig. 3.1 (b), the photomultipliers are oriented to record light originating from the injector nearfield. This arrangement is more suitable than the one in which the PM couple is oriented in the downstream direction because important variations of the flame length under strong modulations have a direct impact on the signal level recorded by the system. In some tests, the signal completely disappears when the flames are made shorter during strong acoustic coupling. After several trials, it was found that observation of the injector nearfield was less affected by the changes in flame length and provided a suitable signal level. The PM signals are recorded at a rate of 40 kHz, during the whole hot fire test.

3.2.2 Experimental procedure

The experimental procedure is specifically designed to study the coupling of transverse acoustic modes and multiple cryogenic jet flames. To obtain the largest amplitudes, it is important to identify the resonant modes of the system. As in chapter 1 and 2, the method consists of imposing a constant acceleration to the wheel to obtain linear frequency modulation (**LFM**). The frequency is swept linearly in a range which contains the expected eigenfrequencies. Sig-

Fastcam SA1	
Image size	[576 × 400] pixels
Resolution	263 μm/pixel
Lens	Nikkor 105mm
Aperture	F/2.8
Shutter speed	1/362000s
Frequency	24 kHz
Fastcam APX	
Image size	[512 × 128] pixels
Resolution	204 μm/pixel
Lens	Nikkor 200mm
Aperture	F/5.6
Shutter speed	1/150000s
Frequency	24 kHz

Table 3.1: *Camera settings.*

nals recorded by the pressure transducers are then processed to determine the short time spectral content and identify the eigenmodes, which correspond to the maximum frequency response. In contrast with previous experiments the wheel must be in rotation when combustion is initiated. This is so because the burnt gases exhausted by the nozzles induce heat fluxes which can only be dissipated by the wheel in motion. During the design process, it has been shown that forced convection due to rotation was necessary to keep an acceptable temperature. Values of the system eigenfrequencies identified in the first stage are then used in continuous wave modulation (**CWM**) tests in order to study combustion dynamics under resonant conditions.
It is also important to use baseline operating conditions to examine combustion in the absence of modulation. In the present configuration this is not easy to obtain because the VHAM has to be removed and the nozzle throat diameter has to be modified to keep the same mass flow rate.
The different types of modulation are applied to the five operating points under investigation, designated as PF1 to PF5. Injection conditions have been chosen to study the influence of flow parameters such as mean pressure, momentum flux ratio $J = \rho_{CH4} v_{CH4}^2 / \rho_{LOx} v_{LOx}^2$ and mixture ratio $E = \dot{m}_{LOx}/\dot{m}_{CH4}$. One of these points is defined to allow for comparison with results obtained during previous hot fire tests carried out on the Mascotte facility. The flow parameters corresponding to the five operating points are gathered in Table 3.2.
During the hot fire tests, the modes observed for the different operating points were quite similar, whatever the injection conditions, and this was confirmed

Points	P_{ch}	E	J
PF1	1 MPa	1.3	5
PF2	2.6 MPa	1.33	2
PF3	2.6 MPa	1.33	6
PF4	5.9 MPa	1.13	3.8
PF5	5.5 MPa	1.13	11.3

Table 3.2: *Operating points studied during the hot fire tests. Three mean pressures are investigated. The difference between PF2 and PF3 and between PF4 and PF5 is the momentum flux ratio J. For all tests, the mixture ratio E is kept nearly constant. Injection temperature for methane and liquid oxygen are also kept constant at $T_{CH_4} = 280\ K$ and $T_{LOx} = 80\ K$ respectively.*

later during the post-processing period. By comparing information obtained for the different operating points and numerical estimates, it was possible to precisely identify the various modes. It was decided to adopt a standard designation of the various spectral peaks determined in these experiments:

- Spectral peak one (SP1), refers to the first strong resonance observed during the linear frequency modulation (LFM). This corresponds to the first transverse mode (1T).

- Spectral peak two (SP2) is the second peak observed during the LFM. This has been identified to correspond to the coupled transverse and longitudinal mode (1T1L).

- Spectral peak three (SP3) is the third peak observed during the LFM. This peak is not present for all operating points, for reasons discussed later. It refers to the second longitudinal mode (2L).

- Spectral peak four (SP4) is the fourth peak observed during the LFM. It is also a coupled transverse and longitudinal mode (1T2L).

3.3 Numerical simulation

The modal analysis of the chamber is an important step in the interpretation of the following experimental data. Eigenmodes and eigenfrequecies are determined numerically with AVSP. The geometry is the same as that described in section 2.3. It is first necessary to determine flow parameters in the combustion chamber. Resonant frequencies and pressure distributions are discussed next.

3.3.1 Thermodynamic conditions in the chamber

Table 3.2 defined injection conditions. To obtain the hot gases composition, one first establishes the mixture composition and temperature before combustion, as already described in the cold flow experiments. An enthalpy balance defines these initial conditions. Composition and adiabatic temperature of the burnt products are determined in a second step.

Calculations are carried out for PF1, PF2-3 and PF4-5 (the injected mass flow rates are identical for these operating points).
Adiabatic temperature, sound velocity and main species mass fraction for the final mixtures are gathered in table 3.3.

Operating point	T_{ad} (K)	γ	W (g mol^{-1})	$\overline{\rho}$ (kg m^{-3})	c (m s^{-1})
PF1	1280	1.32	12.1	1.15	1079
	Y_{CH_4}	Y_{H_2O}	Y_{CO_2}	Y_{CO}	Y_{H_2}
	1.37	9.5	7.2	71.9	10
Operating point	T_{ad} (K)	γ	W (g mol^{-1})	$\overline{\rho}$ (kg m^{-3})	c (m s^{-1})
PF2 and **PF3**	1480	1.31	12.5	2.7	1130
	Y_{CH_4}	Y_{H_2O}	Y_{CO_2}	Y_{CO}	Y_{H_2}
(%)	0.31	13.6	7.3	69.6	9.2
Operating point	T_{ad} (K)	γ	W (g mol^{-1})	$\overline{\rho}$ (kg m^{-3})	c (m s^{-1})
PF4 and **PF5**	1354	1.29	12.7	6.9	1065
	Y_{CH_4}	Y_{H_2O}	Y_{CO_2}	Y_{CO}	Y_{H_2}
(%)	7.6	12.1	8	63.8	8.6

Table 3.3: *Properties of the final mixture for the 5 operating points.*

As already mentioned in the determination of the sound velocity of cold flow experiments (section 2.3), there are several uncertainties which have an influence on the final result. The mixture is not homogeneous because liquid oxygen is distributed in the injection area, helium flows near the walls... This is not taken into account and the predicted values can only approximately match the exact values. It is also observed that for some operating conditions, the flames are not fully contained in the chamber. As a result, the temperature in the system may be overestimated in these cases.

On the other hand, it is found that sound velocities corresponding to all operating points belong to a relatively narrow range of values (between 1065 and 1130 m s^{-1}). It was therefore felt that the calculations could be carried out for a single value of the sound velocity $c = 1050$ m s^{-1}. It is interesting to note that this value is close to that ($c = 1000$ m s^{-1}) used by Richecoeur (2006) in

his doctoral thesis. The objective is to obtain an approximate value of the expected eigenfrequencies, and determine the corresponding modal distributions of pressure.

3.3.2 Modal frequencies and spatial distributions

This analysis provides the eigenfrequencies gathered in table. 3.4. These eigenfrequencies correspond to the spatial pressure distribution, displayed in Fig. 3.3.

mode	1L	1T	1T1L	2L	1T2L
Frequency (Hz)	1383	1897	2334	2651	3153

Table 3.4: *Eigenfrequencies calculated using AVSP and a uniform temperature distribution. The sound velocity is* $c = 1050\ m\ s^{-1}$

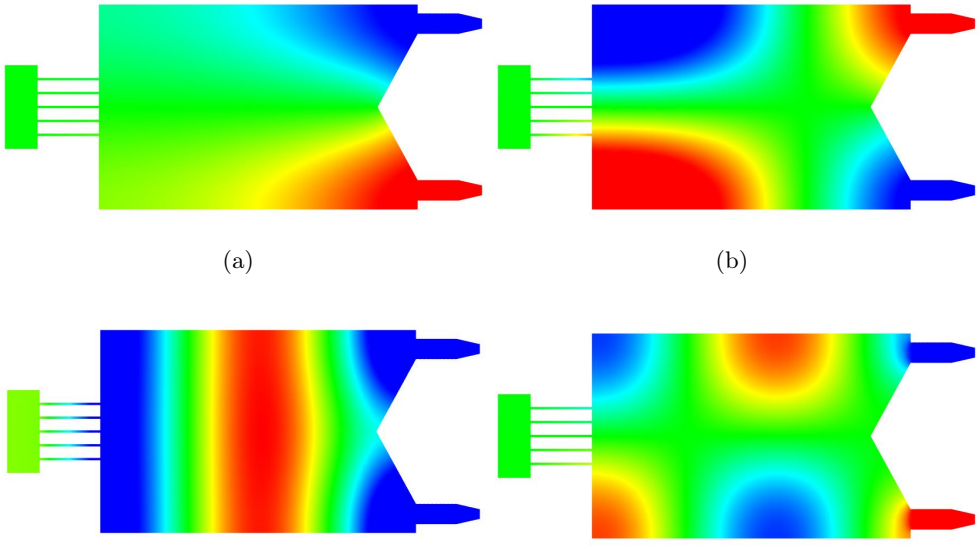

Figure 3.3: *Spatial pressure distributions in the MIC for eigenfrequencies located in the range of study - (a) 1T mode (1897 Hz) - (b) 1T1L mode (2334 Hz) - (c) 2L mode (2651 Hz) - (d) 1T2L mode (3153 Hz)*

Some important features can be pointed out, as already done in chapter 2. They are briefly recalled here.

- For the first transverse mode (1T), in Fig. 3.3, the amplitude of the acoustic mode is significantly more important near the backplane than in the

vicinity of the injection plane. This will be observed in the experiments.

- For the 1T1L mode, the amplitude is more important near the injection plane. Moreover, in the longitudinal direction, the mode is not symmetric. The pressure antinode located near the injection plane occupies a longer region compared to those situated near the backplane. Since the window, in the experiments, aims at visualizing the beginning of the flames, this would appear like a 1T mode. The response of the HF3 and HF4 sensors will not be easy to interpret as well. Because these sensors are located in the middle of the chamber, they will probably be influenced by the pressure antinodes formed near the injection plane. HF1 and HF3 would be in phase, and this would be the case for HF2 and HF4.

- For the 1T2L mode (Fig. 3.3 (d)), a clear coupled transverse and longitudinal structure should be observed. All pressure sensors are located in the vicinty of pressure antinodes.

3.4 Operating point PF1

Injection parameters defining operating point PF1 are gathered in table 3.5. As shown in this table these conditions are close to those used for operating point F50-T280 investigated by Richecoeur (2006) in his doctoral thesis which was found to give rise to a strong response to external perturbations. It is here used to link the present study to previous work. The most important difference between these two operating points is that the F50-T280 corresponds to a configuration with three coaxial injectors instead of five in the current injection head. This explains why, for nearly the same mass flow rates and mean pressure the injection velocities are so different. The objective was to keep similar mean chamber pressure, mixture ratio E and momentum flux ratio J. The exhaust nozzle diameters is limited by the teeth size (11.25 mm) in the rotating wheel.

Points	P_{ch}	E	J
PF1	1 MPa	1.3	5
F50-T280	0.9 MPa	1.2	5.4

Table 3.5: *Injection parameters for operating point PF1 (current test series) and operating point F50-T280 (investigated by Richecoeur (2006)). This operating point corresponds to a low pressure and an intermediate value of the momentum flux ratio.*

Three trials were made during the campaign for PF1. These tests are listed in table 3.6 and described in the following sections.

Type	LFM	CWM1	CWM2
frequency (Hz)	$1300 \rightarrow 3400$	$2245 - 2700$	3120

Table 3.6: *Types of excitation and corresponding frequencies investigated for operating point PF1.*

3.4.1 Operation under weak modulation (OWM)

The test case without modulation was not carried out for this operating point to diminish the number of hot fire experiments. However, it was considered that information on the baseline operation (OWM) could be obtained from the LFM test in a range where the acoustic modulation is weak and the flame hardly responds to the low level of external forcing. These conditions are particularly well fulfilled in the beginning of the linear sweep, when the frequency is below 1400 Hz. Figures 3.4 (a) and (b) show the temporal evolution of the pressure during the sweep and the related time-frequency diagram, obtained by short time Fourier processing of the temporal response. The horizontal axis corresponds to time, while the vertical axis pertains to frequency. At the beginning of the test, the wheel is rotating at 2053 tr min^{-1}, which corresponds to an excitation at 1300 Hz. At 14.2 s, the sweep starts. The straight line in the diagram indicates that the frequency is swept linearly. Eventually, the frequency ramp reaches its final value of 3400 Hz. The wheel rotation rate is at that point of 5368 tr min^{-1}.

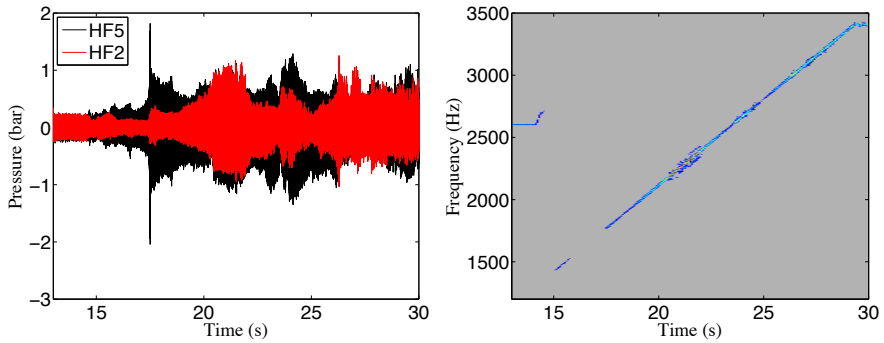

(a) (b)

Figure 3.4: *PF1 during the LFM - (a) Sensor responses during a frequency sweep. Four peaks emerge from the background noise - (b) Temporal evolution of HF2 power spectral density.*

To obtain this time-frequency diagram, pressure signals are numerically high-pass filtered with a cut-off frequency of 400 Hz, and analyzed with the short

time Fourier transform. Since the sampling frequency is 40 kHz, the highest frequency which can be resolved is 20 kHz.
Before the beginning of the ramp, the acoustic amplitude is - compared with what follows - relatively low. In fact, the power spectral density plotted in Fig. 3.5 in dB, indicates that the amplitude is not negligible. Nevertheless, during the initial instants the flame modification due to acoustic excitation is less important.

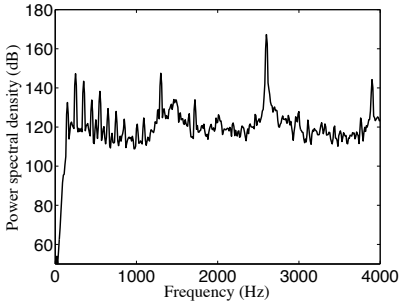

Figure 3.5: *PF1 at the beginning of the LFM during 0.3 s - Power spectral density. The amplitude of the modulation is relatively weak, allowing to use this test as a OWM test. Processing parameters: $f_a = 40$ kHz (frequency of acquisition), 3 Hanning windows with an overlapping of 2/3, $\Delta_f = 3.3$ Hz.*

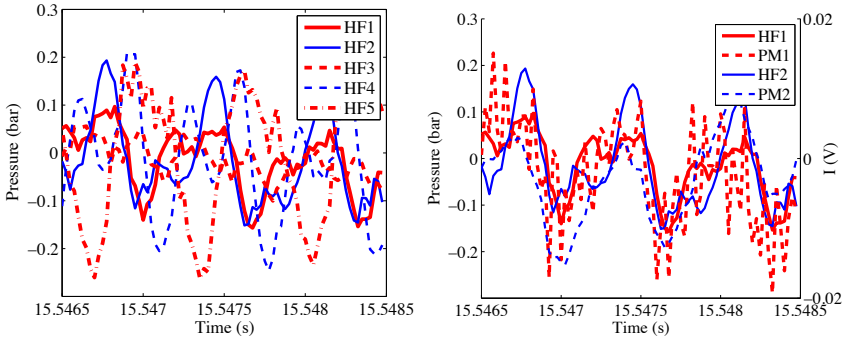

(a) (b)

Figure 3.6: *PF1 at the beginning of the LFM - (a) Response of the HF transducers - (b) Near injection pressure sensors HF1 and HF2 plotted with the PM signals - The excitation frequency appears, but the amplitude is low, which confirms that this part of the test can be used as a OWM test.*

Fig. 3.6 shows the filtered signals recorded by the photo-multipliers when the modulation is still weak. An oscillation, at the frequency of excitation, is noticeable. The relative fluctuation of light intensity $G_I = I'/\overline{I}$ is low and

$G_I \approx 2\%$, for both photo-multipliers. This value is small enough to consider that the flame develops freely. One can study the related flame structure and consider that it corresponds to the baseline case.

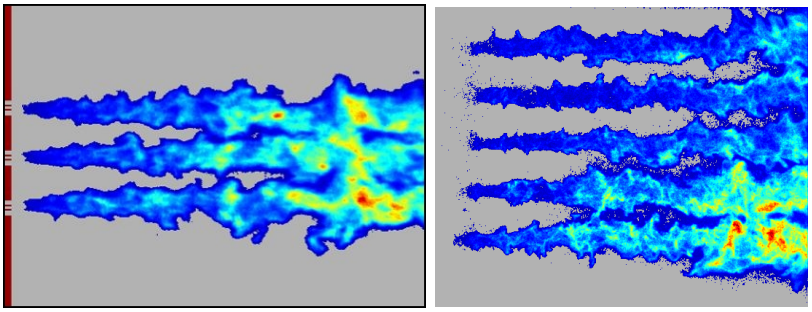

(a) (b)

Figure 3.7: *(a) F50-T280 operating point (Richecoeur 2006) - Instantaneous OH* emission (ICCD camera) - (b) PF1 at the beginning of the LFM - Instantaneous OH* emission (ICCD camera).*

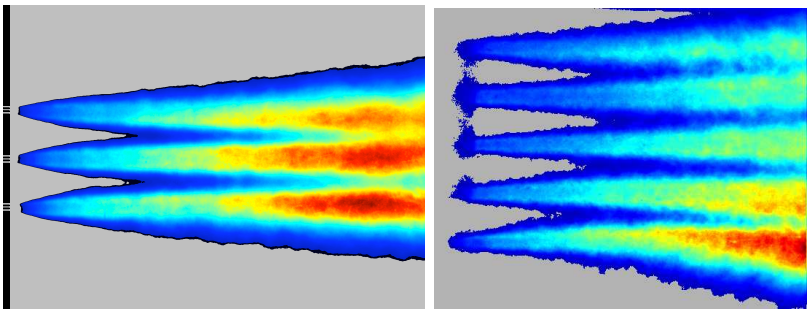

(a) (b)

Figure 3.8: *(a) F50-T280 operating point (Richecoeur 2006) - Average OH* emission image (ICCD camera) - (b) PF1 at the beginning of the LFM - Average OH* emission (ICCD camera).*

Fig. 3.7 shows an instantaneous image recorded by the ICCD camera. Images gathered during the time interval extending from 13 to 17 seconds corresponding to a low level of pressure amplitude have been averaged (Fig. 3.8). The flame length is important, and the window is not sufficiently long to visualize the total combustion area. In general, the flames are quite similar to those observed by Richecoeur. The backlighting images recorded by the APX camera give indications on the atomization process and its dynamics. The frame rate of 24 kHz is sufficiently high and droplets can be followed through several images.

One of them is shown in Fig. 3.9. The blurred area at the beginning of the jet is due to condensation created during the flame initiation process. This region is also blurred for every ICCD frame of this test case. Here, the flames can hardly be distinguished, thanks to the filter used with the APX camera and because the spot light is intense.

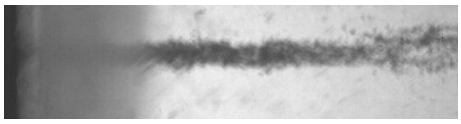

Figure 3.9: *PF1 at the beginning of the LFM - Image of the liquid jet recorded by the APX camera. The blurred area in the left part of this image is due to condensation. Formation of droplets can be observed in the second part of the jet.*

This baseline case indicates that injection conditions are not favorable to atomization and the flame extends beyond the window boundary. It also seems that the mass flow rates delivered through injectors 1, 2 located in the top part of the chamber and by the central injector are less important. It has been observed during cold flow tests that the liquid jet length was shorter for these injectors. This point would necessitate further investigations.

3.4.2 Linear frequency modulation (LFM)

The remaining part of the LFM test is examined in what follows. Fig. 3.4 shows four resonant peaks which clearly emerge above the background noise. The amplitude of these peaks are somewhat similar, but they do not have the same characteristics. For example, the first peak is characterized by an intense response of HF5 but a weaker response of the other sensors. It is then interesting to analyze this feature as will be done later. The relative amplitude detected by the pressure sensors is influenced by the eigenmode being excited, mean flame shape, flame dynamics and evolution of the acoustic mode during the test. The characteristics of the various peaks described in what follows are retrieved in other hot fire tests which generalizes the discussion.
Fig. 3.10 shows frames recorded by a DV control camera. These images give a good idea of the experimental configuration and of the way the flame structure is modified by the acoustic field. The different flame patterns are discussed in the following sections.

First spectral peak (SP1) A first maximum is obtained for an excitation at 1770 Hz. The amplitude of the pressure oscillation at transducers HF1 to HF4 is relatively weak and the signal contains an important first harmonic component of the excitation frequency. The response measured by HF5, located near the exhaust nozzles is stronger with an amplitude of 1.7 bar ($\approx$ 17% of the chamber

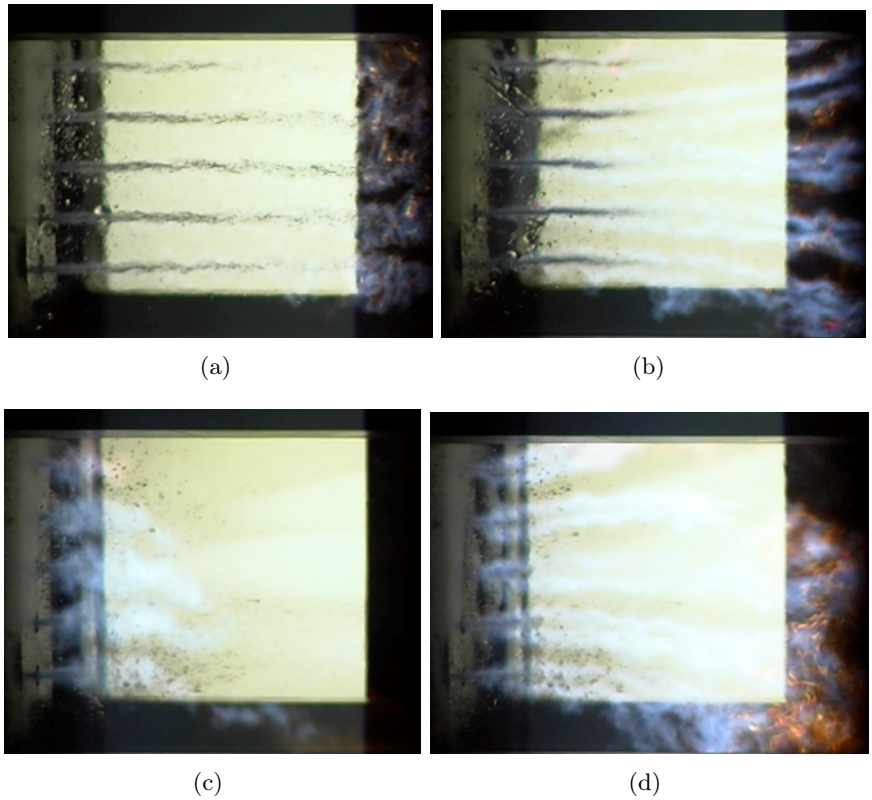

Figure 3.10: *PF1 during the LFM - (a) Beginning of the LFM (OWM) - (b) First Spectral Peak (SP1) - (c) Second Spectral Peak (SP2) - (d) Fourth Spectral Peak (SP4).*

mean pressure). The modal amplitude increases and decreases rapidly, as can be seen in Fig. 3.12 (a). The impact on the flame structure is quite significant, as shown in Fig. 3.12 (b). The signal amplitude detected by HF5 rises sharply when the modal frequency is approached. The time to establish a new regime of combustion is relatively short (less than the time period between two ICCD frames, 1/15 s $\simeq$ 60 ms). Photomultipliers PM1 and PM2 are out of phase ($\Delta\phi \simeq \pi$) indicating that heat release is oscillating in the transverse direction. Considering numerical results obtained with the acoustic solver, this modal resonance is close to that expected for the 1T mode. One of its salient characteristics is that the amplitude near the exhaust plane is more important, which agrees with calculations. However, the phase difference between the HF sensors does not clearly demonstrate that the oscillation corresponds to the first transverse mode. Other operating points investigated in what follows will consolidate this interpretation.

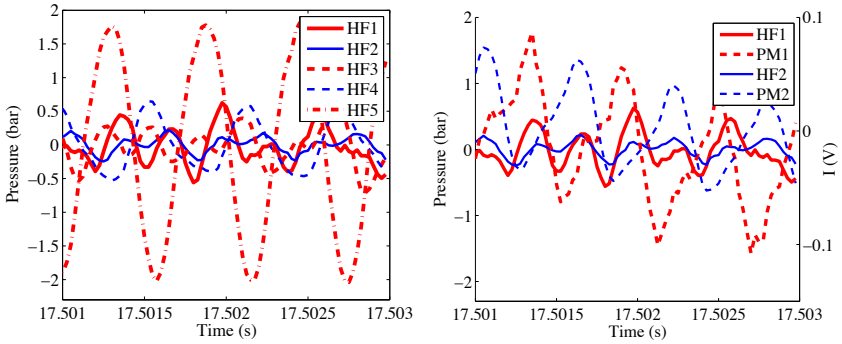

(a) (b)

Figure 3.11: *PF1 during the LFM at SP1 (f =1770 Hz) - (a) Response of the HF transducers - (b) Near injection pressure sensors HF1 and HF2 plotted with the PM signals.*

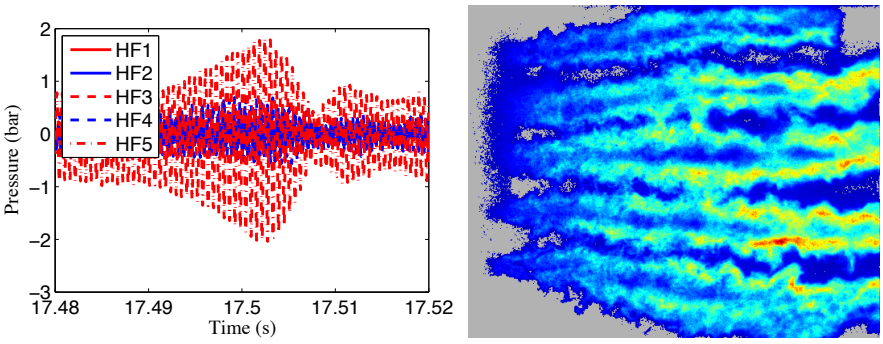

(a) (b)

Figure 3.12: *PF1 during the LFM at SP1 (f =1770 Hz) - (a) Response of the HF transducers signals near the spectral peak - (b) Instantaneous OH* emission of the flames excited near the peak.*

Second spectral peak (SP2) The associated frequency is now 2200 Hz. This mode has a transverse structure: HF1 and HF3 are in phase, HF2 and HF4 are are also in phase but their phase is opposed to that of HF1 and HF3. The HF5 sensor gives an information which is more difficult to interpret. It is almost in phase with HF2 and HF4.The amplitude of all transducers pressure transducers have nearly the same levels. The photomultiplier signals are in phase opposition. HF1 and PM1 are in phase, HF2 and PM2 as well, which is a strong evidence of a transverse structure. The relative intensity level reaches a value $G_I \approx 20\%$. The pressure in the injection dome only weakly oscillates indicating that the coupling between the chamber and the feed system does not intervene in the driving process.
The previous clues indicate that the situation is close to that shown in Fig. 3.3 (d) for the 1T1L modal structure. Indeed, one expects that HF5 is in phase with HF2 and HF4. The couples HF1-HF3 and HF2-HF4 are in phase because the pressure antinode regions begining at the injection plane extend over a long distance, in relation with the chamber geometry.
The flame structure corresponding to this pressure distribution and frequency is shown in Fig. 3.14. The flames markedly differ from those observed so far. The configuration ceases to be symmetric. In the upper part of the chamber, the flames are short and they are directed downwards. Because this mode is excited during a fairly long time interval, it is possible to obtain an average image by summing six ICCD images. The transient regime is quite long: five ICCD frames (0.33 s) describe how the flames progressively become more compact and point downwards. As the flames become quite short they are essentially modulated by the initial transverse modal structure established near the injection plane and are not sensitive to the phase changes taking place further downstream in the chamber.
The pressure evolution obtained when the modulation frequency is close to the second spectral peak eigenfrequency shown in Fig. 3.15 has an interesting feature. When the frequency of modulation imposed by the rotating wheel differs from the eigenfrequency of the chamber, an oscillation in amplitude is observed by the various transducers. This gives rise to a beat between the frequency of modulation and the eigenfrequency, the frequency of which is approximately 40 Hz. This influences the flames shapes recorded by the ICCD camera. The flame length oscillates in response to the beating process.

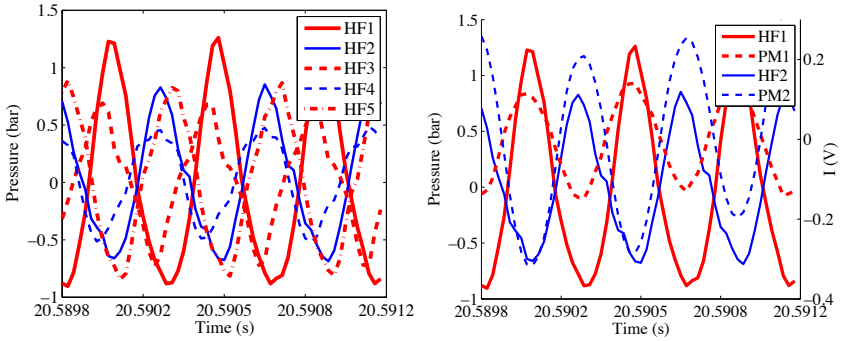

(a) (b)

Figure 3.13: *PF1 during the LFM at SP2 ($f = 2200$ Hz) - (a) Response of the HF transducers - (b). The pressure sensors HF1 and HF2 located near the injection plane are plotted with the PM signals.*

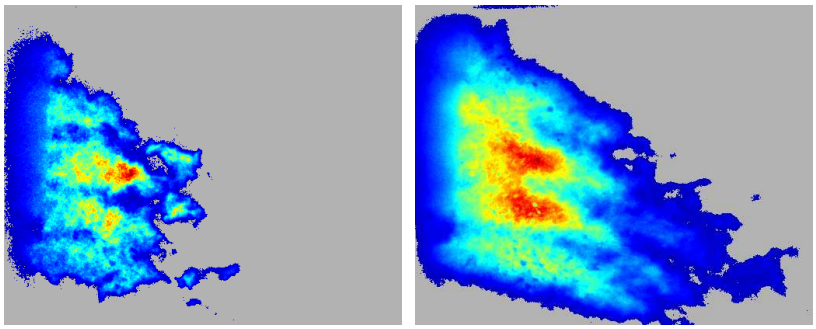

(a) (b)

Figure 3.14: *PF1 during the LFM at SP2 ($f = 2200$ Hz) - (a) Instantaneous OH* emission of the flames - (b) Average OH* emission image obtained by summing 6 successive ICCD images. Flames are compact, they are directed downwards and the distribution of light emission is asymmetric.*

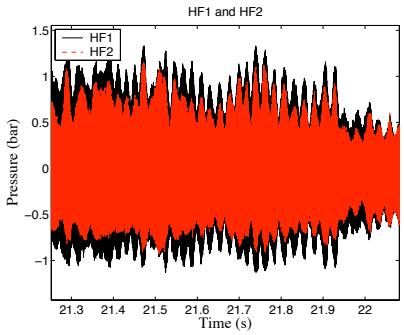

Figure 3.15: *PF1 during the LFM at SP2 ($f = 2200$ Hz) - Frequency beat observed after the second peak. The low frequency oscillation of amplitude ($\simeq$ 40 Hz), which appears similarly on all the sensors, is characteristic of a beating.*

Third spectral peak (SP3) The third spectral peak found at a frequency of 2700 Hz, features a complex structure during the frequency ramp. The transducers do not respond at the same frequency (Fig. 3.16). The amplitude on HF1 decreases while the amplitude on HF4 increases. The temporal evolution of the various signals (Fig. 3.17) cannot be used to precisely identify the eigenmode corresponding to this third peak but the frequency range matches that of the 2L mode. This point will be examined more precisely in the analysis of the CWM.

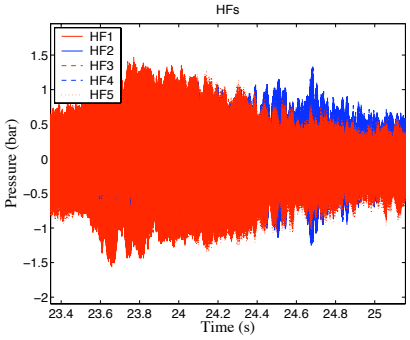

Figure 3.16: *PF1 during the LFM at SP3 (f = 2700 Hz) - Pressure response for the five HF sensors. The amplitude of the HF1 signal decreases while that detected by HF4 increases.*

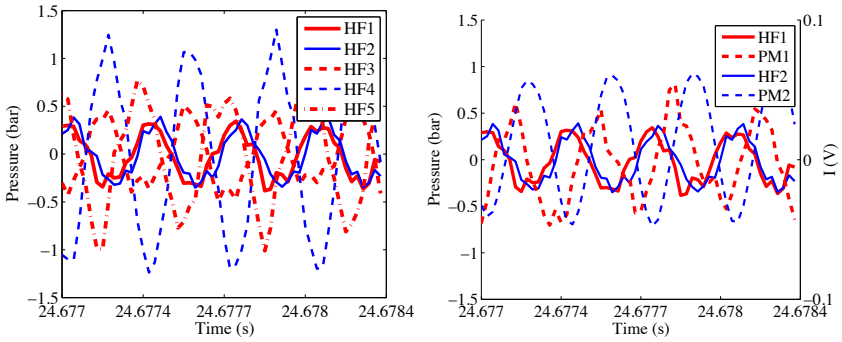

(a) (b)

Figure 3.17: *PF1 during the LFM at SP3 (f = 2700 Hz) - (a) Response of the HF transducers - (b) Near injection pressure sensors HF1 and HF2 plotted with the PM signals.*

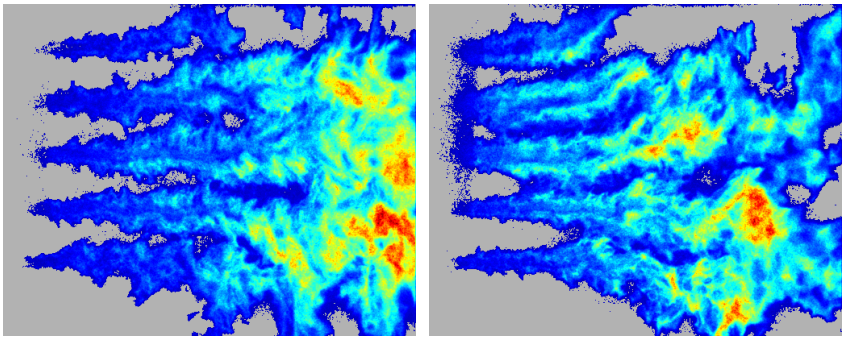

(a) (b)

Figure 3.18: *Instantaneous OH* emission of the flames - (a) PF1 during the LFM at SP3 ($f = 2700$ Hz) - Flames are perturbed but not as strongly as for SP1 and SP2 - (b) PF1 during the LFM at SP4 ($f = 3250$ Hz).*

Fourth spectral peak (SP4) Fig. 3.19 (a) shows that the fourth spectral peak corresponds to a coupled transverse and longitudinal mode. Considering the range of frequency, it is likely that this resonance pertains to the 1T2L mode. The coupling with combustion is illustrated in Fig. 3.19 (b). PM1 does not exhibit oscillations because it is oriented in the downstream direction and detects very little emission from the shorter flames in the top part of the chamber (see Fig. 3.18 (b)). The photomultiplier observing the bottom part of the chamber (PM2), where flames are longer, shows that pressure and heat release are in phase.

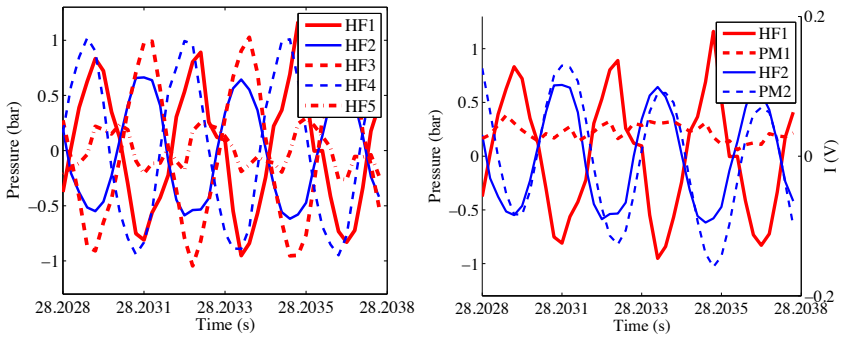

(a) (b)

Figure 3.19: *PF1 during the LFM at SP4 ($f = 3250$ Hz) - (a) Response of the HF transducers - (b) Near injection pressure sensors HF1 and HF2 plotted with the PM signals.*

This mode will be studied in the next section as well.

3.4.3 Continuous wave modulation (CWM1)

Two continuous wave (CWM) hot fire tests have been carried out at the nominal pressure of 10 bar to examine the response at three eigenfrequencies. This is made possible by changing the frequency in the middle of a test by applying a short ramp to the wheel. Two frequencies are excited during CWM1: 2245 Hz (SP2), which was identified as a 1T1L mode and 2700 Hz (SP3), which was assumed to be a 2L mode. In CWM2, the frequency 3120 Hz (SP4) is investigated.
The time history of the CWM1 test case is summarized in Fig. 3.20. When the system is ignited, the modulation frequency is set to 2245 Hz. This frequency is excited for a short time, then a ramp leads to the second eigenfrequency (2700 Hz). Fig. 3.21 (a) shows that the mean pressure was not fully established during the first continuous wave modulation, indicating that the transient regime was not terminated. This has the consequence that the flame geometry (Fig. 3.21 (b)) was not identical to that observed during the LFM hot fire test. There is no asymmetry in the mean emission pattern and the flames remain quite long. Nevertheless, the response of the pressure sensors and images delivered by the two high speed cameras indicate that the system sensitivity is high.

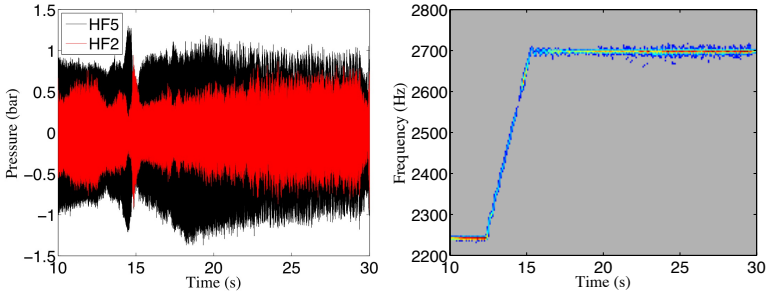

(a) (b)

Figure 3.20: *PF1 during CWM1 (study of SP2 (2245 Hz) and SP3 (2700 Hz) - ((a) Sensor response - (b) Temporal evolution of the HF2 power spectral density.*

The liquid jet, shown in Fig. 3.22, is oscillating in the transverse direction following the acoustic field.
The effect of the acoustic field on the flames is well illustrated in Fig. 3.23. It is clear that the fluctuating velocity field associated with the acoustic wave is responsible for the spatial oscillation of the flames. This in turn increases the intensity of light emission and augments the level of the volumetric rate

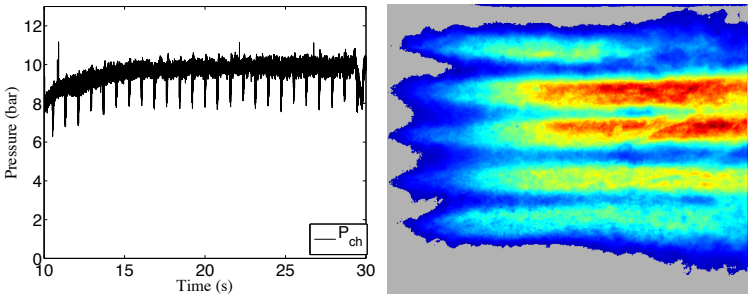

(a) (b)

Figure 3.21: *PF1 during CWM1- (a) Evolution of mean pressure - (b) Average OH* emission of the flames during SP2 (2245 Hz).*

Figure 3.22: *PF1 during CWM1 at SP2 (2245 Hz) - Backlighting image obtained with the APX camera. The liquid jet oscillates due to the acoustic modulation.*

of heat release. This quantity is a central factor in the growth of oscillations. The streak film, dispayed in Fig. 3.24, illustrates the same phenomenon using a different representation. The method, exploited for example by Tischler and Male (1956) (see Fig. 3.24 (b)) consists in recording light emitted in a thin window placed in the axial or transverse direction. Light emitted by combustion through this window is recorded at a high frequency providing a space-time film of the light intensity in the interrogation window. During the early period of combustion instability research (the 1950's and 1960's) the method was used because of technical limitations in experimentation and data acquisition. At that time, it was not possible to record more than one thin slice of the chamber. The present data provide more information and it would be possible to define various types of slices and examine the space time evolution of light intensity in these image slices. It is informative to use this type of data processing and compare the streak film obtained in this way with those recorded in the early days of high frequency combustion instability research and reconsider the different conclusions deduced from these experiments. This point will be addressed in the discussion at the end of this chapter (section 3.9).
The structure of the SP3 mode (2700 Hz) was not fully identified during the LFM hot fire test. The high speed film provided by the SA1 camera provides further clues. Flames do not oscillate in the transverse direction and essentially

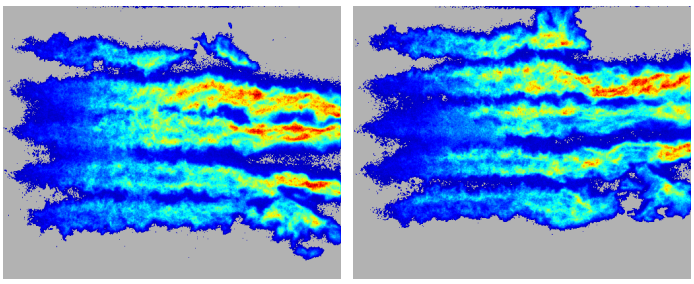

(a) (b)

Figure 3.23: *PF1 during CWM1 at SP2 (2245 Hz) - Instantaneous OH* emission of the flames at $\phi = 0$ (a) and $\phi = \pi$ (b).*

feature a longitudinal motion. The frequency indicates that the motion is probably associated with the second longitudinal mode (2L) as assumed previously. The pressure signals (Fig. 3.25), at the end of the excitation, validate this hypothesis: HF1, HF2 (placed near the chamber head) and HF5 (at the end of the chamber) are in phase, while HF3 and HF4 are also in phase. The two groups are in phase opposition. In Fig. 3.25 (b), one can see that the two PM are almost in phase, which is consistent with the longitudinal mode hypothesis. Fig. 3.25 (c) shows the average OH* emission during the 2L modulation. While the pressure level at the pressure sensors is strong, the flame structure does not change much compared to the modulation free case. Transverse modes have a much more visible influence on the flame structure, a feature which is probably a key factor in the occurence of combustion instability.

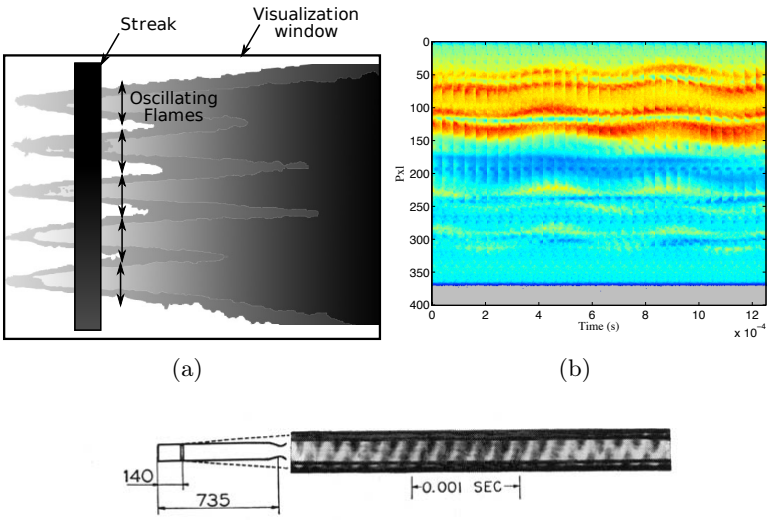

Figure 3.24: *(a) Schematic representation of the visualization window used to synthesize the streak film. The motion of the flames is illustrated by setting side by side the same streak recorded at successive instants by the SA1 camera ($f = 24$ kHz) - (b) Streak film obtained at 2245 Hz (SP2) - (c) Typical streak film obtained by Tischler and Male (1956) for a single injector combustor.*

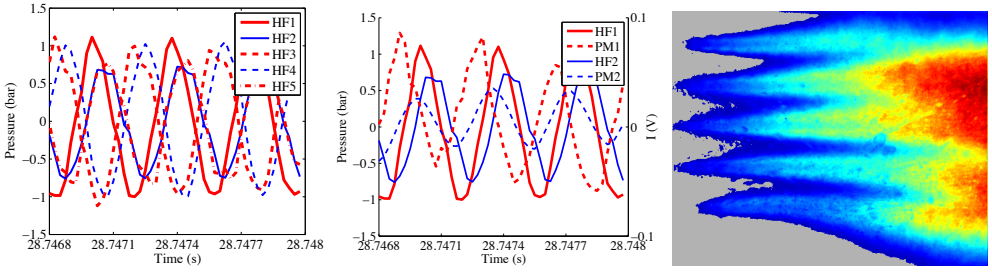

Figure 3.25: *PF1 during CWM1 at SP2 (2700 Hz) - (a) Response of the HF transducers - (b) Near injection pressure sensors HF1 and HF2 plotted with the PM signals - (c) Averaged OH* emission of the flames.*

3.4.4 Continuous wave modulation (CWM2)

A second continuous wave test was carried out at the third spectral peak (SP3, $f = 3120$ Hz). Fig. 3.26 provides a map of the pressure response during this test. Instead of growing, the signal is diminishing during the major part of the test. At the initial instants (Fig. 3.27 (a)) the pressure sensors indicate that this mode has a coupled transverse/longitudinal structure. HF1-HF4-HF5 are in phase, HF2-HF3 are in phase as well, and these two groups are in phase opposition. High speed films also confirm these modal characteristics by exhibiting a coupled longitudinal and transverse motion.

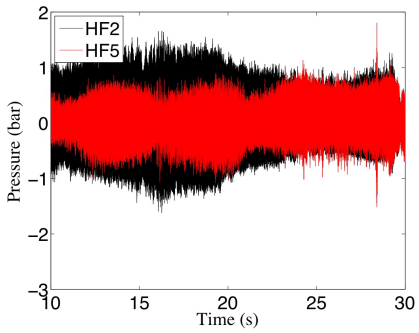

Figure 3.26: *PF1 during CWM2 at SP3 (3120 Hz) - Evolution of unsteady pressure during the test.*

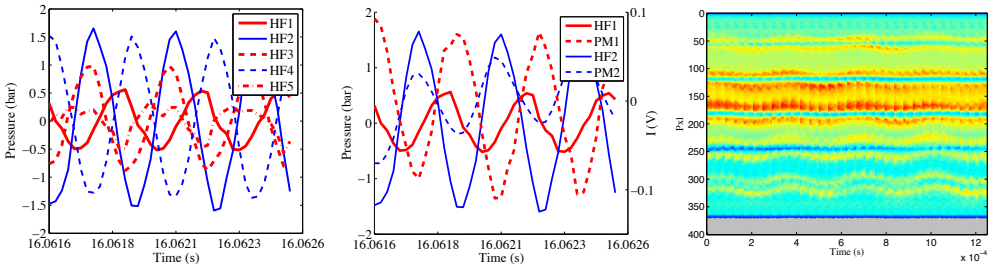

(a) (b) (c)

Figure 3.27: *PF1 during CWM2 at SP3 (3120 Hz) - (a) Response of the HF transducers - (b) Near injection pressure sensors HF1 and HF2 plotted with the PM signals - (c) Streak film taken near the injection plane.*

The decrease in amplitude during modulation can be explained in various ways. It is first possible that the Rayleigh source term, which appears in the acoustic energy balance can be negative and act as a stabilizing term at this frequency of operation and for this set of injection parameters. This corresponds to an

unsteady rate of heat release and an acoustic pressure field which are out of phase. A second explanation is related to the observed evolution of the pressure field during the test (see Fig. 3.28). It appears that the pressure field "looses" its clear 1T2L modal structure as the test proceeds. Since the frequency of excitation does not change, one has to admit that it is the 1T2L eigenfrequency of the chamber which drifts from its initial value during the test. Since all injection parameters remain constant, one possibility is that the temperature field distribution changes during the test and that the eigenfrequency moves away from its initial value.
The mechanism would then be as follows. The modulation is applied at $f = 3120$ Hz and the 1T2L mode is excited. This changes the shape of the flames, modifying the mean temperature field significantly and changing the eigenfrequency which is no longer equal to 3120 Hz.
This mechanism explains the present situation, although it appears to be in opposition with previous observations and results to come in following sections, for continuous wave modulations. In some cases the flame pattern is significantly modified, but the acoustic response is still strong. One could argue that, in these situations, the frequency shift is small in comparison to the frequency range in which the cavity is potentially excited. This proposition would require further investigation.

3.5 Operating point PF2

Parameters corresponding to operating point PF2 are gathered in table 3.7. The exhaust nozzles are those used in the PF1 test case. The higher pressure of 2.6 MPa is obtained by imposing larger propellant mass flow rates. The mixture ratio E of 1.3, is close to that used in the PF1 test case. During this test series, the mixture ratio has always been set between 1.1 and 1.3. An important change here is that the momentum flux ratio has a relatively low value $J = 2$ and one expects that the primary atomization process will be quite poor. The aim of this experiment is to obtain an inefficient atomization process which would be sensitive to acoustic coupling.

Points	P_{ch}	E	J
PF2	2.6 MPa	1.33	2

Table 3.7: *Injection parameters for the PF2 operating point. These conditions yield an intermediate value of pressure with relatively poor atomization corresponding to a low value of the momentum flux ratio ($J = 2$).*

Five tests were carried out with the flow parameters corresponding to PF2. The different runs are listed in table 3.8 and described in the following sections.

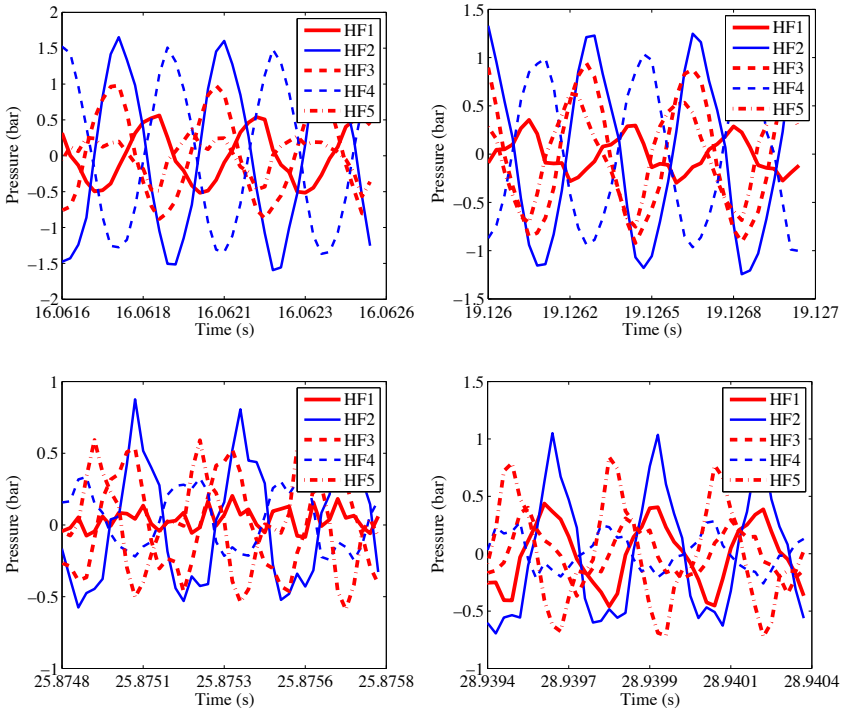

Figure 3.28: *PF1 during CWM2 at SP3 (3120 Hz) - Pressure sensors signals at 4 successive instants. There is a clear modification of the structure of the acoustic pressure field.*

3.5.1 Operation without modulation (OWM)

This hot fire test was carried out by removing the wheel while keeping the same injection parameters. Figure 3.29 shows that during the transient regime, a low frequency instability is triggered. After a few seconds this oscillation is damped and a steady regime is established.
Instantaneous and mean OH* emissions are displayed in Fig. 3.30. Flames are long and extend beyond the visualization window rim. This is due to the inefficient process of atomization. The data gathered by the APX camera, operating in backlighting mode, could not be used to characterize the atomization process because the light emitted by the flame was too intense compared to the light transmitted by the backlighting process. The high speed CH* emission records show that the liquid jet is progressively stripped off by the methane jet.

Type	WM	LFM1	CWM1/LFM2	CWM2	CWM3
freq. (Hz)	0	1100 → 2600	1840/1840 → 3200	2330 - 3200	3200

Table 3.8: *Types of excitation and corresponding frequencies investigated for operating point PF2. The second frequency sweep LFM2 follows a continuous wave modulation at 1840 Hz.*

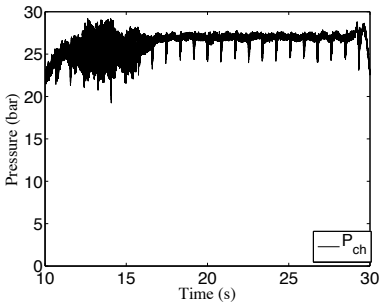

Figure 3.29: *PF2 during OWM - Evolution of mean pressure. Before nominal pressure is reached, a low frequency instability is triggered (between 10 and 15 s after the test start) and is finally damped.*

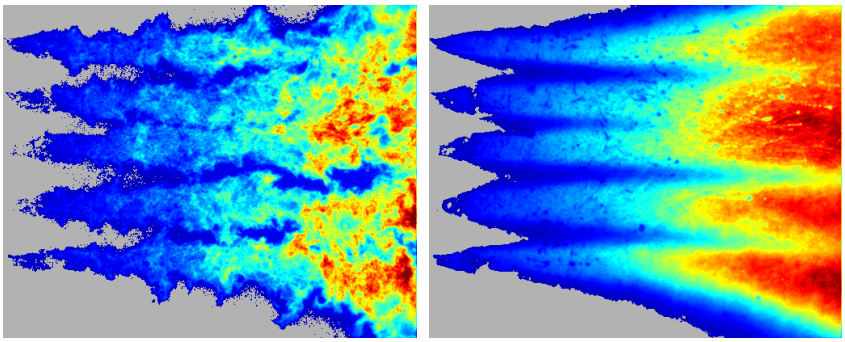

(a) (b)

Figure 3.30: *PF2 during OWM - (a) Instantaneous OH* emission of the flames - (b) Averaged OH* emission of the flames.*

3.5.2 Linear frequency sweeps LFM1 and LFM2

The LFM test has been performed in two ways (LFM1 and LFM2). LFM1 corresponds to a sweep from 1100 Hz to 2300 Hz and can be used to extract the first high amplitude eigenfrequency: $f = 1840$ Hz, which is SP1. Hence, the second LFM test starts by a continuous wave modulation at 1840 Hz and ends at 3200 Hz. These two experiments can be linked together to obtain the eigenmodes and eigenfrequencies of the system. Figures 3.31 and 3.32 show the temporal evolution and the short time Fourier analysis of these two tests. Considering that the mixture ratio E is close to that used in the PF1 case one expects that the eigenfrequencies will be close to those identified previously. This is indeed verified with spectral peaks located at positions similar to those found for PF1.

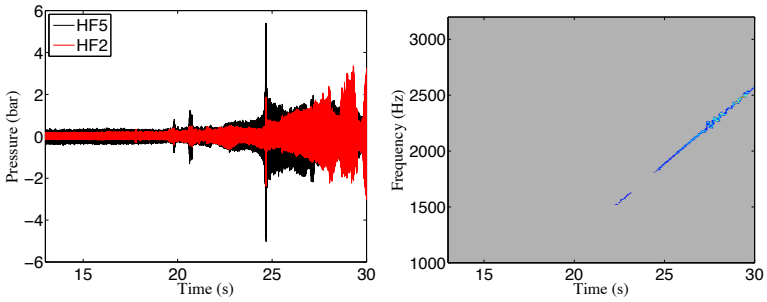

(a) (b)

Figure 3.31: *PF2 during LFM1 - (a) Sensor response. Modulation starts at 1100 Hz and finishes at 2300 Hz, two peaks emerge in this range of frequency - (b) Temporal evolution of the HF2 power spectral density.*

First spectral peak (SP1) The first spectral peak is found at 1840 Hz. The shape of the pressure sensor signals during the ramp (Fig. 3.33), indicates that the mode excited in this case corresponds to the first peak observed at 10 bar (1700 Hz). This is confirmed by the similarities in the heat release pattern, shown in Fig. 3.34. Flames are still relatively long, the light emission is more intense, and the combustion area is increased. Pressure transducers indicate that the acoustic motion is purely transverse. The pressure oscillation is significantly higher near the exhaust plane for this operating point, which is consistent with the PF1 results. The HF5 sensor records a rapid amplitude increase to approximately five bar and then a sudden decrease. This behavior was observed for the 1T mode of the PF1 operating point (Fig. 3.12 (a)). The first spectral peak can be safely attributed to the first transverse mode (1T). The continuous wave modulation presented in the next section provides a deeper

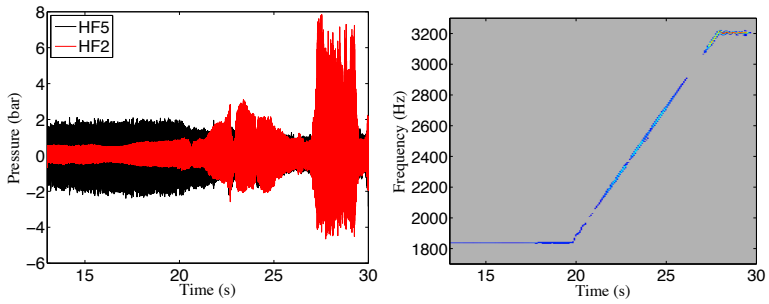

(a) (b)

Figure 3.32: *PF2 during LFM2 - (a) Sensor response. Modulation starts at 1840 Hz (SP1) and terminates at 3200 Hz - (b) Temporal evolution of the HF2 power spectral density.*

understanding of the acoustic mode shape and of its effects on the flame.

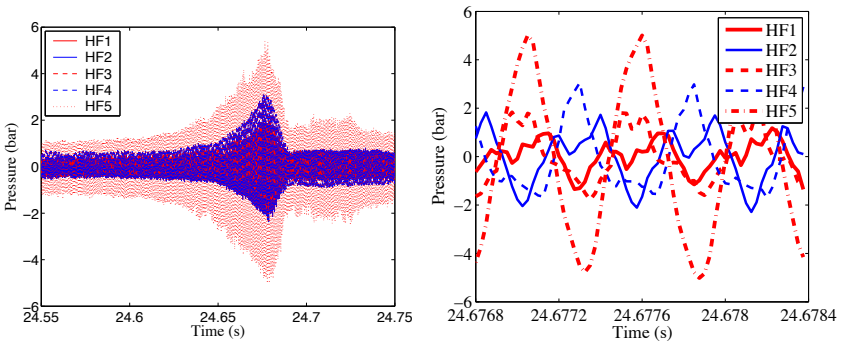

Figure 3.33: *PF2 during LFM1 at SP1 (1840 Hz) - (a) Response of the HF transducers in the vicinity of SP1 - (b) Zoom on the pressure transducers signal.*

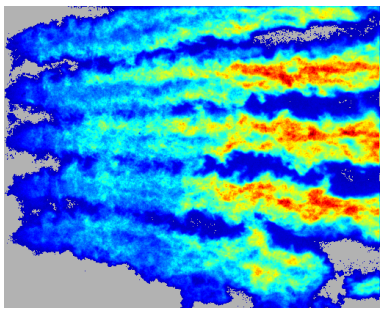

Figure 3.34: *PF2 during LFM1 at SP1 (1840 Hz) - Instantaneous OH* emission of the flames. As observed at SP1 for operating point PF1, the combustion area is expanded and one can easily distinguish the flame fronts.*

Second and third spectral peaks (SP2 and SP3) The second peak which emerges in the linear frequency modulations extends from 2340 Hz to 2700 Hz. The pressure structure is complex, as shown in Fig. 3.35. Several eigenfrequencies may be close, and the ramp is too fast to identify each mode. The frequency range indicates that the peaks are close to the 1T1L mode (SP2) and 2L mode (SP3), but there are three stages which can be distinguished in the signals. The two first "sub-peaks" are thought to refer to the 1T1L mode, and the change in amplitude may be due to a rapid rearrangement in the flame structure. This is illustrated in Figures 3.37 (f = 2340 Hz) and 3.40 (f = 2427 Hz). The related evolution of the pressure field between these two frequencies is shown in Fig. 3.36 and 3.39.

Fig. 3.38 shows the photomultiplier signals during the hot fire test. At the frequency of 2440 Hz, around 23.3 s, the signal drops to zero. This phenomenon

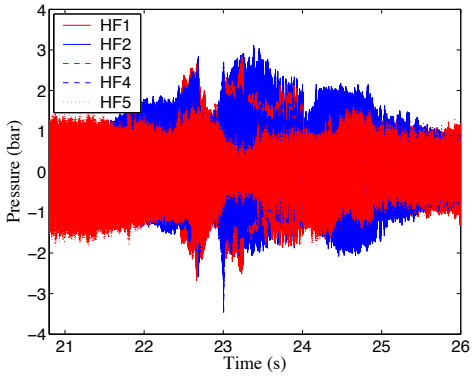

Figure 3.35: *PF2 during LFM2 at SP2 and SP3 - Sensor response. This peak can be divided into three stages. The two first stages refer to SP2 and they are probably separated by a change in the flame structure, the third stage refers to SP3.*

can be explained by examining the ICCD frames recorded in the neighborhood of this instant in time (Fig. 3.40). The flame structure is completely modified by the modulation. The combustion region is reduced to a few injector diameters. Since the photomultipliers region of interest is located downstream, the PM detect very little light when the flames are so short. Successive images taken by the ICCD camera show the large amplitude of the transverse motion of the flames.

The third stage near this peak, closer to 2700 Hz, corresponds to the third spectral peak (SP3) and therefore to the 2L mode. The clear identification of this mode is not straightforward because of the remaining effects of strongly responding modes at lower frequencies. For example, in Fig. 3.41 - (a), HF1 and HF2 pressure sensors are out of phase, which is in contradiction with the 2L hypothesis. However, HF3 and HF4 are in phase, which is in agreement with this hypothesis. Fig. 3.41 (b) gives a decisive evidence: the two photomultipliers are in phase, indicating that the flames oscillate in the longitudinal direction.

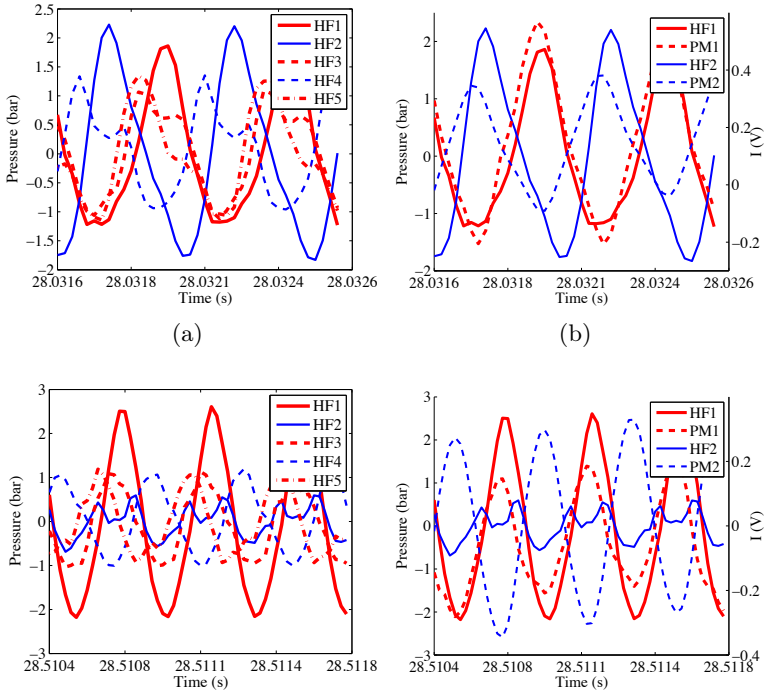

Figure 3.36: *PF2 during LFM1 at SP2 (2340 Hz and 2382 Hz) - (a) Response of the HF transducers (2340 Hz) - (b) Near injection pressure sensors HF1 and HF2 plotted with the PM signals (2340 Hz) - (c) Response of the HF transducers (2382 Hz) - (d) Near injection pressure sensors HF1 and HF2 plotted with the PM signals (2382 Hz) - Rapid evolution of the mode spatial structure.*

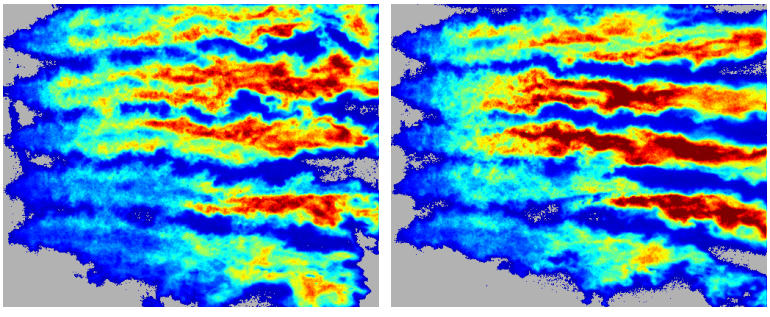

Figure 3.37: *PF2 during LFM1 at SP2 (2340 Hz (a) and 2382 Hz (b)) - Instantaneous OH* emission of the flames.*

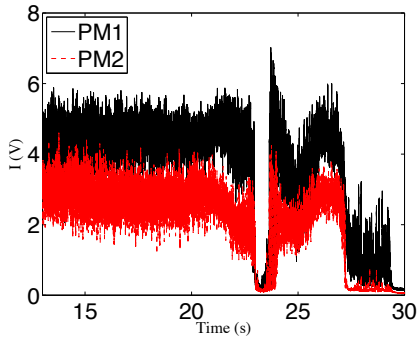

Figure 3.38: *PF2 during LFM2 - Evolution of the PM signals. The signal drops to zero at $t \approx 23$ s and $t \approx 27$ s because flames become very short and are no longer in the line of sight of the photomultipliers.*

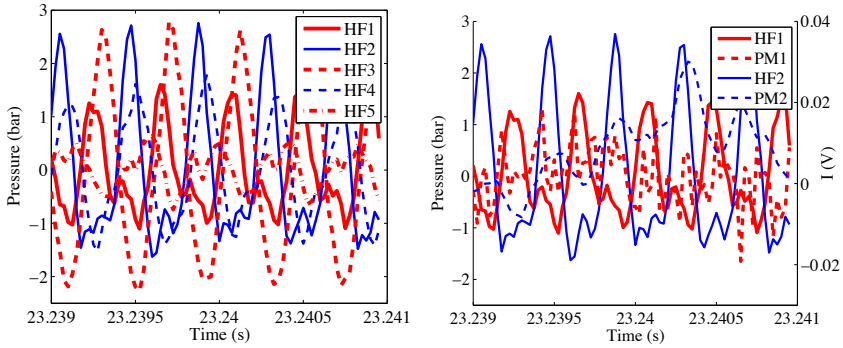

(a) (b)

Figure 3.39: *PF2 during LFM2 at SP2 (2440 Hz) - (a) Response of the HF transducers - (b) Near injection pressure sensors HF1 and HF2 plotted with the PM signals.*

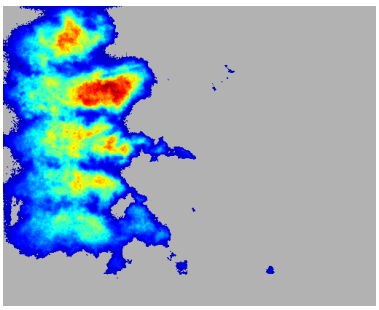

Figure 3.40: *PF2 during LFM2 at SP2 (2440 Hz) - Instantaneous OH* emission of the flames. Flame length has been importantly reduced by the modulation.*

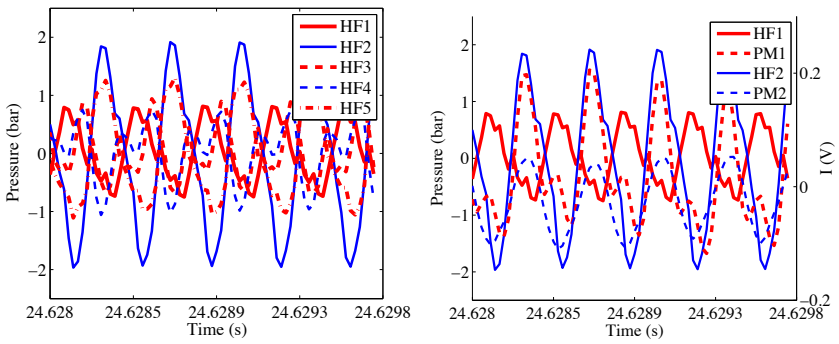

(a) (b)

Figure 3.41: *PF2 during LFM2 at SP3 (2655 Hz) - (a) Response of the HF transducers - (b) Near injection pressure sensors HF1 and HF2 plotted with the PM signals.*

Fourth spectral peak (SP4) By far the strongest response in the second LFM test case is obtained at 3200 Hz. As shown in Fig. 3.32, there is a marked expansion of the acoustic pressure amplitude at this frequency. In Fig. 3.42, the HF2 transducer, located near the injection plane, features an amplitude of about 6 bar. This mode has several interesting characteristics which will be investigated further in the continuous wave test described in the next section. One already notices that at this frequency the flames become quite short too and the combustion region is correspondingly more compact. In Fig. 3.38, the PM1 sensor still detects a signal while PM2 is very low. This can be explained by noting that in Fig. 3.42 (c) there is an important asymmetry between the various flames. Those established in the upper part of the chamber and monitored by PM1 are fairly long, while those formed in the lower part of the chamber are short and PM2 detects a reduced amount of light.

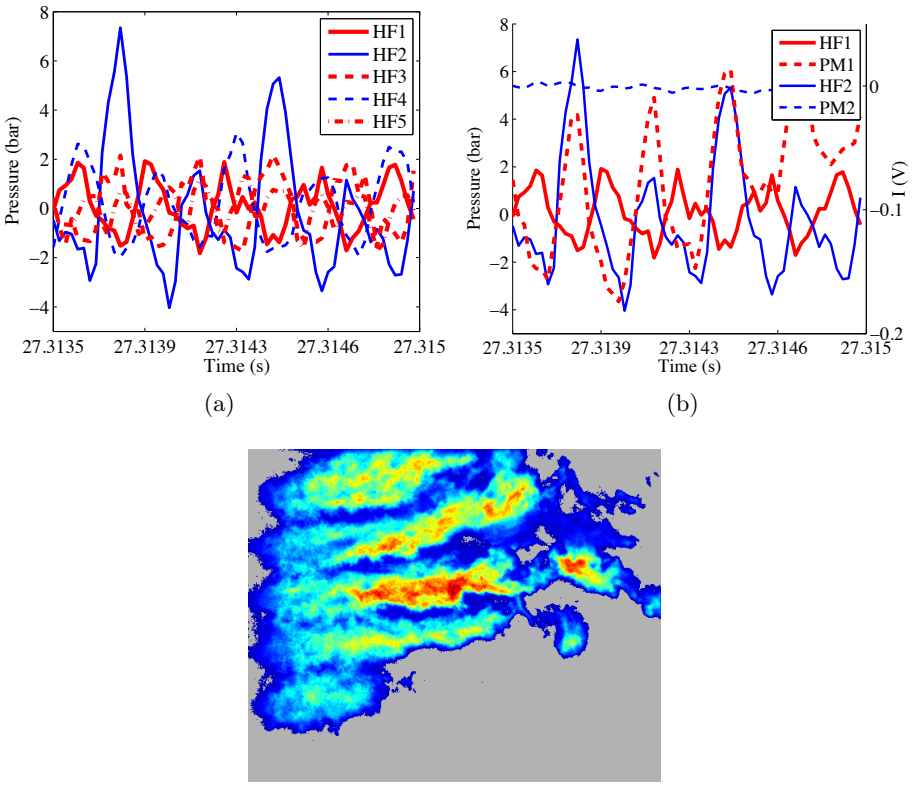

Figure 3.42: *PF2 during LFM2 at SP4 (3200 Hz) - (a) Response of the HF transducers - (b) Near injection pressure sensors HF1 and HF2 plotted with the PM signals - (c) Instantaneous OH* emission of the flames.*

Continuous wave modulations have been carried out for the first three spectral peaks at frequencies of 1840 Hz, 2330 Hz and 3200 Hz.

3.5.3 Continuous wave modulation (CWM1)

CWM1 has been carried out at the beginning of LFM2, as shown in Fig. 3.32. In this figure, one notices that there is no growth of the acoustic amplitude and the flames keep a shape which is close to the original pattern.

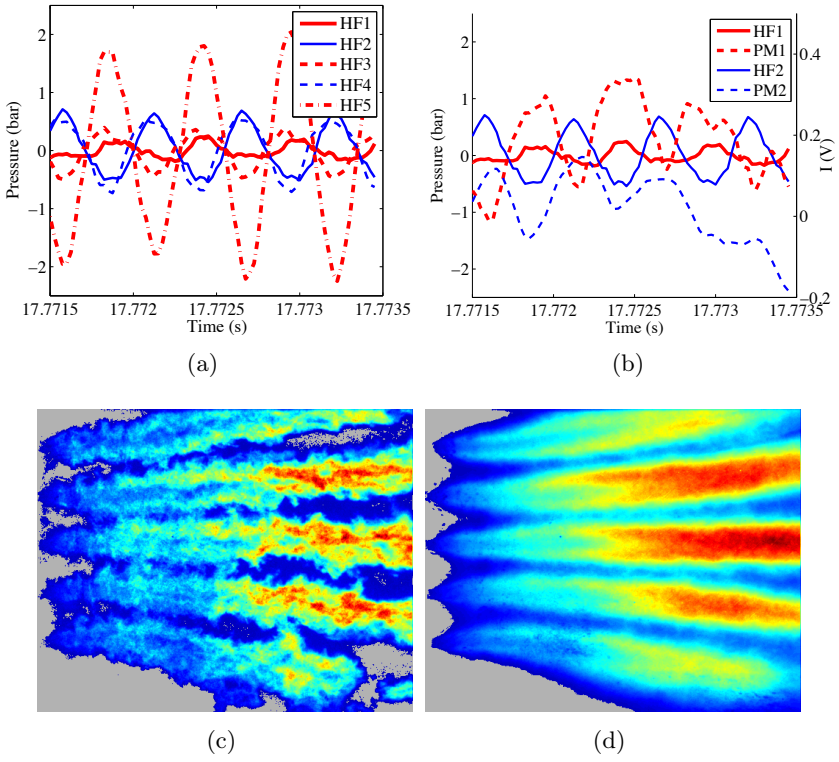

Figure 3.43: *PF2 during CWM1 at SP1 (1840 Hz) - (a) Response of the HF transducers - (b) Near injection pressure sensors HF1 and HF2 plotted with the PM signals - (c) Instantaneous OH* emission of the flames - (d) Average OH* emission.*

Fig. 3.43 confirms the LFM1 data and indicates that $f = 1840$ Hz is the frequency of the 1T mode. Fig. 3.43 (b) shows that heat release and pressure signals are in phase respectively in the upper and lower parts of the chamber. The high speed camera images provide useful information on the coupling mechanism. It is already established that the pressure signals correspond to a transverse mode. The visualization confirms this statement and leaves little doubt on the presence of a strong transverse velocity component. The five flames

oscillate in the transverse direction at the frequency of modulation. It is also possible to formulate an explanation for the relative amplitudes of the pressure signals recorded in this case. The flame oscillation near the chamber aftplane is way more important than near the injection plane. As a consequence, the pressure signal detected near the aftplane (HF5) has a larger amplitude than the signals detected by the other sensors. Fig. 3.44 - (a) and (b) show averaged CH* emission images when the flames are respectively near the maximum or minimum amplitudes of their transverse motion.

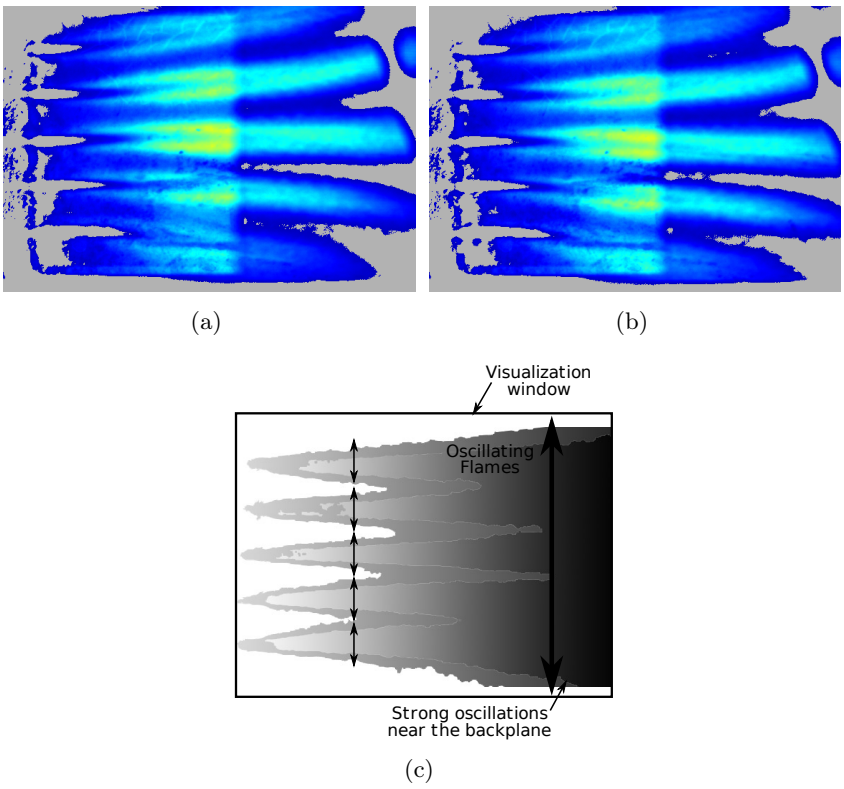

Figure 3.44: *PF2 during CWM1 at SP1 (1840 Hz) - (a) Average CH* emission of the flames phase locked at the top of their motion - (b) Average CH* emission of the flames phase locked at the bottom of their motion - (c) Flames are weakly oscillating near the injection plane but more importantly near the backplane.*

To get a better understanding of the motion of these flames, two streak films have been synthesized from the high speed CH* emission images. Fig. 3.45 - (a) (near the injection plane) and (b) (near the backplane) illustrate the fact that the flame oscillation amplitude is larger near the chamber exhaust.
Because the acoustic field near the injection plane is relatively weak, liquid jet

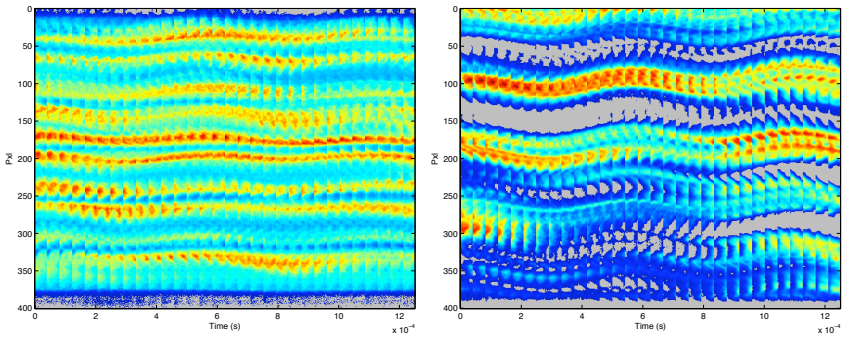

(a) (b)

Figure 3.45: *PF2 during CWM1 at SP1 (1840 Hz) - These streak films are deduced from the SA1 images (CH* emission of the flames) - (a) Near the injection plane - (b) Far from the injection plane - The oscillation amplitude is more important downstream.*

break-up and primary atomization are not modified in this region, explaining why the flames are still long. This is illustrated in Fig. 3.46. The backlighting illumination distinctly shows the length of the liquid core. In contrast with what is observed during the cold flow tests, the liquid jet seems to be unaffected by the transverse acoustic motion, except at the end of the core where one observes an oscillation. Droplets and filaments are ejected from the main core in a quasi perpendicular direction.

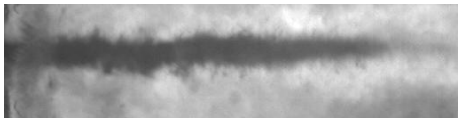

Figure 3.46: *PF2 during CWM1 at SP1 (1840 Hz) - Image of the core length recorded with the APX camera in backlighting mode.*

3.5.4 Continuous wave modulation (CWM2)

The modulation frequency is now set at 2330 Hz, which corresponds to the first part of the SP2 observed during the linear frequency modulation test, when the flames are still quite long (Fig. 3.47).
In this experiment as well, flames oscillate in the transverse direction as can be seen in the SA1 images (Fig. 3.48), confirming the transverse mode hypothesis. The main difference with the first continuous wave test is that flames oscillate almost in the same way near the injection plane and downstream. Correspondingly the pressure sensors have about the same amplitude levels.

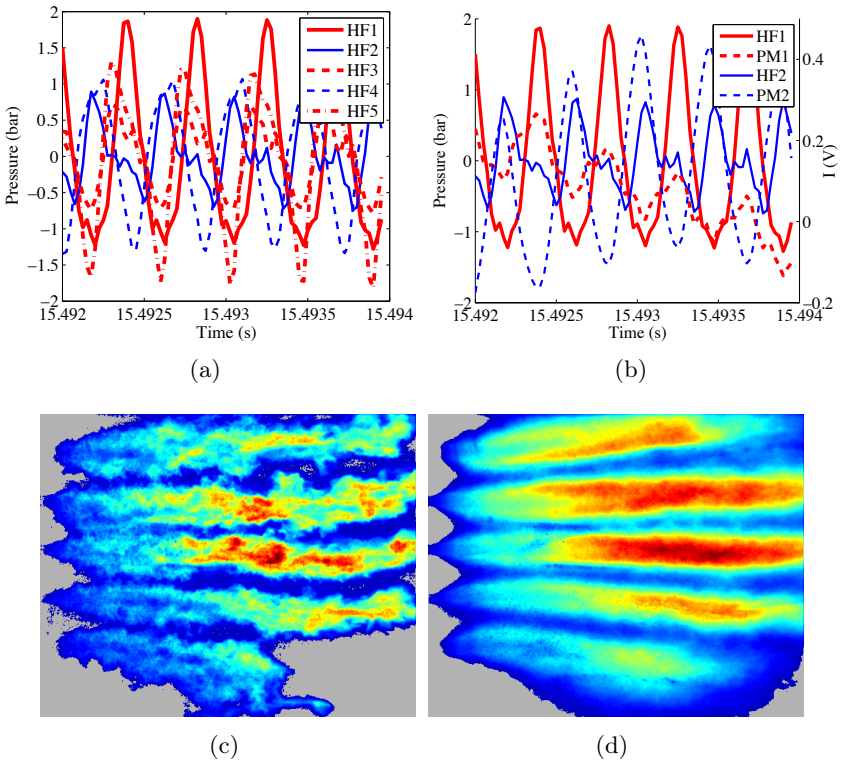

Figure 3.47: *PF2 during CWM2 at SP2 (2330 Hz) - (a) Response of the HF transducers - (b) Near injection pressure sensors HF1 and HF2 plotted with the PM signals.*

Fig. 3.49 shows an image of the liquid core. This is similar to that shown in Fig. 3.46, except that the length of the core is now shorter. This remark is consistent with the fact that the acoustic velocity has a larger amplitude near the injection plane in this case.

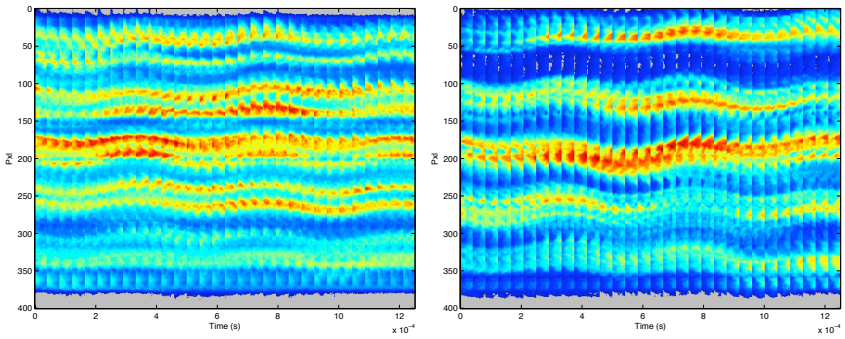

(a) (b)

Figure 3.48: *PF2 during CWM2 at SP2 (2330 Hz) - Streak films formed from images recorded by the SA1 camera. Continuous wave modulation at the second spectral peak - (a) The streak window is near the injection plane - (b) The streak window is far from the injection plane - The oscillation amplitude is still more important downstream, but the difference is not as important as for the CWM1 test case.*

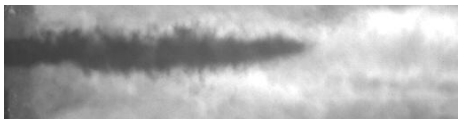

Figure 3.49: *PF2 during CWM2 at SP2 (2330 Hz) - Image of the core length recorded with the APX camera in the backlighting mode.*

3.5.5 Continuous wave modulation (CWM3)

The third CWM test is carried out at SP4 (3200 Hz). It was found during the LFM test that the amplitude reached an important value and that this gave rise to new phenomena. One first notices that the flame pattern looses its symmetry. High speed imaging is now used to understand the mechanisms involved.

The first feature of this CWM modulation test is the important amplitude of the acoustic and heat release response, as illustrated in Fig. 3.50 (a) and (b). At the end of the test case, the amplitude of the acoustic oscillation is around 12 bar, which is almost half of the mean pressure (26 bar). The fluctuations in heat release recorded by the photomultipliers also exhibit a rapid increase during the CWM modulation. When the nominal frequency is reached, the steady state is obtained almost instantly. However, one still observes an increase in amplitude during the test. To characterize this mode, it is interesting to examine the relative phase between the pressure transducers (Fig. 3.51) (a). HF1 and HF4 are in phase, HF2 and HF3 also and the two groups are out of phase: the

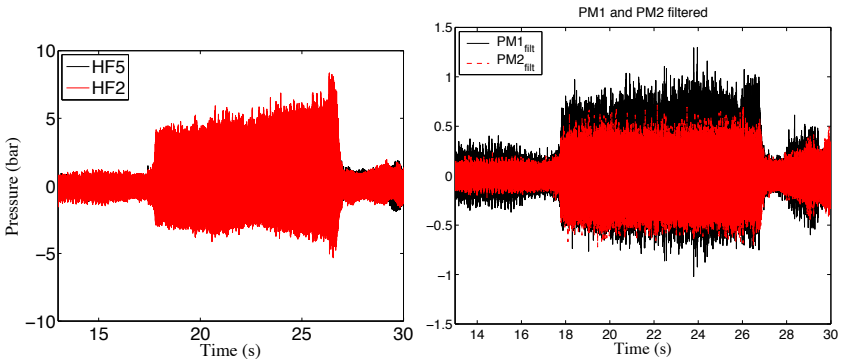

(a) (b)

Figure 3.50: *PF2 during CWM3 at SP4 (3200 Hz) - (a) Sensors response during the continuous wave modulation at the third spectral peak - (b) Filtered PMs response during the CWM3 test case.*

is clearly a coupled longitudinal and transverse mode. The HF5 signal is not clearly in phase with any of the sensors, but the frequency range pertains to the 1T2L mode.

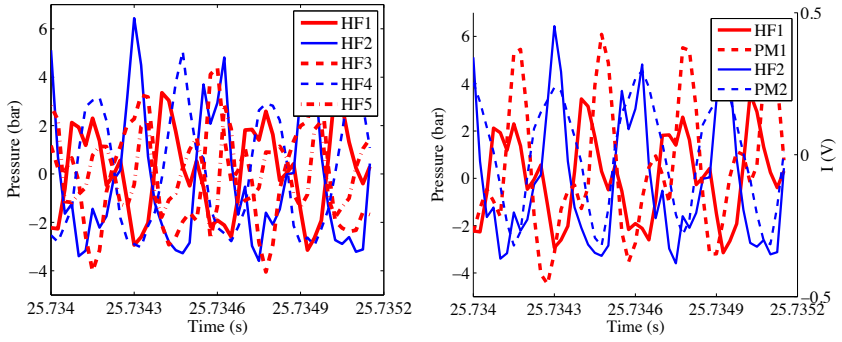

(a) (b)

Figure 3.51: *PF2 during CWM3 at SP4 (3200 Hz) - (a) Response of the HF transducers - (b) Near injection pressure sensors HF1 and HF2 plotted with the PM signals.*

One also finds that the temperature recorded at the bottom wall of the chamber rapidly increases during the continuous wave modulation test case (Fig. 3.52). Other eigenmodes tested before did not show any effect on the temperature at the chamber wall which was always between 350 K and 450 K. This indicates that there is a great difference between the combustion response reported so far and that observed in the present case.

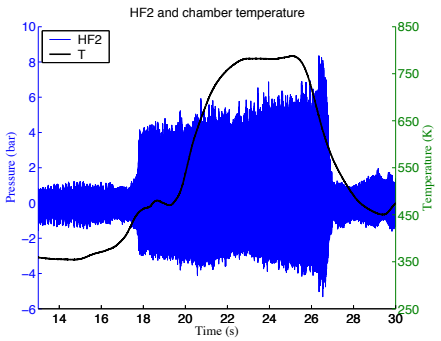

Figure 3.52: *PF2 during CWM3 at SP4 (3200 Hz) - HF2 response plotted together with the temperature recorded at the bottom wall of the chamber. The temperature at the bottom wall reaches 800 K at the end of the continuous wave modulation.*

Another interesting characteristic is shown in Fig. 3.53. Flames are asymmetric and very short, and their length is reduced with respect to the size observed without modulation.
The streak film, presented in Fig. 3.54 (a), provides an interesting information on the mechanism which induces an asymmetric flame pattern.
It shows that flames near the bottom of the chamber have an oscillation amplitude which is larger than that observed for flames located near the top of the chamber. This higher level of modulation improves the atomization process subsequently reducing the flame length. In addition, the amplitude recorded by the transducers at the top wall and at the bottom wall are quite different. This asymmetry is probably linked to that observed for the flames. These observations indicate that the shape of the eigenmode which is being excited is modified by the coupling mechanism as described further in this chapter (section 3.9).
Backlighting visualization is displayed in Fig. 3.54 (b). In this case, the core length is significantly shorter than what was observed for the two previous eigenfrequencies. The three successive images of the core demonstrate the link between the acoustic velocity amplitude of oscillation, the spatial structure of the acoustic field, and the lengths of the flames, which is a direct consequence of the length of the jet core. To compare the three cases, the mean core shapes corresponding to the three frequencies 1840 Hz, 2330 Hz and 3200 Hz are displayed in Fig. 3.55.

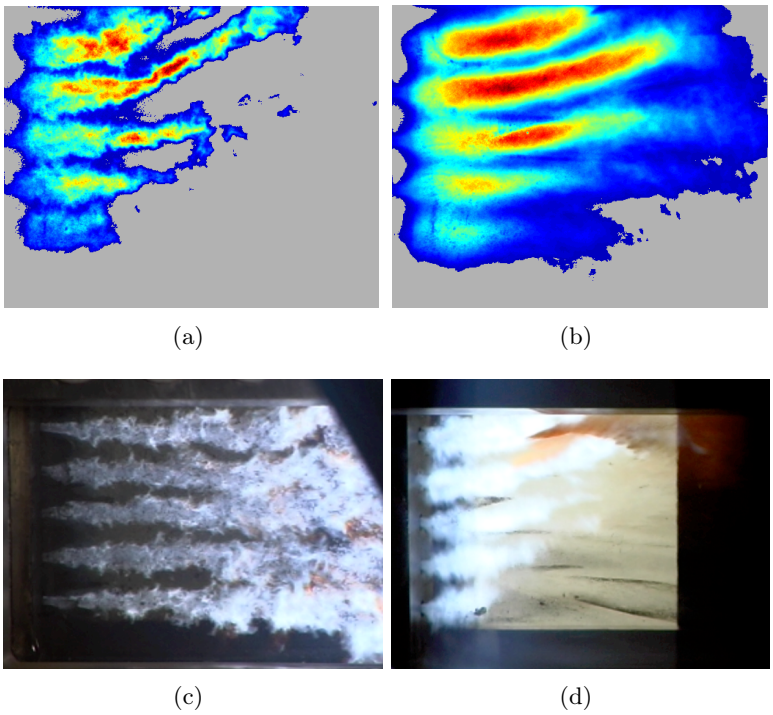

(a) (b)

(c) (d)

Figure 3.53: *PF2 during CWM3 at SP4 (3200 Hz) - (a) Instantaneous OH* emission of the flames recorded during the CWM3 test case - (b) Average OH* emission. Flames are short. Those in the upper part of the chamber are longer than those established in the lower part - (c) Frame recorded by a DV control camera - Without excitation (OWM) - (d) During SP4. These images highlight differences observed in the two cases.*

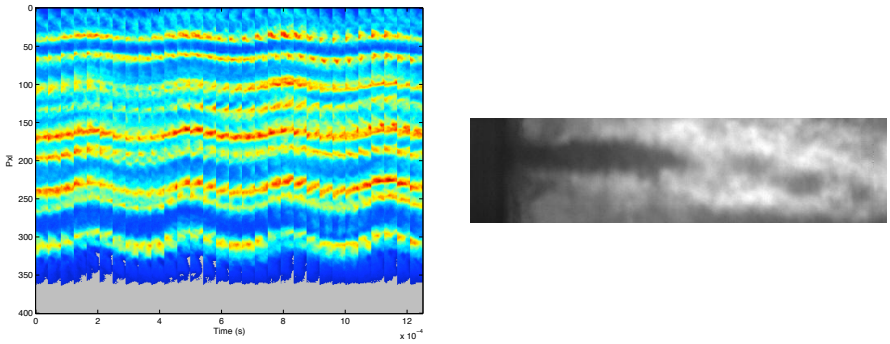

Figure 3.54: *PF2 during CWM3 at SP4 (3200 Hz) - (a) Streak films deduced from the SA1 images. The streak window is located near the injection plane - The amplitude of oscillation is quite important and it is not the same for every flame. Flame oscillation amplitude is largest near the bottom of the chamber - (b) Instantaneous image of the core length recorded with the APX camera in backlighting mode.*

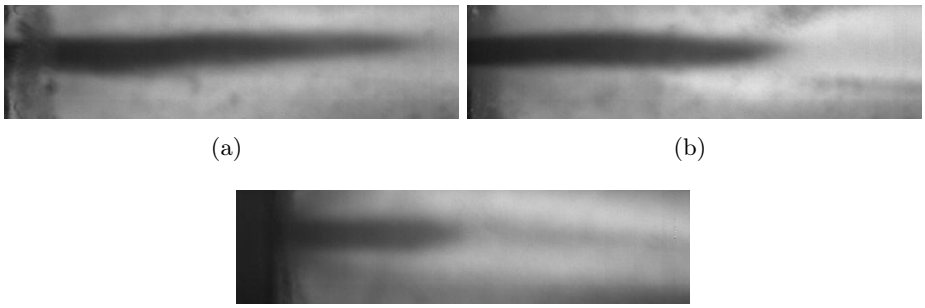

(a) (b)

(c)

Figure 3.55: *PF2 - Average images of the core length recorded with the APX camera in backlighting mode for the three eigenfrequencies - (a) 1840 Hz - (b) 2330 Hz - (c) 3200 Hz.*

3.6 Operating point PF3

The third operating point, PF3, is quite close to PF2 in terms of injection parameters. Mass flow rates, pressure, mixture ratio, oxygen injection velocity are kept constant. The only modification is a decrease of the gas stream injection diameter. Since the same mass flow rate is imposed, the methane velocity and the momentum flux ratio are increased ($J = 6$). PF3 is also close to an operating point which was extensively studied by Richecoeur during the last Mascotte campaign. It is then a good test case to check whether comparisons with previous results are relevant.

Points	P_{ch}	E	J
PF3	2.6 MPa	1.33	6
I5-P30-C	3 MPa	1.33	4.8

Table 3.9: *Injection parameters for operating point PF3 (current test series) and the I5-P30C operating point (studied by Richecoeur (2006)).*

The two runs carried out during the campaign for PF3 conditions are listed in table 3.10 and described in the following subsections.

Type	LFM	CW
frequency (Hz)	$1400 \rightarrow 3400$	3145

Table 3.10: *Types of excitation and corresponding frequencies investigated for operating point PF3.*

3.6.1 Operation under weak modulation (OWM)

As for PF1, no test without the VHAM were carried out to save hot fire tests for modulated situations. As previously, images recorded at the beginning of the ramp, when the modulation amplitude is still low, are used to define the baseline configuration. Fig. 3.56 shows OH* fields compared to those obtained by Richecoeur for the I5-P30-C operating point. The distributions of light emission are in good qualitative agreement.
For this operating point as well flames extend beyond the visualization window rim. The momentum flux ratio J is higher than that corresponding to PF2, but it is still fairly low and one expects a relatively poor atomization process. Nevertheless, the intense area of combustion starts sooner in this experiment than in the PF2 test case, as illustrated in Fig. 3.57.

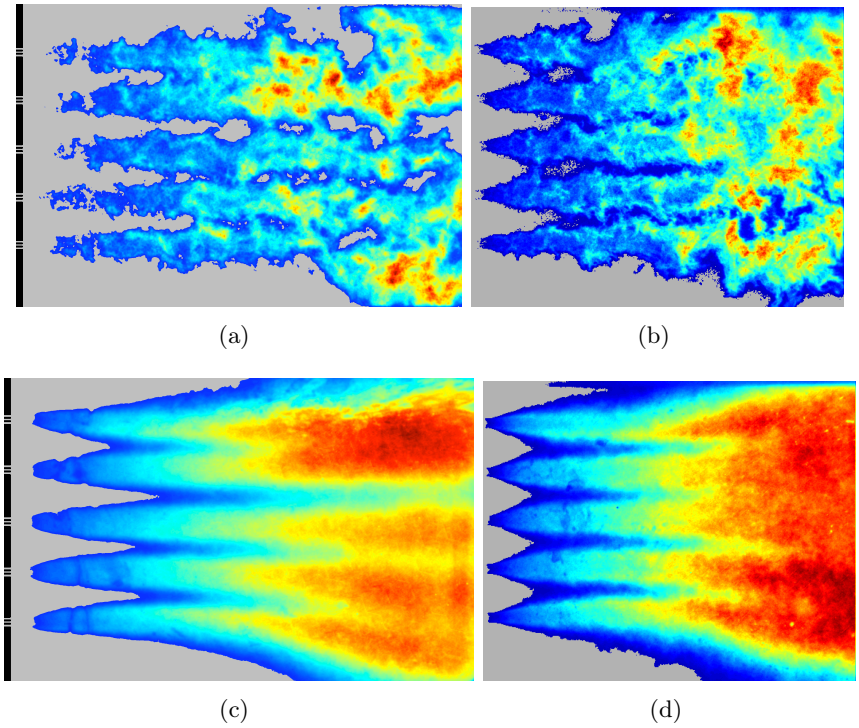

(a) (b)

(c) (d)

Figure 3.56: *Instantaneous (a,b) and averaged (c,d) OH* emission of (a,c) I5-P30-C operating point (Richecoeur (2006)) non-modulated (b,d) PF3 during OWM. The flames expansion angle and the most reactive area are close in the two experiments.*

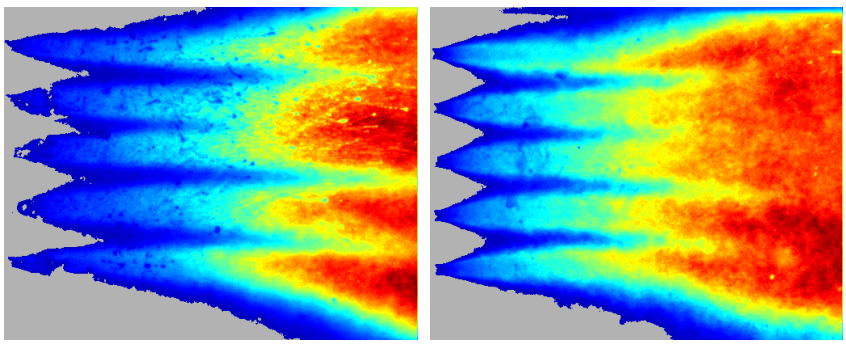

(a) (b)

Figure 3.57: *(a) PF2 during OWM - averaged OH* emission - (b) PF3 during OWM - averaged OH* emission. The better atomization of operating point PF3 leads to shorter flames.*

3.6.2 Linear frequency modulation (LFM)

The time evolution of the five pressure signals during the linear frequency modulation test is displayed in Fig. 3.58 (a). Fig. 3.58 (b) shows the short time Fourier analysis associated with this test case. This plot is obtained by processing the HF2 sensor signal.

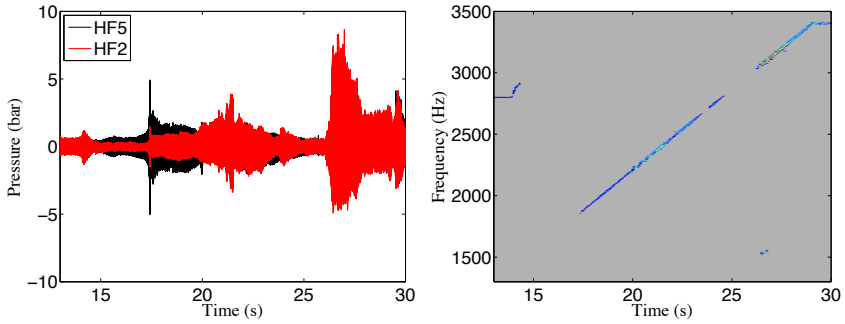

(a) (b)

Figure 3.58: *PF3 during LFM - (a) Pressure sensors response - (b) Temporal evolution of the HF2 power spectral density. Three peaks emerge from the background noise.*

The modulation starts at 1400 Hz and ends at 3400 Hz and its slope is 133 Hz/s. Only three peaks emerge from the background noise. This differs from the PF1 and PF2 cases. There is no identifiable response around 2700 Hz. This is at variance with the idea that it is possible to follow modes from one test to another. One possible explanation is that the eigenfrequency at 2700 Hz has been shifted from its initial value and lies close to another eigenfrequency preventing a clear identification. It is also possible that the rate of frequency sweep is too high for this mode to respond. One last possibility would be that the longitudinal mode exhibits a negligible response at this operating point.
Fig. 3.59 - (a) shows the photomultipliers response to the LFM after filtering. One can distinguish the three peaks, but the response depends on the pressure sensor. One also finds that the third peak is not as important as the second peak.
One central issue in high-frequency combustion instabilities studies is the understanding of interactions between the combustion chamber and the different feeding elements acoustics. It has often been indicated that for high-frequency phenomena, injectors play the role of filters that uncouple the chamber from the feeding system. Recently, this statement has been questioned. Fig. 3.59 (b), which shows the HF2 pressure sensor response during the LFM plotted together with a pressure sensor located in the liquid oxygen injection head, seems to con-

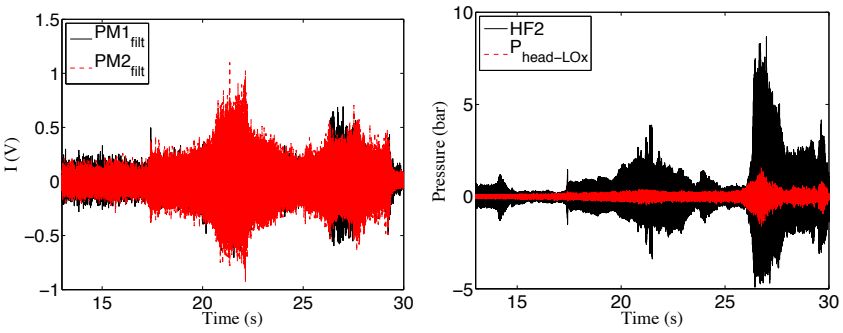

(a) (b)

Figure 3.59: *PF3 during LFM - (a) Filtered PM signal evolution during the frequency sweep - (b) HF2 response during the frequency ramp plotted with the unsteady pressure in the LOx injection head.*

firm that the acoustics of the feedlines must be taken into account. Near the most responding frequency, the oscillations amplitude become relatively strong in the dome as well.

First spectral peak (SP1) It is first informative to examine the pressure evolution in the vicinity of SP1 (f = 1870 Hz), plotted in Fig. 3.60. The spectral peak location is close to the first spectral peak of PF1 and PF2, and can be associated with some confidence to the same eigenmode. This spectral peak has been extensively studied in the PF2 case and one may safely conclude that this corresponds to the first transverse mode. Here too, one finds that the acoustic pressure amplitude is more important near the chamber exhaust and less important near the injection plane.
The relative phase of pressure sensors and photomultipliers displayed in Fig. 3.61 (a) confirms the 1T hypothesis.
The main difference with the PF2 test case at this frequency is that the recorded intensity is greater: the HF5 sensor amplitude is 10 bar (from -5 to 5 bar around the mean pressure) while the other sensors detect a fluctuating pressure amplitude of several bars. This has a visible effect on the flame structure, as shown in Fig. 3.61 (b). The general characteristics of this image recorded at the maximum amplitude differ from those corresponding to the same eigenmode but at different operating points. Flames are significantly shorter in the present case.
It is possible to observe similar features by examining images recorded at instants just after the maximum (Fig. 3.62). The OH* emission from the jet boundaries is more intense than from the core and the expansion angle is augmented with respect to that observed without excitation.

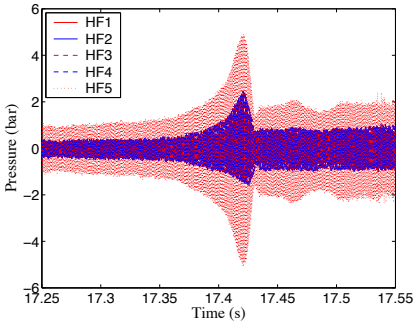

Figure 3.60: *PF3 during LFM at SP1 - Response of the HF transducers in the vicinity of 1870 Hz. The characteristic response of the SP1 observed at PF1 and PF2 can be recognized: the HF5 sensor signal is the most important one and the peak is damped suddenly.*

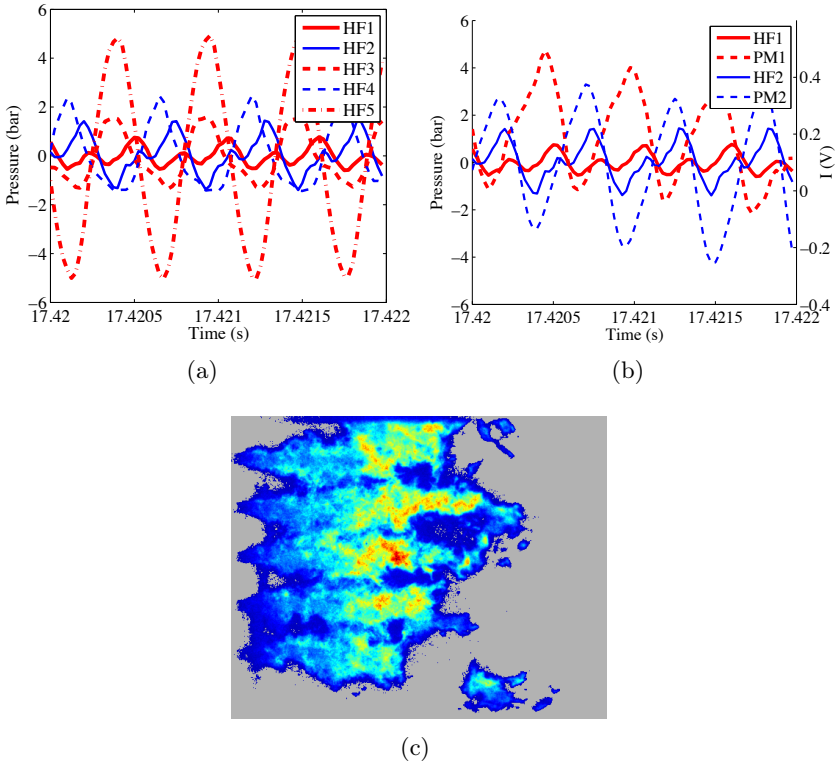

Figure 3.61: *PF3 during LFM at SP1 (1870 Hz) - (a) Response of the HF transducers - (b) Pressure sensors HF1 and HF2 plotted with the PM signals - (c) Instantaneous OH* emission.*

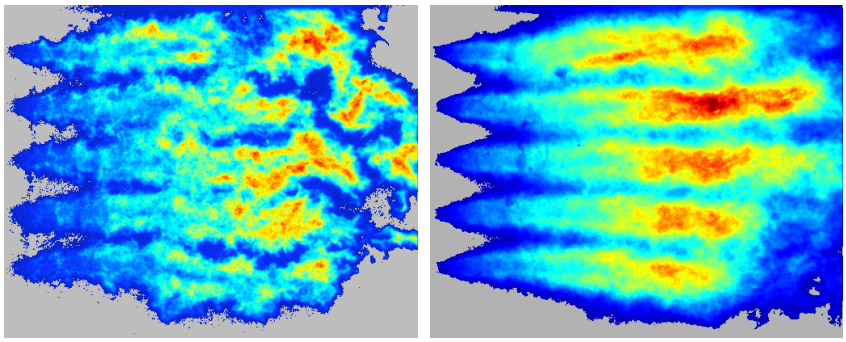

(a) (b)

Figure 3.62: *PF3 during LFM just after SP1 (1870 Hz) - (a) Instantaneous OH* emission just after the peak - (b) Average OH* emission after the peak.*

Second spectral peak (SP2) The second spectral peak is located near 2325 Hz. The pressure evolves in a complex way (Fig. 3.63), possibly indicating that two eigenmodes have merged. It is interesting to distinguish two stages, the first corresponding to a frequency of 2335 Hz while the second corresponds to 2390 Hz. As seen for operating point PF2, this might be linked to the same eigenmode (which would be 1T1L), but to different flame patterns, implying different temperature fields.

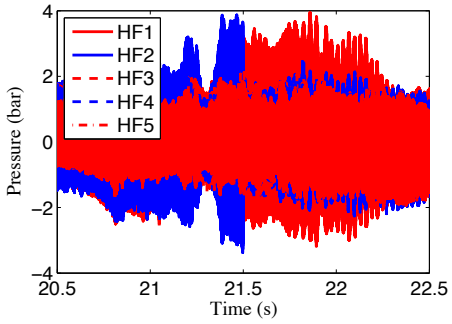

Figure 3.63: *PF3 during LFM at SP2 (2325 Hz) - Response of the HF transducers.*

During the first stage, the flames are compact and occupy only about one half of the visualization window. The pattern is not symmetric as shown by a typical image acquired by the ICCD camera (Fig. 3.64 (c)). Signals delivered by the pressure sensors and by the photomultipliers are plotted in Fig. 3.64 (a) and (b).

At the second stage of SP2, flames are even more compact and become symmetric (Fig. 3.65) (c). No high speed images are available for this operating point, but the amplitude of the motion can be illustrated by examining two successive images recorded by the ICCD camera. One sees in Fig. 3.65 (b) that the filtered PM signal reaches high levels indicating that the flame oscillation amplitude is quite large.

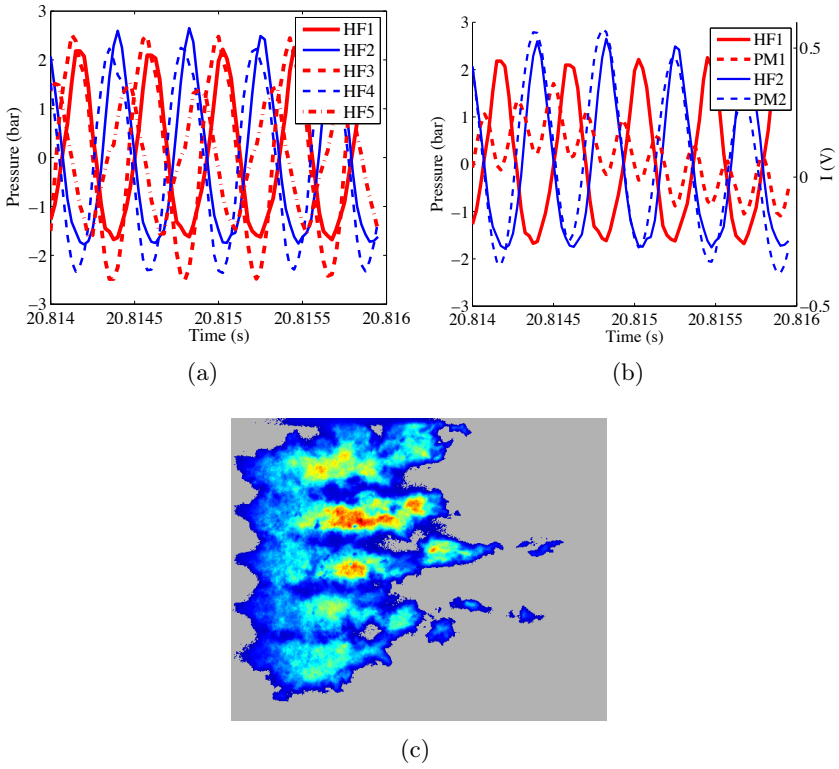

Figure 3.64: *PF3 during LFM at SP2 (2325 Hz) - (a) Response of the HF transducers - (b) Near injection pressure sensors HF1 and HF2 plotted with the PM signals - (c) Instantaneous OH* emission.*

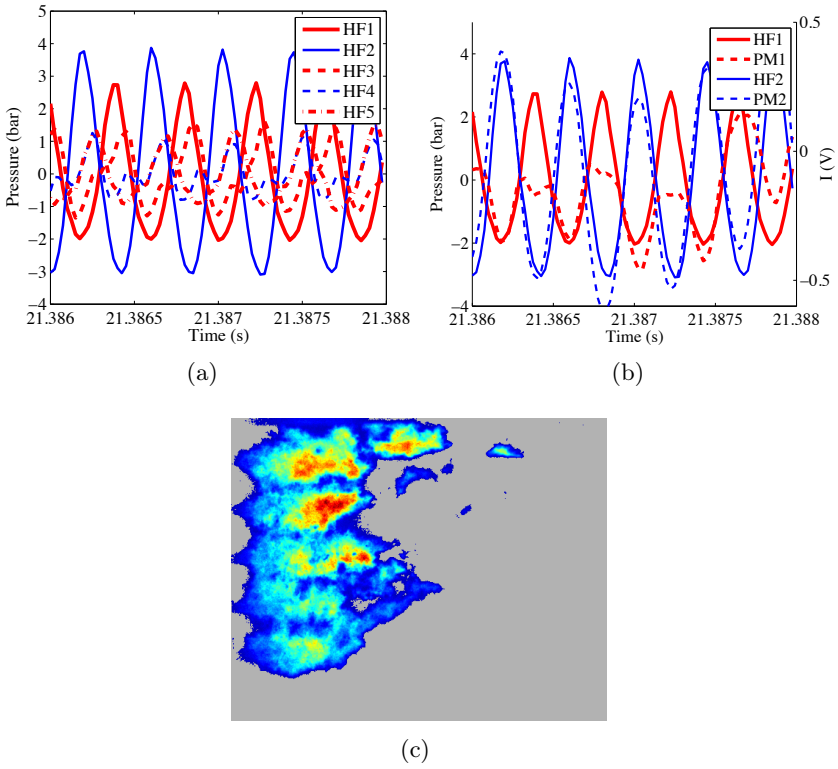

Figure 3.65: *PF3 during LFM at SP2 (2390 Hz) - (a) Response of the HF transducers - (b) Near injection pressure sensors HF1 and HF2 plotted with the PM signals - (c) Instantaneous OH* emission. Flames are shorter in the second stage of SP2.*

Fourth spectral peak (SP4) As previously explained, the third spectral peak (SP3) observed at operating points PF1 and PF2 does not clearly emerge from the background noise, and the fourth spectral peak (SP4) is now discussed. In this linear frequency sweep, SP4 appears near $f = 3150$ Hz. Its level is by far the most important one. The HF2 sensor records levels of fluctuation which covers pressures from -5 to +9 bar. This is illustrated in Fig. 3.66 which displays the pressure signal detected by the HF2 sensor together with the mean temperature, recorded at the bottom wall of the chamber. At this frequency, the system response is the strongest and correspondingly the temperature at the wall increases rapidly by several hundred degrees. This temperature increase at a lateral wall located at a distance from the central reaction region indicates that the interaction induces a considerable intensification of the heat flux reaching the boundary.

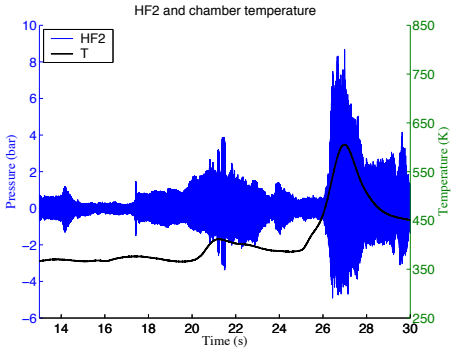

Figure 3.66: *PF3 during LFM - HF2 response plotted with the temperature measured at the chamber lower wall.*

Fig. 3.67 (a), (b) and (c) provide consistent information with SP4 studied for other operating points. This is a coupled transverse and longitudinal mode featuring a large amplitude in the pressure oscillation. The unsteady heat release is in phase with the pressure field indicating a coupling between these two fields. Flames are short, combustion takes place in a compact region and the pattern is asymmetric.

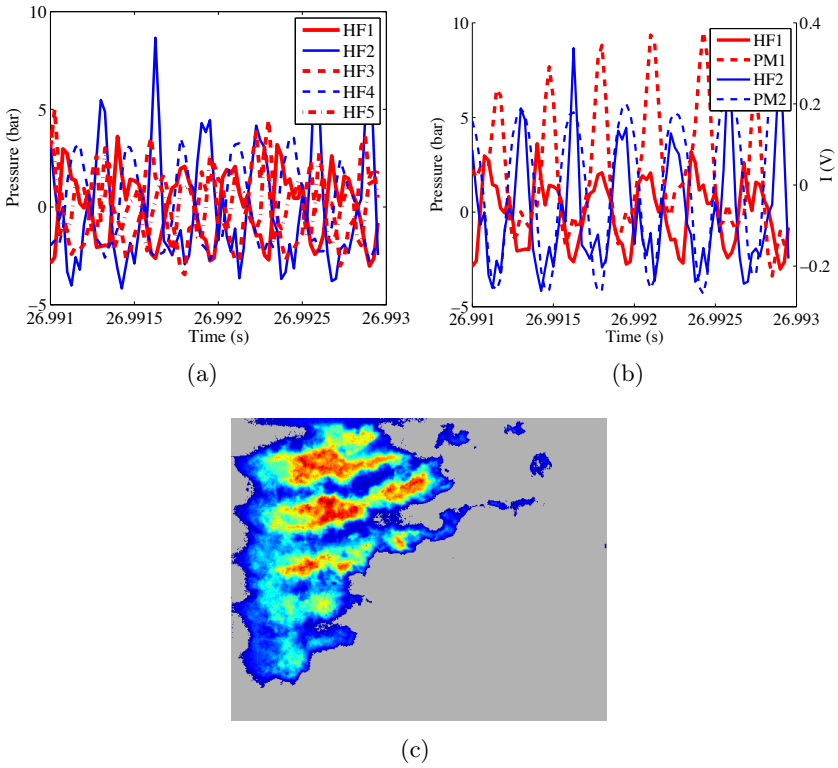

Figure 3.67: *PF3 during LFM at SP4 (3125 Hz) - (a) Response of the HF transducers - (b) Near injection pressure sensors HF1 and HF2 plotted with the PM signals - (c) Instantaneous OH* emission. Flames are short and asymmetric.*

3.6.3 Continuous wave modulation (CWM)

The continuous wave modulation of operating point PF3 is only available for one spectral peak (SP4 at $f = 3125$ Hz). To reduce the number of hot fire tests, it was initially decided to analyze two spectral peaks SP2 ($f = 2325$ Hz) and SP4 during the same test. To do this, it was necessary to modulate the chamber at SP2 before the flames were ignited. Unfortunately this experimental procedure was not feasible. When combustion is initiated, the external modulation interferes with the ignition process and the flames are not suitably established. It was then decided to ignite the system while the wheel was operating at an off resonant frequency and then ramp-up the rotation speed to reach SP4 as illustrated in Fig. 3.68.
The signals obtained during this test are close to those recorded during the PF2-CWM3 test case. The major observations are listed below:

- The mode corresponds to a coupled transverse and longitudinal motion

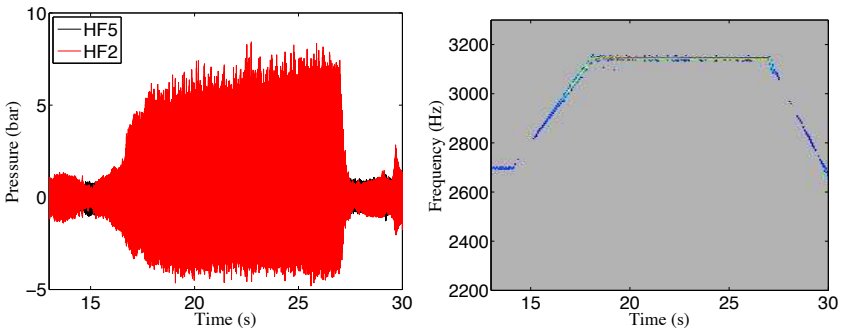

(a) (b)

Figure 3.68: *PF3 during CWM at SP4 (3125 Hz) - (a) Response of the HF transducers - (b) Temporal evolution of the HF2 power spectral density. The test is started at an off resonant frequency, a short ramp leads to $f = 3125$ Hz. The amplitude of oscillations raises during the continuous wave modulation.*

(1T2L) as exemplified in Fig. 3.69 (a) and (b).

- The pressure signal level reaches extremely high amplitudes.
- Combustion takes place in a compact region as shown in Fig. 3.69 (c).
- The pressure amplitude increases during this continuous wave modulation as shown in Fig. 3.68.
- The flame length decreases during the test (Fig. 3.70).
- The temperature at the lower chamber wall rises (Fig. 3.71 (a)).
- The flame pattern becomes asymmetric.
- The acoustic field is also asymmetric.

Many of the previous features are reminiscent of observations made during high frequency instabilities in rocket engines. It is known that high frequency oscillations arising in real systems augment heat loads to the chamber walls and injection backplane often leading to a rapid destruction of the injection units. The present experiments indicate that when the pressure fluctuation level exceeds 20 % of the mean chamber pressure, a rise in temperature is measured at the chamber wall indicating that combustion intensity is enhanced and the heat flux is augmented in this situation. These features constitute strong evidence that the processes observed in this test are similar to those which are actually taking place in a real engine.
It is also worth noting that producing short flames by enhancing atomization and mixing is not a sufficient condition for a strong resonance. For example,

at SP3, flames are as short as at SP4, but the response level is quite different. Mechanisms proposed must account for these differences in behavior. The asymmetry observed in the flame pattern and pressure field may also play a crucial role in the instability triggering and growth.

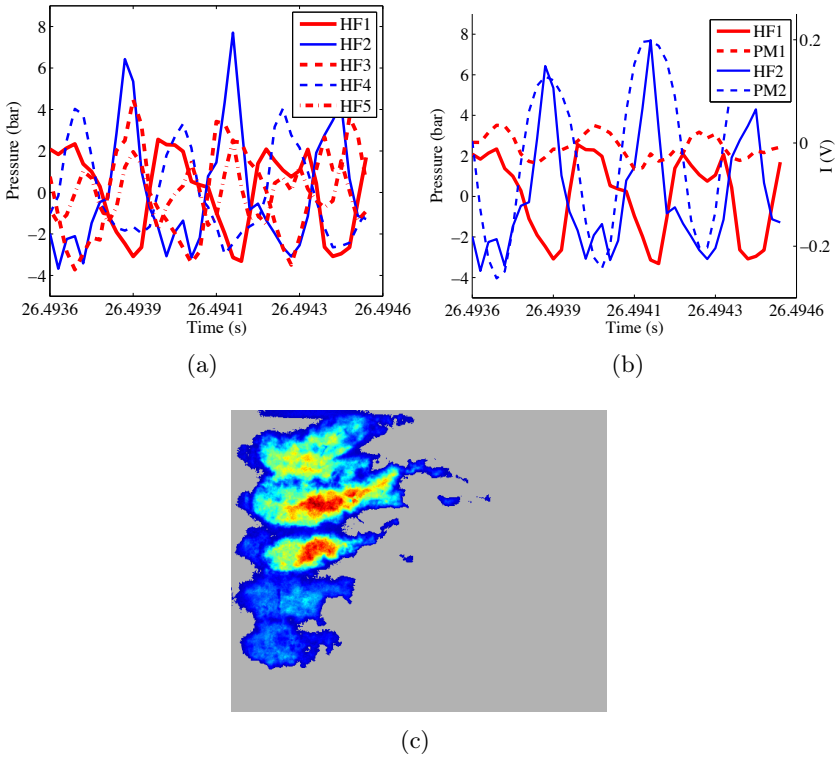

Figure 3.69: *PF3 during CWM at SP4 (3125 Hz) - (a) Response of the HF transducers - (b) Near injection pressure sensors HF1 and HF2 plotted with the PM signals - (c) Instantaneous OH* emission at the end of the continuous wave test. Combustion area has been drastically reduced and flames are concentrated near the injectors.*

It is interesting to illustrate the flame asymmetry with the streak film displayed in Fig. 3.71 (b). This figure shows that flames located in the lower part of the chamber oscillate with a larger amplitude than flames established in the upper part of the chamber. Once again, the amplitude offset between HF2 and HF3 sensors and the streak film displayed in Fig. 3.71 (b) indicate that the eigenmode spatial structure is asymmetric, the velocity antinode being located near the last injector and not at the system central axis as also observed for the PF2 test case. One may conclude that the flame length becomes a function of the acoustic velocity amplitude. When this amplitude is large, atomization, vaporization and mixing are enhanced and the flame pattern is made shorter

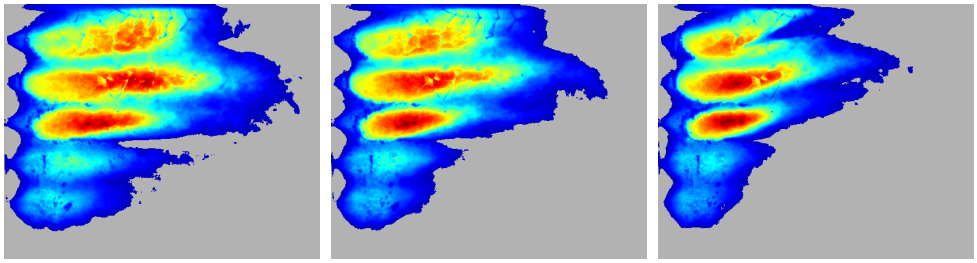

(a) (b) (c)

Figure 3.70: *PF3 during CWM at SP4 (3125 Hz) - Evolution of the averaged OH* emission during the CWM test case. Flames are getting shorter while the amplitude of oscillation increases.*

and the combustion region becomes more compact.

3.7 Operating point PF4

Injection conditions corresponding to operating point PF4 are gathered in table 3.11. Both PF4 and PF5 correspond to high pressure experimental conditions. The nominal pressure is 5.9 MPa. Since the critical value for liquid oxygen is 5.04 MPa, injection conditions defining these two operating points are transcritical, and represent to some extent conditions prevailing in real rocket engines during steady state operation. The other parameters, mass flow rates, E and J are close to those selected for PF2 and PF3. To obtain a higher pressure, the exit nozzle diameters have been reduced.

Points	P_{ch}	E	J
PF4	5.9 MPa	1.13	3.8

Table 3.11: *Injection parameters for operating point PF4. Pressure is over the critical pressure of oxygen, the injection is transcritical. The momentum flux ratio value $J = 3.78$ indicates that the efficiency of mass transfer between dense oxygen and the surrounding stream is low.*

Four tests were carried out during the campaign under conditions corresponding to PF4. These runs are listed in table 3.12 and described in the following sections.

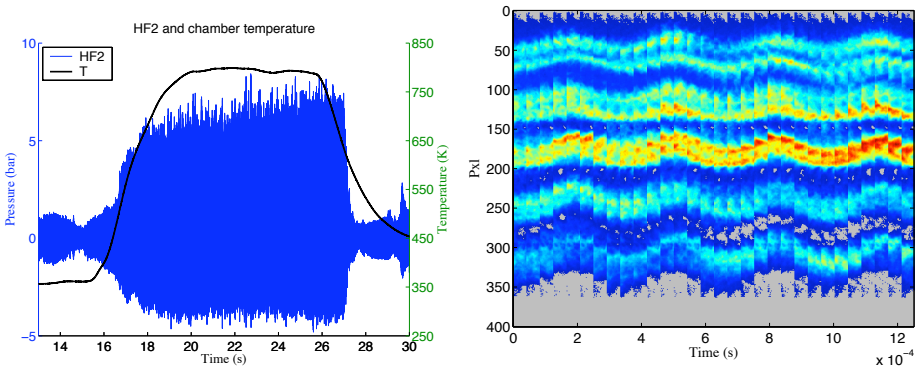

(a) (b)

Figure 3.71: *PF3 during CWM at SP4 (3125 Hz) - (a) HF2 response during the CWM test case plotted with the mean temperature of the chamber. Temperature rapidly reaches 800 K - (b) Streak films rebuilt with the SA1 images. The slice used to form the streak film is located near the injection plane. The flames oscillation is stronger in the lower part of the chamber a feature also observed for the PF2 operating point.*

Type	WM	LFM	CWM1	CWM2
frequency (Hz)	0	$1600 \rightarrow 3600$	$2350 - 3080$	3100

Table 3.12: *Types of excitation and corresponding frequencies investigated for operating point PF4.*

3.7.1 Operation without modulation (OWM)

The modulation free test carried out during this experimental series differs to some extent from the nominal operating point. Table 3.13 shows the main differences. The methane mass flow rate is lower than the selected value and liquid oxygen mass flow rate is higher. This induces a higher mixture ratio with a higher flame temperature. This in turn leads to an augmented chamber pressure which is established at 6.7 MPa instead of the 5.9 MPa value. It is nevertheless possible to consider that the general structure of the flow is similar to that obtained under nominal conditions.
In the high pressure range around 6 MPa, the volumetric rate of heat release is significantly higher than that corresponding to the lower pressure operating points (PF1-3). The levels of light emission from CH* and OH* are higher. In this test, and in most cases for high pressure experiments, the flame emission is too strong compared to the light radiated by the HMI spot. As a consequence, it is not easy to obtain useful backlighted results. On the other hand, the quality of images gathered with the SA1 camera (high speed CH* emission) is

Points	P_{ch}	E	J
PF4	5.9 MPa	1.13	3.8
PF4-OWM	6.7 MPa	1.3	2.1

Table 3.13: *Injection parameters for operating point PF4 and for the point reached during the modulation free test.*

particularly good. This can be seen by comparing the ICCD frame and a SA1 frame at the same instant as in Fig. 3.72.

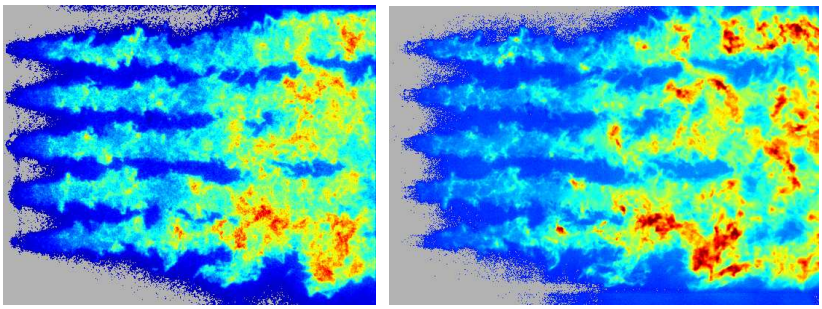

(a) (b)

Figure 3.72: *PF4 during OWM - ICCD (a) and SA1 (b) images taken at the same instant. The flame structure is very well captured by the SA1 camera despite the slight difference in the color scale. Images are consistent.*

The mean OH* emission, obtained by averaging instantaneous images over the entire test case, is shown in Fig. 3.73. This flame structure differs to some extent from those observed so far. It is possible to distinguish two expansion angles, the first is small and corresponds to the near field while the second characterizes the more rapid expansion taking place at a distance from the injection plane. This flame structure is typical of transcritical cryogenic flames as observed in series of studies carried out by Candel and co-workers (for details, see Herding et al. (1998) Juniper et al. (2000) Juniper and Candel (2003) Singla et al. (2005) Singla et al. (2006) Singla et al. (2007) Candel et al. (2006)).

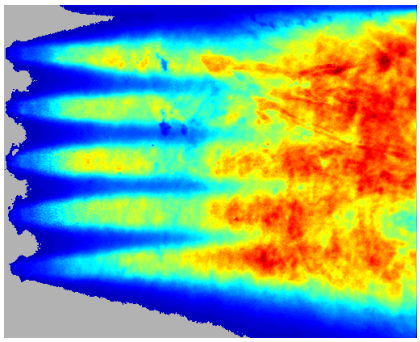

Figure 3.73: *PF4 during OWM - Averaged OH* emission of the flames recorded during the OWM test case.*

3.7.2 Linear frequency sweep (LFM)

The frequency is swept linearly from 1600 Hz to 3600 Hz. Injection parameters are close to those defined nominally, but the mean pressure in the chamber varies during the test case (Fig. 3.74) between 5 and 6 MPa. This range is determined by two factors. At the beginning of the test, the pressure is under the expected value although all the injection parameters are nominal. The difference may be caused by a leak between the wheel and the exit nozzles. Even when a tooth blocks a nozzle, there is a small gap between the nozzle and the wheel which results in a pressure loss (the equivalent diameter of the nozzle is bigger than the actual one). This gap is controlled by the wheel adjustment, but the fine tunning is difficult because of the size and weight of the VHAM. The impact of this setting is more important at high pressure because it is linked to the diameter of the exhaust nozzles. At 2.6 MPa, the diameter is 11.25 mm, and at 5.9 MPa it is only 7.1 mm. A small gap between the wheel and the nozzle has a larger effect when the nozzle diameter is reduced.
The fact that the pressure changes during the test case is probably a consequence of the excitation. This has already been observed in various other tests. Comparing Fig. 3.74 and Fig. 3.75, one finds that the evolution in mean pressure is more pronounced when the system response is stronger.
Fig. 3.75 shows standard characteristics already observed in the low pressure experiments. Three spectral peaks emerge, one at a relatively low frequency (SP1 at $f = 1600$ Hz), where the HF5 sensor responds much higher than the other sensors, one at 2350 Hz (SP2) corresponding to a significant reduction in flame length, and one at 3070 Hz (SP4) with an intense pressure response. Once again, the third spectral peak, corresponding to the 2L eigenmode, does not clearly appear in the linear frequency sweep. The three spectral peaks are briefly examined in what follows.

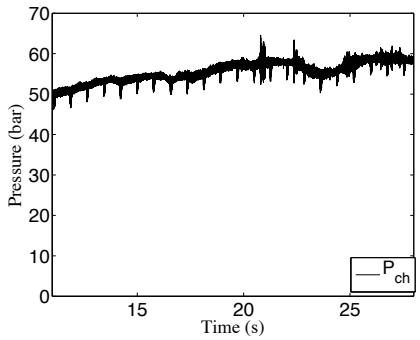

Figure 3.74: *PF4 during LFM - Evolution of the mean pressure in the chamber. The pressure increases from 5 MPa to 6 MPa between the beginning and the end of the test.*

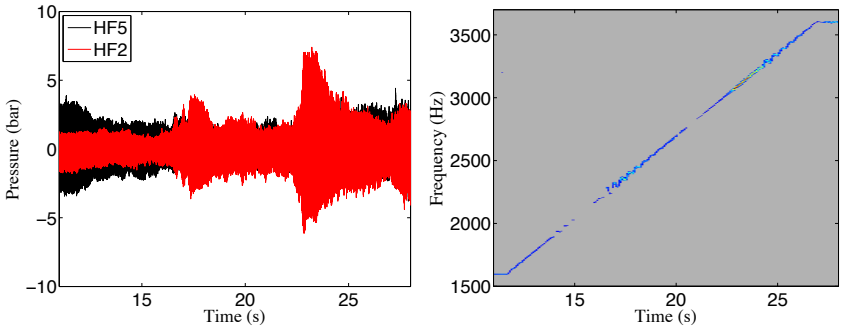

(a) (b)

Figure 3.75: *PF4 during LFM - (a) - Sensor response during the linear frequency sweep (b) - Temporal evolution of the HF2 power spectral density.*

First spectral peak (SP1) The first spectral peak corresponds to a transverse mode with an augmented acoustic level near the chamber exhaust section. This mode was described in the previous analyses. Fig. 3.76 (a) and (b) feature characteristics similar to those found so far. There are some imaging problems at these high pressures as illustrated in Fig. 3.76 (c). It is found that flame ignition is accompanied by production of soot which covers most of the viewing window except for three elongated spots (these spots show a higher level of emission and appear in red in this figure). Most of the light emission is obscured by the soot layer, affecting the light emission distribution. At the end of the test case, the upper part of the window has been cleaned up by the flames.

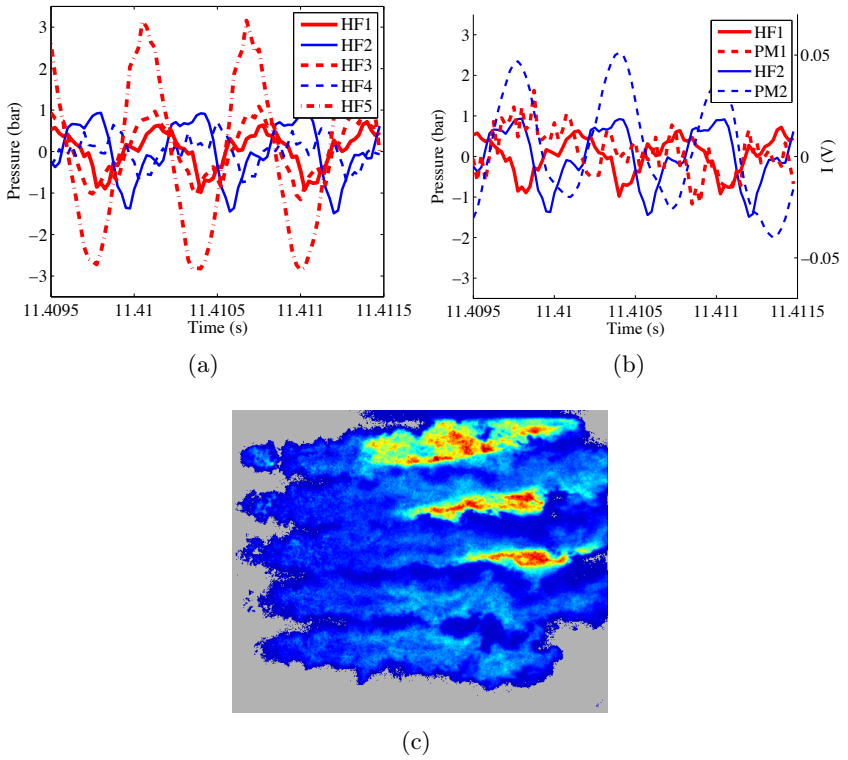

Figure 3.76: *PF4 during LFM at SP1 (1600 Hz) - (a) Response of the HF transducers - (b) Near injection pressure sensors HF1 and HF2 plotted with the PM signals - (c) Instantaneous OH* emission. Most of the visualization window is obscured by soot deposits, except for three spots that appear in red. Flame structure can still be recognized and it is close to other operating points results at SP1.*

Second spectral peak (SP2) The second spectral peak (SP2) appearing at 2350 Hz is related to a transverse mode as well. Images gathered by the ICCD camera show that the flames are asymmetric and short (Fig. 3.77 (c)). Pressure sensors signals indicate that some beating takes place between two frequencies as apparent from Fig. 3.78.

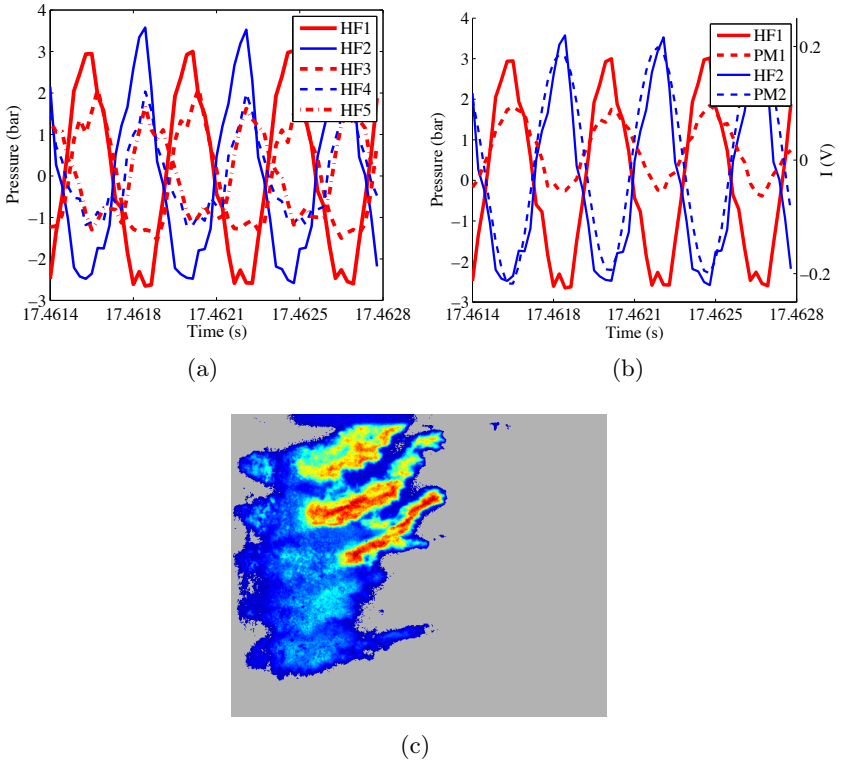

Figure 3.77: *PF4 during LFM at SP2 (2350 Hz) - (a) Response of the HF transducers - (b) Near injection pressure sensors HF1 and HF2 plotted with the PM signals - (c) Instantaneous OH* emission.*

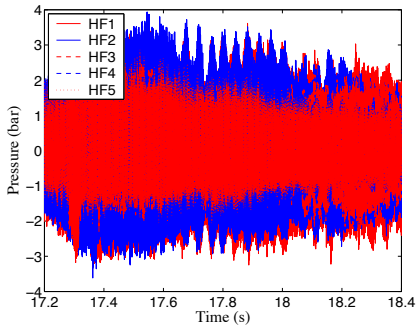

Figure 3.78: *PF4 during LFM at SP2 (2350 Hz) - Beating between two frequencies.*

Fourth spectral peak (SP4) Once again, the third spectral peak (SP3) referring to the 2L mode does not appear in this test.
The fourth spectral peak (SP4) arises in the linear frequency sweep test at 3070 Hz. Here again, signals and imaging (Fig. 3.79) clearly show that this resonance corresponds to the coupled transverse-longitudinal eigenmode already observed during the PF2 and PF3 tests at frequencies of the order of 3000 Hz (1T2L).

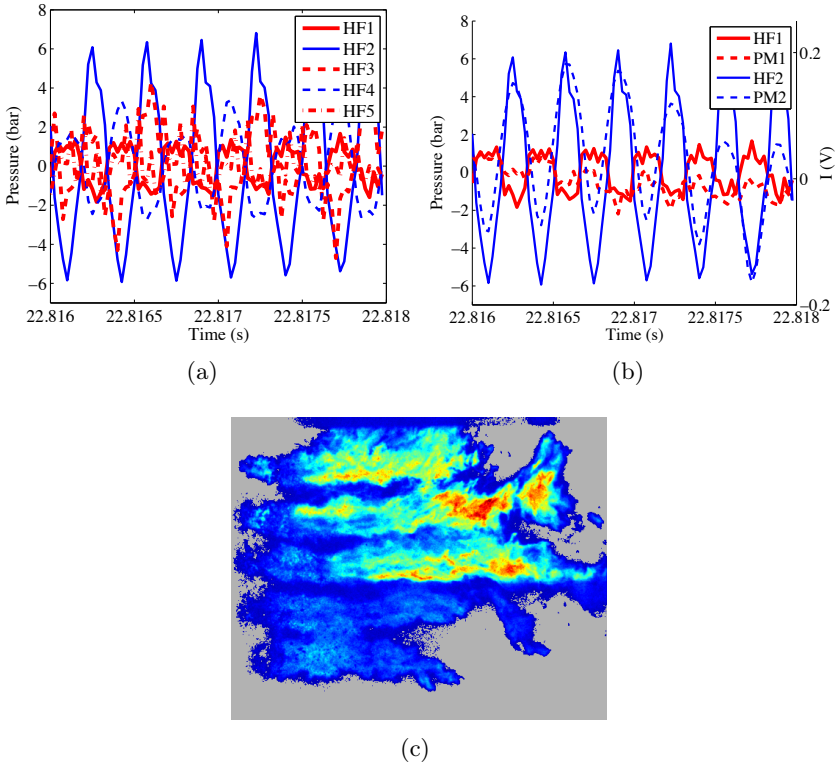

Figure 3.79: *PF4 during LFM at SP4 (3070 Hz) - (a) Response of the HF transducers - (b) Near injection pressure sensors HF1 and HF2 plotted with the PM signals - (c) Instantaneous OH* emission.*

The similarity with previous data is also confirmed by the temperature curve plotted in Fig. 3.80 (a). The system response is quite large, and the temperature measured at the lower combustor wall increases rapidly, indicating that a strong coupling is taking place between combustion and the transverse acoustic modulation.
Another feature of this operating point, is apparent in Fig. 3.80 (b) which shows a low frequency oscillation in the methane injection indicating that some coupling between the chamber and the feedline affects combustion.

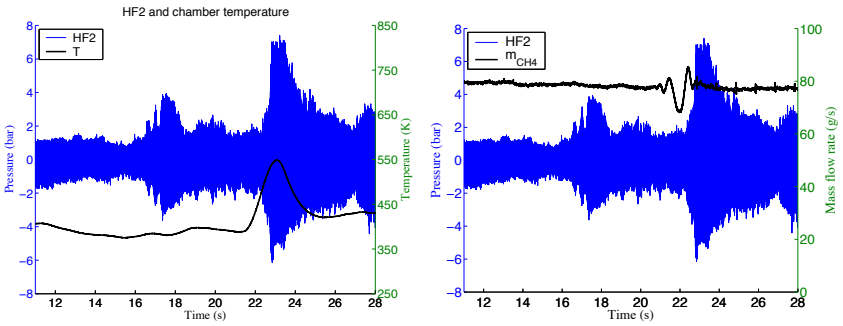

(a) (b)

Figure 3.80: *PF4 during LFM - HF2 response plotted with: (a) temperature at the bottom wall of the chamber - (b) methane injection mass flow rate.*

The test indicates that data obtained under transcritical oxygen injection are qualitatively similar to those obtained at subcritical pressures. Eigenfrequencies nearly match, the relative response is of the same order of magnitude, the flame pattern features similarities with what was found previously (asymmetry, short combustion region). Amplitudes of the pressure signals are close to those measured at 2.6 MPa, but the chamber pressure is more than twice as high. One could have expected that the amplitude would grow by the same amount as the chamber pressure. It turns out that the amplitude of the imposed acoustic field is controlled by the mass flow rate ejected by the nozzles. Since the mass flow rate is close to that used for the PF2 and PF3 operating points the response level remains in the range obtained during these lower pressure runs.

3.7.3 Continuous wave modulation (CWM1)

The continuous wave modulation tests are aimed at investigating the spectral peaks SP2 and SP4. A short ramp is used to reach the second eigenfrequency at 2350 Hz. This frequency is held during a period of 8 s. Another short ramp is then used to obtain a continous modulation at 3070 Hz. This process is illustrated in Fig. 3.81.
The first frequency provides interesting data. The amplitude of oscillation grows all along the test as shown in Fig. 3.82. Signals clearly refer to a transverse mode (Fig. 3.83). The flame pattern changes during the excitation. At the beginning, the symmetry is preserved but the flame geometry changes during the run and the flames are progressively bent upwards (Fig. 3.84). This is more obvious in an average image (Fig. 3.85). At this frequency the temperature measured at the lower wall only slightly increases (Fig. 3.86 (a)).
The flame expansion in the third dimension (in the horizontal plane) has not

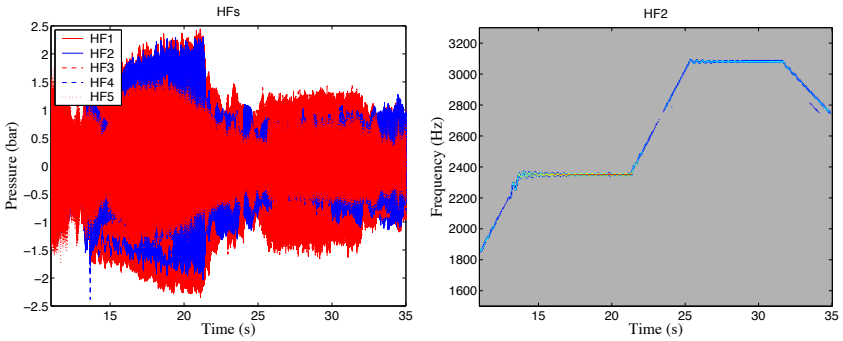

(a) (b)

Figure 3.81: *PF4 during CWM1 at SP2 (2350 Hz) and SP4 (3070 Hz) - (a) Response of the HF transducers - (b) Temporal evolution of the HF2 power spectral density. The second frequency does not respond to the excitation as expected.*

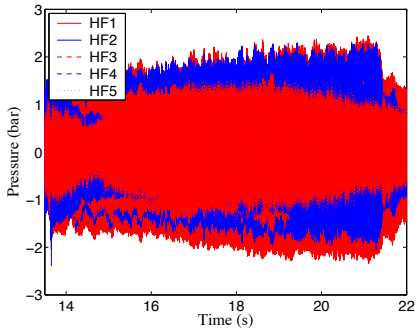

Figure 3.82: *PF4 during CWM1 at SP2 (2350 Hz) - Response of the HF transducers.*

been discussed up to now. This cannot be deduced from the present imaging methods which provide no depth information. Expansion in the transverse direction can certainly have an impact on the process. In the present test case, the flames appear to be flattened when they are submitted to the transverse acoustic field. This process which takes place in the direction perpendicular to the acoustic velocity is manifested by the fact that the flames seem to sweep the lateral quartz windows.

Observation of the second spectral peak using a continuous wave modulation at 3070 Hz does not exhibit the expected behavior. As shown in Fig 3.81, acoustic levels reached during the LFM are not obtained in the present test indicating that the eigenfrequency has drifted away from the value determined in the LFM. Since the frequency peak observed in the ramp was not that sharp, and the injection parameters are relatively close (see table 3.14), the explanation

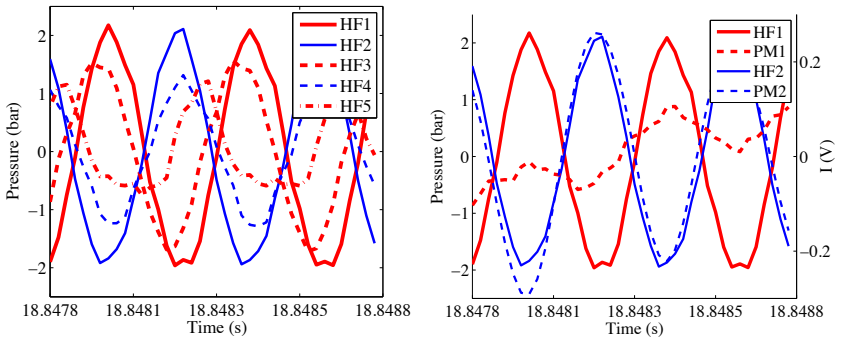

Figure 3.83: *PF4 during CWM1 at SP2 - (a) Response of the HF transducers - (b) Near injection pressure sensors HF1 and HF2 plotted with the PM signals.*

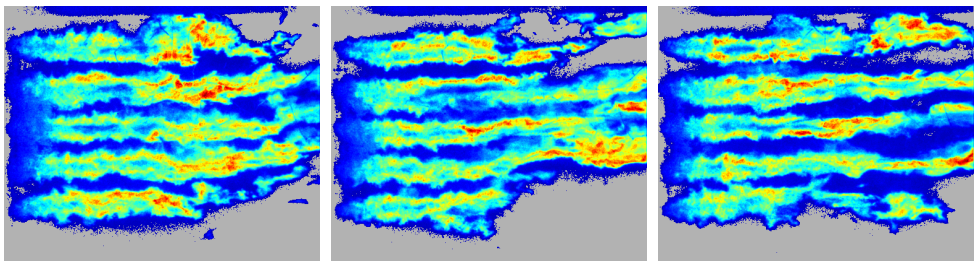

Figure 3.84: *PF4 during CWM1 at SP2 (2350 Hz) - Instantaneous OH* emission taken at three successive instants. Flames are progressively bent towards the top of the chamber.*

may not be straightforward. The main difference is that the mean pressure is not quite that of the LFM test, but this value does not have an important influence on the eigenfrequency. The mixture ratio is the same in the two experiments and the flame temperature should be equal. The problem may perhaps be related to the low-frequency coupling with the methane injection line, as shown in Fig. 3.86 (b). Another possible cause could be the wheel displacement relative to the nozzles during the test case.

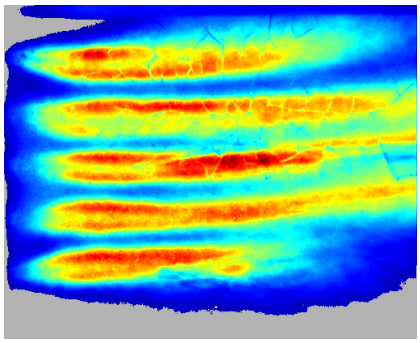

Figure 3.85: *PF4 during CWM1 at SP2 (2350 Hz) - Average OH* emission.*

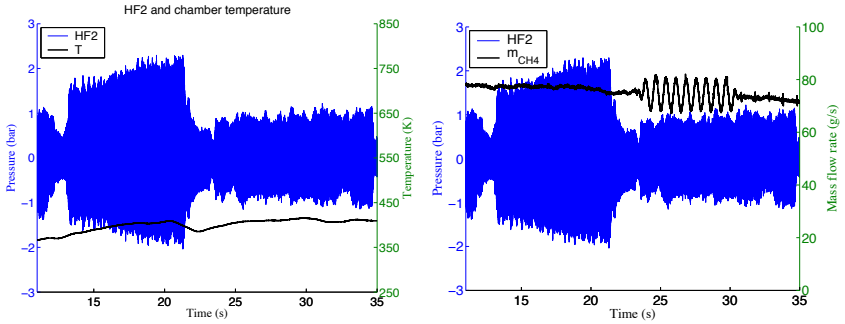

(a) (b)

Figure 3.86: *PF4 during CWM1 - HF2 response plotted with: (a) temperature measured at the lower chamber wall. Temperature is nearly constant during this test case - (b) methane injection mass flow rate. The oscillation indicates some coupling with the feedline.*

Points	P_{ch}	E	J
PF4-LFM	5.5 MPa	1.3	3.4
PF4-CWM1	6.3 MPa	1.3	2.8

Table 3.14: *Injection parameters for the PF4 operating point and for the point reached during the continuous wave modulation test case CWM1.*

3.7.4 Continuous wave modulation (CWM2)

The continuous wave modulation test at the second spectral peak CWM2 does not completely fulfill our expectations either. The pressure signals feature a large amplitude (Fig. 3.87) but the short time spectral analysis in Fig. 3.87(b) indicates that the eigenfrequency has been missed by only a few Hz and that there are two peaks in the two side bands of the selected frequency for the CWM modulation. Nevertheless, the amplitude reached on the top of the chamber, recorded by HF1 sensor, is significant.

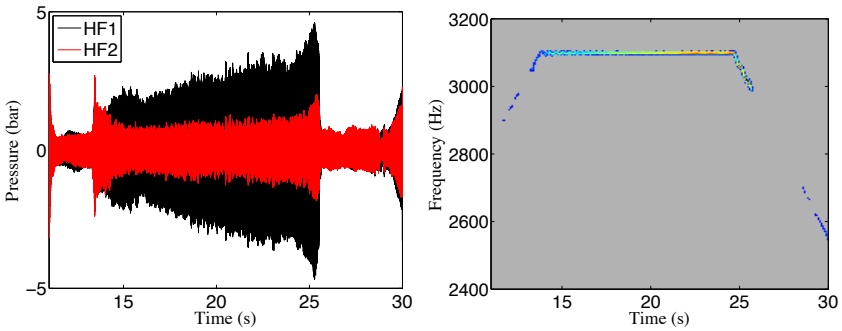

(a) (b)

Figure 3.87: *PF4 during CWM2 - (a) Response of the HF transducers - (b) Temporal evolution of the HF1 power spectral density. The spectral peaks are marked in this figure.*

The methane injection mass flow rate also features an important low-frequency oscillation (Fig. 3.88 (a)). The characteristic time of these oscillations is long compared to that of the acoustic excitation, so it is difficult to interpret this phenomenon. It appears however that the presence of the low frequency beating influences the system dynamics.
The ICCD images are not easy to interpret at this operating point. As mentioned previously, ignition at the beginning of the test creates a large amount of soot which forms a thin layer obscuring the lateral windows. Soot is progressively burnt away during the test. In Fig. 3.89 (d), which shows an average image obtained from the ICCD images, the bottom part is less luminous but this is due to the obscuration associated with the soot deposit. One also observes lines due to the fact that the quartz windows are cracked. This has been caused by the large amplitudes obtained during the first LFM test case.
Despite these various problems, valuable information is obtained by focusing on the peak located just after the continuous wave excitation. In Fig. 3.89 (a), one sees that the amplitude recorded by HF1 is more important than that recorded by the other sensors. Looking at the corresponding ICCD image (Fig. 3.89 (c)),

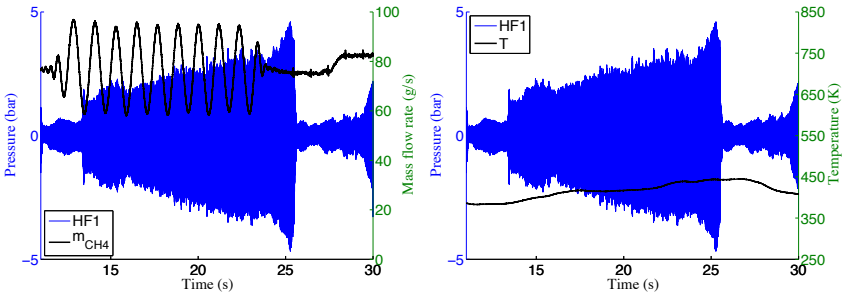

(a) (b)

Figure 3.88: *PF4 during CWM2 at SP4 (3070 Hz) - HF1 response plotted with: (a) the methane injection mass flow rate. The oscillation indicate some coupling with the feedline - (b) temperature measured at the lower chamber wall. Temperature increase is weak.*

one finds that the upper flame is shorter than the others. The velocity antinode is now located near the upper injector in the top part of the chamber. This indicates that the oscillation breaks the symmetry of the acoustic field and of the flame pattern as already observed under subcritical conditions.
Fig. 3.88 (b) gives an additional information. The temperature increase recorded by the thermocouple in the bottom of the chamber presents a weak evolution of temperature. The inversion of symmetry of the acoustic field and flames compared to previous 1T2L test cases suggests that the cause of the temperature increase is the flame distribution itself. As a result, if a thermocouple were located on the top of the chamber, it is likely that it would have recorded a strong temperature increase in this situation.

3.8 Operating point PF5

The last operating point PF5 was not easy to reach due to technical problems. It was difficult to set the wheel close enough to the nozzle exhaust for most of the tests and the chamber pressure was too low and significantly under that corresponding to the critical value of oxygen. In the end, only one hot fire test case was completely satisfactory. This test case fulfills almost all the expected conditions and can be used to obtain the three operating conditions OWM, LFM, and CWM. The main parameters of this operating point are gathered in table 3.15. The frequency range of the test case is given in table 3.16.
The main difference between PF5 and PF4 is the momentum flux ratio. Here, the methane stream is injected at a higher velocity than in the PF4 conditions. This yields a higher momentum flux ratio J and a better mass transfer from the dense oxygen core to the lighter surroundings.

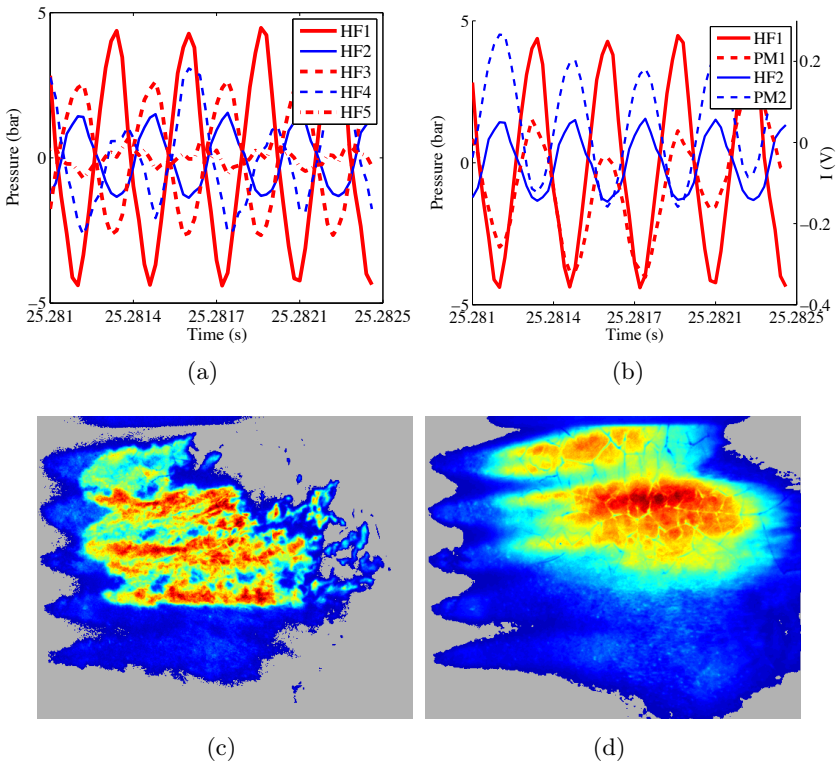

Figure 3.89: *PF4 during CWM2 at SP4 (3070 Hz) - (a) Response of the HF transducers - (b) Near injection pressure sensors HF1 and HF2 plotted with the PM signals - (c) Instantaneous OH* emission - (d) Average OH* emission.*

Since a single test case is used in the following analysis, it is worth describing its main features in detail. The test is carried out in the linear frequency sweep mode (LFM). The wheel operates from 1200 Hz to 3300 Hz. Fig. 3.90 displays the temporal evolution of the five pressure sensors and the short time spectral analysis of the HF2 sensor.

The temporal evolution has the same general characteristics as those found for the other operating points. Three peaks emerge from the background noise, the first features a large amplitude at the HF5 sensor, the last corresponds to an important amplitude level. The eigenfrequencies are f=1900 Hz, f=2375 Hz and f=3200 Hz. The LFM test is terminated by an operation at constant frequency at the final value of 3300 Hz which is close to the third spectral peak. This last part of the test can be used as an approximate continuous wave modulation test at a frequency $f = 3300$ Hz which is slightly higher than the modal eigenfrequency of 3200 Hz, as can be seen in Fig. 3.90.

Points	P_{ch}	E	J
PF5	5.5 MPa	1.13	11.3

Table 3.15: *Injection parameters for operating point PF5. Pressure is over the critical pressure of oxygen, the injection is transcritical. The momentum flux ratio value $J = 11.3$ indicates that the mass transfer between dense oxygen and methane is efficient, leading to naturally shorter flames.*

Type	LFM
frequency (Hz)	$1200 \rightarrow 3300$

Table 3.16: *Range of frequencies investigated in the test case carried out successfully for operating point PF5.*

3.8.1 Operation under weak modulation (OWM)

As indicated in some of our previous analysis, the beginning of the LFM test can be used to replace a modulation free (OWM) test. Instantaneous and average ICCD images, shown in Fig. 3.91, illustrate the influence of the momentum flux ratio J. Mass transfer is more efficient in this case and this produces shorter flames, even when the acoustic modulation is weak.

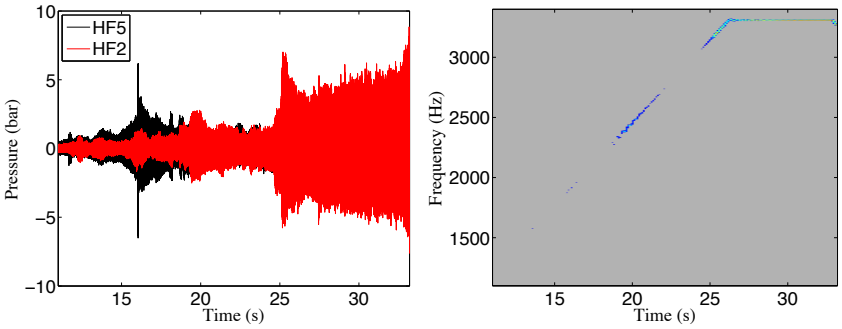

(a) (b)

Figure 3.90: *PF5 during LFM - (a) Sensor response - (b) Temporal evolution of the HF2 power spectral density.*

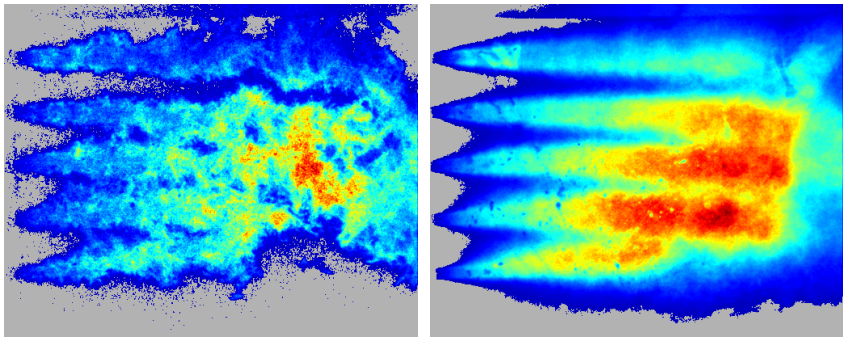

(a) (b)

Figure 3.91: *PF5 during OWM - (a) Instantaneous OH* emission - (b) Average OH* emission image.*

3.8.2 Linear frequency modulation (LFM)

The three peaks are described in what follows. They correspond to SP1, SP2 and SP4.

First spectral peak (SP1) At the first spectral frequency peak the level of the HF5 sensor response is quite strong (Fig. 3.92 (a)and (b)). The flames are shortened and the expansion rate is augmented (Fig. 3.92 (c)).

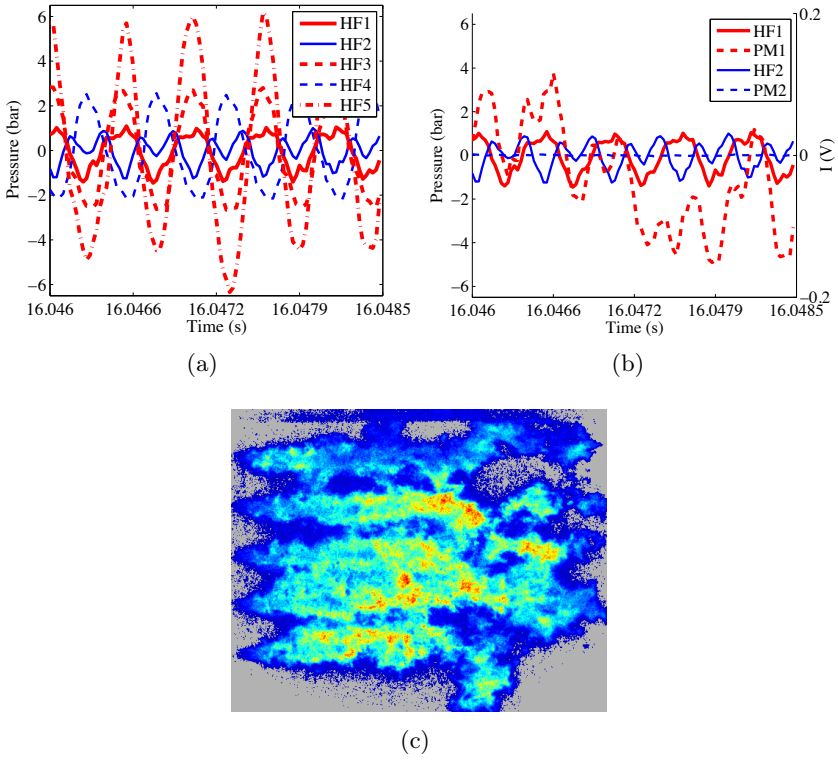

Figure 3.92: *PF5 during LFM at SP1 (1900 Hz) - (a) Response of the HF transducers - (b) Near injection pressure sensors HF1 and HF2 plotted with the PM signals - (c) Instantaneous OH* emission of the flames.*

Second spectral peak (SP2) At the second spectral peak, the flames become quite short and the combustion region is compact and close to the injection plane.

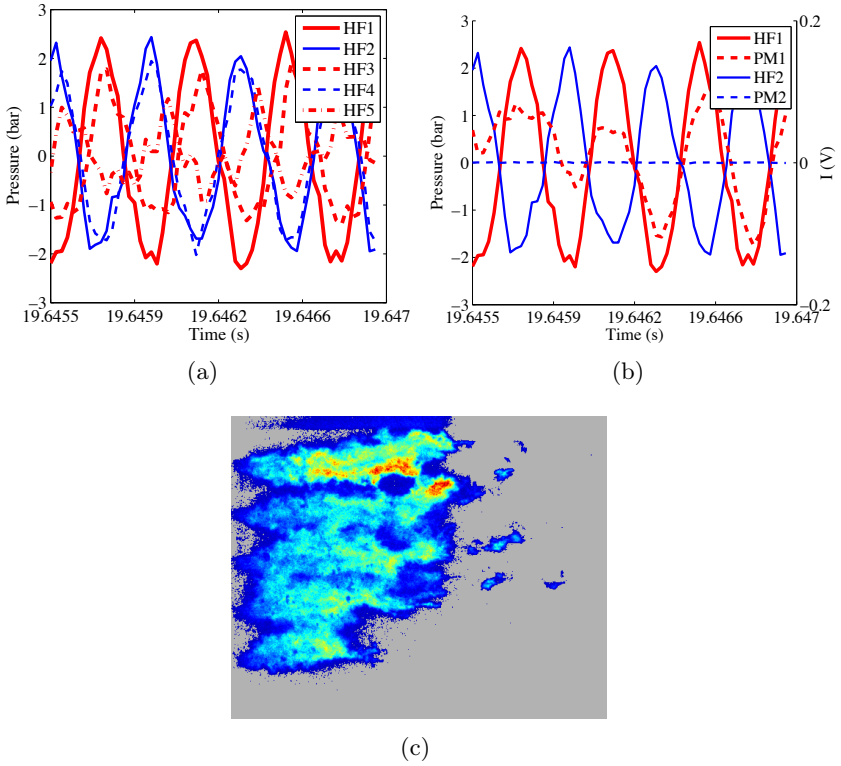

Figure 3.93: *PF5 during LFM at SP2 (2375 Hz) - (a) Response of the HF transducers - (b) Near injection pressure sensors HF1 and HF2 plotted with the PM signals - (c) Instantaneous OH* emission of the flames recorded just after during the second spectral peak.*

Fourth spectral peak (SP4) When the system is modulated at SP4, the flames become very short and the symmetry is destroyed, as observed for previous operating points.

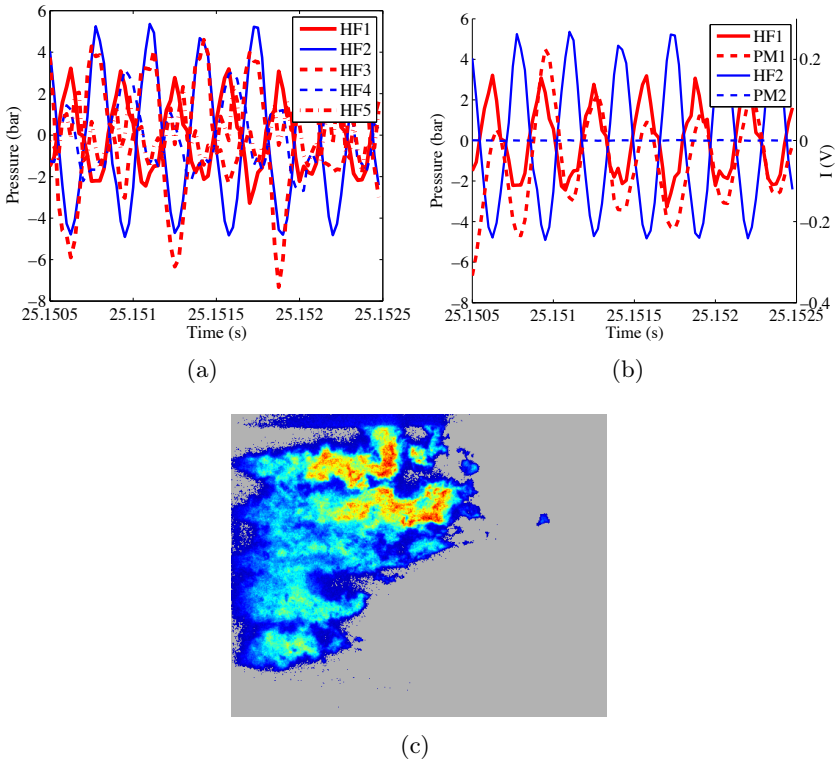

Figure 3.94: *PF5 during LFM at SP4 (3165 Hz) - (a) Response of the HF transducers - (b) Near injection pressure sensors HF1 and HF2 plotted with the PM signals - (c) Instantaneous OH* emission.*

3.8.3 Continuous wave modulation (CWM)

The continuous wave modulation, carried out at a frequency close to SP4 (3300 Hz), presents features which are similar to those observed at previous operating points: a large oscillating pressure amplitude, compact flame pattern and evolution of this shape (Fig. 3.96), asymmetry of the combustion pattern and increase of the chamber wall temperature (Fig. 3.95).

3.9 Discussion

It is pointed out, notably by Mitchell (1995), that little progress was made in modeling the response of combustion processes to oscillations in liquid rocket engines since the 1970s. A difficulty was the lack of experiments necessary to develop models that would accurately represent the major combustion processes (injection, mixing, atomization, vaporization, chemical kinetics) and their re-

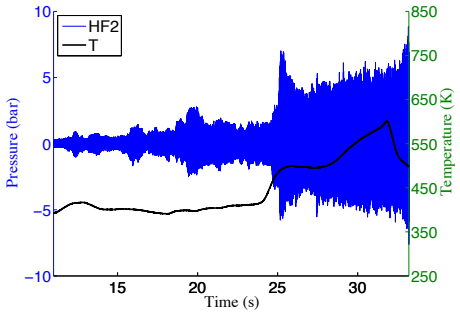

Figure 3.95: *PF5 during LFM at SP4 (3300 Hz) - HF2 response during the CWM test case plotted with the mean temperature of the chamber.*

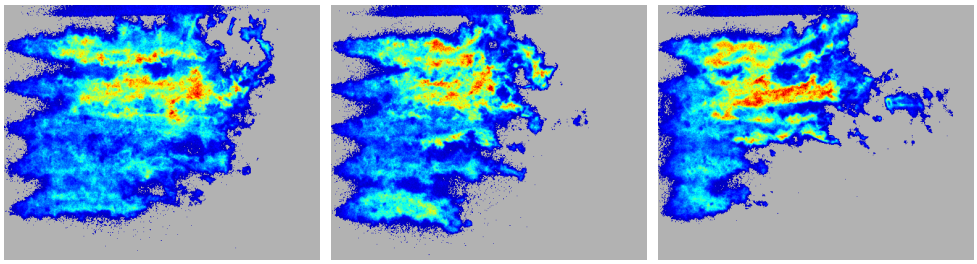

(a) (b) (c)

Figure 3.96: *PF5 during LFM at SP4 (3300 Hz) - Successive images of instantaneous OH* emission during the CWM test case. Flames are asymmetric and they get shorter as the amplitude of oscillation increases.*

sponses to strong acoustic oscillations. Experiments reported in the previous sections have demonstrated some common features which give an experimental basis to derive the physical mechanisms involved in the particular case of the MIC equipped with the VHAM. These results may also be extrapolated to real scale rocket engines. In this last section, we highlight some of the common elements of most operating points and, specifically, we consider the SP4 spectral peak. Major observations are listed below:

- The mode corresponds to a coupled transverse and longitudinal motion (1T2L).
- Flames oscillate in the transverse direction.
- The pressure signal level reaches extremely high amplitudes.
- Combustion takes place in a compact region located near the injection plane.

- The pressure amplitude increases during this continuous wave modulation.
- The flame length decreases during the test.
- The temperature at the lower chamber wall rises.
- The flame pattern becomes asymmetric.
- The acoustic field also becomes asymmetric.
- Flames are curved.

Mechanisms suggested in what follows are put forward to explain these characteristics. It is particularly interesting that, except for PF1, every operating point, regardless of mean pressure or momentum flux ratio, features the same qualitative behavior at SP4. Even the nature of injection, liquid or transcritical, does not seem to have a decisive impact on these mechanisms.

3.9.1 Origin of the heat release fluctuations

Streak films synthesized from images acquired by the high speed camera guide the description of the unsteady heat release related to the acoustic field. This was used as the starting point of much of the analytical work, based on the sensitive time lag model. One important question in this kind of modeling is to see whether the unsteady heat release rate is linked to the pressure or velocity fields. This question is not easy to settle because acoustic velocity and pressure are linked by the linearized momentum balance $\rho_0 \frac{\partial v}{\partial t} = -\nabla p$. One objective of the present investigation is to consider the possible coupling processes and identify the most probable mechanisms. It is therefore worth listing some of the various possibilities:

- Unsteady pressure modifies the heating and vaporization of droplets, changing the mass rate of oxidizer generated per unit volume and the rate of heat release.
- Velocity induced by the acoustic motion enhances the liquid jet breakdown, primary and secondary atomization associated with inertial stresses augmenting the rate of vaporization of oxidizer and subsequently the rate of heat release.
- Pressure perturbations in the chamber induce mass flow rate fluctuations at the injector exhausts giving rise to fluctuating rates of heat release.

It is first interesting to note that experiments carried out by Tischler and Male with a single injection unit give qualitatively similar results, and it is reasonable

to say that the physical processes driving the two experiments are of the same type.
Visualization of the whole chamber and high speed imaging of the light emission carried out in the present study provides strong evidence that the unsteady heat release rate must be caused by the large oscillations of the flames in the chamber, which are directly linked to the acoustic velocity field.

3.9.2 Flame shortening, temperature and pressure increase

Flame shortening, temperature and pressure increases are typically found under high frequency oscillation as observed in numerous tests during engine developments. Experiments presented in the present document feature these phenomena and provide a new perspective to understand instabilities. Flame shortening is illustrated in Fig. 3.97, for operating point PF2. Flames are shorter due to acoustic modulation and their shape is modified. However, Fig. 3.97 (b) shows a change in the nature of the combustion process which does not imply an important change in the flame length.
It is likely that secondary atomization is modified by the intense acoustic field. Secondary atomization is controlled by the Weber number (We= $\rho v^2 l/\sigma$). For a particular droplet, when We is over a critical value (of the order of 20), the droplet splits. This changes the spray characteristics, increasing the rate of vaporization and the reaction rate. To describe accurately the spray, one has to consider the acoustic velocity in the calculation of the Weber number.
For flames shown in Fig. 3.97 - (c) and (d), it seems the modification of secondary atomization is not sufficient to explain the shortening of the reaction zone. Primary atomization is modified as well, quite significantly. This is illustrated in Fig. 3.98: when the acoustic field is intense near the injection plane (c), the core length is shorter, which in turn gives rise to shorter flames. The momentum flux ratio J, that drives primary atomization, has to be calculated taking into account the acoustic velocity.
It has been shown that the transverse acoustic motion changes the atomization process. It is however not easy to link the intensity of the acoustic wave to the flame length and this aspect needs further investigation.
Enhancement of the atomization process leads to the confinement of the flames in the vicinity of the injectors. When the oscillation grows, flames get shorter, as illustrated in Fig. 3.99 and the combustion region becomes more compact. As most of the heat release takes place near the injection plane, the heat flux is intensified and this can eventually lead to a melting of injectors. This process is accompanied by an increase of the wall temperature as observed in Fig. 3.100.

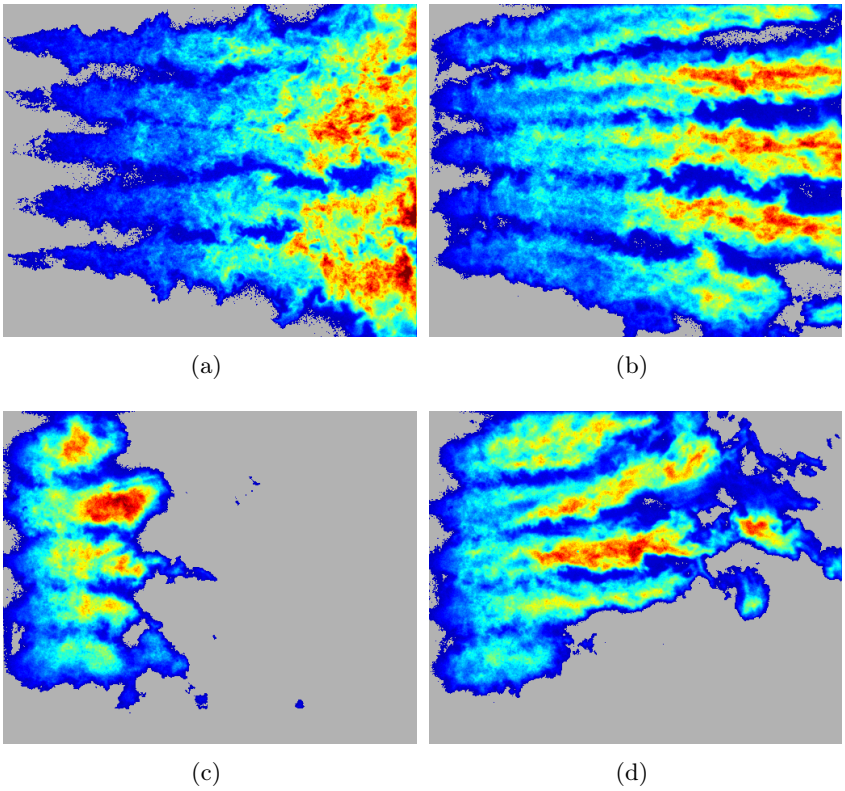

Figure 3.97: *Instantaneous OH* emission at PF2 - (a) OWM - (b) SP1 - (c) SP2 - (d) SP4.*

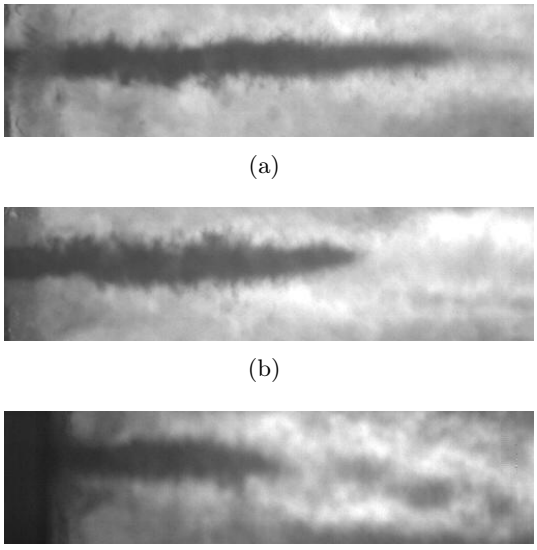

(a) (b) (c)

Figure 3.98: *Instantaneous backlighting images of the dense jet - (a) SP1 - (b) SP2 - (c) SP4.*

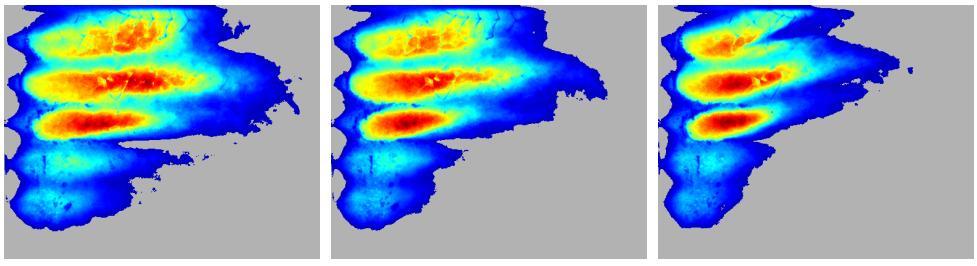

(a) (b) (c)

Figure 3.99: *PF3 during CWM at SP4 (3125 Hz) - Evolution of the averaged OH* emission during the CWM test case. Flames are getting shorter when the amplitude of oscillation increases.*

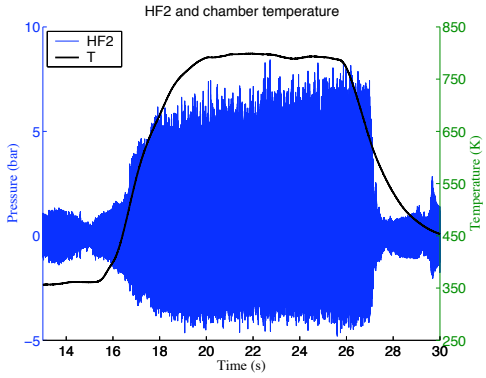

Figure 3.100: *PF3 during CWM at SP4 (3125 Hz) - HF2 response during the CWM test case plotted with the mean temperature of the chamber. Temperature rapidly reaches 800 K.*

3.9.3 Asymmetry of the combustion pattern and of the acoustic field

It has been established in the previous subsection that the flame length is linked to the acoustic field which accelerates the atomization process. In several tests, and specifically for those which feature the strongest response, an asymmetry in the flame distribution is observed coupled with an asymmetry in the acoustic field.

The link between the flame pattern asymmetry and the difference between the pressure amplitudes detected at the top and at the bottom of the chamber is demonstrated by considering operating point PF2 at the spectral peak SP4 (3200 Hz). One finds that the asymmetry in the flame pattern is reflected in the asymmetry of the acoustic field. This is underlined by an interesting “flip" phenomenon observed during a continuous wave modulation test at 3200 Hz. For most of this test the flames point upwards, except for a period of 0.5 s where the flame pattern is inverted and the flames point downwards (Fig. 3.101). This inversion is probably caused by a flow perturbation. The net result is a change in the amplitudes recorded by the transducers located on both sides of the chamber (Fig. 3.101 (c)). This leaves no doubt on the link between the two observations. When the flames are oriented upwards, the amplitude recorded by HF2 is larger than that detected by HF1, while the opposite is true when the flames point downwards.

The velocity antinode, where the modulation is maximum, is moved to the bottom of the visualization window, probably close to the last injector. This is where the flame motion is greatest, as it is illustrated by the streak films corresponding to these conditions (Fig. 3.102). The short length of this flame appears to be the consequence of an improved atomization due to the huge acoustic velocity in this area. The order of magnitude of this acoustic velocity can be estimated from $v'_{max} \simeq p'_{max}/\rho_0 c$, with p'_{max} detected by the pressure sensors, or from the displacement of the flame in the streak film divided by the angular frequency of excitation, if we assume that the flame follows the acoustic field. The first method gives an acoustic velocity v'_{max} around 100 m.s^{-1}. The second method gives a flame velocity of 50 m.s^{-1}, which tends to demonstrate that the flame follows the acoustic field with a certain inertia due to the liquid core.

Flames located in the upper part of the chamber are then closer to the velocity node and the external modulation is lower. The atomization process is modified to a lesser extent and the flames are longer. Since, of course, the geometry remains the same during the experiment, the asymmetry in the acoustic mode reveals an inhomogeneity in the chamber which is probably due to the temperature field. The pressure field is modified in turn explaining the differences in response between the upper and lower pressure sensors.

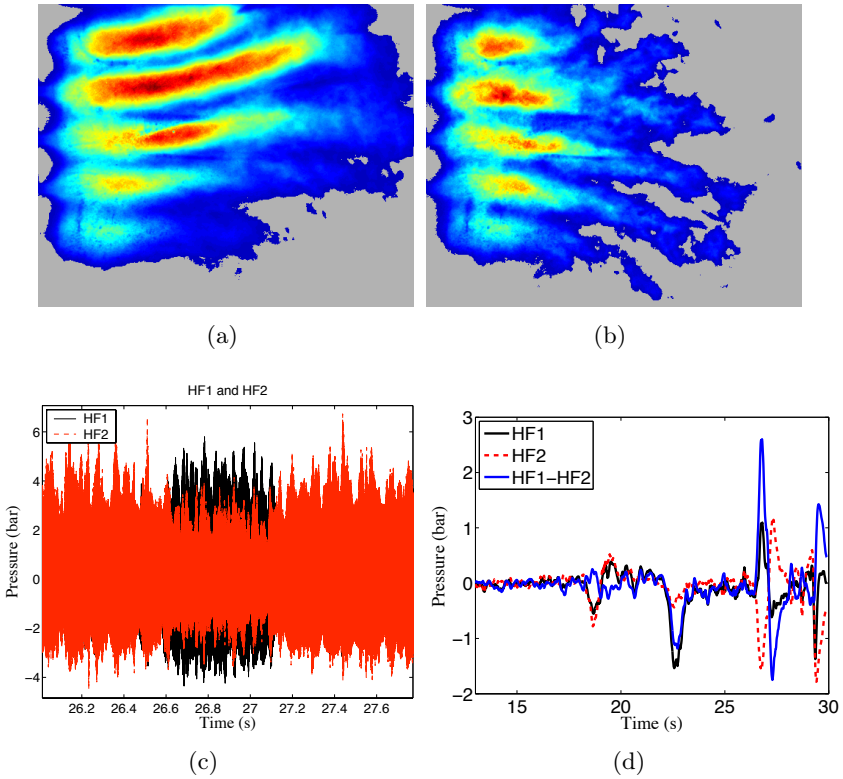

Figure 3.101: *PF2 during CW at SP4 (3200 Hz) - (a) Average OH* emission during the monofrequency excitation except between 26.6 s and 27.1 s - (b) Averaged OH* emission between 26.6 s and 27.1 s - (c) Close-up view of the HF1 and HF2 signals during the constant frequency excitation. Between 26.6 s and 27.1 s, the HF2 response decreases and the HF1 response increases - (d) Signals HF1, HF2 and the difference HF1-HF2 are averaged every 1/10 s and plotted during the entire test case.*

Another phenomenon, which has not been discussed yet, is the curved shape of the flames observed, for example in Fig. 3.101 (a) and (b). It seems that an auxiliary force changes the flames' shape, pushing them towards the top or the bottom of the chamber. In linear acoustics, the resultant force is necessarily equal to zero. Regarding the acoustic level reached in the present experiments, it is natural to consider non-linear phenomena which could induce the curvature of the flames. According to Baillot et al. (2009), in an investigation of the influence of acoustics on liquid jets, acoustic streaming (i.e. non-zero mean flow) and radiation pressure (i.e. non-zero mean pressure) are foreseeable. Fig. 3.101 (d) provides experimental material to determine which phenomenon is likely to be the cause of the observed curvature. In this graph, pressure at the top and at the bottom are averaged on 1/10 s and plotted throughout the test case. Pres-

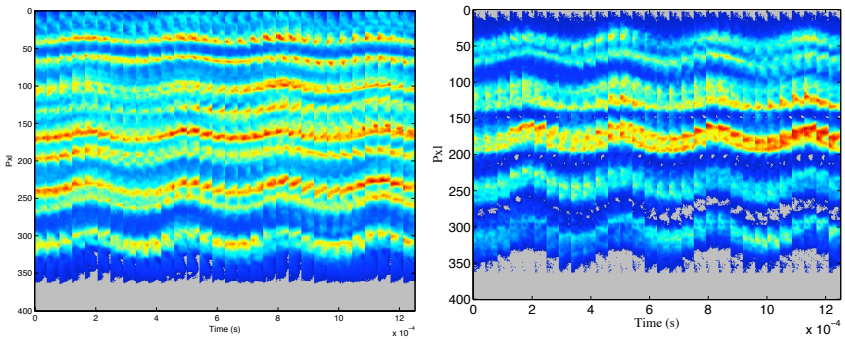

(a) (b)

Figure 3.102: *Streak films deduced from the SA1 images - (a) PF2 during CW3 at SP4 (3200 Hz) - (b) PF3 during CW at SP4 (3125 Hz). The shape of the acoustic field can be inferred from the relative motions of the flames. The flame located in the bottom, that oscillates with the most important amplitude, is close to the velocity antinode.*

sure transducers are set in dynamic mode, which means that eventually, they tend naturally to have a null average. The interesting part of this graph is that, during transient regimes, when symmetry is broken, the difference between HF1 and HF2 becomes important. At t=22 s, for instance, when the 1T2L mode is being excited and flames curve toward the top of the chamber, the resultant mean pressure in the top of the chamber is weaker than in the bottom. When flames curve in the opposite direction (t=26.6 s), mean pressure in the bottom becomes less important. These elements show that radiation pressure may be responsible for flame curvature in the experiments. The expression of the radiation pressure force on a droplet of size D_G is:

$$\frac{4F_{rad}}{\rho_g c^2 D_G^2} = -\pi \left(\frac{P_{ac}}{\rho_g c^2}\right)^2 \sin\left[\left(\frac{4\pi}{L_c}\right)\left(y - \frac{L_c}{4}\right)\right] f(\kappa), \tag{3.1}$$

with L_c the height of the chamber, ρ_g the gas density, c the sound speed and $f(\kappa) = kR$, with k the acoustic wave number and R the radius of the sphere. This expression illustrates an interesting piece of information on the radiation force: it is null at the pressure nodes and antinodes, maximum in the middle of these two planes, and directed from the pressure antinodes to the pressure nodes. It has been demonstrated above that when pressure oscillations in the bottom of the chamber are more important than pressure oscillations in the top (the pressure node moves nearer to the top wall), flames curve upward, i.e. they are submitted to a force directed to the pressure node. Thus, these two interpretations are consistent.

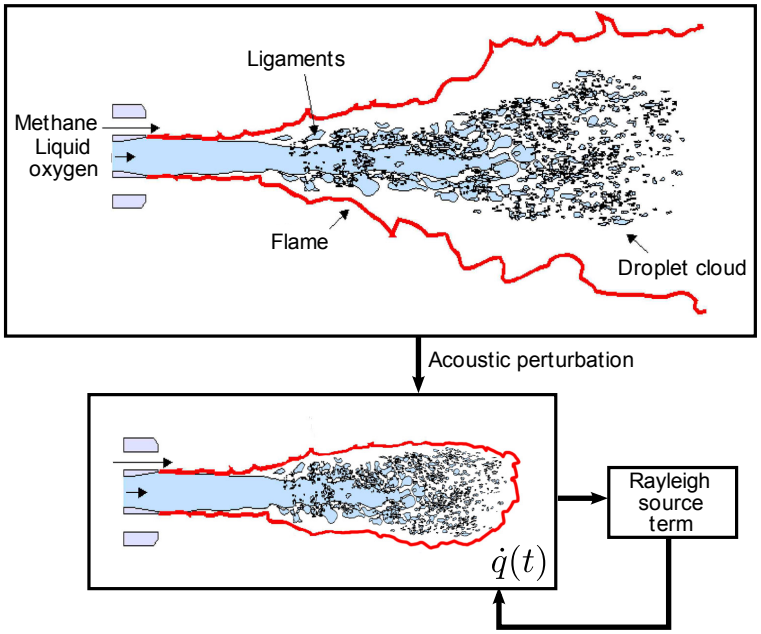

Figure 3.103: *Mechanism*

Asymmetry of the acoustic field, asymmetry of the flame pattern, flame curvature and flame length reduction are then different aspects of the same mechanism, which will be addressed in section 4.7.

3.9.4 Conclusion

This discussion indicates that the acoustic field can strongly influence the liquid jet atomization process. The large acoustic velocity increases shear stress acting on the liquid jets and droplets accelerating the break-up process and the division of large droplets by secondary atomization. This in turn reduces the flame length augmenting the rate of heat release per unit volume and the temperature at the chamber walls and injection plane. The smaller droplets produced in this way closely follow the acoustic field and their vaporization and subsequent heat release is phased with the pressure, a situation which leads to the growth of the oscillation. The growth is then enhanced by the asymmetry of the flame pattern. This mechanism, represented in Fig. 3.103, is more thoroughly investigated in the following chapter. Two models are suggested to represent these phenomena.

Part II

Low Order Modeling

Chapter 4

Heat release low order modeling

In this chapter, an effort is made to obtain a theoretical model which represents previously depicted observations. First, the Flame Acoustic Motion Equations (FAME) are described. In this model, the flame is considered as an infinitely thin element which follows the acoustic velocity field in a Lagrangian fashion. This assumption, a translation of experimental observations, gives an explicit expression for the unsteady heat release term. The pressure effect on the flame reaction rate is then added to the formulation. It is demonstrated that, near the walls, it is of the same order of magnitude as the velocity effect in the center of the domain. The Spray Dynamics Model (SDM) is introduced to take into account the liquid phase, neglected in FAME, which plays a central role in the mechanism deduced from experiments. Balance equations for the liquid phase lead to a new set of relationships. A delay, related to the droplets inertia, is naturally introduced. The stability margin is determined by the comparison between a global acoustic Weber number, related to the level of acoustic velocity, and a critical Weber number, which represent the velocity necessary for a droplet to break up. The two approaches (FAME and SDM) are compared and their range of validity outlined. A short analysis of the flame asymmetry observed during experiments is carried out at the end of this chapter.

4.1 Introduction

Experiments presented in the previous chapters have brought forth new elements which can be used to address the central problem of defining the driving sources of transverse combustion instabilities. Models presented in the following sections assist in the theoretical understanding of the fundamental mechanisms which intervene in this process. With this in mind, it is necessary to outline the main experimental observations and the impact of these findings on the

different possibilities. This is not an easy task because of the complex nature of the experiment itself. In the MIC experiments, the chamber geometry and the number of injectors differ from those of real liquid rocket engines (LRE). In these tests, oscillations are induced by a modulator (VHAM) while self-sustained instabilities occur naturally in the absence of such a device. Forced oscillations obtained with the VHAM may not be representative of free oscillations defining self-sustained instabilities. Another issue is that the five injectors in the multiple injector combustor (MIC) are located near the chamber central plane, i.e. near the velocity antinode but far from the pressure antinodes of the chamber transverse modes. This is also at variance with the situation found in a typical LRE where injectors cover the thrust chamber backplane and operate in the pressure and velocity antinodes of the chamber transverse modes. These aspects will have to be considered in the study.
However, the strong coupling described in the previous chapter indicates that some essential features of transverse instabilities have been observed. The theoretical work developed in what follows is intended to model these features.

The central problem is to obtain a suitable representation of the unsteady heat release rate $\dot{q}'$. It is here useful to consider the balance of acoustic energy. For simplicity we only consider a situation where the flow velocity is small and can be neglected. The instantaneous acoustic energy balance takes the form (see for example Poinsot and Veynante (2001)).

$$\frac{\partial \mathcal{E}}{\partial t} + \nabla \cdot \mathcal{F} = \mathcal{S} - \mathcal{D} \text{ with } \mathcal{E} = \frac{1}{2}\overline{\rho}\boldsymbol{u}'^2 + \frac{1}{2}\frac{p'^2}{\overline{\rho}c^2} \text{ , } \mathcal{F} = p'\mathbf{u}\text{'} \text{ and } \mathcal{S} = \frac{\gamma - 1}{\gamma \overline{p}} p'\dot{q}' \quad (4.1)$$

In this expression $\mathcal{E}$, $\mathcal{F}$, $\mathcal{S}$ and $\mathcal{D}$ represent the acoustic energy density, the acoustic energy flux, the acoustic energy source and damping respectively. The instantaneous balance equation may be integrated over a period of oscillation T yielding:

$$\begin{aligned} \frac{\partial E}{\partial t} + \nabla \cdot F = S - D \text{ with } E = \frac{1}{2}[\frac{1}{2}\overline{\rho}\boldsymbol{u}' \cdot \boldsymbol{u}'* + \frac{1}{2}\frac{p'p'*}{\overline{\rho}c^2}], \\ F = \frac{1}{2}Re[p'\boldsymbol{u}'*] \text{ and } S = \frac{1}{2}\frac{\gamma - 1}{\gamma \overline{p}}Re[p'\dot{q}'*], \end{aligned} \quad (4.2)$$

where E, F, S and D are period averages of the instantaneous quantities. In the previous expressions the star symbol indicates a complex conjugate of the corresponding variable. This equation indicates that the energy density may increase if the source term S exceeds the damping term D. This requires in turn that S be positive or equivalently that the product $p'\dot{q}'$ integrated over a period be positive, a result initially uncovered by Rayleigh in the form of a

criterion. This result indicates that the oscillation amplitude increases if pressure and heat release fluctuations are in phase. If the integral of this term over the domain exceeds the losses, then the acoustic wave gains energy during a period. This is what happens during combustion instabilities. The term S can also act as a sink term if p' and $\dot{q}'$ are out of phase and the acoustic energy decreases. In combustion instability analysis it is not too difficult to obtain accurate representations of the acoustic field $p'(\mathbf{x}, t)$ but it is less easy to derive a suitable model for the unsteady heat release. This is specifically the case for high frequency combustion instabilities associated with transverse acoustic modes. Because experimental data was lacking, much of the modeling of $\dot{q}'$ has relied on the sensitive time lag concept $n - \tau$ model (Section 4.2.2) which only offered a phenomenological representation of the process.

The following sections essentially focus on the modeling of $\dot{q}'$. The other aspects of the problem, which are also of importance in driving instabilities, like the description of the coupled acoustics of the chamber and dome etc., will be treated in chapter 5 where a simulation tool is developed to assemble the various mechanisms intervening in the process.

The point of view adopted in the following sections is that the flame motion is responsible for the heat release fluctuations. The mechanism presented and discussed is as follows: if a sufficiently powerful acoustic field is present in the chamber, the atomisation process is modified and gives rise to shorter and therefore more intense flames. As shown in experiments, flames are then locked on or “attached" to the acoustic field. It will be further demonstrated (Section 4.3) that this gives rise to a source term in the acoustic energy balance equation, which leads to a growth in instability.

This mechanism raises two important issues. The first is the initial growth of the instability. In this mechanism, the initial presence of the acoustic field is assumed. This reflects the experiment itself where this field is induced by an external modulator. The VHAM imposes the acoustic field necessary to trigger the instability. Consequently, understanding this phenomenon by interpreting experimental data is not straightforward. It will be shown, however, that the theoretical models developed here give insight into this part of the instability process (Section 4.4.4). The second issue is the asymmetry observed in the flame pattern. This asymmetry always correlates with the most responding eigenmodes, and seems to play an important role in the instability mechanism. This asymmetry has a strong impact on the flame response, but can be treated independently from the main mechanism (Section 4.7). The asymmetry augments the response by changing the spatial distribution of the acoustic field, but it is the motion of the flames that creates the source term in the acoustic

balance equation.

The following analysis successively considers the two steps which can be identified in the instability process as they appear in the aforementioned experiments. During hot fire tests carried out at a modulation frequency equal to an eigenfrequency of the chamber, there is a short period during which the atomisation changes, the flame structure is modified and the pressure wave amplitude increases. During continuous wave modulations, this lasts about 100 ms. Once the flame structure is established, the acoustic wave can keep its amplitude (Fig. 4.1 (a)) or continue to grow (Fig. 4.1(b)), albeit on a significantly longer time scale. The growth of the instability in the case of the PF3 for the 1T2L mode lasts approximately eight seconds and could have lasted longer if the excitation had been continued. High speed imaging gives access to the latter process, and the first model presented in this chapter (Section 4.3) will be based on the interpretation of these images. The idea is to follow the flame in a lagrangian way and deduce the unsteady heat release from its displacement. This analysis demonstrates a possible coupling mechanism but does not account for the accelerated break up of the jet and the resulting more compact flame structure, observed during the first period of the instability. Another framework is then developed (Section 4.5) which follows the same principle but introduces droplets of liquid or transcritical (dense) oxygen.

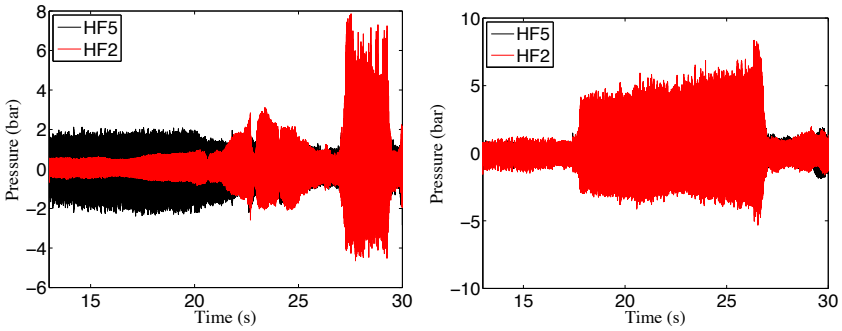

(a) (b)

Figure 4.1: *(a) PF2 during LFM2. The first six seconds correspond to a monofrequency excitation on the 1T mode (1840 Hz), there is no growth of the acoustic amplitude - (b) PF2 during CWM3 at the 1T2L mode. The amplitude increases from 4 bar to 6 bar during this 8 seconds test.*

4.2 Description of the analytical framework

Low-order modeling consists in replacing complex coupled processes with simpler descriptions. These simplified models are treated independently and linked

together in the final stage. The objective is to obtain a state space description of the coupled dynamics of the system under investigation. This description includes a finite system of differential equations in combination with a set of algebraic relations. Stability calculations are then carried out in the time or frequency domains.

4.2.1 Acoustic description

To formulate the combustion models which are developed in this section one has first to provide a description of the acoustic field in the chamber. This will be based on the chamber eigenmodes. The calculation of these eigenmodes will be studied in the next chapter. We assume that these modes are known and introduce the modal expansion method and its essential results.
All variables are written as sums of mean and fluctuating parts, $p = \overline{p} + p'$, etc. Here, $\overline{p}(\boldsymbol{x}) = 1/T \int_0^T p(\boldsymbol{x}, t)dt$. The mean velocity is assumed to be negligible for simplicity. Mean pressure and density are assumed to be uniform. Finally, damping and forcing terms are not considered in this section but will be studied in the next chapter. The analysis is based on the following set of linearized equations:

$$\begin{cases} \dfrac{1}{c^2}\dfrac{\partial p'}{\partial t} + \overline{\rho}\boldsymbol{\nabla}\cdot\boldsymbol{v}' = \dfrac{\gamma-1}{c^2}\dot{q}' \\ \\ \overline{\rho}\dfrac{\partial \boldsymbol{v}'}{\partial t} + \boldsymbol{\nabla}p' = 0 \end{cases}$$

This set can be rearranged to obtain a wave equation. In the simplest possible model for pressure perturbations in a reactive medium, the pressure field is governed by

$$\frac{1}{c^2}\frac{\partial^2 p'}{\partial t^2} - \boldsymbol{\nabla}^2 p' = \frac{\gamma-1}{c^2}\frac{\partial \dot{q}'}{\partial t}, \tag{4.3}$$

where $\dot{q}'$ designates the nonsteady heat release rate.
The associated boundary conditions are

$$\frac{\partial p'}{\partial \boldsymbol{n}} = -f, \tag{4.4}$$

where $\boldsymbol{n}$ is the normal direction (positive outward), and f is commonly expressed in terms of a local admittance characterizing the unsteady behavior of the boundary in response to acoustic fluctuations. If the boundary is a wall, eq. 4.4 reads: $\partial p'/\partial n = 0$ or $\boldsymbol{v}' = 0$.
It is well established that acoustics and combustion play a central role in combustion instability and that these two aspects need to be considered in conjunction. The unified approach introduced by Zinn and Lores (see Culick (1976))

and applied in various studies, Culick (1988) and Culick and Yang (1995) for instance, provides a suitable starting point. The pressure field is expanded over a basis of eigenmodes, and the evolution of the amplitude of each mode, which depends only on time, is solved independently. One attractive feature of this method is that it provides a tool for the nonlinear analysis of acoustic motion as demonstrated by Culick and his co-workers.
In the unified approach the unsteady pressure field is expanded in terms of the normal modes

$$p'(\boldsymbol{x},t) = \sum_{m=0}^{\infty} \eta_m(t)\Psi_m(\boldsymbol{x}) \tag{4.5}$$

In this expansion, the modal amplitudes η_m depend on time t and they have the dimension of pressure. The eigenmodes $\Psi_m(\boldsymbol{x})$ satisfy a Helmholtz equation:

$$\nabla^2\Psi_m + k_m^2\Psi_m = 0, \tag{4.6}$$

$$\frac{\partial\Psi}{\partial n} = 0, \tag{4.7}$$

with $k_m = \omega_m/c$. The $\Psi_m(\boldsymbol{x})$ functions verify $\int_V \Psi_m(\boldsymbol{x})^2 dV = \Lambda_m$. The term $m = 0$ represents a shift of the average pressure. Since the normal modes Ψ_m satisfy boundary condition (4.7) on the entire wall surface, the series (4.5) does not converge uniformly where the boundary condition differs from that used to define the eigenmodes. Nevertheless, expression (4.5) is suitable for calculating the pressure in the cavity and everywhere on the wall surface, including where boundary conditions differ from those which must be imposed to the pressure field. This result is indicated in Morse and Ingard (1968) and it is demonstrated by Ventres (see Dowell (1974)).

There are alternate possibilities such as that used by Pieringer et al. (2005), where acoustic propagation is solved within the fluid dynamic equations, using a source term for energy. In that approach the acoustic perturbation equations are integrated numerically and the chamber eigenmodes are not needed. This track is not followed here because it is felt that the eigenmodes are naturally present in combustion instabilities. The modal expansion yields a direct description in terms of a differential system of equations allowing parametric studies. It is also interesting to separate acoustic processes from combustion dynamics so that the latter can be described with increasing degrees of detail. The modal structures and frequencies can be determined in various ways. A complete description of the system acoustics is given in the next chapter (section 5.2) while the following description is only an introduction to the formalism.
Inserting the pressure expansion in terms of eigenmodes and assuming that the modes are orthogonal, one finds after projection a set of second order differential

equations:

$$\ddot{\eta}_m + \omega_m^2 \eta_m = \frac{\gamma - 1}{\Lambda_m} \int_V \frac{\partial \dot{q}'}{\partial t} \Psi_m(\boldsymbol{x}) dV \tag{4.8}$$

In this formulation, effects of mean flow have been neglected and it is assumed that the sound speed is constant. The nonlinear coupling of modes associated to large amplitudes is also not taken into account. These three aspects can be handled but this is not done here for the sake of simplicity. They may be included in a later version of the model.

4.2.2 Nonsteady heat release modeling

The source terms which appear in the differential system of equations (4.8) correspond to the projection of the nonsteady rate of heat release on the normal modes. The problem is closed if it is possible to express the nonsteady heat release rate in terms of other variables like the pressure and velocity perturbations:

$$\dot{q}' = f(\boldsymbol{x}, t, p', \boldsymbol{v}', ...). \tag{4.9}$$

The modeling of the nonsteady rate of heat release is one of the central issues in combustion dynamics. Among the many different representations, three possibilities are described in what follows.

4.2.2.1 The sensitive time lag (STL) formalism

A model which has been widely used in the past makes use of the time lag concepts introduced in the early fifties by Summerfield, Crocco and Tsien (see for example Crocco and Cheng (1956)). One considers that propellants which are converted into products at time t were introduced in the chamber at time $t - \tau$. The delay τ itself is a function of variables defining conditions in the combustion region like pressure, temperature, etc. It is then shown that the mass rate of conversion of reactants into products can be linked to the rate of change of the time lag and that the nonsteady heat release may be deduced from the difference between the pressure perturbation at time t and the pressure perturbation at time $t - \tau$. The gain of this process is usually called the "interaction index" n. The sensitive time lag (STL) model, also designated as the $n - \tau$ model can be applied to the relative heat release fluctuation and written in the form

$$\frac{\dot{q}'}{\overline{q}} = n \frac{p'(\boldsymbol{x}, t) - p'(\boldsymbol{x}, t - \tau)}{\overline{p}}, \tag{4.10}$$

where $\overline{p}$ and $\overline{q}$ are the mean pressure and mean heat release respectively.

Models of this type have been widely used to analyze longitudinal instabilities arising in the low frequency range (see for example Crocco and Cheng). The time lag τ corresponds to the processes which precede combustion (primary and secondary atomization, heating, vaporization, mixing and chemical reactions). The interaction index n describes the intensity of the coupling between combustion and pressure perturbations in the chamber. The pressure coupling which appears in this formulation is less well justified in the case where the coupling involves transverse modes but it is used in most studies of this type of instability. The model is simple and easy to implement and there are few alternatives, as mentionned in Culick and Yang (1995) and Mitchell (1995). The major drawback of the sensitive time lag model, besides its lack of physical justification as far as transverse oscillations are concerned, is that the interaction index n and delay τ must be determined from experiments. As a result, they are usually adjusted to fit a particular data set but the degree of generality is low and conclusions cannot be extended to other cases. Moreover, the STL model cannot represent the diversity observed in real scale experiments (see for example Hulka and Hutt (1995) for a review).

A path that is followed in this document is to develop a physical analysis of the driving processes and reformulate the STL, with n and τ expressed as functions of flow parameters.

Remark
It is often considered that instabilities are driven by the existence of delay processes. This was initially introduced because it was apparent that the combustion process involved many delays between injection of propellants and their final chemical conversion. The total delay was then defined by the sum of times required for jet break-up, atomization, droplet heating, vaporization and combustion. The time lag concept is well suited to the description of low frequency dynamics of certain classes of propellants (storable propellants) but may be less adequate if one wishes to analyze transverse instabilities of cryogenic reactants. The existence of a delay is not needed to obtain a positive Rayleigh source term in the acoustic energy balance equation (eq. 4.1). For example, if $\dot{q}'(\boldsymbol{x}, t) = \alpha p'(\boldsymbol{x}, t - \tau)$, with α a positive real number, the source term is stronger when τ is close to zero. This seems obvious but it is worth recalling. Numerous studies are focused on the delays that can be observed for the different processes: break up, heating, burning, etc., and the usual conclusion is that the longer the delay (or the closer to a chamber mode period), the more likely it is to have an impact on combustion stability. Though it is natural to assume that time lags are at the source of instability this can also be misleading. The characteristic time for the atomization process, for example, is usually quite short compared to the acoustic mode period. Nevertheless, its impact on the

flame structure is important as highlighted in previous sections. It changes the heat release distribution and hence may have an important role to play in the instability mechanism. As a result, it is necessary to set up a global framework to understand the relative influence of the different processes involved.

4.2.2.2 Droplet response

An alternative view of the coupling problem most notably adopted by Sirignano (see Sirignano et al. (1995) for a review) and his co-workers consists in examining the response of a droplet or an array of droplets to external perturbations of pressure and velocity to describe their collective response in the spray formed by rocket injectors. In this framework, one determines the respective influence of pressure and velocity on the droplet heating and vaporization to deduce the unsteady rate of heat release.

The main idea is that perturbations of pressure and velocity affect the vaporization process. Hence, energy can be released in phase or out of phase with pressure, leading to an increase or decrease of acoustic energy, depending on the Rayleigh source term. During the development of the F1 rocket engine of the Apollo program, vaporization was analytically studied as a rate-controlling mechanism for instability (Harrje and Reardon 1972). At the beginning, thermal inertia was assumed infinite in the model and the liquid droplet did not respond to the fluctuations. The model then could not provide evidence that vaporization was the driving mechanism. A large amount of theoretical work has been carried out on the transient heating and vaporization of fuel droplets in combustion chambers. This work resulted in the model described in Abramzon and Sirignano (1989), which gives accurate vaporization rate and temperature distribution in the droplets for realistic conditions.

It has been shown that spatial variations of temperature through the droplets can be important. The work of Tong and Sirignano (1989), based on similar studies for the droplet response, investigates the contribution of vaporization on combustion instabilities. In this article, the response of a set of droplets is evaluated when they are submitted to different oscillating fields for several frequencies. First, fluctuations of pressure and velocity are applied independently. Then, acoustic waves are imposed: traveling waves, when pressure and velocity fluctuations are in phase and standing waves, when pressure and velocity are out of phase. The first conclusion of this study is that velocity fluctuations are the one whose impact on vaporization are the more important. The second conclusion is that it is possible that vaporization itself can cause self-sustained combustion instabilities.

Nevertheless, there are limitations in this conclusion. First, the study is performed on longitudinal instabilities, and the frequencies investigated are small. For instance, the only frequency that is found to be unstable for a standing wave is near 100 Hz under conditions considered by Tong and Sirignano. And for this particular case, the growth rate is weak. One limitation of the model is that it does not account for the motion of the droplets and for the dynamics of the spray. The eulerian framework used in this study serves to evaluate the energy release related to enhanced vaporization process but the transport of droplets is not considered. The droplet motion induced by the acoustic field can have a significant role as shown in the following development.

4.2.2.3 Coupling of cavities

Another possible contributor to the instability process is the coupling between the thrust chamber and the dome. It is often argued that coupling between these two elements is of importance in the low frequency range but has less influence at high frequency because the propellants inertia in the injection channels damps the level of perturbation reaching the dome. In standard practice, the low frequency coupling is controlled by augmenting the head loss in the injection units to a level of about 10 to 15 %. One does not know, however if this has an effect on high frequency dynamics and reduces the possibility of coupling in the high frequency range.
The acoustic coupling between several cavities has been examined in recent studies. Cheuret (2005) and Oschwald et al. (2008) have studied the coupling between a combustion chamber and damping cavities. Evesque and Polifke (2002) have investigated the coupling between the upstream manifold and the chamber for gas turbines. This problem is often envisaged with acoustic tools. This is however an important limitation because it cannot account for the dynamics of injection units and of its impact on the oscillations in the dome and thrust chamber.

4.2.2.4 Recent developments

The link between the unsteady heat release and fundamental physical processes is investigated in some recent studies. It is shown for example by Richecoeur (2006), Richecoeur et al. (2007) that coupling can be envisaged by considering a global mass balance (GMB) in the thrust chamber. In the rectangular geometry of the MIC, control volumes are defined in the upper and lower sides of the cavity. The transverse motion induces an alternate accumulation of reactants in these two volumes. Burning takes place after a delay τ yielding an unsteady fluctuation of the rate of heat release:

$$\dot{q}'(y,t) = \beta \text{sign}\left[\frac{\partial v'}{\partial y}(y,t-\tau)\right] v'(y,t-\tau), \tag{4.11}$$

where y is the transverse space variable, v' is the transverse velocity component, and β is an interaction index.
Following similar ideas but considering a local balance of mass, it is possible to derive an alternative expression (LMB[1] model):

$$\dot{q}'(y,t) = (-\Delta h^0_{LOx}) Y_{LOx} \overline{\rho} \frac{\partial v'}{\partial y}(y, t-\tau), \tag{4.12}$$

where Δh^0_{LOx} is the heat of combustion related to oxygen consumption, Y_{LOx} is the liquid oxygen mass fraction and $\overline{\rho}$ is the mean density.

Both expressions are derived from mass balance equation as shown in the following subsections. We first consider the transverse acoustic field and its influence on the distribution of reactants. The transverse field modifies the droplet dynamics and influences the spatial distribution of droplets. The heat release location is strongly correlated to the droplet positions and the velocity field generates a heterogeneity in this distribution. The time lag τ is associated to the relaxation time corresponding to the drag forces acting on the droplets and to the time required for mass transfer from the droplets to the surrounding gas. The problem is then to determine the space-time distribution of droplets and deduce the non-steady heat release distribution resulting from heterogeneities in the droplet density. The main idea of this model is similar to that developed in Section 4.5 where more rigorous equations are derived and expressions for n and τ are obtained.

These two models demonstrate the possibility of a coupling driven by the transverse velocity fluctuation but they also have the drawback of comprising phenomenological parameters, an interaction index and a delay in the GMB model and a delay in the LMB model. One may then wish to explore models which will be based on a more physical description of the coupling.

4.2.3 Conclusion

It appears from the previous review that modeling of heat release fluctuations may be tackled in different ways and that a variety of physical mechanisms may drive high frequency combustion instabilities. A short list is given below:

- Effect of pressure and velocity on vaporization (**M1**),
- Unsteady mass flow rates induced by coupling of dome and thrust chamber (**M2**),

[1] Local Mass Balance

- Effect of spray/flame motion, caused by the acoustic field, on the acoustic energy source term (**M3**).
- Effect of unsteady pressure on the heat release fluctuations (**M4**).

The last coupling mechanism, which is generally not put forward, is related to the effect of pressure on heat release rate. The article of Pons et al. (2008) demonstrates through infinitely fast chemistry and finite complex chemistry calculations that heat release is proportional to the square root of pressure: $\dot{q} \propto \sqrt{p}$. It is then expected that when pressure oscillates by several bar, this will have an impact on the unsteady heat release rate. This aspect is investigated in section 4.4.2.
In the previous list the sensitive time lag model is not listed as such, because its physical justification mainly stands for low frequency instabilities.

The goal of the next section is to sort out the prevailing mechanisms but a number of additional issues must be considered. It is likely that the different physical phenomena operate in combination in an actual system, and it is necessary to establish a framework which will be able to represent their simultaneous influence. It is also important to model mechanisms which control combustion in liquid rocket engines. In this respect atomization plays a central role in the low pressure range. This process does not appear explicitly in the acoustic balance equation, but defines the dynamics of the spray and as demonstrated by experiments, plays a crucial role and must be taken into account.

Summary
In the context of low order modeling it is convenient to expand the pressure field on a set of normal modes of the chamber. The amplitudes of these modes are then solution of a system of differential equations featuring as source terms a projection of the rate of change of nonsteady heat release on the modal functions.

$$\boxed{\begin{aligned} p'(\boldsymbol{x},t) &= \sum_{m=1}^{N} \eta_m(t)\Psi_m(\boldsymbol{x}) \\ \ddot{\eta}_m + \omega_m^2\eta_m &= \frac{\gamma-1}{\Lambda_m}\int_V \frac{\partial \dot{q}'}{\partial t}\Psi_m(\boldsymbol{x})dV \\ \dot{q}' &= f(\boldsymbol{x},t,p',\boldsymbol{v}',...) \end{aligned}} \tag{4.13}$$

The modeling of the nonsteady heat release which constitutes the central issue in this problem is envisaged in the following sections.

4.3 Flame Acoustic Motion Equations (FAME)

4.3.1 Introduction

To devise a low order model for the unsteady heat release it is useful to review experimental data and sort out the main features of the interaction between transverse acoustic fields and combustion. Experiments carried out by Richecoeur (2006) indicated that the unsteady heat release rate (characterized by the light intensity detected by two photomultipliers) was in phase with pressure. When the combustion region in the MIC was submitted to a 1T transverse modulation, the heat release rate in the upper part of the chamber was in phase with the unsteady pressure measured at the upper wall while the heat release in the lower part of the chamber was in phase with the unsteady pressure detected on the lower wall. These results are consistent with those found in our experiments. The phase relation prevails for all operating points and eigenmodes. This central feature defines a generic situation in which the Rayleigh source term in the balance of acoustic energy is systematically positive.
It is thus natural to explore *why* the unsteady heat release is in phase with pressure, and get a physical understanding of the driving processes. The next sections are intended to demonstrate that the flame motion induced by the acoustic field can explain this observation. To do this, one first establishes a link between the photomultiplier signals and high speed images (subsection 4.3.2). It is then possible to use the high speed camera images alone to deduce the experimental heat release fluctuations (subsection 4.3.3). A theoretical framework is developed on this basis in susbsection 4.3.4. The consistency between theoretical and experimental flame dynamics is checked in the final subsection 4.3.5.

4.3.2 Photomultiplier signals and high speed imaging

The high speed cameras provide a large number of image data. The spatial distributions of light intensity in these images are interpreted to be proportional to heat release rate. The frame rate is sufficiently high so that the evolution of the heat release rate distribution is resolved in space and time. Light intensity is also detected by two photomultipliers providing the evolution of the intensity signals integrated over two windows. The high speed cameras only record signals during a second and the image quality is not always sufficient. The two photomultipliers, on the other hand measure the light intensity during the whole test duration but the spatial resolution is lost. It is then interesting to compare images delivered by the HS camera with signals detected by the two PMs and see if data recorded with these different diagnostics match. This can then be used to select one of these diagnostics depending on its availability.

The interrogation windows monitored by PM1 and PM2 are shown schemati-

cally in Fig. 4.2. The drawing is only qualitative because the window boundaries are not known precisely. The important point is that PM1 and PM2 are directed towards the top and bottom parts of the chamber respectively. The high speed camera SA1 records all the information at once. In the limit of the camera resolution, it is possible to follow the heat release evolution at all points in the chamber, each pixel in the CCD unit acting as a local light sensor.

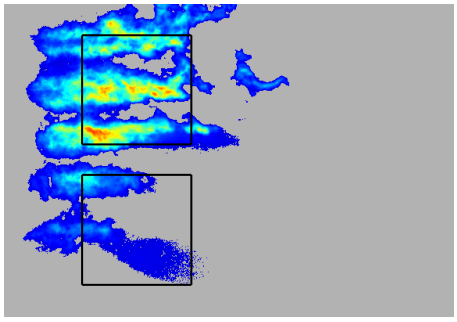

Figure 4.2: *PF3 during CWM at SP4 (3125 Hz) - Instantaneous CH* emission recorded by SA1 camera. The two windows drawn in this image show the area of interest for the two photomultipliers.*

Comparison between data delivered by the HS camera and by the PMs can be carried out by summing the light intensity detected by the camera over the two windows. Intensities detected by pixels located in each interrogation window are added to obtain a mean intensity value for each window and each time step. The resulting signals are plotted in Fig. 4.3. The difference in amplitude is caused by the uncertainty in the window location and by the signal normalization methods. This figure indicates that the respective signals are in phase and that the two diagnostics are consistent. It is then possible to move a step further in the high speed images analysis as explained in the next subsection.

4.3.3 Heat release rate fluctuation

The heat release rate fluctuations are now characterized by processing the high speed camera images. Camera SA1 records $I(\boldsymbol{x}, t)$, which is here considered to be proportional to $\dot{q}(\boldsymbol{x}, t)$. To obtain the fluctuation $\dot{q}'(\boldsymbol{x}, t)$, one subtracts the mean signal from the instantaneous data:

$$\dot{q}'(\boldsymbol{x}, t) = \dot{q}(\boldsymbol{x}, t) - \overline{\dot{q}}(\boldsymbol{x}), \tag{4.14}$$

where $\overline{\dot{q}}(\boldsymbol{x})$ is obtained from $\overline{I}(\boldsymbol{x})$, which is the average of all images of a test case. The space time field of $\dot{q}'$ obtained in this way is perturbed by turbulence. To get rid of such disturbances and only retain phenomena synchronized by the acoustic modulation, it is natural to calculate a phase average. This leads to

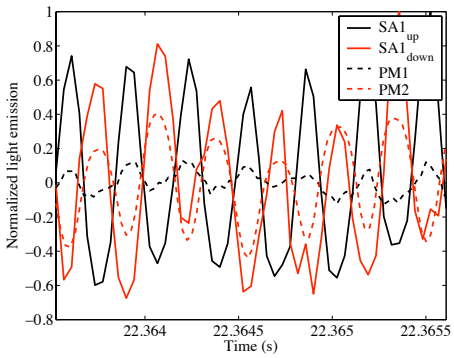

Figure 4.3: *PMs signals plotted together with the signals deduced from the SA1 camera images by summing the light intensities detected by the pixels located in the two interrogation windows.*

images shown in Fig. 4.4, where $\dot{q}'(\boldsymbol{x}, \phi)$ is plotted for two opposite phases and for two different eigenfrequencies.

The data displayed in Fig. 4.4 give a better understanding of the fluctuations observed in Fig. 4.2 and 4.3. When $\phi = \pi/2$, $\dot{q}'$ recorded by the upper PM (PM1) is smaller than when $\phi = 3\pi/2$, the opposite is true for the lower PM (PM2). This corresponds well with what is seen in Fig. 4.3 but it also provides new information on the coupling mechanism.

In Section 4.2.2 we have already identified three major types of interactions which can lead to fluctuations of $\dot{q}'$. The first may be caused by the droplet response to acoustic perturbations (**M1**), the second corresponds to a coupling with the dome and yields modulations of the mass flow rate in each injector (**M2**), and the third is associated to the flame displacement induced by the acoustic field (**M3**). Combinations of these different mechanisms control the dynamics of the system.

To sort out the dominant coupling, it is useful to examine what would be observed in each case. If the driving phenomenon were the droplet response associated with heating and vaporization (**M1**), the flame intensity would change during a cycle of oscillation. This feature, if it is present, is hardly noticeable in the experiments compared to the fluctuations shown in Fig. 4.4. Actually, the comparison between Fig. 4.4 (a) and (b) can be misleading. The second and third flames starting from the top of the window are more intense in the latter. This is induced by the asymmetry of the flame motion. To be more precise, if the **M1** mechanism were the driving process, the flames in the bottom would be more intense at $\phi = \pi/2$ and the flames in the top would be more intense at $\phi = 3\pi/2$. Here, the light intensity of all flames is enhanced at $\phi = 3\pi/2$, but at a different *location*. The difference of intensity between the two opposite phases is thought to be a combination of the asymmetry of the flames and of the effect of pressure on heat release (**M4**). This is explained and modeled in

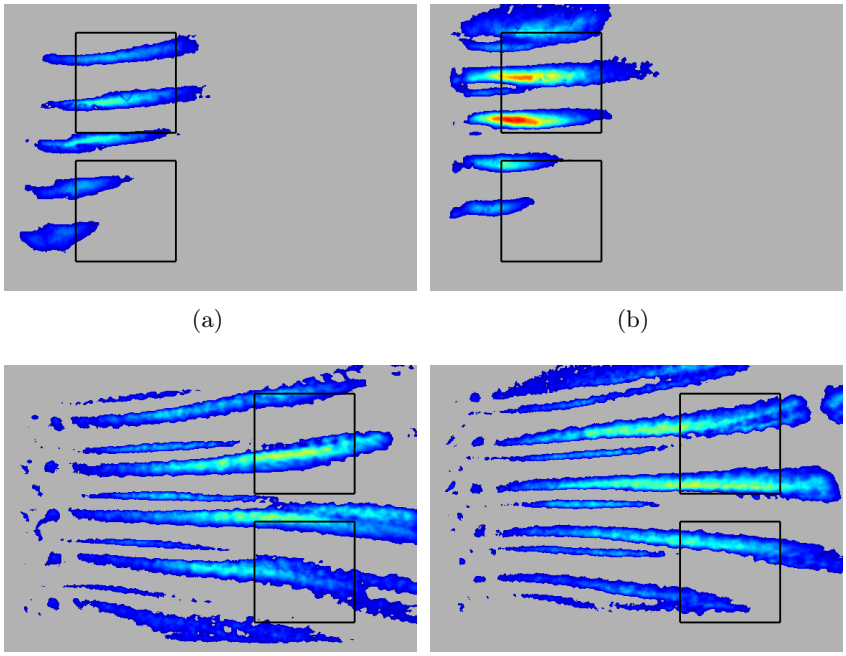

Figure 4.4: *Phase averaged images of $I(\boldsymbol{x},t)-\overline{I}(\boldsymbol{x},t)$, with I the instantaneous CH* emission recorded by SA1 camera for two modes - (a) 1T2L at $\phi=\pi/2$ - (b) 1T2L at $\phi=3\pi/2$ - (c) 1T at $\phi=\pi/2$ - (d) 1T at $\phi=3\pi/2$ - When $\phi=\pi/2$, $\dot{q}'$ recorded by the upper PM (PM1) is smaller than when $\phi=3\pi/2$, the opposite is true for the lower PM (PM2).*

section 4.7.

If the driving were due to a coupling with the dome inducing mass flow rate modulations in the injection units (**M2**), one would expect to find a flame oscillation in the longitudinal direction (the direction of injection). This is not observed in the various test cases. The heat release rate is essentially oscillating in the transverse direction around the mean position. The oscillation is observed over a region corresponding to this motion, which confirms the third assumption (**M3**). This mechanism is analyzed in the following sections.

Note

It is important to underline that the previous conclusions have a limited range of validity. The first limitation is that the five flames in the hot fire experiment are located near the center of the chamber close to a velocity antinode and far from the pressure antinodes. The instability mechanism may also involve a coupling with pressure related to heating and vaporization of the spray or

unsteady injection, but such effects will be less easy to identify in the present configuration because the pressure perturbation is weak in the region of interaction. It is however worth noting that a strong coupling has been observed in several test cases and one can expect that some of the mechanisms driving instabilities have occured.

4.3.4 Analysis and modeling of the flame motion

In the present analysis the flame is represented in a simplified form as a thin sheet which is transported in the transverse direction by the velocity perturbation associated with the acoustic field. The central assumption of this analysis is that the unsteady heat release rate is due to flame motion and not to a modification in their structure in agreement with what is observed experimentally. The thin flame sheet representation is used in what follows to determine the unsteady heat release rate and obtain an explicit relationship between p' and $\dot{q}'$ through u'.
The first step consists in finding the equation of motion of a flame in a transverse acoustic field. Using the unified framework introduced previously, the pressure field in the gas phase is expanded over the normal modes of the chamber:

$$p'(\boldsymbol{x},t) = \sum_{m=0}^{\infty} \eta_m(t)\Psi_m(\boldsymbol{x}). \tag{4.15}$$

It is reasonable to consider that the modal amplitudes $\eta_m(t)$ vary slowly compared to the period of oscillation of the various modes. The velocity field can be deduced from the momentum equation and its transverse velocity component may be cast in the form (Culick 1976):

$$u'(\boldsymbol{x},t) = \frac{c^2}{\overline{p}\gamma} \sum_{m=1}^{\infty} \frac{1}{\omega_m^2}\dot{\eta}_m(t)\boldsymbol{\nabla}\Psi_m(\boldsymbol{x}). \tag{4.16}$$

There is no transverse velocity fluctuation for the pressure component corresponding to $m = 0$, so this contribution does not appear in (4.16).
The following equations are written for a single flame, and the model is later extended to any number of flames. The flame sheet follows the acoustic field and its position $\boldsymbol{x}(t)$ is such that:

$$\frac{d\boldsymbol{x}(t)}{dt} = \frac{c^2}{\overline{p}\gamma} \sum_{m=1}^{\infty} \frac{1}{\omega_m^2}\dot{\eta}_m(t)\boldsymbol{\nabla}\Psi_m(\boldsymbol{x}), \tag{4.17}$$

It is convenient to use the reference frame and system of coordinates defined in Fig. 4.5.
For simplicity, it is now assumed that the acoustic field only induces a transverse motion corresponding to the 1T mode. This may seem a fairly restrictive

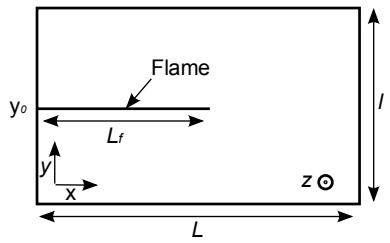

Figure 4.5: *Schematic representation of the rectangular chamber with the reference frame of coordinates used in the analytical development. The initial flame position y_0 and its length L_f are also shown.*

assumption, since the greatest response was obtained by exciting the 1T2L mode. This is actually not a problem because what matters in the present context is the acoustic field experienced by the flames. During the tests excited at the 1T1L and 1T2L resonant modes, the modification of atomization induced by the strong acoustic modulation shortens the flames (this coupling will be investigated in section 4.5.2). Most of the heat release takes place near the injection plane in one third of the chamber. Flames are then mainly submitted to the acoustic field in this region which is quite similar to a first transverse mode, as represented in Fig. 4.6.

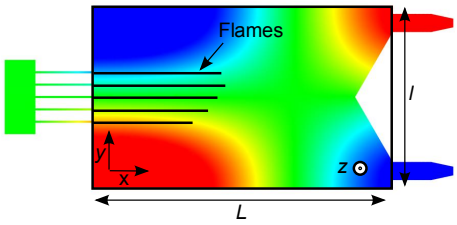

Figure 4.6: *Schematic representation of the shortened flames with the 1T1L pressure field in background. In the flames frame of reference, the pressure distribution is essentially transverse.*

It is then reasonable to use the 1T mode eigenfunction $\Psi_1(y) = \cos(\pi y/l)$ and deduce the flame displacement from:

$$\dot{y}(t) = -\frac{c}{\bar{p}\gamma\omega_1}\dot{\eta}_1(t)\sin(\frac{\pi}{l}y). \tag{4.18}$$

The method of separation of variables leads to:

$$y(t) = \frac{2l}{\pi}\arctan(\tan(\frac{\pi y_0}{2l})e^{-\frac{\eta_1(t)}{\bar{p}\gamma}}), \tag{4.19}$$

where y_0 is the mean flame position.
These results can be used to obtain the value of $\dot{q}(x,t)$. It is interesting to note that the steady heat release of one flame formed by a single injector $\mathcal{Q}$ is

directly related to the mass flow rate of oxygen (methane is injected in excess) $\mathcal{Q} = \dot{m}_{LOx}\Delta h_T$ where $\dot{m}_{LOx}$ and Δh_T respectively designate the mass flow rate of oxygen and the heat release per unit mass of oxygen ($\Delta h_T = 12.5$ MJ kg^{-1}). In the hot fire tests corresponding to a total mass flow rate of oxygen $\dot{m}_{LOx} \simeq 100$ g s^{-1}, the heat release per injector is $\mathcal{Q} \simeq 2.5\ 10^5$ W. If the flame is infinitely thin, the expression for the heat release is:

$$\dot{q}(\boldsymbol{x},t) = \frac{\mathcal{Q}}{L_f}\delta(y-y(t))\delta(z-z_0), \quad (4.20)$$

$$\bar{\dot{q}}(\boldsymbol{x}) = \frac{1}{T}\int_0^T \frac{\mathcal{Q}}{L_f}\delta(y-y(t))\delta(z-z_0)dt, \quad (4.21)$$

$$\dot{q}'(\boldsymbol{x},t) = \frac{\mathcal{Q}}{L_f}\left(\delta(y-y(t))\delta(z-z_0) - \frac{1}{T}\int_0^T \delta(y-y(t))\delta(z-z_0)dt\right), \quad (4.22)$$

where L_f is assumed to be constant and z_0 is the position of the flame in the spanwise direction.
Acoustic equations defining the modal amplitudes η_m feature a source term:

$$\ddot{\eta}_m + \omega_m^2\eta_m = \frac{\gamma-1}{\Lambda_m}\int \frac{\partial\dot{q}'}{\partial t}\Psi_m dV, \quad (4.23)$$

where Λ_m is the square of the norm of Ψ_m. Under the previous assumptions, the equation defining the first modal amplitude can be written as:

$$\ddot{\eta}_1 + \omega_1^2\eta_1 = \frac{\gamma-1}{\Lambda_1}\iiint \frac{\partial\dot{q}'}{\partial t}\cos(\frac{\pi}{l}y)dxdydz, \quad (4.24)$$

$$\Lambda_1 = \iiint \cos^2(\frac{\pi}{l}y)dxdydz = \frac{Lhl}{2}.$$

In this calculation we do not consider the damping factor but this will be introduced later in the complete dynamical system model. Inserting the expression of $\dot{q}'$ (4.22), one finds:

$$\ddot{\eta}_1 + \omega_1^2\eta_1 = -\frac{\gamma-1}{\Lambda_1}\mathcal{Q}\dot{y}(t)\frac{\pi}{l}\sin(\frac{\pi}{l}y(t)), \quad (4.25)$$

$$\ddot{\eta}_1 + \omega_1^2\eta_1 = \frac{\gamma-1}{\Lambda_1}\mathcal{Q}\frac{\dot{\eta}_1}{\bar{p}\gamma}\sin^2(\frac{\pi}{l}y(t)), \quad (4.26)$$

Finally:

$$\ddot{\eta}_1 + \omega_1^2\eta_1 = 4\frac{\gamma-1}{\gamma}\frac{\mathcal{Q}}{\bar{p}\Lambda_1}\dot{\eta}_1\frac{\tan^2(\frac{\pi y_0}{2l})e^{\frac{-2\eta_1(t)}{\gamma\bar{p}}}}{\left(1+\tan^2(\frac{\pi y_0}{2l})e^{\frac{-2\eta_1(t)}{\gamma\bar{p}}}\right)^2}. \quad (4.27)$$

It is worth noting that the right hand term is proportional to $\dot{\eta}_1$ and that the function appearing as a factor is always positive. This term acts as a negative damping inducing a growth of the amplitude. Usually, the growth rate is weak, except when the heat released by the flame is high. In the MIC the power release per injector is $\mathcal{Q}_{MIC} \simeq 0.25$ MW. In the Vulcain engine this parameter $\mathcal{Q}_V \simeq 7.5$ MW takes values which are about 30 times larger than in the MIC and the growth rate is significantly augmented. In addition there are numerous closely packed flames in the engine configuration. When multiple flames are involved, the source term on the right hand side features a sum over all the flames and the previous equation becomes:

$$\ddot{\eta}_1 + \omega_1^2 \eta_1 = \frac{\gamma - 1}{\Lambda_1} \mathcal{Q} \frac{\dot{\eta}_1}{\overline{p}\gamma} \sum_{n=1}^{N_f} \sin^2\left(\frac{\pi}{l} y^n(t)\right), \tag{4.28}$$

$$\ddot{\eta}_1 + \omega_1^2 \eta_1 = 2\frac{\gamma - 1}{\gamma} \frac{\mathcal{Q}}{\overline{p}\Lambda_1} \dot{\eta}_1 \sum_{n=1}^{N_f} \frac{\tan^2\left(\frac{\pi y_0^n}{2l}\right) e^{\frac{-2\eta_1(t)}{\gamma \overline{p}}}}{\left(1 + \tan^2\left(\frac{\pi y_0^n}{2l}\right) e^{\frac{-2\eta_1(t)}{\gamma \overline{p}}}\right)^2}, \tag{4.29}$$

where N_f is the total number of flames, $y^n(t)$ and y_0^n are respectively the instantaneous and mean locations of the n-th flame. This relationship clearly highlights collective effects. When only one flame is involved, the source term is small compared to the case where combustion is distributed in a large number of flames as in typical rocket engines. In the intermediate case of the multiple injector combustor featuring five flames, an external excitation must be used to bring the amplitude of motion to a significant level to obtain a positive growth rate.

4.3.5 Conformity between experimental and theoretical flame motions

The model described in the previous subsection involves the flame motion. The acoustic field induces a transverse displacement of the heat release regions and this in turn creates an unsteady heat release rate. In other words, the FAME model is based on one assumption. If the flame *does* follow the acoustic velocity field, there is an associated Rayleigh source which has the expression (4.28). One may ask whether this source term is sufficient to explain high frequency combustion instabilities. This will be addressed in the following sections. It is however necessary to check the basic assumption of this model which relies on the assumption that the flames move with the acoustic field.

The principle is to compare theoretical and experimental motions. The details of this verification is described bellow. From experiments, acoustic pressure

is known at five locations in the chamber corresponding to the sensors flush mounted at the chamber walls. It is easy to extrapolate the data to get the pressure field in the domain. This yields an experimental distribution:

$$p'_{exp}(\boldsymbol{x}, t). \tag{4.30}$$

This pressure field corresponds rigorously to an acoustic velocity field $v'_{th}(\boldsymbol{x}, t)$. In practice, $v'_{th}(\boldsymbol{x}, t)$ can be deduced from $p'_{exp}(\boldsymbol{x}, t)$ by applying the acoustic equations described in section 4.2.1. Once $v'_{th}(\boldsymbol{x}, t)$ is known, the theoretical motion of infinitely thin flames is calculated with equations described in the previous section. This gives the equation of motion of each flame:

$$y^n_{th}(t). \tag{4.31}$$

The equation of motion $y^n_{th}(t)$ corresponds to the measured acoustic pressure field $p'_{exp}(\boldsymbol{x}, t)$. To verify that this assumption is correct, we compare $y^n_{th}(t)$ to the observed motion of the flames, which is recorded by SA1 high speed camera. The comparison is carried out for operating point PF3, on the 1T2L mode and is shown in Fig. 4.7. For the theoretical curves, a fixed pressure oscillation has been chosen for each flame, for the sake of simplicity. The pressure oscillation is set so that it is close to that measured by the top sensor (HF1) for the top flames and to the bottom sensor (HF2) for the bottom flame. The theoretical and experimental motions of the flames match quite well thus validating the underlying assumption. The amplitude of $y^n_{th}(t)$ is slightly more important than the one recorded by the SA1 camera. Some of the acoustic energy is probably dissipated to put the flames and jets in motion.

4.4 Implications and extension of FAME

The experimental justification and the basic equations of the model are established in the previous section. Implications of the FAME are now examined. In the first subsection, the growth rate predicted by the model is presented and its link with the acoustic energy rate of growth is considered. The second subsection gives an extension of the FAME where the effect of local pressure on the heat release is taken into account. In the last paragraph of this section, the model is used to explain the role of hydrodynamic instabilities in the instability process. We show that, under certain conditions, these instabilities can also trigger high frequency instabilities.

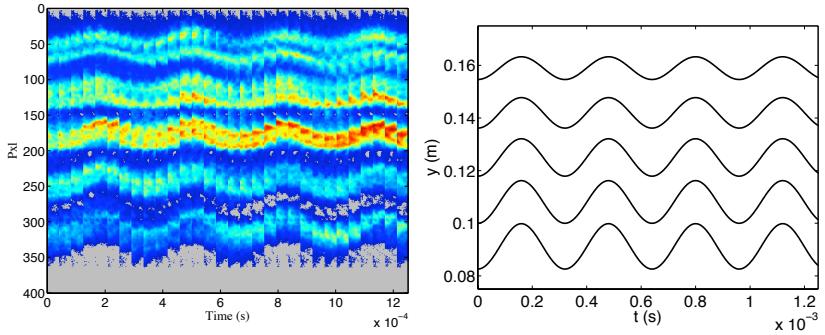

(a) (b)

Figure 4.7: *(a) Streak film of the flames recorded during a 1T2L excitation at PF3 - (b) Theoretical reconstruction of a similar streak film using the pressure signals HF1 and HF2 as inputs. Theoretical and experimental motions of the flames match quite well.*

4.4.1 Growth factor

It is first interesting to examine the growth factor associated with FAME. In a differential equation of the general form:

$$\ddot{y} + 2\xi\omega\dot{y} + \omega^2 y = 0,$$

the second term corresponds to a damping factor $\alpha = \xi\omega$. The solution of the previous equation is of the form:

$$y(t) = Ce^{-\xi\omega t}(cos(\omega\sqrt{1-\xi^2}t + \phi), \tag{4.32}$$

where C and ϕ are two constants depending on initial conditions. If ξ is negative, the solutions take the same form but oscillations grow exponentially. α now corresponds to a growth factor. In eq. 4.33, the factor, which is found on the right hand side of the dynamical equation yields a growth rate of form:

$$\alpha_1 = 2\frac{\gamma-1}{\gamma}\frac{\mathcal{Q}}{\overline{p}\Lambda_1}\sum_{n=1}^{N_f}\frac{\tan^2(\frac{\pi y_0^n}{2l})e^{\frac{-2\eta_1(t)}{\gamma\overline{p}}}}{\left(1+\tan^2(\frac{\pi y_0^n}{2l})e^{\frac{-2\eta_1(t)}{\gamma\overline{p}}}\right)^2}. \tag{4.33}$$

One may note that α_1 is not constant, as it depends on $\eta_1(t)$, and in principle, the solution cannot be written as in eq. 4.32. Still, the time varying term $\eta_1/\overline{p}$ can be considered to be small so that $\exp(-2\eta_1(t)/(\gamma\overline{p}))$ remains close to 1.

Link with the energy density

It is interesting to link the previous result to the growth rate of the acoustic energy density. This can be analyzed by examining the source term in the balance of acoustic energy. The source term is positive when the unsteady pressure and heat release are in phase. In this section, $\mathcal{E}(\boldsymbol{x},t)$, $\mathcal{E}_1(t)$ and $\langle E_1\rangle(t)$ refer respectively to local instantaneous, spatially integrated and time averaged. In the absence of mean flow and in an isentropic medium, the local instantaneous acoustic energy reads:

$$\mathcal{E}(\boldsymbol{x},t) = \frac{1}{2}\frac{p'^2}{\overline{\rho c^2}} + \frac{1}{2}\overline{\rho}u'^2.$$

To estimate this quantity it is convenient to consider that the domain is rectangular and that the acoustic field corresponds to the first transverse mode. p' and u' are replaced by their expression:

$$p'(\boldsymbol{x},t) = \eta_1(t)\cos(\frac{\pi}{l}y),$$

$$u'(\boldsymbol{x},t) = -\frac{c}{\overline{p}\gamma\omega}\dot{\eta}_1(t)\sin(\frac{\pi}{l}y),$$

and the global instantaneous energy is deduced:

$$\mathcal{E}_1(t) = \frac{hlL}{4\overline{p}\gamma}(\eta_1^2(t) + \frac{\dot{\eta}_1^2(t)}{\omega_1^2}). \tag{4.34}$$

To obtain the link between pressure and energy one may assume that the amplitude evolves exponentially and that the growth rate is small compared to the angular frequency ($\alpha_1 \ll \omega_1$). Using the complex formalism, we can write:

$$\eta_1(t) = p_0 e^{(\alpha_1 + i\omega_1)t}.$$

To calculate averages over a period of products of harmonic variables it is convenient to use the following result:

$$\frac{1}{T}\int_0^T abdt = \frac{1}{2}Re(ab^*),$$

where the $*$ symbol designates the complex conjugate and Re is the real value. This expression can be be used to calculate the time average of the acoustic energy density:

$$\langle E_1\rangle(t) = \frac{hLl}{4\overline{p}\gamma}p_0^2 e^{2\alpha_1 t}(1 + \frac{1}{2}\frac{\alpha_1^2}{\omega_1^2}). \tag{4.35}$$

Assuming that $\eta_1(t)$ grows exponentially with a growth factor α_1, $\langle E1\rangle$ has a growth factor of $2\alpha_1$. This factor can be retrieved in the following way:

$$\frac{1}{\langle E_1\rangle}\frac{d\langle E_1\rangle}{dt} = 2\alpha_1.$$

One may now consider the balance equation for the acoustic energy integrated over a period eq. 4.2 and reproduced below for convenience:

$$\frac{\partial E}{\partial t} + \boldsymbol{\nabla}\cdot F = S - D \text{ with } E = \frac{1}{2}[\frac{1}{2}\overline{\rho}\boldsymbol{u}'\cdot\boldsymbol{u}'* + \frac{1}{2}\frac{p'p'*}{\overline{\rho}c^2}],$$
$$F = \frac{1}{2}Re[p'\boldsymbol{u}'*] \text{ and } S = \frac{1}{2}\frac{\gamma-1}{\gamma\overline{p}}Re[p'\dot{q}'*], \tag{4.36}$$

This equation can be easily integrated over the combustor volume. In the absence of damping and assuming that the sum of the acoustic fluxes traversing the boundaries is equal to zero one obtains:

$$\frac{1}{\langle E_1\rangle}\frac{d\langle E_1\rangle}{dt} = \frac{\langle S\rangle}{\langle E_1\rangle} = 2\alpha_1.$$

This result can now be used to evaluate α_1. One assumes here that the oscillation amplitude changes slowly during a cycle of oscillation. One can estimate the time average source term:

$$\langle S\rangle = \frac{1}{T}\frac{\gamma-1}{\gamma\overline{p}}\int_0^T\iiint p'\dot{q}'dV, \tag{4.37}$$

where $p' = p_0\cos(\omega t)$, $\dot{q}' = \mathcal{Q}/L_f\delta(y-y(t))\delta(z-z_0)$ and $y(t) = 2l/\pi\arctan(\tan(\pi y_0/(2l))\exp(-p_0\cos(\omega t)/(\overline{p}\gamma)))$. Since the heat release rate is concentrated in thin layers represented by Dirac delta functions the integration over space is facilitated:

$$\langle S\rangle = \frac{1}{T}\frac{\gamma-1}{\gamma\overline{p}}\int_0^T p_0\cos(\omega t)\mathcal{Q}\cos(\frac{\pi}{l}y(t))dt, \tag{4.38}$$

and one can proceed with the integration over time numerically. The value of $\langle E_1\rangle$ is obtained from eq. 4.35 by neglecting α_1^2 in this expression. One finally deduces the value of $2\alpha_1$ as a function of the injector position y_0. This dependence is shown in Fig. 4.8 (a). The calculation corresponds to conditions defining the PF3 Mascotte test, with $p_0 = 4$ bar for the acoustic pressure amplitude. When injectors are located near the central plane, the Rayleigh term is higher. It vanishes near the lateral walls, because the flame motion becomes negligible in this region. Adding the growth factors for the five injectors gives the total growth factor for the MIC configuration. The calculation yields $\alpha_1 = 24.5\ \mathrm{s}^{-1}$. This value may be compared to that deduced from eq. 4.33, plotted in Fig. 4.8 (b). In this figure, α_1 slightly oscillates around $24.5\ \mathrm{s}^{-1}$, which proves that the growth rate obtained from the dynamical equation is consistent with the acoustic energy balance estimate.

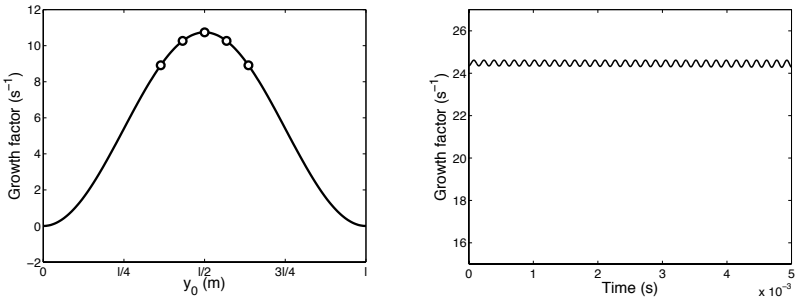

(a) (b)

Figure 4.8: *(a) - Value of the growth factor depending on the position y_0 of the injector on the injection plane. The five dots correspond to the injector locations in Mascotte. When they are located near the center, the Rayleigh term is higher. It is zero near the lateral walls, because the flame motion is negligible in this area - (b) Growth factor obtained by solving eq. 4.33.*

4.4.2 Extension of the model

It is shown in the previous sections that the flame motion leads to an important contribution in the acoustic balance equation. While results of this analysis are in agreement with the present experiments, some features might have been missed. It is known for example from an investigation carried out by Pons et al. (2008) that the heat release per unit area of a nonpremixed strained flame varies like the square root of pressure. This result also holds in the unsteady case when the response time which characterizes the flame is shorter than the period of the pressure perturbation. The characteristic time of fast chemistry flames is essentially given by the inverse of the strain rate $1/a$, where a is the strain rate. If the strain rate is well above the excitation frequency $a > f_e$, the heat release closely follows the pressure. If this is not the case the unsteady pressure is filtered out and the effect on the heat release is reduced.

In Mascotte experiments, and more generally in rocket engines, the typical strain rate is high and reaches values in excess of 10000 s^{-1} in the injection plane nearfield while the excitation frequency is below 3500 Hz. As a result, the pressure dependence of the heat release may have a strong effect in the final Rayleigh term. This direct effect of pressure is envisaged in what follows.

The same approach and notations are used but it is convenient to assume that $\mathcal{Q}$ now varies with the square root of pressure. One assumes in the subsequent

development that

$$\mathcal{Q}(t) = \mathcal{Q}_0\sqrt{\frac{p}{\overline{p}}}, \tag{4.39}$$

$$= \mathcal{Q}_0\sqrt{1+\frac{\eta_1(t)}{\overline{p}}\cos(\frac{\pi}{l}y)}, \tag{4.40}$$

where $\mathcal{Q}_0$ is the mean value of heat release per flame ($\mathcal{Q}_0 = 2.510^5$ W in Mascotte).
This expression is chosen so that, for the spatial pressure distribution of the first transverse mode, $\mathcal{Q}(t)$ varies like the square root of $\eta_1(t)$ and such that: $1/T\int_0^T \mathcal{Q}(t)dt = \mathcal{Q}_0$. This is true for small amplitudes of η_1 compared to $\overline{p}$, which is a reasonable assumption. Indeed, if $\eta_1(t) = p_0\cos(\omega_1 t)$, $\epsilon = \cos(\pi y/l)p_0/\overline{p}$,

$$\frac{1}{T}\int_0^T \mathcal{Q}_0\sqrt{1+\epsilon\cos(\omega_1 t)}dt \simeq \mathcal{Q}_0 + \frac{\epsilon}{2}\frac{\mathcal{Q}_0}{T}\int_0^T \cos(\omega_1 t)dt \simeq \mathcal{Q}_0.$$

An expression for the heat release is deduced:

$$\dot{q}(\boldsymbol{x},t) = \frac{\mathcal{Q}_0}{L_f}\sqrt{1+\frac{\eta_1(t)}{\overline{p}}\cos(\frac{\pi}{l}y)}\delta(y-y(t))\delta(z-z_0). \tag{4.41}$$

This equation is injected in the balance equation of pressure and projected on the eigenmodes yielding:

$$\begin{aligned}
\ddot{\eta_1}+\omega_1^2\eta_1 &= \frac{\gamma-1}{\Lambda_1}\iiint\frac{\partial\dot{q}'}{\partial t}\cos(\frac{\pi}{l}y)dxdydz,\\
&= 2\frac{\gamma-1}{hLl}\int_0^l\frac{\partial}{\partial t}\left[\mathcal{Q}_0\sqrt{1+\frac{\eta_1(t)}{\overline{p}}\cos(\frac{\pi}{l}y)}\delta(y-y(t))\right]\cos(\frac{\pi}{l}y)dy,\\
&= 2\frac{\gamma-1}{hLl}\mathcal{Q}_0\int_0^l\Bigg[\underbrace{\frac{\cos(\frac{\pi}{l}y)/\overline{p}}{2\sqrt{1+\frac{\eta_1(t)}{\overline{p}}\cos(\frac{\pi}{l}y)}}\dot{\eta}_1\delta(y-y(t))}_{A} -\\
&\underbrace{\sqrt{1+\frac{\eta_1(t)}{\overline{p}}\cos(\frac{\pi}{l}y)}\dot{\delta}(y-y(t))\dot{y}(t)}_{B}\Bigg]\cos(\frac{\pi}{l}y)dy,
\end{aligned} \tag{4.42}$$

The derivative of the delta function $\dot{\delta}$ is defined by:

$$\int_{-\infty}^{\infty}\dot{\delta}(x)f(x)dx = -\dot{f}(0).$$

The term B is then calculated by differentiation in the y coordinate:

$$\frac{\partial}{\partial y}\left(\sqrt{1+\frac{\eta_1(t)}{\overline{p}}\cos(\frac{\pi}{l}y)}\cos(\frac{\pi}{l}y)\right) = \frac{1}{2\sqrt{1+\frac{\eta_1(t)}{\overline{p}}\cos(\frac{\pi}{l}y)}}\frac{-\pi}{l}\frac{\eta_1}{\overline{p}}\sin(\frac{\pi}{l}y)\cos(\frac{\pi}{l}y) + \sqrt{1+\frac{\eta_1(t)}{\overline{p}}\cos(\frac{\pi}{l}y)}\frac{-\pi}{l}\sin(\frac{\pi}{l}y). \tag{4.43}$$

Combining eq. 4.42 and eq. 4.43, and after some manipulations, one obtains the following relation:

$$\ddot{\eta_1}+\omega_1^2\eta_1 = 2\frac{\gamma-1}{hLl}\mathcal{Q}_0\frac{\dot{\eta}_1}{\overline{p}\gamma}\frac{1}{\sqrt{1+\frac{\eta_1(t)}{\overline{p}}\cos(\frac{\pi}{l}y)}} \times\left[\sin^2(\frac{\pi}{l}y(t))\left(1+\frac{3}{2}\frac{\eta_1}{\overline{p}}\cos(\frac{\pi}{l}y(t))\right)+\frac{\gamma}{2}\cos^2(\frac{\pi}{l}y(t))\right] \tag{4.44}$$

where $y(t)$ is already given by: $y(t)=\frac{2l}{\pi}\arctan(\tan(\frac{\pi y_0}{2l})\exp(\frac{-\eta_1(t)}{\overline{p}\gamma}))$.
It is interesting to compare Eq. 4.44 to the expression obtained previously in the absence of pressure effect on the heat release rate:

$$\ddot{\eta_1}+\omega_1^2\eta_1 = 2\frac{\gamma-1}{hLl}\mathcal{Q}_0\frac{\dot{\eta}_1}{\overline{p}\gamma}\sin^2(\frac{\pi}{l}y(t)) \tag{4.45}$$

If one simplifies eq. 4.44, by considering that $\eta_1/\overline{p}$ is relatively small, one obtains a sum of two terms. The first evolves like $\sin^2$, and corresponds to the initial model of flame displacement. Since the flame motion has the largest amplitude near the chamber center plane at the velocity antinode, its contribution is maximum when y_0 is close to the center of the chamber ($y_0 = l/2$). The second term, in $\gamma/2\cos^2$, is the contribution of the fluctuating pressure. This term has the same order of magnitude as the first term, but its distribution is different.

The contribution of the second term is predominant near the pressure antinode, i.e. in the vicinity of the lateral boundaries, and is weak in the center of the chamber. This explains why the present experimental program could not highlight this mechanism. It is shown in what follows that in the MIC configuration this effect only slightly modifies the growth rate.
Fig. 4.9 (a) shows the growth factor depending on the position of the injector on the injection plane for the initial FAME and for the extended FAME including the effect of pressure on heat release. This shows that when injectors

are gathered near the centerline, the two models give similar results. The calculated growth factor obtained by summing the contribution of each injector, is 26.2 s^{-1}, which is close to the previous value 24.5 s^{-1}. The growth factor obtained from the differential equation,

$$\alpha_1 = \frac{\gamma-1}{hLl}\mathcal{Q}_0\frac{\dot{\eta}_1}{\overline{p}\gamma}\frac{1}{\sqrt{1+\frac{\eta_1(t)}{\overline{p}}\cos(\frac{\pi}{l}y)}}$$
$$\times\left[\sin^2(\frac{\pi}{l}y(t))\left(1+\frac{3}{2}\frac{\eta_1}{\overline{p}}\cos(\frac{\pi}{l}y(t))\right)+\frac{\gamma}{2}\cos^2(\frac{\pi}{l}y(t))\right], \tag{4.46}$$

plotted in Fig. 4.9 (b), provides the same value.

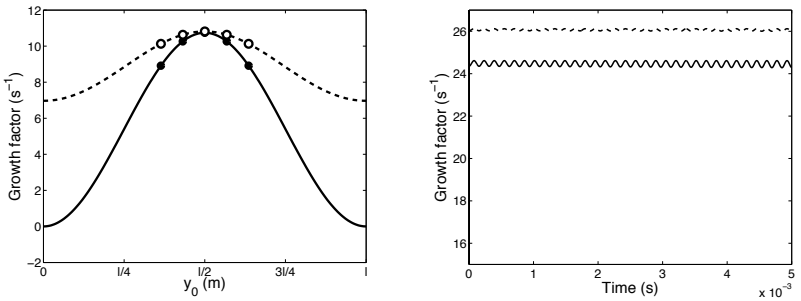

(a) (b)

Figure 4.9: *(a) - Value of the growth factor depending on the position y_0 of the injector on the injection plane. The initial model which does not account for the effect of pressure corresponds to the solid line. The extension is shown as dashed line. The two models differ near the combustor walls - (b) Growth factor obtained by solving eq. 4.46.*

In contrast, when injectors are located near the chamber walls, the situation is reversed. This is exemplified in Fig. 4.10 which shows what would happen if the five injectors were equally distributed in the injection plane. The growth factor would shift from 13.5 $s^{-1}$with FAME to more than 22 $s^{-1}$with extended FAME. This indicates that the extension of the model is important to account for pressure effects.

4.4.3 Evaluation of a rocket engine growth factor

In previous sections, it is shown that FAME model predicts a growth factor of 26.2 s^{-1}in the MIC. It is interesting to have a rough idea of what is expected in a real rocket engine when an initial perturbation generates a coherent acoustic wave. The following equations give an estimate, and a more accurate investi-

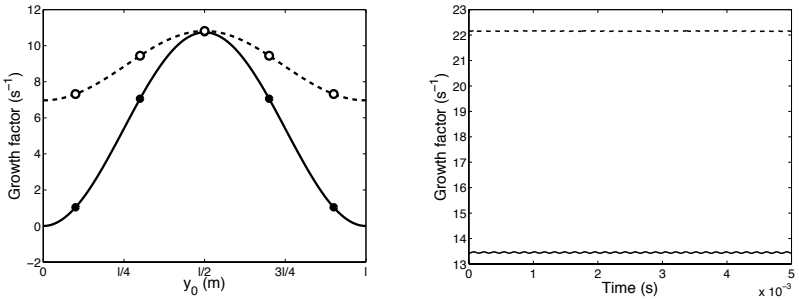

(a) (b)

Figure 4.10: *(a) - Growth factor value depending on the position y_0 of the injectors in the injection plane. The model which does not account for the effect of pressure corresponds to the solid line. The extension is shown with the dashed line. The two models differ near the walls - (b) Growth factor obtained by solving eq. 4.46.*

gation will be carried out in the next chapter (section 5.8).

If we consider that the ratio $\eta_1/\overline{p}$ is small, then $y(t) \approx y_0$ and the growth factor for one injector reads:

$$\alpha_1^n = \frac{\gamma - 1}{\gamma \overline{p}} \frac{\mathcal{Q}_0}{hLl} f(y_0^n), \tag{4.47}$$

where $f(y_0^n) = \sin^2(\frac{\pi}{l} y_0^n) + \frac{\gamma}{2} \cos^2(\frac{\pi}{l} y_0^n)$. Since $\mathcal{Q}_0 = \dot{m}_{LOx}^i \Delta h_{LOx}$ for an injector, the growth factor can also be written:

$$\alpha_1^n = \frac{\gamma - 1}{c^2} \frac{\dot{m}_{LOx}^n \Delta h_{LOx}}{\overline{\rho} V} f(y_0^n). \tag{4.48}$$

If one now considers, as a simplifying assumption, that $f(y_0^n) \approx 1$, the total growth rate is:

$$\alpha_1 = \sum \alpha_1^n, \tag{4.49}$$

$$= \frac{\gamma - 1}{c^2} \frac{\Delta h_{LOx}}{\tau}, \tag{4.50}$$

with $\tau = M/\dot{m}_{LOx}^{tot}$, where M is the mass in the chamber ($M = \overline{\rho} V$). The variable τ stands for the residence time in the chamber. This term characterizes the possible growth rate. More precisely, this provides an upper bound for two reasons. First, $f(y_0^n)$ is actually smaller than one, and second, it is probable that flames do not exactly follow the acoustic field.

For the MIC,

$$\tau = \frac{M}{\dot{m}_{LOx}^{tot}} = \frac{(4.28 \times 4.4)10^{-3}}{0.1} = 188\ 10^{-3} s,$$

which leads to the growth rate:

$$\alpha_1 = 26.5\ s^{-1}.$$

This is consistent with previous estimations.
We consider now the Vulcain 2, main engine of the european rocket Ariane V. The mass flow rate of oxygen injected is $\dot{m}_{LOx} = 250$ kg s^{-1}. At a nominal pressure of 10 MPa, $\overline{\rho} \approx 16$ kg m^{-3}, and the volume of the chamber is approximately 40 liters. The residence time is then:

$$\tau = 3.2\ 10^{-3} s.$$

The growth factor is estimated by eq. 4.49:

$$\alpha_1 \approx 4700\ s^{-1}.$$

This value is significantly greater than the one found for the MIC, which would explain why this kind of instabilities are more likely to appear when the power density is high.

4.4.4 The role of hydrodynamic instabilities

The unified framework exploited in the previous sections may also be adopted to understand one of the possible mechanisms responsible for the growth of transverse combustion instabilities. In the previous sections, the flame was represented by a thin sheet set in motion by the acoustic field. An initial perturbation is implicitly assumed. This description is valid when pressure and heat release fluctuations caused by the flames themselves are negligible compared to the fluctuations of the acoustic field.
By comparing the natural frequency of the liquid jet characterized by the Strouhal number and the first transverse mode of the cavity, it has been noticed in several experimental and numerical studies that instabilities can be triggered when the two frequencies match.
The previous set of equations can still be used, but this time without assuming any preexisting acoustic field at the initial instant. Now, one possible source term is due to the oscillations of heat release created by the shear layer instability. To put this in the simplest form, one may assume that the flame position is defined by a single coordinate $y(t)$. It is a strong assumption but the aim of this short analysis is mainly to explore a potential coupling. The heat release is written:

$$\dot{q}'(\boldsymbol{x},t) = \frac{\mathcal{Q}}{L_f}\left(\delta(y-y(t))\delta(z-z_0) - \frac{1}{T}\int_0^T \delta(y-y(t))\delta(z-z_0)dt\right), \quad (4.51)$$

where $y(t)$ is a function of the Strouhal number. The frequency of the jet is:

$$f_c = \frac{u\mathrm{St}_c}{D}, \quad (4.52)$$

where u is a characteristic velocity of the fluid system, D the diameter of the liquid jet and St_c is the characteristic Strouhal number. In the case of wakes behind various types of bluff bodies, Ongoren and Rockwell (1988) indicate that the characteristic Strouhal number is 0.194. The motion of the flame $y(t)$ is then assumed to have the form:

$$y(t) = y_0(1 + \frac{\epsilon}{y_0}\cos(\omega_c t)), \quad (4.53)$$

which indicates that the flame oscillates as a sinusoidal wave around its mean position y_0 with a small amplitude ϵ and with an angular frequency $\omega_c = 2\pi u\mathrm{St}_c/D$. This expression can be projected on the eigenmodes of the system. Considering the first transverse mode only one obtains:

$$\ddot{\eta}_1 + \omega_1^2\eta_1 = -2\frac{\gamma-1}{l}\mathcal{Q}\dot{y}(t)\frac{\pi}{l}\sin(\frac{\pi}{l}y(t)) \quad (4.54)$$

This expression becomes

$$\ddot{\eta}_1 + \omega_1^2\eta_1 = 2\frac{\gamma-1}{l}\mathcal{Q}\epsilon\omega_c\sin(\omega_c t)\frac{\pi}{l}\sin(\frac{\pi}{l}y_0(1+\frac{\epsilon}{y_0}\cos(\omega_c t))). \quad (4.55)$$

Since ϵ is small, the last expression can be simplified:

$$\ddot{\eta}_1 + \omega_1^2\eta_1 = \underbrace{\left(2\pi\frac{\gamma-1}{l^2}\mathcal{Q}\epsilon\omega_c\sin(\frac{\pi}{l}y_0)\right)}_{\text{Constant}}\sin(\omega_c t), \quad (4.56)$$

which is a second order differential equation with a sinusoidal forcing. Solutions of the homogeneous equation vanish and the stationary solution which remains reads:

$$\eta_1^S = \frac{2\pi\frac{\gamma-1}{l^2}\mathcal{Q}\epsilon\omega_c\sin(\frac{\pi}{l}y_0)}{\omega_1^2-\omega_c^2}\sin(\omega_c t). \quad (4.57)$$

Clearly, the amplitude is augmented when the characteristic hydrodynamic frequency of the fluid system and the first transverse mode frequency get close. This is in agreement with observations.

The mechanism is then the following: when there is no initial perturbation, the hydrodynamic frequency of the fluid system creates a source term in the acoustic energy equation of the chamber. The response of the chamber is strong if the frequency of the flow is close to one of the eigenfrequencies of the chamber. If the acoustic field reaches a certain amplitude, the complete flame collection is set in motion by the acoustic field, as described in the first subsection.
This mechanism may be investigated in further detail by making use of large eddy simulations to get insight in the possible coupling between the natural instabilities of the flow and external acoustic modes.

4.4.5 Influence of initial conditions

The precise influence of initial conditions, perturbations, and damping is addressed in the next chapter. In this subsection, we only intend to illustrate an important feature of the FAME formulation. It is shown here that this model is not suitable for predicting the instability triggering. The analysis starts from the evolution equation for pressure which can be written in the form:

$$\begin{aligned} \ddot{\eta_1} + \omega_1^2 \eta_1 = \frac{\gamma-1}{\Lambda_1} \mathcal{Q}_0 \frac{\dot{\eta_1}}{\overline{p}\gamma} \sum_{n=1}^{N} \frac{1}{\sqrt{1+\frac{\eta_1}{\overline{p}}\cos(\frac{\pi}{l}y^n(t))}} \\ \times \left[\sin^2(\frac{\pi}{l}y^n(t)) \left(1 + \frac{3}{2}\frac{\eta_1}{\overline{p}}\cos(\frac{\pi}{l}y^n(t))\right) + \frac{\gamma}{2}\cos^2(\frac{\pi}{l}y^n(t)) \right], \end{aligned} \tag{4.58}$$

where y^n is given by: $y^n(t) = \frac{2l}{\pi}\arctan(\tan(\frac{\pi y_0^n}{2l})\exp(\frac{-\eta_1(t)}{\overline{p}\gamma}))$ and y_0^n is the n-th injector position.

If $\eta_1/\overline{p}$ is small, which is a reasonable assumption at the beginning of an instability, $y^n(t) \approx y_0^n$ and

$$\ddot{\eta_1} + \omega_1^2 \eta_1 = \frac{\gamma-1}{\Lambda_1} \mathcal{Q}_0 \frac{\dot{\eta_1}}{\overline{p}\gamma} \sum_{n=1}^{N} \left[\sin^2(\frac{\pi}{l}y_0^n) + \frac{\gamma}{2}\cos^2(\frac{\pi}{l}y_0^n(t)) \right], \tag{4.59}$$

$$= C\dot{\eta_1}, \tag{4.60}$$

where C is a constant which depends on geometry, mean chamber pressure, heat release per flame, and injectors positions.

In instability studies, damping is usually modeled by a first order term:

$$\ddot{\eta_1} + 2\xi_1\omega_1\dot{\eta_1} + \omega_1^2\eta_1 = C\dot{\eta_1}, \tag{4.61}$$

which can be written

$$\ddot{\eta_1} + (2\xi_1\omega_1 - C)\dot{\eta_1} + \omega_1^2\eta_1 = 0, \tag{4.62}$$

This equation shows that, with this formulation, the stability of the system does not depend on initial conditions. Even if an important over-pressure in a section of the chamber is assumed, the only parameter that defines stability is the level of damping in the cavity. The physical explanation is that the main cause of triggering, identified in the experimental results, is not considered in the present model which does not account for a modification of the liquid jet when it is submitted to perturbations. This creates smaller droplets that follow the acoustic field more closely. Another formulation is needed to take into account the liquid phase. This is developed in the following section.

4.5 Spray dynamics modeling (SDM)

4.5.1 Introduction

The FAME model derived previously serves to identify a new source term in the acoustic balance equation. This contribution to the Rayleigh term is found by considering the flame motion and deducing the resulting heat release fluctuation. The model does not account for the liquid oxygen dynamics. The flame keeps its shape and spatial structure, both of which are the result of complex atomisation, vaporisation and mixing processes. The purpose of the present analysis is to bring forth theoretical tools to model these phenomena.
The present development relies on the same reasoning as before, except that the liquid jet and resulting spray are introduced. The acoustic field is responsible for the transverse motion of the jet. Consequently, the heat release associated with the moving flames oscillates in the transverse direction and this in turn creates the source term in the acoustic balance equation.
The inclusion of the liquid phase in the model raises several new challenges. First, liquid droplets have an inertia which depends on their mass and they no longer follow the acoustic field. This introduces a delay associated to momentum relaxation. Secondly, droplets have a spatial density distribution which strongly influences the local heat release rates. It is then more convenient to treat the problem in an eulerian framework, which changes the formalism compared to the previous model. This also limits the study to a small perturbation analysis.

Hypotheses

The main hypotheses of the low-order model developed in this section are as follows:

- The temperature field in the chamber is uniform. Temperature non-uniformity can be handled in the determination of eigenmodes. This is achieved by solving a modified Helmholtz equation in which the square of the sound velocity appears inside the divergence operator ($\boldsymbol{\nabla} \cdot c^2 \boldsymbol{\nabla} \Psi + \omega^2 \Psi = 0$). The eigenmode orthogonality is still verified for Neumann or Dirichlet boundary conditions.

- The mean flow velocities are not considered. This assumption is adequate for the liquid stream which is injected at low speed. It is less suitable for the gaseous stream which enters the chamber at very high speed. It will be used in what follows because it brings notable simplifications to the analysis.

- The density and velocity fluctuations are small enough to allow linearization.

- The result of the atomization process is a set of droplets of approximately the same size (monodisperse spray). As a result, the evaporation rate is proportional to the local density of droplets.

- Combustion occurs instantaneously after vaporization. Oxygen, the limiting reactant, is only present in liquid form.

4.5.2 Liquid droplets and spray dynamics

The balance equations for mass and momentum for the liquid phase can be written in the form:

$$\frac{\partial \rho_{LOx}}{\partial t} + \boldsymbol{\nabla} \cdot (\rho_{LOx} \boldsymbol{u}_{LOx}) = 0, \tag{4.63}$$

$$\frac{\partial}{\partial t}(\rho_{LOx} u_{LOx}) + \boldsymbol{\nabla} \cdot (\rho_{LOx} \boldsymbol{u}_{LOx} \boldsymbol{u}_{LOx}) = \rho_{LOx}(\frac{\boldsymbol{u}_g - \boldsymbol{u}_{LOx}}{\tau_p}), \tag{4.64}$$

where τ_p is the Stokes relaxation time, linked to the momentum exchange between the droplet spray and the gas stream, ρ_{LOx} designates the partial density of liquid oxygen (the mass of liquid oxygen per unit volume).
It is convenient to describe the gas phase dynamics with a linearized momentum equation and with a balance of mass with a source term. (This last equation is obtained by combining the standard mass balance with the energy equation written for the entropy fluctuation):

$$\overline{\rho_g} \frac{\partial \boldsymbol{u}'_g}{\partial t} + \boldsymbol{\nabla} p'_g = 0, \tag{4.65}$$

$$\frac{1}{c^2} \frac{\partial p'_g}{\partial t} + \overline{\rho_g} \boldsymbol{\nabla} \cdot u'_g = \frac{\gamma - 1}{c^2} \dot{q}'. \tag{4.66}$$

In these expressions the subscript g designates the gas phase. The liquid oxygen partial density and velocity are decomposed in a mean value and a fluctuation: $\rho_{LOx}(\boldsymbol{x},t) = \overline{\rho_{LOx}}(\boldsymbol{x}) + \rho'_{LOx}(\boldsymbol{x},t)$, with $\overline{\rho_{LOx}}(\boldsymbol{x}) = (1/T)\int_0^T \rho_{LOx}(\boldsymbol{x},t)dT$, and $\boldsymbol{u}_{LOx} = \boldsymbol{u}'_{LOx}$. This leads to the system

$$\frac{\partial \rho'_{LOx}}{\partial t} + \boldsymbol{\nabla}\cdot(\overline{\rho_{LOx}}(\boldsymbol{x})\boldsymbol{u}'_{LOx}) = 0, \tag{4.67}$$

$$\frac{\partial \boldsymbol{u}'_{LOx}}{\partial t} + \frac{\boldsymbol{u}'_{LOx}}{\tau_p} = \frac{\boldsymbol{u}'_g}{\tau_p}. \tag{4.68}$$

Eq. 4.68 can be seen as a first order differential equation with a forcing term $(\boldsymbol{u}'_g/\tau_p)$. If the acoustic field is known, the spatial distribution of droplets can be deduced from this equation. The solution of the homogeneous equation is $\boldsymbol{u}'^H_{LOx} = \boldsymbol{A}(\boldsymbol{x})e^{-t/\tau_p}$, and the final expression, obtained with the method of variation of parameters takes the form:

$$\boldsymbol{u}'_{LOx}(\boldsymbol{x},t) = \boldsymbol{A}(\boldsymbol{x})e^{-t/\tau_p} + \int \frac{\boldsymbol{u}'_g(\boldsymbol{x},t')}{\tau_p} e^{t'/\tau_p} dt' e^{-t/\tau_p}. \tag{4.69}$$

To obtain an expression for the unsteady heat release, it is convenient to assume that the acoustic field is known and that its amplitude is fixed. This hypothesis is not so strong, because the response of heat release to the acoustic field occurs within a couple of periods and during this short time the modal amplitude can be considered to be constant. In other words one assumes that the unsteady pressure field amplitude varies slowly.
The pressure field expansion

$$p'_g(\boldsymbol{x},t) = \sum_{m=0}^{\infty} \eta_m(t)\Psi_m(\boldsymbol{x}) \tag{4.70}$$

is then written

$$p'_g(\boldsymbol{x},t) = \sum_{m=0}^{\infty} p_0^m \cos(\omega_m t)\Psi_m(\boldsymbol{x}), \tag{4.71}$$

where p_0^m is the amplitude of the acoustic pressure component corresponding to the m-th mode. The velocity field is then given by:

$$\boldsymbol{u}'_g(\boldsymbol{x},t) = \sum_m \frac{p_0^m}{(\overline{\rho_g}\omega_m)} \sin(\omega_m t)\boldsymbol{\nabla}\Psi_m(\boldsymbol{x}). \tag{4.72}$$

This expression can then be inserted in (4.69) to obtain after some algebra:

$$\boldsymbol{u}'_{LOx}(\boldsymbol{x},t) = \boldsymbol{A}(\boldsymbol{x})e^{-t/\tau_p} + \sum_{m=1}^{\infty} \frac{p_0^m}{\overline{\rho_g}\omega_m} \frac{1}{\sqrt{1+(\omega_m\tau_p)^2}} \times \sin[\omega_m t - \arctan(\omega_m\tau_p)]\boldsymbol{\nabla}\Psi_m(\boldsymbol{x}). \tag{4.73}$$

One may then use Eq. 4.67 to deduce ρ'_{LOx}. After a time integration, one finds:

$$\begin{aligned}\rho'_{LOx}(\boldsymbol{x},t) &= B(\boldsymbol{x}) + \overline{\rho_{LOx}}(\boldsymbol{x})\tau_p \boldsymbol{\nabla}\cdot\boldsymbol{A}(\boldsymbol{x})e^{-t/\tau_p} \\ &\quad - \sum_{m=1}^{\infty} \frac{p_0^m}{\overline{\rho_g}\omega_m^2\sqrt{1+(\omega_m\tau_p)^2}}\cos[\omega_m t - \arctan(\omega_m\tau_p)] \\ &\quad \times \left(\boldsymbol{\nabla}\overline{\rho_{LOx}}\cdot\boldsymbol{\nabla}\Psi_m + \overline{\rho_{LOx}}\boldsymbol{\nabla}^2\Psi_m\right). \end{aligned} \tag{4.74}$$

In the steady state regime, and recalling that Ψ_m is a solution of a Helmholtz equation, the droplet density field can be written in the form:

$$\begin{aligned}\rho'_{LOx}(\boldsymbol{x},t) &= \sum_{m=1}^{\infty} \frac{p_0^m}{\overline{\rho_g}\omega_m^2\sqrt{1+(\omega_m\tau_p)^2}}\cos(\omega_m(t-\tau_a^m)) \\ &\quad \left(\frac{\omega_m^2}{c^2}\overline{\rho_{LOx}}\Psi_m - \boldsymbol{\nabla}\overline{\rho_{LOx}}\cdot\boldsymbol{\nabla}\Psi_m\right), \end{aligned} \tag{4.75}$$

where $\tau_a^m = \arctan(\omega_m\tau_p)/\omega_m$. In the previous derivation, the pressure amplitude was assumed to be constant. It is however possible to consider that it is a slowly varying function, recall that $p_0^m\cos(\omega_m t)$ was used in place of $\eta_m(t)$ and change $p_0^m\cos(\omega_m(t-\tau_a^m))$ into $\eta_m(t-\tau_a^m)$. The result of this derivation takes the form:

$$\rho'_{LOx}(\boldsymbol{x},t) = \sum_{m=1}^{\infty} \frac{\eta_m(t-\tau_a^m)}{\overline{\rho_g}\omega_m^2\sqrt{1+(\omega_m\tau_p)^2}}\left(\frac{\omega_m^2}{c^2}\overline{\rho_{LOx}}\Psi_m - \boldsymbol{\nabla}\overline{\rho_{LOx}}\cdot\boldsymbol{\nabla}\Psi_m\right). \tag{4.76}$$

It is interesting to simplify this expression by considering that the density field is uniform and that a single mode dominates the pressure field expansion. In that case the liquid oxygen density fluctuation is given by

$$\rho'_{LOx}(\boldsymbol{x},t) = \frac{\overline{\rho_{LOx}}}{\overline{\rho_g}c^2\sqrt{1+(\omega_m\tau_p)^2}}p'_g(\boldsymbol{x},t-\tau_a). \tag{4.77}$$

This indicates that the fluctuation in liquid oxygen partial density is proportional to a delayed value of the local pressure disturbance. Taking into account the spray naturally introduces a delay in the equations.

4.5.3 An estimate of the unsteady heat release

It is now possible to estimate the unsteady heat release rate. For this we use as a starting point expression (4.77) for the liquid oxygen density. In general the local heat release rate is given by

$$\dot{q} = -\sum_k \Delta h_{f,k}^0 \dot{\omega}_k, \tag{4.78}$$

where $\Delta h^0_{f,k}$ is the formation enthalpy for species k. Oxygen being the limiting reactant, one can write: $\dot{\omega}_k = (W_k\nu_k)/(W_{O_2}\nu_{O_2})\dot{\omega}_{O_2}$, where W_k is the molar mass of species k and ν_k the stoichiometric coefficients in the global balance equation:

$$CH4 + 2O_2 \rightarrow CO_2 + 2H_2O. \tag{4.79}$$

This leads to:

$$\dot{q} = (-\frac{11}{16}\Delta h^0_{f,CO_2} - \frac{9}{16}\Delta h^0_{f,H_2O} + \frac{1}{4}\Delta h^0_{f,CH_4} + \Delta h^0_{f,O_2})\dot{\omega}_{O_2}, \tag{4.80}$$

$$\dot{q} = \Delta h_T \dot{\omega}_{O_2}. \tag{4.81}$$

From the assumption that evaporated oxygen is instantaneously converted into products it is possible to write:

$$\dot{\omega}_{O_2}(\boldsymbol{x}, t) = -\dot{\Omega}_{O_2}(\boldsymbol{x}, t), \tag{4.82}$$

where $\dot{\Omega}_{O_2}(\boldsymbol{x}, t)$ corresponds to the mass of liquid oxygen which is evaporated per unit volume and time. This expression can be evaluated by first examining the evaporation of a single droplet and in a second step by extending this expression to a spray.

Vaporization of a single spherical droplet

For an isolated droplet, $m_d = (1/6)\rho_l \pi d^3$, where ρ_l is the density of liquid oxygen ($\rho_l \simeq 1190$ kg/m^3). It is convenient to assume that vaporization follows the d^2 law: $d^2 = d_0^2 - Kt$ where d_0 is the initial diameter of the droplet and K is the vaporization constant. K is a function of several parameters and its determination will be discussed later. The mass rate of evaporation can be obtained by differentiating the mass of the droplet and using the rate of change of the droplet diameter. This yields:

$$\dot{m}_d = \rho_l \frac{\pi}{6}\frac{d}{dt}(d_0^2 - Kt)^{\frac{3}{2}}, \tag{4.83}$$

$$= -K\rho_l \frac{\pi}{4} d. \tag{4.84}$$

Spray vaporization

The spray evaporation rate can be deduced from the previous rate by multiplying by the droplet number density n_{O_2} (number of droplets per unit volume). In doing so, one implicitely assumes that droplet evaporation takes place as if all droplets were isolated. This assumption is clearly an approximation but is used here for its simplicity. The mass flow rate per unit volume of gaseous oxygen generated by the spray becomes:

$$\dot{\Omega}_{O_2} = n_{O_2}\dot{m}_d \tag{4.85}$$
$$\dot{\Omega}_{O_2} = -Kn_{O_2}\rho_l\frac{\pi}{4}d. \tag{4.86}$$

It is now interesting to use the partial density of liquid oxygen:

$$\rho_{LOx} = n_{O_2}\rho_l\frac{\pi d^3}{6}, \tag{4.87}$$

and introduce this expression in the mass rate of oxygen per unit volume:

$$\dot{\Omega}_{O_2} = -\frac{3}{2}K\frac{\rho_{LOx}}{d^2}. \tag{4.88}$$

Unsteady heat release
An expression for the unsteady heat release rate per unit volume is then easily deduced from the previous result:

$$\dot{q}' = \Delta h_T\frac{3}{2}K\frac{\rho'_{LOx}}{d^2}. \tag{4.89}$$

4.5.4 Unsteady pressure dynamics

It is now possible to gather the previous results and deduce an equation for the unsteady pressure amplitude. This is done by successively assuming that the steady state distribution of liquid oxygen is uniform and by considering in a second step that there are non-uniformities in this distribution.

Uniform distribution of liquid oxygen
For a single mode one may use eq. 4.77 to get the following expression for the unsteady heat release rate

$$\dot{q}'(\boldsymbol{x},t) = \Delta h_T\frac{3}{2}\frac{K}{d^2}\frac{\overline{\rho_{LOx}}}{\overline{\rho_g}c^2\sqrt{1+(\omega\tau_p)^2}}p'_g(\boldsymbol{x},t-\tau_a^m). \tag{4.90}$$

This expression indicates that $\dot{q}'$ is proportional to the the pressure perturbation taken at a time $t-(\arctan(\omega\tau_p)/\omega)$. From this equation, it is straightforward to obtain the differential equation which governs the evolution of pressure.

In a more general case where the pressure field is formed by a combination of modes, one may start with the general form (4.76) and deduce the following expression of $\dot{q}'$

$$\dot{q}'(\boldsymbol{x},t) = \Delta h_T\frac{3}{2}\frac{K}{d^2}\frac{\overline{\rho_{LOx}}}{\overline{p}\gamma}\sum_{m=0}^{+\infty}\frac{1}{\sqrt{1+(\omega_m\tau_p)^2}}\eta_m(t-\tau_a^m)\Psi_m(\boldsymbol{x}), \tag{4.91}$$

This yields the following dynamical equations for the pressure amplitudes (using eq. 4.23):

$$\ddot{\eta}_m + \omega_m^2 \eta_m = \overline{\rho_{LOx}} \frac{\gamma - 1}{\overline{p}\gamma} \Delta h_T \frac{3}{2} \frac{K}{d^2} \frac{1}{\sqrt{1 + (\omega_m \tau_p)^2}} \dot{\eta}_m (t - \tau_a^m). \tag{4.92}$$

Non-uniform distribution of liquid oxygen

When the steady state distribution of liquid oxygen is not uniform one has to start from eq. 4.76. The following expression for the nonsteady heat release rate can be derived:

$$\dot{q}'(\boldsymbol{x}, t) = \Delta h_T \frac{3}{2} \frac{K}{d^2} \sum_{m=1}^{\infty} \frac{\eta_m (t - \tau_a^m)}{\overline{\rho_g} \omega_m^2 \sqrt{1 + (\omega_m \tau_p)^2}} \left(\frac{\omega_m^2}{c^2} \overline{\rho_{LOx}} \Psi_m - \boldsymbol{\nabla} \overline{\rho_{LOx}} \cdot \boldsymbol{\nabla} \Psi_m \right) \tag{4.93}$$

This yields the dynamical equation for the m^{th} component of the pressure by projecting over the modal basis:

$$\begin{aligned} \ddot{\eta}_m + \omega_m^2 \eta_m &= \frac{\gamma - 1}{\overline{\rho_g} \omega_m^2} \Delta h_T \frac{3}{2} \frac{K}{d^2} \frac{\dot{\eta}_m (t - \tau_a^m)}{\sqrt{1 + (\omega_m \tau_p)^2}} \\ &\quad \times \frac{1}{\Lambda_m} \underbrace{\int_V \frac{\omega_m^2}{c^2} \overline{\rho_{LOx}} \Psi_m^2 - \boldsymbol{\nabla} \overline{\rho_{LOx}} \cdot (\Psi_m \boldsymbol{\nabla} \Psi_m) dV}_{I} . \end{aligned} \tag{4.94}$$

It is interesting to cast the integral I appearing in the previous expression in a simpler form. To do this one can use Green's theorem to replace the second volume integral by a sum of a surface integral and a volume integral. The surface integral is eliminated by applying the homogeneous boundary conditions and the Helmholtz equation is then used to suppress two of the remaining terms. This process leads to:

$$I = \int_V [\frac{\omega_m^2}{c^2} \overline{\rho_{LOx}} \Psi_m^2 - \boldsymbol{\nabla} \overline{\rho_{LOx}} \cdot (\Psi_m \boldsymbol{\nabla} \Psi_m)] dV, \tag{4.95}$$

$$= \int_V \frac{\omega_m^2}{c^2} \overline{\rho_{LOx}} \Psi_m^2 dV - \underbrace{\int_S [\overline{\rho_{LOx}} (\Psi_m \boldsymbol{\nabla} \Psi_m \cdot \boldsymbol{n})] \, dS}_{=0}$$

$$+ \int_V \overline{\rho_{LOx}} \boldsymbol{\nabla} \cdot (\Psi_m \boldsymbol{\nabla} \Psi_m) dV, \tag{4.96}$$

$$= \int_V \frac{\omega_m^2}{c^2} \overline{\rho_{LOx}} \Psi_m^2 dV + \int_V \overline{\rho_{LOx}} (\boldsymbol{\nabla} \Psi_m)^2 dV$$

$$+ \int_V \overline{\rho_{LOx}} \Psi_m \boldsymbol{\nabla}^2 \Psi_m dV, \tag{4.97}$$

$$I = \int_V \overline{\rho_{LOx}} (\boldsymbol{\nabla} \Psi_m)^2 dV \tag{4.98}$$

The last expression for I may now be inserted in eq. 4.94 to get:

$$\ddot{\eta}_m + \omega_m^2 \eta_m = \frac{\gamma - 1}{\overline{\rho_g}\omega_m^2} \Delta h_T \frac{3}{2} \frac{K}{d^2} \frac{\dot{\eta}_m(t - \tau_a^m)}{\sqrt{1 + (\omega_m \tau_p)^2}} \frac{1}{\Lambda_m} \int_V \overline{\rho_{LOx}} (\boldsymbol{\nabla} \Psi_m)^2 dV. \quad (4.99)$$

It is interesting to check whether this expression coincides with that obtained previously when assuming that $\overline{\rho_{LOx}}$ is constant. This is accomplished by noting that

$$\begin{aligned} \frac{1}{\Lambda_m} \int_V \overline{\rho_{LOx}} (\boldsymbol{\nabla} \Psi_m)^2 dV &= \overline{\rho_{LOx}} \frac{1}{\Lambda_m} \int_V (\boldsymbol{\nabla} \Psi_m)^2 dV & (4.100) \\ &= \overline{\rho_{LOx}} \frac{1}{\Lambda_m} [\int_S \Psi_m \boldsymbol{\nabla} \Psi_m \cdot \boldsymbol{n} dS \\ &\quad - \int_V \Psi_m \boldsymbol{\nabla}^2 \Psi_m dV] & (4.101) \end{aligned}$$

Using the homogeneous boundary conditions and the Helmholtz equation one finds that

$$\frac{1}{\Lambda_m} \int_V \overline{\rho_{LOx}} (\boldsymbol{\nabla} \Psi_m)^2 dV = \overline{\rho_{LOx}} \frac{\omega_m^2}{c^2} \quad (4.102)$$

and the result (4.92) obtained in the homogeneous case is retrieved.

4.5.5 Driving mechanism

The set of equations describing the spray response to external pressure perturbations includes the previous relation in combination with expressions for the droplet diameter and partial density of liquid oxygen. The droplet diameter mainly depends on the Weber number which defines the ratio of inertial and surface tension forces. The partial density of oxygen $\overline{\rho_{LOx}}$ mainly depends on momentum exchange between the gaseous and liquid streams and can be linked to the liquid core intact length L_c. This last quantity is mainly determined by a momentum flux ratio. These representations summarized below are discussed

in more detail in the next subsections.

$$\begin{aligned}
\dot{q}'(\boldsymbol{x},t) &= \Delta h_T \frac{3}{2}\frac{K}{\bar{d}^2}\sum_{m=1}^{\infty}\frac{\eta_m(t-\tau_a^m)}{\overline{\rho_g}\omega_m^2\sqrt{1+(\omega_m\tau_p)^2}} \\
&\quad\times\left(\frac{\omega_m^2}{c^2}\overline{\rho_{LOx}}\Psi_m - \boldsymbol{\nabla}\overline{\rho_{LOx}}\boldsymbol{\nabla}\Psi_m\right), \qquad (4.103)\\
\tau_p &= \frac{\rho_l d^2}{18\mu}, \qquad (4.104)\\
\tau_a^m &= \frac{\arctan(\omega_m\tau_p)}{\omega_m}, \qquad (4.105)\\
d &= f(\mathrm{We}_{ac}), \qquad (4.106)\\
L_c &= g(J_{ac}). \qquad (4.107)\\
\overline{\rho_{LOx}} &= h(L_c). \qquad (4.108)
\end{aligned}$$

Acoustic Weber number and momentum flux ratio

The jet break-up and atomization processes giving rise to the spray depends on conditions prevailing in the injection region. In the presence of high amplitude acoustic oscillations this may be described by considering, in addition to the more standard dimensionless groups, a Weber number and a momentum flux ratio based on the acoustic velocity We_{ac} and J_{ac}. Experimental observations indicate that jet break-up and primary atomization (controlled by J) and secondary atomization (controlled by We) are completely modified under an important acoustic modulation, due to the transverse velocity oscillations. At this point it is not necessary to precisely define We_{ac} and J_{ac} and the functional dependencies f and g. The determination of these functions is a difficult process, since even in the absence of modulation there are no general expressions giving the liquid core intact length and droplet mean diameter and the resulting flame length. It is however possible to list some of the features of f and g. Both of these functions are decreasing. When the excitation level is augmented, the droplet size and the flame length diminish. It is also known that there is secondary atomization when the Weber number exceeds a critical value We_c of the order of 10. This can be represented by introducing a discontinuity in f when We_{ac} exceeds this critical threshold. When the acoustic modulation amplitude is large enough, droplets split into smaller droplets.

Stokes relaxation time τ_p

When the droplet size is diminished by secondary atomization the relaxation time is reduced and the phase lag between the pressure field and the droplet motion is reduced. In the limit of very small droplet sizes the time lag τ_p vanishes and $\dot{q}'$ is in phase with p_g' (eq. 4.103). The Rayleigh source term in the balance equation of acoustic energy is positive and energy is added to the

oscillation. This mechanism is the one identified in hot fire tests on the MIC, described in section 3.9.4 and represented schematically in Fig. 3.103.
The previous process begins when the droplets in the spray are divided into smaller entities. This can be caused by different factors. When there is an external modulation induced by the VHAM, the acoustic velocity is large and the droplets are submitted to inertial forces which bring the Weber number above the critical threshold. In real rocket engines submitted to bomb testing, the disturbance associated to the explosion produces a spike in the Weber number inducing secondary atomization. After this droplet subdivision the size is reduced and the oscillation can be enhanced by the Rayleigh source term.

This model solves the problem raised in section 4.4.5 where it was shown that in the FAME formulation, initial conditions had no impact on the stability of the system and that it depended only on the damping coefficient, total heat release of the flame and source terms. In the VHAM experiments, which are carried out in a stable regime (flames alone are insufficient to sustain high acoustic amplitudes), the FAME model could predict the source term associated with the flame motion and the corresponding increase of acoustic pressure amplitude. In a real rocket engine, when no external excitation preexists, the mechanism which triggers the instability, and described above cannot be excluded. The framework described in this section (SDM) accounts for this aspect and is therefore more suitable to describe high frequency rocket engine instabilities.

Mean distribution of liquid oxygen

The spatial distribution of liquid oxygen mean density $\overline{\rho_{LOx}}$ controls the power density in the chamber. In this respect, the Multiple Injector Combustor mounted on the Mascotte test bench features a much lower power density or liquid oxygen mean density than that of a real engine. In the MIC, the chamber comprises five injectors which deliver a mass flow rate of liquid oxygen $\dot{m}_{LOx} = 100$ g s^{-1}. A typical high performance LRE like Vulcain comprises more than 500 injectors operating at a nominal mass flow rate of oxygen $\dot{m}_{LOx} = 250$ kg s^{-1}. A rough estimate of the average liquid oxygen partial densities gives 60 kg m^{-3} in the Vulcain engine and about 2 kg m^{-3} in the MIC. The relatively low value of this quantity explains why the response of the MIC to external modulations remains moderate. The previous estimates were obtained by taking volume averages but it would be more suitable to determine the spatial distribution of this variable $\overline{\rho_{LOx}}(\boldsymbol{x})$ from a simulation. This is however a challenging task which will not be carried out in the present investigation.

4.6 Link between the two models

The FAME and SDM formulations described so far are roughly based on the same assumptions. In both cases, the fluctuations of heat release are due to the convection of the reactants by the acoustic field. Nevertheless, the precise hypotheses and the domain of validity are different. To prove the consistency of these theories, and also to better understand the relevance of each, it is interesting to compare them by taking limits of their respective hypotheses. This will be carried out by two complementary approaches. Briefly, in the first one, a uniform distribution of oxygen is assumed in the chamber. In this case, the idea is to rewrite the FAME model to meet this condition. In the second situation, we consider only one flame modeled by a Dirac distribution of heat release/liquid oxygen density. The idea is here to reformulate the spray model into the FAME model. It is convenient to discuss the details before examining these two limit cases.

The FAME model is written in the particular case of a rectangular box and for the first transverse mode only. The extension of the model (section 4.4.2) is not taken into account in this section, because the effect of strain was not considered in the SDM formulation. The corresponding equation for the spray model is equation 4.99. It is then interesting to write the expression of the first component evolution obtained with the two models:

$$\textbf{FAME:} \quad \ddot{\eta}_1 + \omega_1^2 \eta_1 = \frac{\gamma - 1}{\Lambda_1} \mathcal{Q} \frac{\dot{\eta}_1}{\overline{p}\gamma} \sum_{n=1}^{N} \sin^2\left(\frac{\pi}{l} y^n(t)\right), \tag{4.109}$$

$$\textbf{SDM:} \quad \ddot{\eta}_1 + \omega_1^2 \eta_1 = \frac{\gamma - 1}{\Lambda_1 \overline{p}\gamma} \Delta h_T \frac{3}{2} \frac{K}{d^2} \frac{\dot{\eta}_1(t - \tau_a^m)}{\sqrt{1 + (\omega_1 \tau_p)^2}} \times \iiint \overline{\rho_{LOx}}(\boldsymbol{x}) \sin^2\left(\frac{\pi}{l} y\right) dx dy dz. \tag{4.110}$$

To compare these two models one must first assume that the droplets exactly follow the acoustic field and have no inertia. This implies that $\tau_p = 0$. One can also write that the heat released per unit time in the steady state is equal to the product of the heat released per unit mass by the total mass of oxygen injected per unit time:

$$\mathcal{Q} = \Delta h_T \dot{m}_{LOx},$$

A second assumption is needed with respect to the spatial distribution of the flames. This can be approached in two ways:

- The distribution of liquid oxygen is uniform in the chamber: $\overline{\rho_{LOx}}(\boldsymbol{x}) = \overline{\rho_{LOx}}$. Since there is no representation of oxygen in the FAME model, it corresponds in this case to a uniform distribution of flames. (**A1**)

- Liquid oxygen is localized on the flame centerline and can be modeled by Dirac distributions (**A2**).

These assumptions will be considered independently. Hypothesis (**A1**) is more convenient to use for the spray formulation while (**A2**) is closer to the FAME formulation.

4.6.1 Uniform distribution of liquid oxygen (A1)

Under this assumption one finds a simple expression for the conservation of mass from the injection of liquid oxygen in the chamber to what is evaporated from the droplet:

$$\dot{m}_{LOx} = \dot{\Omega}_{O_2} V, \tag{4.111}$$

where V is the volume of the chamber ($V = lLh$ here). If this is combined with eq. 4.88, it leads to

$$\overline{\rho_{LOx}} = \frac{\dot{m}_{LOx}}{\frac{3}{2}\frac{K}{d^2}V}, \tag{4.112}$$

Moreover, $\mathcal{Q} = \Delta h_T \dot{m}_{LOx}$.
This leads to a new system:

$$\textbf{FAME:} \quad \ddot{\eta}_1 + \omega_1^2 \eta_1 = \frac{\gamma - 1}{\Lambda_1} \mathcal{Q} \frac{\dot{\eta}_1}{\overline{p}\gamma} \sum_{n=1}^{N} \sin^2\left(\frac{\pi}{l} y^n(t)\right), \tag{4.113}$$

$$\textbf{SDM:} \quad \ddot{\eta}_1 + \omega_1^2 \eta_1 = \frac{\gamma - 1}{V} \mathcal{Q} \frac{\dot{\eta}_1(t)}{\overline{p}\gamma}. \tag{4.114}$$

Hypothesis (**A1**) can now be applied to the FAME to unify the two formulations. The discrete notation:

$$\sum_{n=1}^{N} \sin^2\left(\frac{\pi}{l} y^n(t)\right)$$

is replaced by a continuous formulation:

$$I = \frac{1}{l} \int_0^l \sin^2\left(\frac{\pi}{l} y^\alpha(t)\right) d\alpha.$$

If the flames displacement is small with respect to their steady state position, i.e. if they slightly move around their non-excitated position $y(t) \simeq y_0^\alpha$, then

$$I = \frac{1}{l} \int_0^l \sin^2\left(\frac{\pi}{l} y_0^\alpha\right) d\alpha,$$

which leads to

$$I = \frac{1}{2}.$$

Since $\Lambda_1 = V/2$, one retrieves exactly the same expressions from the two models:

$$\ddot{\eta}_1 + \omega_1^2 \eta_1 = \frac{\gamma - 1}{V} \mathcal{Q} \frac{\dot{\eta}_1(t)}{\overline{p}\gamma}.$$

This identity is demonstrated by assuming that in the FAME formulation:

- Flames are uniformly distributed in the combustor
- The flame displacement with respect to the steady state is small.

For the SDM formulation:

- The droplets are small and their momentum relaxation time is negligible
- The rate of evaporation of the liquid droplets is constant.

4.6.2 Dirac distribution of the liquid oxygen (A2)

It is here convenient to consider for simplicity a *single* flame. The distribution of liquid oxygen density $\overline{\rho_{LOx}}$ is now concentrated on a single line

$$\overline{\rho_{LOx}}(\boldsymbol{x}) = \frac{M_{LOx}}{L_c} \delta(y - y_0)\delta(z - z_0),$$

where M_{LOx} is the total mass of liquid oxygen in the chamber and L_c is the length of the liquid core. Hence M_{LOx}/L_c corresponds to a linear distribution of mass density. With these hypotheses, eqs. 4.109 and 4.110 become

$$\textbf{FAME:} \qquad \ddot{\eta}_1 + \omega_1^2 \eta_1 = \frac{\gamma - 1}{\Lambda_1} \mathcal{Q} \frac{\dot{\eta}_1}{\overline{p}\gamma} \sin^2\left(\frac{\pi}{l} y(t)\right), \tag{4.115}$$

$$\textbf{SDM:} \quad \ddot{\eta}_1 + \omega_1^2 \eta_1 = \frac{\gamma - 1}{\Lambda_1 \overline{p}\gamma} \Delta h_T \frac{3}{2} \frac{K}{d^2} \dot{\eta}_1 M_{LOx} \sin^2\left(\frac{\pi}{l} y_0\right). \tag{4.116}$$

In these expressions we have only retained the first transverse mode corresponding to the $\sin^2$ functions appearing in the previous equations. To introduce the link between the total mass and the injected mass flow rate of liquid oxygen, one writes:

$$\dot{m}_{LOx} = \int \dot{\Omega}_{O_2} dV. \tag{4.117}$$

We substitute $\dot{\Omega}_{O_2}$ thanks to eq. 4.88 and we apply the relation:

$$M_{LOx} = \int \overline{\rho_{LOx}}(\boldsymbol{x}) dV. \tag{4.118}$$

Finally, we obtain the relationship:

$$M_{LOx} = \frac{\dot{m}_{LOx}}{\frac{3}{2}\frac{K}{d^2}}. \tag{4.119}$$

Relation $\mathcal{Q} = \Delta h_T \dot{m}_{LOx}$ still holds. This yields the following equations for the two models:

$$\textbf{FAME:} \quad \ddot{\eta}_1 + \omega_1^2 \eta_1 = \frac{\gamma - 1}{\Lambda_1} \mathcal{Q} \frac{\dot{\eta}_1}{\overline{p}\gamma} \sin^2(\frac{\pi}{l} y(t)), \tag{4.120}$$

$$\textbf{SDM:} \quad \ddot{\eta}_1 + \omega_1^2 \eta_1 = \frac{\gamma - 1}{\Lambda_1} \mathcal{Q} \frac{\dot{\eta}_1}{\overline{p}\gamma} \sin^2(\frac{\pi}{l} y_0). \tag{4.121}$$

Considering that the displacement is a small perturbation, one may use: $\sin^2(\frac{\pi}{l} y(t)) \simeq \sin^2(\frac{\pi}{l} y_0)$, and obtain two identical models.

4.7 Asymmetry of the flame pattern under external modulation

Up to now, we have essentially considered that the modes and flame patterns are symmetrical. However, experiments indicate that the signals recorded on the upper and lower walls do not have the same amplitudes and that the flame pattern becomes asymmetric. When this occurs it is also found that the amplitude reaches its highest values. It is also worth recalling that up to a certain level of modulation the flame pattern remains symmetrical. One may then conclude that injection or a bias induced by the rotating wheel are not the main causes of the observed asymmetry. When the flame pattern is notably modified, it is logical to consider that this reflects the asymmetry of the acoustic mode which in turn may be caused by a non-uniform temperature field. This reveals a possible coupling mechanism between the flame shape, the temperature field associated with the flame distribution and the acoustic field.
Experiments indicate that the flame asymmetry and acoustic field asymmetry are jointly present. It is then natural to examine the possible influence of a non-uniformity in the temperature field. To understand the mechanism brought forth in this section, a simple model is implemented. We consider propagation in the transverse direction which can be modeled by considering a one-dimensional cavity with two rigid ends corresponding to the upper and lower walls: $v' = 0$ at $y = -L$ and $y = +L$. In the region $-L < y < 0$, the temperature is fixed at T=1300 K, while in the region $0 < y < L$, the temperature is fixed at T=800 K. Using the classical acoustic equations in these two constant temperature regions and continuity conditions of pressure and volume velocity ($p_1'(0) = p_2'(0)$ and $v_1'(0) = v_2'(0)$) one obtains the dispersion relation:

$$\sin(\frac{\omega}{c_1}L)\cos(\frac{\omega}{c_2}L)c_1 + \sin(\frac{\omega}{c_2}L)\cos(\frac{\omega}{c_1}L)c_2 = 0. \tag{4.122}$$

The first mode is found at $f = 1883$ Hz. The roots of this equation are calculated numerically, and the fields of pressure and velocity are deduced from the relations:

$$p_1'(y) = C\cos(\frac{\omega}{c_1}L)\cos(\frac{\omega}{c_1}(x+L)) \tag{4.123}$$

$$p_2'(y) = C\frac{\cos^2(\frac{\omega}{c_1}L)}{\cos(\frac{\omega}{c_2}L)}\cos(\frac{\omega}{c_2}(x-L)) \tag{4.124}$$

$$v_1'(y) = \frac{C}{\rho_1 c_1}\sin(\frac{\omega}{c_1}L)\sin(\frac{\omega}{c_1}(x+L)) \tag{4.125}$$

$$v_2'(y) = \frac{C}{\rho_2 c_2}\frac{\sin(\frac{\omega}{c_1}L)\cos(\frac{\omega}{c_1}L)}{\cos(\frac{\omega}{c_2}L)}\sin(\frac{\omega}{c_2}(x-L)) \tag{4.126}$$

Fig. 4.11 displays the pressure and velocity fields.

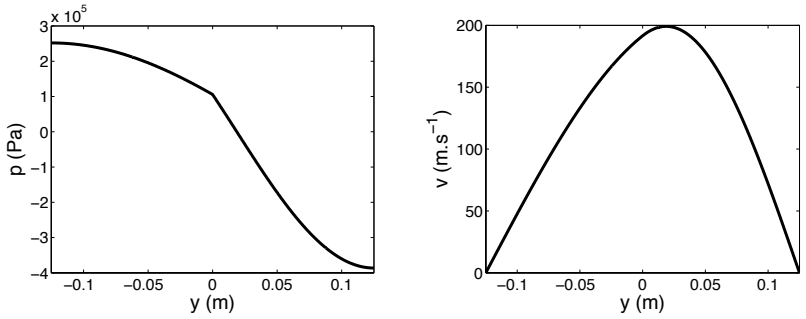

(a) (b)

Figure 4.11: *(a) Spatial distribution of unsteady pressure in a one dimensional cavity with a non-uniform distribution of temperature - (b) Related spatial distribution of velocity*

It is interesting to discuss this figure using the models developed in the previous sections. This study is not completed at this stage, but some interesting features are presented here.

It has been shown that the Rayleigh source term corresponds to the flame motion which is directly linked to the velocity field associated to the acoustic mode. One finds from Fig. 4.11 that in the low temperature region, the amplitude of the pressure field is more important and this is also the case for the velocity field. The source term is then substantially increased in this region. In other words, there are two concurrent effects that enhances the acoustic response in the low temperature region: the pressure oscillation *and* the velocity oscillation

amplitudes are more important. Consequently, for a flame located in the low temperature area, the response term is more important than it would have been for the same flame in a symmetrical situation.
For this remark to be relevant, the comparison must be carried out between two acoustic waves with the same energy. The expression for a symmetrical standing wave is deduced from eq. 4.35:

$$\langle E_1 \rangle(t) = \frac{hLl}{4\overline{p}\gamma} 2p_0^2. \tag{4.127}$$

One must remember that the transverse dimension is $2L$ in this example. A similar expression is obtained using eqs 4.123-4.126. After several manipulations, the expression becomes:

$$\langle E_1 \rangle(t) = \frac{hLl}{4\overline{p}\gamma} p_0^2 \left[1 + \frac{\cos^2(\frac{\omega}{c_1} L)}{\cos^2(\frac{\omega}{c_2} L)} \right]. \tag{4.128}$$

A quantitative study should be undertaken, using this expression for the acoustic energy and adapting the FAME model for an asymmetrical configuration.

4.8 Conclusion

Experimental data obtained on the multiple injector combustor (MIC) are used in this chapter to guide the development of two low order models for the simulation of interactions between acoustic waves and flames in the case of high frequency instabilities. The effect of transverse modes is specifically considered. The unsteady heat release source term appearing in the balance of acoustic energy density is specified explicitly in terms of flow parameters. In the two models, the coupling is caused by the motion associated with the acoustic field. If an acoustic wave preexists in the combustion chamber, flames - or droplets - are displaced by the velocity field. It is shown that the moving regions of heat release acting on a non-uniform pressure field create a Rayleigh term in the balance of acoustic energy. If the flames follow the acoustic field without any time lag, the Rayleigh term is always positive when integrated over a period of oscillation. If a time lag exists between the acoustic wave motion and heat release in the flame (this may be caused for example by momentum relaxation between droplets and the gas stream) a time lag will also appear in the Rayleigh term.

The fairly general conclusions reached from the present analysis seem to have been overlooked in previous investigations of high frequency instabilities coupled by transverse acoustic modes and more generally in studies carried out in laboratory scale combustors. This is probably so because the flame motion

revealed in the present experiments was not often observed in previous studies. Another reason is perhaps that the mechanism is dependent on the energy density in the system. The growth rate is proportional to $\mathcal{Q}/V$ in the FAME formulation or to $\overline{\rho_{LOx}}(\boldsymbol{x})$ the liquid oxygen mean density in the chamber in the SDM formulation. This last quantity is also proportional to the energy density. When a 100 kW flame is submitted to a small amplitude acoustic wave, the source term associated with the model is small and the growth rate is usually less than the damping rate in the system. When five 300 kW flames are submitted to a very high amplitude acoustic wave (as is the case in the VHAM experiments), the effect is more pronounced with a measurable response. If several hundred flames of 1 MW each are concerned as is it the case in a real engine, it is likely that the perturbation necessary to trigger the phenomenon will have a more limited amplitude.

The analysis also indicates that the spatial pressure gradient is an influential parameter. Self-sustained transverse instabilities have been observed in single flame configurations (see for example (Tischler and Male 1956)). These instabilities were observed in cavities with a relatively small transverse dimension. In that situation the transverse mode pressure gradient was high, enhancing the source term.

Another effect is taken into account in the FAME formulation (section 4.4.2). It is known from previous work that the pressure variations directly influence the rate of heat release per unit flame area. If the flame elements in the flame are highly strained (if they are submitted to high strain rates) they respond to an external pressure variation in a quasi-steady fashion and the associated heat release per unit area changes like the square root of pressure with a characteristic time which is of the same order of magnitude as that of the strain rate. Since the strain rates take values which are well above those of the first eigenfrequencies of the chamber, one may consider that the response is instantaneous. This coupling is large near the wall of the chamber, where the pressure oscillations are greatest.

It is next important to discuss how the instability arises. In the two models developed in this chapter, an acoustic wave is assumed to be present in the combustor. The natural disturbances that can occur are denominated by “spikes" and “pops". It is generally admitted that a “spike" is a significant chamber over-pressure formed upon ignition of the engine, which can be attributed to the explosion or deflagration of the propellants collected in the thrust chamber or accumulated on its walls during the period corresponding to the ignition delay. A “pop" is a similar over-pressure, but occurring spontaneously during mainstage operation.

The direct link between these pressure perturbations and the present models is that they can give rise to an acoustic mode in the chamber which has a sufficient amplitude to trigger the instability. Moreover, when an over-pressure arises, a pressure wave propagates inducing a finer atomization. As the droplet size decreases, the local heat release increases and flames become shorter and more compact. This enhances the source term in the acoustic energy balance. The instability may also be triggered by the natural hydrodynamic modes of the injected propellant jets (see section 4.4.4). Since all jets have the same typical frequency, this may give rise to a collective motion which in turn induces a source term in the acoustic energy balance.
Among the triggering mechanisms, one should also consider processes giving rise to asymmetric flame patterns. It is concluded from experiments that the asymmetry enhances the source term in the balance of acoustic energy density and may intervene in the instability rate of growth and in the mechanisms sustaining the oscillation.

At this point it is worth considering some of the possible extensions of the present analysis. It is shown in this chapter that the flame motion and associated heat release plays a central role in the mechanism of instability. The distribution of heat release is mainly imposed by the transport of the liquid or transcritical oxygen phase. This aspect is treated in a simple way in the previous development. This could be represented with a more elaborate model which would describe the dynamics of the dense phase when submitted to the external acoustic field. The droplet spatial distribution could be followed in a Lagrangian framework. An alternative approach also consists in using an Eulerian description for the evaporating spray. This possibility is explored in appendix A by making use an eulerian tool developed by de Chaisemartin et al. (2007). The motion of density field of liquid droplets is obtained in this way. The coupling with acoustic waves can be carried out with this flow solver. Heating and vaporization processes are already implemented in the code, leading to a description of a space-time distribution of heat release in the flowfield. This opens a possible improvement of the present models with a more exact treatment of the motion of the dense oxidizer phase.

There are many other aspects which limit the current modeling and require further examination. The effect of a strong acoustic field on the jet break-up and atomization process is not well documented. This influences the triggering of instability because a sudden change in the droplet size changes the time lag between the acoustic perturbation and the droplets. In the transcritical regime prevailing at high pressure the effect of the acoustic motion on mass transfer from the dense phase is also not known. This may influence the development of the instability by augmenting the rate of heat release. These aspects will

require further experimentation and simulations.

In the theoretical analysis carried out in this section we have constantly neglected nonlinear effects on the acoustic field. This admittedly rough simplification was used to obtain practical expressions for the source term in the amplitude equations defining the pressure in the system. To account for acoustic nonlinearities, it would be possible thanks to the extensive studies of Culick and his co-workers. The amplitude equations would then be modified by including coupling terms between the different modes while keeping the heat release source term in its present form. This extension is rather straightforward but will not be pursued in what follows. We choose instead to proceed with the validation of the model using the MIC data. This validation is carried out in the next chapter.

Chapter 5

Low order modeling tool

This chapter reports the development of STAbility HF (STAHF), a program designed to predict instabilities in a rocket combustion chamber. First, several techniques are described to determine acoustic modes of the chamber. Analytical solutions are presented, followed by the technique of cavity coupling, a semi-analytic method which takes into account the presence of injectors in the spatial distribution of pressure. This technique is then validated using AVSP, the third available tool to calculate eigenmodes and which can deal with complex geometries. Finally, a theoretical study of the injector response is presented. Acoustic modes are then a parameter of a system of differential equations, which gives the temporal evolution of components on each mode. To close the problem, models for source terms (VHAM, flame response) and sink terms (damping coefficients on each mode) are presented. The damping coefficients are determined using results from cold flow experiments. The tool is then validated with Mascotte hot fire tests. It is shown that experimental observations are reasonably well represented in this case. The low order model is also applied to the analysis of instabilities in the configuration of a real scale rocket engine to illustrate the capacity of the model to represent the triggering of high frequency instabilities.

5.1 Introduction

It has been shown in previous chapters that high frequency combustion instabilities result from a subtle combination of complex processes. This statement is specifically relevant when one considers high frequency combustion dynamics in liquid rocket engines.
The main objective of low-order modeling (LOM) in combustion instability studies is to offer a comprehensive but simplified description of the system dynamics. This objective can be reached by deriving approximate descriptions of

the driving and coupling processes. The development requires a set of assumptions which must be carefully evaluated. Because the fundamental processes are complex, the model selection introduces challenging issues and determines the range of application of LOM. One has to sort out the most important features of the main dynamical processes including propellant jet break-up, atomization, vaporization from liquid droplets and inclusions or mass transfer from a transcritical fluid, acoustics of coupled systems, injector and nozzle response to perturbations etc. In low-order modeling, one has to devise simplified descriptions of these processes and to prove that the underlying assumptions are indeed justified.

The objective of the present chapter is to examine some of the basic phenomena, evaluate their impact and set up a global framework for a low-order computational tool integrating recent advances in experimentation and simulation. This framework should be sufficiently general to host a broad range of dynamical models for the main components of the system, and can be based on a standard method in which the nonsteady perturbation of pressure is expanded on a modal basis, as presented in 4.2.1. The formulation takes the form of a coupled system of differential equations which may be cast in the general form:

$$p'(\mathbf{x},t) = \sum_{m=1}^{N} \eta_m(t)\Psi_m(\mathbf{x}), \tag{5.1}$$

$$\ddot{\eta}_m + \omega_m^2\eta_m = \underbrace{\frac{\gamma-1}{\Lambda_m}\int_V \frac{\partial \dot{q}'}{\partial t}\Psi_m(\mathbf{x})dV}_{Chemical\ energy} + \underbrace{F}_{Forcing} - \underbrace{D}_{Damping}, \tag{5.2}$$

$$\dot{q}' = f(\mathbf{x},t,p',v',...). \tag{5.3}$$

This determines the general structure of the numerical tool, called STAbility HF (STAHF), and highlights some of the challenges arising in its construction. The first issue is the correct modeling of heat release fluctuations. This is the main focus of the previous chapter and the conclusions obtained are applied in what follows. An accurate description of the chamber acoustics is needed. It is also necessary to devise a model for an external excitation. This corresponds to the VHAM in our experiment. The damping of the chamber and of the different constituents of the system also needs to be carefully evaluated. These various components are shown schematically in Fig. 5.1.
The main objective is to set up the framework, validate the method with results obtained with the VHAM experiments, and extend the analysis to an idealized representation of a liquid rocket engine. It is important to make sure that the low order model structure will accommodate progressive implementations and improvements of submodels.

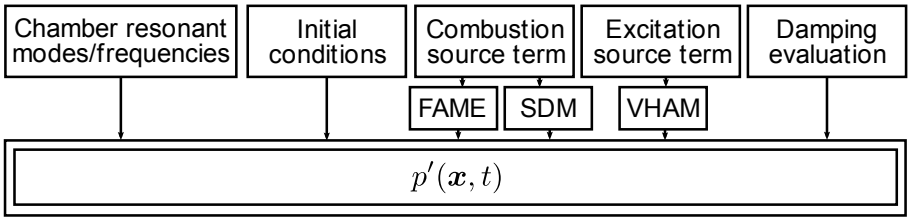

Figure 5.1: *Principal constituents of the modeling tool STAbility HF (STAHF).*

Components of this general framework are described in the next sections. The determination of the acoustic eigenmodes and eigenfrequencies is discussed in section 5.2. The specification of initial conditions and the modeling of an external modulator are considered in section 5.3. Acoustic damping in the system is discussed in section 5.4. The choices of a combustion response model is considered in section 5.5. A general diagram of the low order modeling tool is discussed in section 5.6. A validation of the numerical tool is carried out in section 5.7. Extension to a practical engine configuration is considered in the last section of this chapter.

5.2 Acoustic analysis of combustion chambers and injection systems

The acoustic response of combustion systems is conveniently described in terms of eigenfrequencies and eigenmodes. This provides a physical description of the dynamical response of most systems and corresponds to what is observed in experiments where oscillations arise at resonant frequencies. The objective is to solve the Helmholtz equation in geometries of interest for liquid rocket propulsion.

$$\begin{cases} \nabla^2 \Psi_m + k_m^2 \Psi_m = 0, \\ \\ \frac{\partial}{\partial \boldsymbol{n}} \Psi_m = -f \end{cases}$$

where $k_m = \omega/c$, $\boldsymbol{n}$ is the normal coordinate on the wall and f is a function defining the boundary value of the normal derivative of the pressure.
The eigenfrequencies and eigenmodes can be obtained in various ways. For simple geometries, one can use separation of variable techniques. For more complex configurations such as those found in liquid rocket engines, the modal analysis can be carried out by employing an approximate matching procedure between pressure fields in the thrust chamber and injection dome. Such configurations may also be treated by making use of Helmholtz equation numerical solvers which can deal with complex geometries and impedance boundary conditions.

In the special case of liquid rocket engines, it is also possible to account for the injector dynamics by expanding the pressure field in the dome and thrust chamber in terms of their respective eigenmodes. The injector response is then described by a differential equation relating the mass flow rate and the pressure difference between the two sides of the injection units. These various methods are described in what follows.

The analytical modeling is first described (Section 5.2.1). It can be used in simple geometrical configurations like a rectangular box or a cylindrical cavity. In section 5.2.2, a method is developed to cope with the problem of coupling between cavities connected by injection elements. These configurations are found in LRE where the propellant domes are coupled to the thrust chamber through injectors. The third part presents the acoustic code AVSP which deals with more general geometries. Finally, a new approach is developed to study the injector response taking into account the mean flow.

The modeling presented in the present chapter is based on an expansion of the pressure field on the chamber eigenmodes. Hence, the first step is to calculate the eigenmodes of the chosen geometry for particular thermodynamic conditions (sound velocity, boundary conditions...).

It is found in some previous studies that coupling between the combustion chamber and injection dome can be an important source of instability. In general, it is believed that this coupling is important in the low frequency range but less influential in the high frequency domain. To reduce low frequency oscillations it has become standard to use a head loss of about 10-15% of the chamber pressure to decouple the feed system and the thrust chamber (see for example Preclik and Spagna (1988)). There is however evidence that coupling is also possible in the high frequency range and that this may give rise to oscillations (see for example Hutt and Rocker (1995)). Recent experiments carried out by Richecoeur (2006) indicate that dynamical perturbations are present in the propellant manifold. Such perturbations have also been observed in experiments reported in chapter 3. The possible influence of a coupling between the chamber and the injection dome is already discussed in the previous chapter. From an examination of available data, it is concluded that this mechanism does not intervene in the VHAM experiments. However, this cannot be taken as a general conclusion because injectors are located near the pressure node where the pressure fluctuation is at its minimum. The response of injectors situated near the pressure antinode may be more effective and this could give rise to mass flow rate oscillations which would in turn feed one of the transverse modes. It is then necessary to derive an accurate description of the system acoustics. This will allow an evaluation of the effects of a coupling between the chamber and the dome and assess possible feedback mechanisms between these two elements.

5.2.1 Analytical determination of eigenfunctions

The propellant manifold and thrust chamber geometries found in liquid rocket engines can be fairly complex. This is also the case but to a lesser degree in the experimental setup used in the present investigation. However, it is often possible to approximate the geometry with very simple shapes. For example, a rocket combustion chamber is often close to a cylinder and the Mascotte test facility combustor can be roughly described as a rectangular box. These assumptions can be used to obtain expressions for eigenfrequencies and eigenmodes which may be found in classical textbooks or more specialized reports (see Yang et al. (1995) and Culick (2006) for instance).

Rectangular chamber configuration

The normal modes Ψ_n are obtained by using separation of variables: $\Psi_m(\boldsymbol{x}) = f_1(x)f_2(y)f_3(z)$. When this expression is inserted in eq. 5.2 one obtains an independent equations for each f_i. Assuming that the velocity vanishes at the chamber walls and at the chamber exhaust one obtains boundary conditions for each function and the eigenfunction takes the general form

$$\Psi_n(\boldsymbol{x}) = \cos(\frac{\pi p}{L}x)\cos(\frac{\pi m}{l}y)\cos(\frac{\pi s}{h}z)$$

where p, m and s are positive integers and

$$k_n^2 = \frac{\omega_n^2}{c^2} = \pi^2((\frac{p}{L})^2 + (\frac{m}{l})^2 + (\frac{s}{h})^2).$$

Here, the subscript n designates the triplet (p, m, s) chosen so that $\omega_{n+1} \geq \omega_n$.

Cylindrical chamber configuration

For a chamber with length L and radius R, there are two possible modes for each frequency:

$$\Psi_n = \cos(\frac{\pi p}{L}x)J_m(\kappa_{ms}r)\cos(m\theta) \tag{5.4}$$

$$\Psi_n = \cos(\frac{\pi p}{L}x)J_m(\kappa_{ms}r)\sin(m\theta) \tag{5.5}$$

with

$$k_n^2 = \frac{\omega_n^2}{c^2} = (\frac{\pi p}{L})^2 + (\kappa_{ms})^2$$

where $(\kappa_{ms}R)$ is the s-th positive zero of the function $dJ_m(r)/dr$ for $s \neq 0$ and $\kappa_{ms} = 0$ for $s = 0$.

5.2.2 Approximate analysis of coupled cavities

It is natural to first consider that the dome and chamber are coupled by a set of cylindrical ducts. Injectors are assumed to behave like one dimensional channels. Injector head losses and mean velocities are not considered. There are in reality two injection domes in an engine, one for the oxidizer and one for the fuel. This is not considered in this section where the geometry features a single LOx dome connected to the thrust chamber. This is similar to the configuration found in the Mascotte testbed, where methane is directly delivered to the five injectors without traversing a dome. In what follows, injection dome and injectors correspond to the liquid oxygen feed system. In an engine, the liquid oxygen manifold is also most influential because oxygen is the limiting reactant and fluctuations of its mass flow rate would possibly have the greatest impact on heat release.

With these hypotheses, the acoustics of the system of coupled cavities is derived, based on the work of Evesque and Polifke (2002). The geometry includes the dome, connecting injectors, and chamber. Eigenmodes are determined for the coupled system formed by these three parts.

System of equations

In this analysis the system comprises two cavities, linked by channels, which represent injectors. The LOx injection dome is a rectangular cavity of length, height and depth l_1, L_1 and h_1 respectively. Injectors are characterized by their length l_2 and diameter d. The combustion chamber is a rectangular cavity of length l_3, height L_3 and depth h_3. In what follows, quantities marked with the subscripts 1, 2 and 3 refer to the injection dome, injectors and combustion chamber respectively. The reference frame of coordinates is shown in Fig. 5.2.

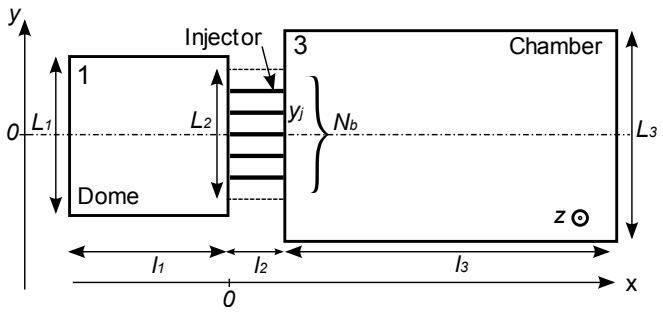

Figure 5.2: *Geometry and reference frame of the coupled cavity case.*

In each cavity, p'_i is solution of eq. 5.2. The separation of variable technique, described in the previous section, can be used in the present context. One assumes that h_i is small compared to the other dimensions of the chamber. The eigenfrequencies corresponding to this spanwise direction are high and can be neglected. The pressure field may be expressed in terms of the eigenmodes

$$p'_i(x,y) = \sum_{m=0}^{N-1} \cos\left(\frac{\pi m}{L_i}(y - L_i/2)\right)[f_i^m(x) + g_i^m(x)], i \in \{1,3\} \quad (5.6)$$

$$p_2^{'j}(x) = f_2^j(x) + g_2^j(x), j \in [1, N_b] \quad (5.7)$$

where N_b is the number of injectors and where the Riemann invariants are given respectively by

$$f^m(x) = F^m e^{-ik_x^m x}, \quad (5.8)$$

$$g^m(x) = G^m e^{ik_x^m x}. \quad (5.9)$$

The Riemann invariants, sometimes designated as p^+ and p^-, refer to traveling waves in the downstream and upstream directions. In these equations,

$$k_{x_i}^m = \sqrt{(\frac{\omega}{c_i})^2 - (\frac{\pi m}{L_i})}, i \in \{1,3\} \quad (5.10)$$

$$k_{x_2} = \frac{\omega}{c_2}. \quad (5.11)$$

The velocity fields in each cavity are deduced from the linearized momentum equation.

$$u'_i(x,y) = \sum_{m=0}^{N-1} \frac{k_{x_i}^m}{\omega\rho_i} \cos\left(\frac{\pi m}{L_i}(y - L_i/2)\right)[f_i^m(x) - g_i^m(x)], \quad i \in \{1,3\} \quad (5.12)$$

$$u_2^{'j}(x) = \frac{1}{c_2\rho_2}(f_2^j(x) - g_2^j(x)), j \in [1, N_b] \quad (5.13)$$

Boundary conditions are then specified at the dome inlets at $x = -l_1$ for p'_1 and at the chamber exhaust $x = l_3$ for p'_3. In the general case, these conditions are given in terms of frequency dependent impedances $Z_{in}(\omega)$ and $Z_{out}(\omega)$ defined by

$$Z_{in}(\omega) = p'_1(x = -l_1)/u'(x = -l_1), \quad (5.14)$$

$$Z_{out}(\omega) = p'_3(x = l_3)/u'(x = l_3). \quad (5.15)$$

In the present analysis, a rigid wall condition is imposed at the dome inlet and at the outlet, which corresponds to infinite impedances.

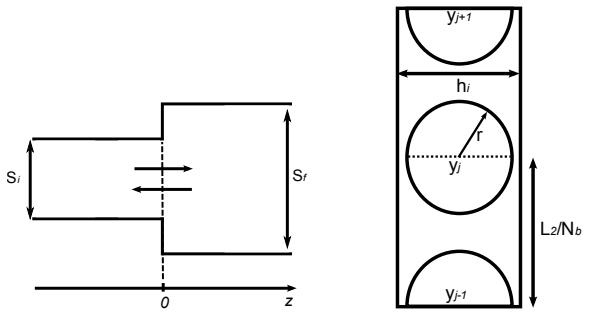

(a) (b)

Figure 5.3: *(a) Channel with a change of section - (b) Change of section between a rectangular cavity and a multiple injector configuration.*

The system dispersion relation may be obtained by writing matching conditions between the three elements of the geometry. In simple cases, when there is a change of section between two channels (see Fig. 5.3 (a)), these jump conditions express the continuity of pressure and volume flow rate:

$$p_i'(0) = p_f'(0), \tag{5.16}$$
$$S_i u_i'(0) = S_f u_f'(0). \tag{5.17}$$

Because of the individual description of the set of injectors, the pressure and velocity continuity conditions between dome and injectors, and between injectors and chamber, must be fulfilled at a certain number of collocation points at the interfaces. The collocation points are taken on the injector centerlines at $x = 0$ and $x = l_2$. If y_j defines the ordinate of the center of the j^{th} injector, one has at $x = 0$, for $j \in [1, N_b]$ and for the upstream and downstream cavity respectively:

$$p_1'(0, y_j) = p_2^{'j}(0), \tag{5.18}$$
$$p_2^{'j}(l_2) = p_3'(l_2, y_j). \tag{5.19}$$

This expresses the continuity of pressure. The condition pertaining to velocity is not that corresponding to a single channel. The change of section is in this case not well defined because there are several output channels for a single cavity. It is natural to assume in addition that the channels are equally spaced and distribute the area change in an equal fashion (Fig. 5.3 (b)). This respectively yields for the upstream and downstream cavities:

$$\int_{y_j-\frac{L_2}{2N_b}}^{y_j+\frac{L_2}{2N_b}} h_1 u_1'(0,y)dy = \pi r^2 u_2^{'j}(0), \tag{5.20}$$

$$\pi r^2 u_2^{'j}(l_2) = \int_{y_j-\frac{L_2}{2N_b}}^{y_j+\frac{L_2}{2N_b}} h_3 u_3'(l_2,y)dy. \tag{5.21}$$

The complete set of equations describing acoustic propagation in the different parts of the system are summarized in Appendix A.
Using these equations one obtains a homogeneous system of $4N_b+2N$ equations for $4N+2N_b$ unknowns, where N_b is the number of injectors and N is the number of modes considered. By taking $N = N_b$, a square matrix M of size $6N_b \times 6N_b$ is obtained and the system can be written in the form $MX = 0$, with

$$\begin{aligned} X \quad = \quad & (F_1^0, ..., F_1^{N-1}, G_1^0, ..., G_1^{N-1}, F_2^1, ..., F_2^{N_b}, \\ & G_2^1, ..., G_2^{N_b}, F_3^0, ..., F_3^{N-1}, G_3^0, ..., G_3^{N-1}), \end{aligned} \tag{5.22}$$

A nontrivial solution is obtained when the determinant of this matrix vanishes. This yields a set of eigenfrequencies ω and vectors defining the eigenmodes and the corresponding spatial distributions.

Remarks

- It is possible to reduced the matrix to a size $4N_b \times 4N_b$ by substituting the boundary conditions in the remaining equations because these conditions are not coupled with the rest of the system. The numerical solution is then easier to obtain.
- An accurate description of modes in the dome and combustion chamber is obtained for m lower or equal to $N_b/2$. This can be explained by an analogy with the sampling theory (see Evesque and Polifke (2002)). This means that modes with a transverse component equal to or greater than 3T are not reliably calculated. This limitation is acceptable in the present applications.

5.2.3 Numerical determination of eigenfrequencies and eigenmodes

The numerical determination of eigenmodes can be carried out by making use of a general purpose Helmholtz solver like AVSP. This software is used in this

document to estimate eigenfrequencies corresponding to cold flow and hot fire experiments (sections 2.3 and 3.3).

AVSP solves the Helmholtz equation in an arbitrary geometry. An overview of the code is given for example by Nicoud et al. (2007). Such a three dimensional acoustic solver is more flexible than the analytical method described previously and it can be used for design purposes. It is possible to impose complex impedance boundary conditions. AVSP allows a non-uniform temperature field. It is also possible to specify a local heat release, and take into account the flame pattern in the modal determination. The flame can be considered as an active element which can modify the system stability.

5.2.4 Comparison between approximate coupling model and numerical simulations

The AVSP solver is already well validated mainly in gas turbine combustor configurations. It is interesting to use this code in the coupled cavity situation found in liquid rocket engines or in the representative geometry of the MIC. It is also useful to compare AVSP calculations with the approximate coupled model solutions presented in section 5.2.2.

5.2.4.1 Geometry and boundary conditions

The geometry selected for the comparison is shown in Fig. 5.4.

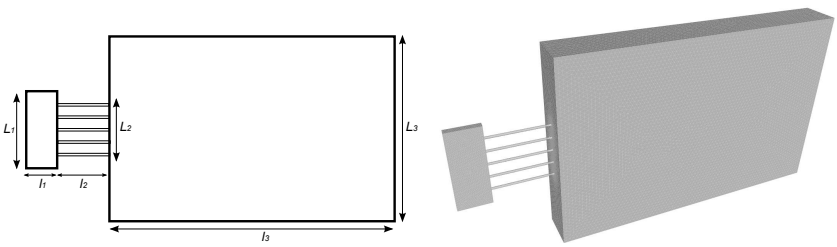

(a) (b)

Figure 5.4: *Geometry of the calculated case - (a) with characteristic dimensions - (b) volume of the computed case.*

This is a simplification of the Mascotte geometry (the two exit nozzles are not represented). The LOx injection dome is treated as a rectangular cavity. The five injectors feed a rectangular combustion chamber.
The thermodynamical state chosen for the computations are the same as those used for the complex geometry computations, presented in the chapter dealing with hot fire tests (section 3.3). One assumes that mean flow effects can be neglected. The dome and injectors contain liquid oxygen at 80 K, with $\rho_{LOx} =$

1195 kg.m^{-3} and $c_{LOx} = 997$ m.s^{-1}. In the chamber, the conditions are given by the injected mixture and one assumes a uniform temperature field. The sound velocity is fixed at:

$$c = 1050 \text{ m.s}^{-1}, \tag{5.23}$$

which is the value used for the calculations with a more complex geometry. Rigid wall boundary conditions are used everywhere. The computational mesh comprises 64806 nodes and 321564 cells. A slice of the mesh is shown in Fig. 5.5.

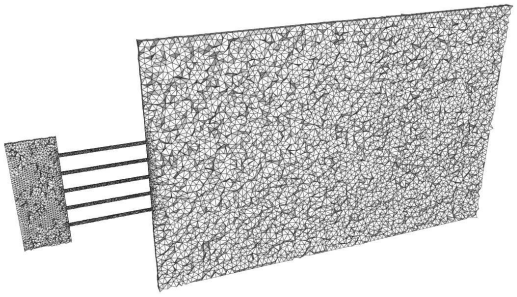

Figure 5.5: *Slice in the mesh used for the AVSP calculation.*

5.2.4.2 Results

The twelve first eigenmodes are calculated with AVSP.
Table 5.1 gathers eigenfrequencies found from the approximate analytical model described in section 5.2.2 and the numerical estimates obtained with AVSP. In spite of the relatively complex geometry, one finds a very good agreement with the analytical model. The differences do not exceed a few Hz.

Eigenmode	1L	1T	1T1L	2L	1T2L	3L
Model freq. (Hz)	1365	2100	2504	2727	3442	4091
Numerical freq. (Hz)	1365	2099	2502	2727	3441	4089
Eigenmode	2T	2T1L	1T3L	1T(dome)	2T2L	4L
Model freq. (Hz)	4200	4416	4598	4875	5008	5454
Numerical freq. (Hz)	4197	4411	4596	4831	5002	5449

Table 5.1: *Comparisons between eigenfrequencies found with the analytical model and numerical results obtained with AVSP for a fixed set of geometrical parameters.*

The eigenmode pressure fields computed with the approximate model and with AVSP are compared in Fig. 5.6, for four different modes (1T, 1T1L, 1T2L and 1T in the dome). The colormap distributions are not exactly identical but the spatial structures are quite similar.

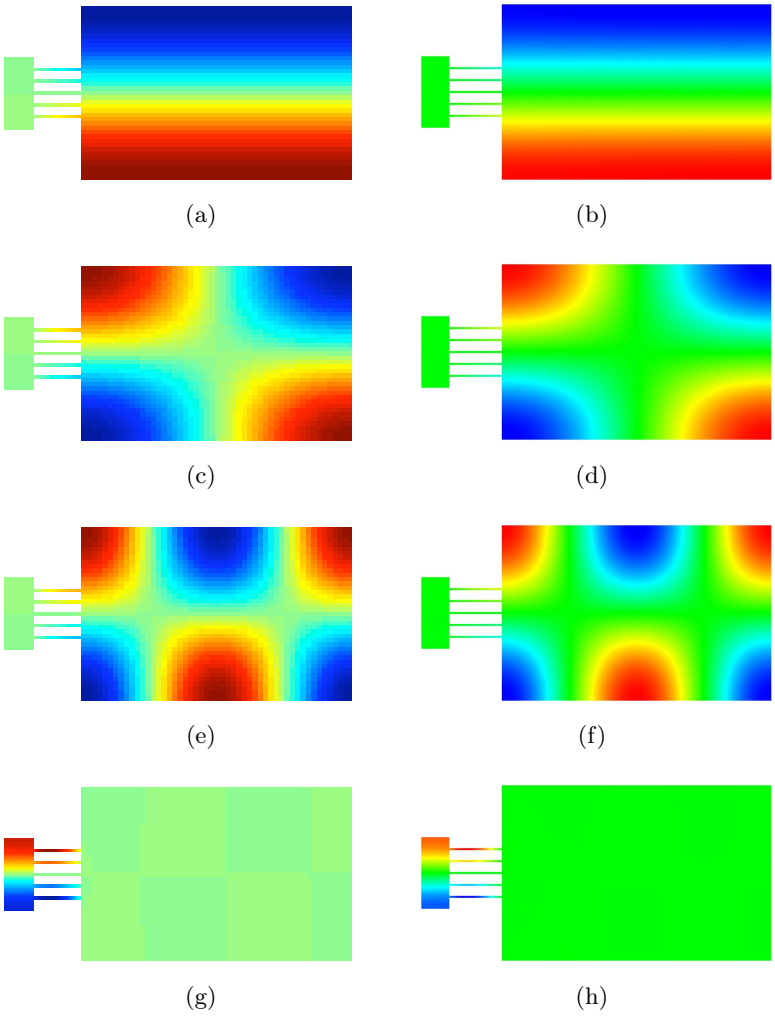

Figure 5.6: *Comparisons of pressure amplitude for the eigenmodes computed with the approximate model ((a) (c) (e) and (g)) and with AVSP ((b) (d) (f) and (h)) - (a) and (b): 1T - (c) and (d): 1T1L - (e) and (f): 1T2L - (g) and (h): 1T (dome). Note that colormaps are not exactly identical.*

In conclusion, both methods are consistent and it is possible to use both depending on the context. The main assets of the approximate coupling model is the ease of use and low CPU time required. The twelve modes are calculated in a few seconds. The approximate model is however limited to simple geometries. If one needs to take into account the VHAM, with the two exit nozzles with impedances, etc., the appropriate tool is AVSP. In that case, the geometry and mesh are built before the calculation, then the mesh is converted into AVSP format; an independent tool is used to impose the thermodynamical state in

the cavity, and the calculation is executed. Solutions are analyzed in a second stage with visualization software.

5.2.5 Modal expansion and injector response analysis

Techniques presented so far are based on linear acoustics and do not account for the injector dynamics. They provide eigenfrequencies and eigenmodes but cannot predict the response of injectors in terms of mass flow rate. One may then use an alternate formulation which relies on a modal expansion in the two cavities (see for example (Culick 1976) or the previous chapter - section 4.2.1 - for details) and on dynamical equations for the injection units. Rather than calculating the modes for a complex geometry comprising injectors and cavities, one considers the two simple cavities linked by injectors. The modes of the two cavities are calculated independently and injector dynamical equations provide conditions linking the two cavities. There are some attempts of this type in the previous literature but results obtained are difficult to assess (Hutt and Rocker 1995). There are also a number of references dealing with the injection system impedance and in particular those due to Zinn and coworkers (Janardan et al. (1976), Zinn (1970)). We can also cite the work Ménoret and Searby (2010), adapted from Hutt and Rocker (1995). These studies are mostly carried out in the frequency domain. In the method described here, the resolution is performed in the time domain.

One asset of the following formulation is that it yields a realistic description of the injector response and provides the unsteady mass flow rate in these units. This is specifically important if one wishes to examine the feed system influence. The injector head loss and mean flow velocity are taken into account. These two parameters and in particular the head loss, are often invoked to decouple the dynamics of feed system dynamics and thrust chamber.

5.2.5.1 Injector dynamics

One considers an injection system comprising a straight channel of length l and cross section A. This unit delivers a mass flow rate $\dot{m}$. The mean velocity in the channel is $\overline{v}$ and there is a head loss at the entrance of the channel which has the classical form $\Delta p = k\rho\overline{v}^2/2$ (Fig. 5.7).

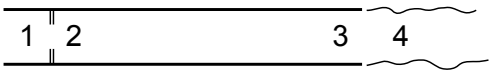

Figure 5.7: *Scheme of an injector.*

The dynamics of this system is described by the following set of equations:

$$p_1 - p_2 = \Delta p = k\frac{1}{2}\rho\overline{v}^2, \tag{5.24}$$

$$(p_2 - p_3)A = l\frac{d\dot{m}}{dt}, \tag{5.25}$$

$$p_3 - p_4 = \frac{\dot{m}^2}{2\rho S^2}, \tag{5.26}$$

Eq. 5.25 is obtained by writing an unsteady momentum balance between sections 2 and 3. In Eq. 5.26, S is the area of the propellant jet delivered by this injector. It is assumed for simplicity that $S = A$ so that:

$$p_3 - p_4 = \frac{1}{2}\rho\overline{v}^2.$$

Combining the previous expressions, one finds

$$p_1 - p_4 = \frac{l}{A}\frac{d\dot{m}}{dt} + k\frac{1}{2}\rho\overline{v}^2 + \frac{1}{2}\rho\overline{v}^2.$$

It is now possible to examine fluctuations around the mean value

$$p_1' - p_4' = \frac{l}{A}\frac{d\dot{m}'}{dt} + k\rho\overline{v}v' + \rho\overline{v}v',$$

and use

$$\Delta p = k\frac{1}{2}\rho\overline{v}^2$$

and

$$\rho v' A = \dot{m}'.$$

The previous equation may then be cast in the form

$$\begin{aligned} p_1' - p_4' &= \frac{l}{A}\frac{d\dot{m}'}{dt} + 2\Delta p\frac{v'}{\overline{v}} + \frac{\overline{v}}{A}\dot{m}', \\ &= \frac{l}{A}\frac{d\dot{m}'}{dt} + (\frac{2\Delta p}{\overline{\dot{m}}} + \frac{\overline{v}}{A})\dot{m}', \end{aligned}$$

or equivalently

$$\frac{A}{l}(p_1' - p_4') = \frac{d\dot{m}'}{dt} + (\frac{2\Delta pA}{l\overline{\dot{m}}} + \frac{\overline{v}}{l})\dot{m}'. \tag{5.27}$$

This equation defines the dynamical response of an injector submitted to an unsteady pressure difference $p_1' - p_4'$ It is interesting to define a characteristic delay τ such that

$$\frac{1}{\tau} = \frac{2\Delta pA}{l\overline{\dot{m}}} + \frac{\overline{v}}{l}.$$

and write the injector dynamical equation in the form:

$$\frac{d\dot{m}'}{dt} + (\frac{1}{\tau})\dot{m}' = \frac{A}{l}(p_1' - p_4'). \tag{5.28}$$

This first order differential equation indicates that the injector behaves like a low-pass filter. This can be seen more explicitly by examining the frequency domain response. One has

$$\frac{\tilde{\dot{m}}'}{\tilde{p_1'} - \tilde{p_4'}} = \frac{A}{l}\frac{\tau}{1 - i\omega\tau}. \tag{5.29}$$

It is interesting to study the limiting behavior corresponding to low and high frequency ranges.

Low frequency range
In the low frequency range, when $\omega\tau \ll 1$ one finds:

$$\begin{aligned}
\frac{\tilde{\dot{m}}'}{\tilde{p_1'} - \tilde{p_4'}} &\approx \frac{A}{l}\tau, &(5.30)\\
&= \frac{A/l}{\frac{2\Delta\overline{p}A}{l\overline{\dot{m}}} + \frac{\overline{v}}{l}}, &(5.31)\\
&= \frac{A/l}{\frac{2\Delta\overline{p}A}{l\overline{\dot{m}}}(1 + \frac{\overline{v}\overline{\dot{m}}}{2\Delta\overline{p}A})}, &(5.32)\\
&= \frac{\overline{\dot{m}}}{2\Delta\overline{p}}\frac{1}{(1 + \frac{1}{k})}. &(5.33)
\end{aligned}$$

When the head loss coefficient is large ($k >> 1$),

$$\frac{\tilde{\dot{m}}'}{\tilde{p_1'} - \tilde{p_4'}} = \frac{\overline{\dot{m}}}{2\Delta p},$$

or equivalently

$$\frac{\tilde{\dot{m}}'/\overline{\dot{m}}}{(\tilde{p_1'} - \tilde{p_4'})/\overline{p}} = \frac{1}{2\Delta p/\overline{p}}.$$

For a head loss of 10% of the mean chamber pressure, $\tilde{\dot{m}}'/\overline{\dot{m}} \approx 5(\tilde{p_1'} - \tilde{p_4'})/\overline{p}$, the relative fluctuation in mass flow rate is five times the relative fluctuation in pressure.

High frequency range
In the high frequency range, when $\omega\tau \gg 1$,

$$\frac{\tilde{\dot{m}}'}{\tilde{p_1'} - \tilde{p_4'}} = \frac{A}{l}\frac{i}{\omega}, \tag{5.34}$$

$$\frac{\tilde{\dot{m}}'/\overline{\dot{m}}}{(\tilde{p_1'} - \tilde{p_4'})/\overline{p}} = \frac{A\overline{p}}{l\overline{\dot{m}}}\frac{i}{\omega}, \tag{5.35}$$

It is convenient to define a new characteristic delay

$$\tau' = \frac{l\overline{\dot{m}}}{A\overline{p}}.$$

Now

$$\tau \approx \frac{l\overline{\dot{m}}}{A2\Delta p}, \tag{5.36}$$

$$\tau' = \tau\frac{2\Delta p}{\overline{p}}, \tag{5.37}$$

and

$$\frac{\tilde{\dot{m}}'/\overline{\dot{m}}}{(\tilde{p_1'} - \tilde{p_4'})/\overline{p}} = \frac{i}{\omega\tau'} = \frac{i}{\omega\tau}\frac{1}{2\Delta p/\overline{p}}.$$

Thus even in the high frequency range where $\omega\tau \gg 1$ the previous ratio may be of order one. For example, assuming that $\omega\tau = 5$ and that $\overline{p}/(2\Delta\overline{p}) = 5$ one has

$$\frac{\tilde{\dot{m}}'/\overline{\dot{m}}}{(\tilde{p_1'} - \tilde{p_4'})/\overline{p}} \approx i.$$

In that case, the pressure oscillations and the unsteady mass flow rate through the injector are in quadrature.

5.2.5.2 Complete system analysis

A precise description of injectors is derived in the previous subsection. The objective is now to link this description with the formalism presented in section 5.1. The system considered in what follows remains fairly general. Two cavities are linked together by N injectors, as shown schematically in Fig. 5.8. In this figure the combustor and dome are rectangular, but the following analysis is more general regardless of the cavity shape. The rectangular geometry is used in the end of this section to allow comparison with calculations carried out previously.
The cavities are associated with subscripts 1 and 4, which correspond to the dome and the main chamber respectively. In each cavity, the acoustic pressure field is expanded as a sum of eigenmodes.

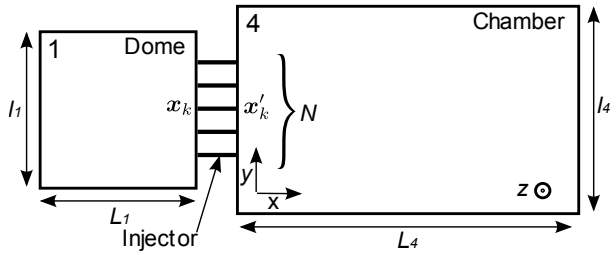

Figure 5.8: *Schematic representation of the injection dome and combustion chamber linked by a set of N injectors. The injector locations are defined by their position in the dome* $\boldsymbol{x}_k$ *and in the chamber* $\boldsymbol{x}'_k$.

$$p'_1(\boldsymbol{x},t) = \sum_1^{M^1} \eta_n^1(t)\Psi_n^1(\boldsymbol{x}), \tag{5.38}$$

$$p'_4(\boldsymbol{x},t) = \sum_1^{M^4} \eta_n^4(t)\Psi_n^4(\boldsymbol{x}). \tag{5.39}$$

From this formulation, and combining with eq. 5.27, one obtains a differential equation for each injector:

$$\frac{d\dot{m}_k}{dt} = \frac{A}{l}\left[\sum_1^{M^1} \eta_n^1(t)\Psi_n^1(\boldsymbol{x}_k) - \sum_1^{M^4} \eta_n^4(t)\Psi_n^4(\boldsymbol{x}'_k)\right] - \frac{\dot{m}_k}{\tau}, \tag{5.40}$$

with k taking values between 1 and N, and $\tau = \left(\frac{2\Delta pA}{l\dot{m}} + \frac{\overline{v}}{l}\right)^{-1}$.

Positions $\boldsymbol{x}_k$ and $\boldsymbol{x}'_k$ are the coordinates of the kth injector in the injection dome and in the chamber respectively. In both cavities, the equation of pressure can be written:

$$\frac{1}{c_i^2}\frac{\partial^2 p'_i}{\partial t^2} - \nabla^2 p'_i = \sum_{k=1}^{N} \frac{\partial \dot{m}_k}{\partial t}\delta(\boldsymbol{x}-\boldsymbol{x}_k), \tag{5.41}$$

for i equal to 1 and 4.
This equation projected on eigenmodes becomes:

$$\ddot{\eta}_n^1 + (\omega_n^1)^2\eta_n^1 = \frac{c_1^2}{\Lambda_n^1}\sum_{k=1}^{N}\frac{d\dot{m}_k}{dt}\Psi_n^1(\boldsymbol{x}_k), \tag{5.42}$$

$$\ddot{\eta}_n^4 + (\omega_n^4)^2\eta_n^4 = \frac{c_4^2}{\Lambda_n^4}\sum_{k=1}^{N}\frac{d\dot{m}_k}{dt}\Psi_n^4(\boldsymbol{x}'_k) \tag{5.43}$$

The system of equations defined by eqs. 5.40, 5.42 and 5.43 is then solved using an ordinary differential equation solver. The vector of unknowns comprises the modal amplitudes in the two cavities and the mass flow rates in the injection units:

$$X = (\eta_1^1, \dot{\eta}_1^1, ..., \eta_{M_1}^1, \dot{\eta}_{M_1}^1, \eta_1^4, \dot{\eta}_1^4, ..., \eta_{M_4}^4, \dot{\eta}_{M_4}^4, \dot{m}_1, ..., \dot{m}_N)$$

5.2.6 Conclusion on eigenmode determination

The method described above is not integrated in the following comparisons and in the code because it is in an early stage of development. The study will be pursued in the future.

Table 5.2 compares numerical estimates and experimental values of the modal eigenfrequencies. The differences observed have at least three possible origins. First, the exhaust system formed by the two nozzles is represented by a rigid wall. Second, the mean temperature is not precisely estimated and this may influence the final result. Third, the spatial distribution of temperature and the presence of liquid cores of cold and dense oxygen are not taken into account.

Eigenmode	1T	1T1L	2L	1T2L
Model freq. (Hz)	2100	2504	2727	3442
Numerical freq. (Hz)	1897	2334	2651	3153
Exp. freq. (Hz) - PF2	1840	2340	2655	3200

Table 5.2: *Comparisons between eigenfrequencies found with the analytical model, numerical results obtained with AVSP for a fixed set of geometrical parameters and experimental values obtained at PF2.*

The most important difference which can be noticed in this table is that the coupling model frequencies are invariably above the experimental and numerical ones by a couple of hundred hertz. This value is non negligible, and one may wonder why such a difference exists. As demonstrated in section 5.2.4, this is not a problem of the model: eigenmodes are solved accurately. The problem is caused by the approximation of geometry. Neglecting the nozzles has a strong impact on the standing waves spatial structure and, hence, frequency. To understand the influence of additional cavities, one may refer to a recent article of Oschwald et al. (2008), where the influence of an absorber cavity on a combustor is studied. It is shown that the frequency of a given mode decreases when the absorber cavity length increases.

Here, exit nozzles act like two absorber cavities, and decrease the mode resonant frequencies. Even if the frequency predictions are not accurate, the model still has important features which make it a useful tool: it is simple, modes are computed in a few seconds and it takes into account the possible coupling

between injection and combustion chamber. The spatial structure of the mode gives a good approximation of the real spatial structure.

5.3 Initial conditions and description of external modulation

The low order model requires initial conditions to begin the time integration. It is also necessary to derive a representation of an external modulation like that induced by the VHAM. These two aspects are envisaged in this section.

5.3.1 Defining the initial field

To solve the differential equations presented in the first section of this chapter, one has to specify initial values for the modal amplitudes ($\eta_m(0)$) and for their time derivative ($\dot{\eta}_m(0)$). One may consider that the initial pressure field is uniform except perhaps in a region of the chamber where ignition takes place and can be be modeled by a gaussian distribution of pressure. This field is then projected on the eigenmodes of the cavity. This ensures that the initial field satisfies the boundary conditions at the combustor walls.

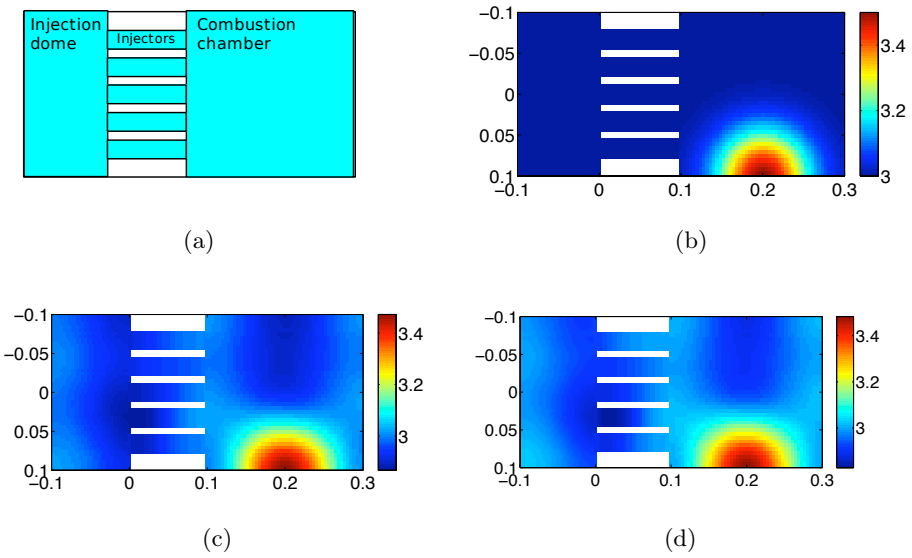

Figure 5.9: *(a) geometry - (b) Imposed initial pressure field - (c) Projected initial pressure field - (d) Re-projected initial pressure field (from (c))*

Theoretically, the initial pressure field can be expanded as:

$$p'(\boldsymbol{x},0) = \sum_{m=1}^{+\infty} \eta_m(0)\Psi_m(\boldsymbol{x}), \tag{5.44}$$

since the eigenmodes of the cavity form a basis for all the possible pressure fields. In practice, this infinite sum must be truncated. It is reasonable to consider the first N eigenmodes and determine the corresponding initial amplitudes:

$$\eta_m(0) = \frac{1}{\Lambda_m}\int_V p'(\boldsymbol{x},0)\Psi_m(\boldsymbol{x})dV,\ \forall m \in \{1,...,N\} \tag{5.45}$$

with $\Lambda_m = \int_V \Psi_m^2 dV$.
The integration is carried out on the grid used to solve the Helmholtz equation. This yields N initial amplitudes $\eta_m(0)$. The modal expansion can then be verified by reconstructing the initial field and comparing the calculated distribution with the pressure distribution specified at the outset

$$p'_{modeled}(\boldsymbol{x},0) = \sum_{m=1}^{N} \eta_m(0)\Psi_m(\boldsymbol{x}), \tag{5.46}$$

Fig. 5.9 (c) shows that the truncated modal expansion is in good agreement with the imposed initial pressure field. The two fields are not exactly the same for two reasons: (1) The imposed field does not satisfy the acoustic equations and boundary conditions and cannot be retrieved by a sum of physical modes, (2) Only a finite number of modes is retained in the modal expansion. To evaluate the latter issue, calculations have been carried out by keeping a larger number of eigenmodes ($N = 40$ instead of 12). Results are closer to the initial field but the computational time is augmented. Other calculations indicate that when the field specified initially is a solution of the acoustic equations, its truncated modal expansion is much closer to the specifed distribution as can be seen in Fig. 5.9 (d).

To obtain the initial derivatives of the modal amplitudes $\dot{\eta}_m(0)$ one applies a similar procedure to the initial distribution of the pressure time derivative, $\dot{p}'(\boldsymbol{x},0)$:

$$\dot{\eta}_m(0) = \frac{1}{\Lambda_m}\int_V \dot{p}'(\boldsymbol{x},0)\Psi_m(\boldsymbol{x})dV,\ \forall m \in \{1,...,N\} \tag{5.47}$$

5.3.2 Energy deposition

In the previous section, a local over-pressure is modeled by imposing a spatial distribution for the initial field. As already mentioned, it would be natural

to impose a distribution of the temporal derivative of pressure, which would physically corresponds to the complementary velocity field. This is not easy to define *a priori*. In this section, a perturbation, which could also be attributed to a “bomb" or to other types of perturbations that naturally occur in a rocket engine (“spike" or “pops"), is modeled.

The model is based on the work of Lacaze et al. (2009), in which ignition of rocket engines by a laser is modeled in a LES framework by defining an energy deposition scheme. The power added to the energy equation solved by the LES code follows a Gaussian distribution in space and time.

$$\dot{q}(x,y,z,t) = \frac{\epsilon_i}{4\pi^2\sigma_r^3\sigma_t} e^{-\frac{1}{2}(\frac{r}{\sigma_r})^2} e^{-\frac{1}{2}(\frac{t-t_0}{\sigma_t})^2} \tag{5.48}$$

where r is the distance to the laser focus center, t_0 is the time when $\dot{q}$ is maximum, ϵ_i is the total amount of deposited energy, and σ_r and σ_t are the spatial and temporal widths of the deposition.

To adapt this technique to the present purpose, one first imposes the characteristic energy ϵ_i of the perturbation. This energy can vary, and a parametric study of this parameter would be useful to establish the range of stability of a rocket engine. Then, the additional power is considered to be completely unsteady, which means that $\dot{q}' = \dot{q}$. Finally, one has to determine the contribution of this additional energy to each mode. This corresponds to the projection of the Rayleigh source term:

$$S_{exc}^m(t) = \frac{\gamma - 1}{\Lambda_m} \int_V \frac{\partial \dot{q}'}{\partial t}(\boldsymbol{x}, t)\Psi_m(\boldsymbol{x})dV. \tag{5.49}$$

In contrast with previous method of imposing a perturbation, the modulation has a given temporal extent, and is therefore not an initial condition. Moreover, there is no analytical solution to eq. 5.49, even with a very simple form for the mode $\Psi_m(\boldsymbol{x})$. This integration is then carried out for every time step during a small time interval (typically $6\sigma_t$).

5.3.3 Modeling of the VHAM excitation

It is next important to derive a method allowing a description of an imposed external modulation. We specifically consider a VHAM actuator. This device may be represented as a combination of two isolated acoustic sources operating in phase opposition. These sources appear as fluctuating mass flow rates in the mass balance equation:

$$\frac{\partial \rho}{\partial t} + \nabla \cdot \rho \mathbf{v} = \dot{m}_1 + \dot{m}_2, \tag{5.50}$$

It is natural to use point source distributions for these fluctuating mass flow rates $\dot{m}_i = \dot{m}_i \delta(\mathbf{x} - \mathbf{x_i})$ and to place the two sources on the centerline of the exhaust nozzles. The resulting wave equation takes the form:

$$\frac{1}{c^2}\frac{\partial^2 p'}{\partial t^2} - \nabla^2 p' = \frac{\partial \dot{m}_1}{\partial t}\delta(\mathbf{x} - \mathbf{x_1}) + \frac{\partial \dot{m}_2}{\partial t}\delta(\mathbf{x} - \mathbf{x_2}). \tag{5.51}$$

This equation is now solved by expanding the acoustic pressure in terms of the system eigenmodes:

$$p' = \sum_{m=1}^{\infty} \eta_m(t)\Psi_m(\mathbf{x}). \tag{5.52}$$

Inserting this expansion in the wave equation, assuming that the eigenmodes are orthogonal and projecting on the m-th eigenmode yields a differential system for the modal amplitudes:

$$\ddot{\eta}_m + \omega_m^2 \eta_m = \frac{1}{\Lambda_m}\left(\frac{d\dot{m}_1}{dt}\Psi_m(\mathbf{x_1})c^2 + \frac{d\dot{m}_2}{dt}\Psi_m(\mathbf{x_2})c^2\right), \tag{5.53}$$

The total mass flow rate is modulated by the VHAM and $\dot{m}_1 + \dot{m}_2 = \dot{m}_{tot}$. One can assume a sinusoidal modulation, leading to the following expressions:

$$\dot{m}_1 = \frac{\dot{m}_{tot}}{2}(1 + \cos(\omega_e t)), \tag{5.54}$$

$$\dot{m}_2 = \frac{\dot{m}_{tot}}{2}(1 - \cos(\omega_e t)), \tag{5.55}$$

where ω_e is the modulation angular frequency. One finally obtains:

$$\ddot{\eta}_m + \omega_m^2 \eta_m = \left[\frac{\dot{m}_{tot}}{2\Lambda_m}\omega_e c^2(\Psi_m(\mathbf{x_1}) - \Psi_m(\mathbf{x_2}))\right]\sin(\omega_e t), \tag{5.56}$$

which corresponds to a second order differential equation with a source term.

5.4 Damping modeling

A variety of processes induces damping effects. This modifies the chamber response and resonance properties and can be characterized in terms of a quality factor. Damping results from natural energy losses through the nozzle, but can also be augmented by connecting resonators or quarter wave cavities to the thrust chamber or by inserting baffles to subdivide the injection backplane. Under hot fire conditions, damping may be induced by temperature fluctuations (see Richecoeur et al. (2009)), mass momentum and heat transfer relaxation associated with the spray of droplets. Acoustic non-linearities may have a great

impact. They are not damping phenomena *per se*, but it has been shown (by Culick and Yang (1995) for instance) that non-linear terms explain the limit cycle observed during high-frequency instabilities. These phenomena are not discussed in this document. However, the framework presented here allows to introduce these non-linear terms.
For the time being, limit cycles are determined by constant parameters, which are typically added at the differential equations of the system as first order components. In a way, this method hides the contribution of non-linear terms. This is convenient, but has an important limitation when source terms caused by heat release fluctuations and damping coefficients are of the same order of magnitude (which is not the case in the VHAM). If the source term becomes more important than damping, the system becomes invariably unstable and no limit cycle is found: pressure oscillations grow infinitely, which has no physical meaning. In actual situations, non-linear terms modify apparent damping coefficients so that a limit cycle is reached.

A realistic estimation of the chamber acoustic damping is difficult to achieve in the general case. One may for example try to estimate the linear damping at the chamber walls following the analytical method devised by Searby et al. (2008). This is carried out in the next section. One finds that the corresponding damping rate is well below the actual value and that there are additional contributions to the damping process.
An alternative approach based on cold flow experiments, presented in section 5.4.2, provides a realistic estimate of damping coefficient without addressing complex theoretical damping phenomena.

5.4.1 Linear damping

It is interesting to obtain an estimate of the linear damping induced in the viscous boundary layers and by heat transfer at the wall. This is based on analytical expressions given in a recent study (Searby et al. 2008). Since the goal is to find an order of magnitude, one may consider that the MIC has the simplified geometry of a rectangular box and only examine damping associated with the first transverse mode. In this analysis, we will refer to section 4.4.1 of the previous chapter, where the growth rate is deduced from an energy balance. We simplify the expressions of acoustic pressure and velocity assuming constant amplitude:

$$p'(\boldsymbol{x},t) = p_0 \cos(\frac{\pi}{l}y) \cos\omega_1 t, \tag{5.57}$$

$$u'(\boldsymbol{x},t) = \frac{p_0}{\bar{\rho}c} \sin(\frac{\pi}{l}y) \sin\omega_1 t, \tag{5.58}$$

with $\omega_1 = \pi c/l$.

Total acoustic energy

The total energy associated with the acoustic wave is calculated in a first step. Eq. 4.34, is used and gives for a constant amplitude wave:

$$\mathcal{E}_1 = \frac{hlL}{4\overline{p}\gamma} p_0^2. \tag{5.59}$$

Viscous and thermal losses are evaluated in a second step.

Viscous losses

Viscous losses are computed by integrating over the wall surface the expression:

$$\langle \frac{de_1}{dt} \rangle_\nu = \frac{1}{2}\overline{\rho} u_y'^2 \sqrt{\frac{\omega\nu}{2}}, \tag{5.60}$$

with $u_y' = p_0/(\overline{\rho}c)\sin(\pi y/l)$. One obtains:

$$\langle \frac{d\mathcal{E}_1}{dt} \rangle_\nu = \frac{l}{2}\frac{p_0^2}{\overline{p}\gamma}\sqrt{\frac{\omega\nu}{2}}(h+L). \tag{5.61}$$

The damping factor associated to viscous losses is then given by:

$$\sigma_\nu = \frac{1}{\mathcal{E}_1}\langle \frac{d\mathcal{E}_1}{dt} \rangle_\nu, \tag{5.62}$$

$$= 2\sqrt{\frac{\omega\nu}{2}}\left(\frac{1}{L}+\frac{1}{h}\right). \tag{5.63}$$

Thermal losses

This contribution is determined by integrating the following relation on the chamber walls:

$$\langle \frac{de_1}{dt} \rangle_{th} = \frac{1}{2}(\gamma-1)\frac{p_y'^2}{\overline{p}\gamma}\sqrt{\frac{\omega D_{th}}{2}}, \tag{5.64}$$

with $p_y' = p_0\cos(\pi y/l)$. It gives

$$\langle \frac{d\mathcal{E}_1}{dt} \rangle_{th} = \frac{1}{2}(\gamma-1)\frac{p_0^2}{\overline{p}\gamma}\sqrt{\frac{\omega D_{th}}{2}}(2hL+Ll+hl). \tag{5.65}$$

The damping factor associated to thermal losses reads:

$$\sigma_{th} = \frac{1}{\mathcal{E}_1}\langle \frac{d\mathcal{E}_1}{dt} \rangle_{th}, \tag{5.66}$$

$$= 2(\gamma-1)\sqrt{\frac{\omega D_{th}}{2}}\left(\frac{2}{l}+\frac{1}{L}+\frac{1}{h}\right). \tag{5.67}$$

Total damping
The total damping is the sum of the thermal and viscous damping terms.

$$\sigma_{e_1} = \sigma_\nu + \sigma_{th}, \tag{5.68}$$

$$= 2\sqrt{\frac{\omega\nu}{2}}\left[\left(\frac{1}{L}+\frac{1}{h}\right)\left(1+\frac{\gamma-1}{\sqrt{\mathrm{Pr}}}\right)+2\frac{\gamma-1}{l\sqrt{\mathrm{Pr}}}\right], \tag{5.69}$$

where Pr=ν/D_{th} is the Prandtl number. The damping coefficient for pressure is deduced with the relationship:

$$\sigma_p = \frac{\sigma_{e_1}}{2}. \tag{5.70}$$

It is now possible to estimate the linear damping in one of our test cases. The cold experiment OP1 is chosen for that purpose. Mean pressure is 7.5 bar and the temperature is 137 K (see section 2.3 for details). In this situation, Pr=0.8, $\nu = 4.7\ 10^{-7}\mathrm{m}^2\mathrm{s}^{-1}$and $\gamma = 1.491$, using NIST thermodynamical tables. For the first transverse mode (f_1=600 Hz), this leads to:

$$\sigma_p = 1.11\ \mathrm{s}^{-1}, \tag{5.71}$$

$$\xi_1 = 3\ 10^{-4}, \tag{5.72}$$

with $\sigma_p = \omega_1\xi_1$. The evaluation of damping by the method developed in the next section shows that the actual damping of the chamber is at least two orders of magnitude above this value. The presence of a mean flow and various nonlinear effects have a strong influence in this case and it is not easy to obtain a theoretical estimate of the damping rate. Moreover, the two exhaust nozzles can act like resonators and add significant damping to the system. Their contribution should be taken into account, but the presence of the mean flow differs from the theoretical model hypotheses.

5.4.2 Experimental determination of damping

An accurate estimation of damping based on theoretical considerations seems out of reach. It is however important to get an estimate of this quantity to be able to predict the level of oscillation in the system. Consider, as a model problem, a second order differential equation with constant coefficients and a sinusoidal driving term,

$$\ddot{\eta} + 2\xi\omega\dot{\eta} + \omega^2\eta = F\sin(\omega_e t),$$

The final amplitude is $F/(2\xi\omega)$, which highlights the importance of a correct evaluation of ξ. If ξ is taken equal to half of its actual value, the oscillation amplitude is multiplied by two.

In what follows, we choose to add a damping coefficient in the governing equation and to adjust the value of ξ_m to obtain a suitable response under cold flow experimental conditions. The system dynamics is described by the following equation

$$\ddot{\eta}_m + 2\xi_m\omega_m\dot{\eta}_m + \omega_m^2\eta_m = \left[\frac{\dot{m}_{tot}}{2\Lambda_m}\omega_e c^2(\Psi_m(\mathbf{x_1}) - \Psi_m(\mathbf{x_2}))\right]\sin(\omega_e t). \quad (5.73)$$

Considering the frequency response of this system leads to an estimation of ξ_m as a function of $\overline{\eta_m}$, defined by $\eta_m = \overline{\eta_m}e^{i\omega_e t}$:

$$\xi_m = \frac{\left[\frac{\dot{m}_{tot}}{2\Lambda_m}\omega_e c^2(\Psi_m(\mathbf{x_1}) - \Psi_m(\mathbf{x_2}))\right]}{\overline{\eta_m}2\omega_e\omega_m} + \frac{\omega_e^2 - \omega_m^2}{2\omega_e\omega_m}. \quad (5.74)$$

The damping factor is obtained when $\omega_e = \omega_m$, which gives:

$$\xi_m = \frac{\left[\frac{\dot{m}_{tot}}{2\Lambda_m}c^2(\Psi_m(\mathbf{x_1}) - \Psi_m(\mathbf{x_2}))\right]}{\overline{\eta_m}2\omega_m}. \quad (5.75)$$

The variables $\Psi_m(\mathbf{x_1}), \Psi_m(\mathbf{x_2})$ and ω_m can be extracted from the eigenmode calculations, while $\dot{m}_{tot}$ and c are known from the experiments. To determine ξ_m one needs the amplitude reached by the m-th mode, which is directly related to $\overline{\eta_m}$. Since this is not directly available in the experiments, pressure sensor signals are used. In the computations, the pressure sensors can be artificially simulated and a comparison between the simulation and experiments can be used to adjust ξ_m. This procedure is described and used in section 5.7.

5.5 Combustion model

The definition of a combustion model for the low-order modeling tool is already envisaged in the previous chapter on heat release modeling. In this chapter, three combustion models are described. The first (FAME) is based on the flame displacement with respect to an essentially steady acoustic pressure distribution. The second model extends the FAME formulation and accounts for the effect of pressure. These two models define an unsteady heat release distribution. The third model accounts for the spray motion with respect to the acoustic field (SDM).

- Flame displacement FAME
- Extended FAME
- Spray displacement model SDM

These three models yield distributions of unsteady heat release which may be cast in the general form

$$\dot{q}' = f(\boldsymbol{x}, t, p', v', ...).$$

and can be inserted in eqs. 5.3.
The extended FAME model specifies the evolution equation for the first modal amplitude and for a rectangular geometry:

$$\ddot{\eta}_1 + \omega_1^2 \eta_1 = 2\frac{\gamma-1}{hLl}\mathcal{Q}_0 \frac{\dot{\eta}_1}{\overline{p}\gamma} \sum_{n=1}^{N} \frac{1}{\sqrt{1+\frac{\eta_1}{\overline{p}}\cos(\frac{\pi}{l}y^n(t))}} \left[\sin^2(\frac{\pi}{l}y^n(t))\left(1+\frac{3}{2}\frac{\eta_1}{\overline{p}}\cos(\frac{\pi}{l}y^n(t))\right)+\frac{\gamma}{2}\cos^2(\frac{\pi}{l}y^n(t))\right] \tag{5.76}$$

where y^n given by: $y^n(t) = \frac{2l}{\pi}\arctan(\tan(\frac{\pi y_0^n}{2l})\exp(\frac{-\eta_1(t)}{\overline{p}\gamma}))$ and y_0^n is the injector positions.
The SDM model provides a more general formulation, without any assumption on the geometry or the mode. It is however necessary to have a method relating the droplet diameter and the mean liquid oxygen partial density to the acoustic Weber number and intact core length:

$$\ddot{\eta}_m + \omega_m^2 \eta_m = \frac{\gamma-1}{\overline{\rho_g}\omega_m^2}\Delta h_T \frac{3}{2}\frac{K}{d^2}\frac{\dot{\eta}_m(t-\tau_a^m)}{\sqrt{1+(\omega_m\tau_p)^2}}\frac{1}{\Lambda_m}\int_V \overline{\rho_{LOx}}(\nabla\Psi_m)^2 dV. \tag{5.77}$$

The SDM formulation requires functional relations $(\tau_p(d), d(\mathrm{We}_c, u'), K, \overline{\rho_{LOx}}(\boldsymbol{x}))$ which are not easy to define without further experimental or numerical work. In contrast, the FAME formulation can be used without additional input. It also more closely describes what has been observed experimentally. This formulation will be used as a reference in what follows. However, the SDM model is needed to account for the triggering of instabilities, and its formulation is available for any geometry.

To sidestep the problems due to the liquid phase formulation and the distribution of heat release, and to be able to compare the two models, the following assumptions are made:

- The ratio K/d^2 is constant.
- Flames are infinitely thin.

Eq. 5.77 becomes:

$$\ddot{\eta}_m + \omega_m^2 \eta_m = \frac{\gamma-1}{\overline{\rho_g}\omega_m^2}\frac{\dot{\eta}_m(t-\tau_a^m)}{\sqrt{1+(\omega_m\tau_p)^2}}\frac{\mathcal{Q}}{\Lambda_m}\sum_{n=1}^{N_f}(\nabla\Psi_m(\boldsymbol{x}_n))^2, \tag{5.78}$$

where $\boldsymbol{x}_n$ is the position of the n^{th} injector.
When these two models were compared (section 4.6), it was noted that a drawback of the SDM model is that it does not account for the effects of strain, characterized in eq. 5.76 by the term in $\cos^2$. This term has a great importance near the walls, and neglecting it underestimates the combustion response to acoustic perturbations. Another formulation is proposed here, that is a direct extrapolation of the strain term for FAME into SDM model:

$$\begin{aligned}\ddot{\eta}_m + \omega_m^2 \eta_m &= \frac{\gamma-1}{\overline{\rho_g}\omega_m^2}\frac{\mathcal{Q}}{\Lambda_m}\Big[\frac{\dot{\eta}_m(t-\tau_a^m)}{\sqrt{1+(\omega_m\tau_p)^2}}\sum_{n=1}^{N_f}(\nabla\Psi_m(\boldsymbol{x}_n))^2 \\ &\quad +\dot{\eta}_m(t)\sum_{n=1}^{N_f}\frac{\gamma}{2}(\frac{\omega_m}{c})^2(\Psi_m(\boldsymbol{x}_n))^2\Big]. \qquad (5.79)\end{aligned}$$

Eq. 5.79 will be referred to as the *extended SDM model*. When $\tau_p = 0$, for a rectangular box and considering small perturbations, the FAME and SDM formulations become identical. While no theoretical demonstration is provided, this expression compiles the main mechanisms modeled so far.
It is used in the following sections because it presents two essential features: (1) once the atomization has been enhanced by a perturbation and the droplets mainly follow the acoustic field, the limit cycle is the same as that predicted by the FAME model, (2) the threshold due to acoustic atomization enhancement is modeled by making use of the critical Weber number concept. It would be necessary to get a more precise estimate of the range of validity of this expression. Analytical calculations could be used to obtain a theoretically more suitable expression.

The liquid related parameters are then:

$$\tau_a^m = \frac{\arctan(\omega_m\tau_p)}{\omega_m}, \qquad (5.80)$$

$$\tau_p = \frac{\rho_l d^2}{18\mu_g}, \qquad (5.81)$$

$$d = d(\mathrm{We}_c, u'). \qquad (5.82)$$

Molecular viscosity of the gas phase μ_g is often assumed to be independent of the gas composition and close to that of air so that the classical Sutherland law can be used

$$\mu_g = c_1\frac{T^{3/2}}{T+c_2}\frac{T_{ref}+c_2}{T_{ref}^{3/2}} \qquad (5.83)$$

where c_1 and c_2 must be determined so as to fit the real viscosity of the mixture. For air at $T_{ref} = 273$ K, $c_1 = 1.71\text{e-}5$ kg/m.s and $c_2 = 110.4$ K (White 1999).

The only unknown that remains is the function that expresses how droplets submitted to an acoustic wave break up. This is constructed so that when the local Weber number ($We = (\rho_g u_g^2 d)/\sigma_{LOx}$, where $u_g = \overline{u}_g + u'_g$) is greater than a given critical Weber number (here, We_c=1), each droplet is divided in two identical droplets. If d_1 is the diameter of the initial droplet and d_2 is the diameter of the two resulting droplets, a volume balance gives:

$$d_2 = \frac{d_1}{2^{\frac{1}{3}}}. \tag{5.84}$$

Summary

In the following section (5.7), two models are used to obtain theoretical estimates and compare with experiments carried out with the MIC. The model definitions are given for the *extended FAME model* by (eq. 5.77), and for the *extended SDM model* by (eq. 5.79).

A typical rocket engine configuration is investigated in section 5.8 and the extended SDM model is used in this case to carry out the stability computations.

5.6 Diagram of the modeling tool

The structure STAHF is shown in Fig. 5.10.

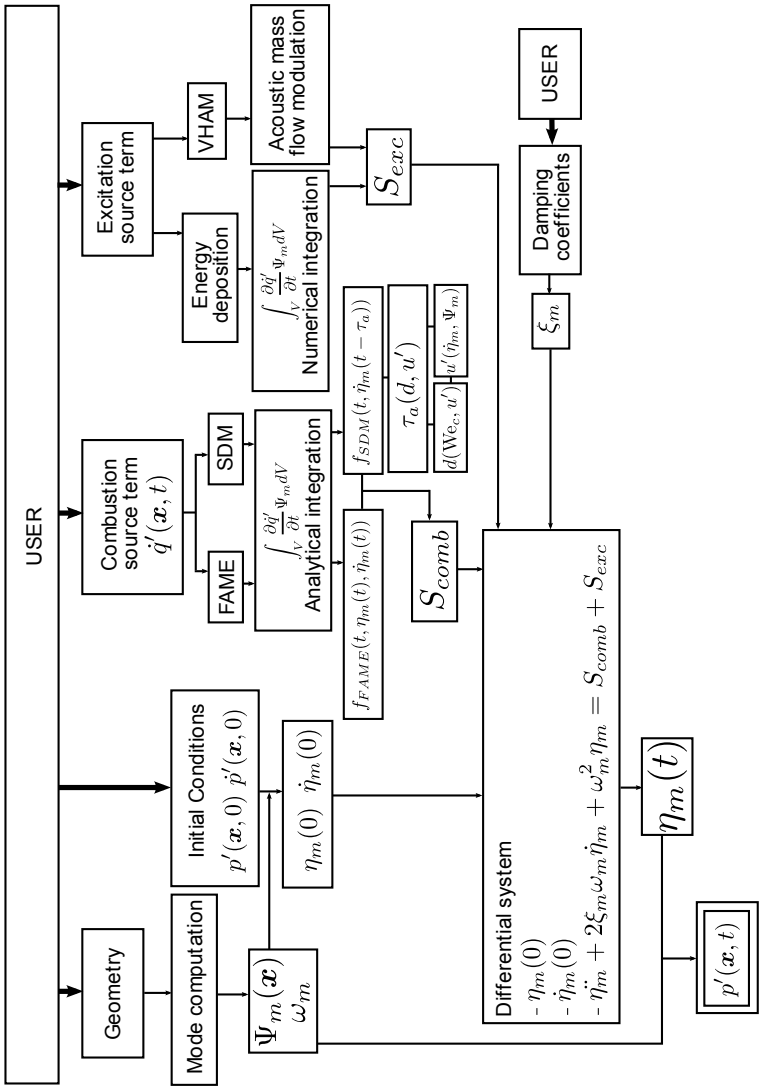

Figure 5.10: *Global framework for the low order modeling tool STAHF.*

5.7 Validation by comparison with Mascotte experiments

It is important to see if the low order model (LOM) described in this chapter can retrieve some of the experimental observations made on the MIC configuration

equipped with the VHAM. The LOM formulation combines ideas deduced from experimental results to devise a set of submodels. It is here worth recalling that this tool relies on a modal expansion and that it includes:

- An acoustic description of the system eigenmodes
- A combustion model
- A model for the external excitation induced by the VHAM
- A damping model

These items are considered successively. The acoustic analysis is carried out with the different tools presented previously. Several combustion models are compared. One difficulty of the validation process is that certain formulations cannot be verified independently. For example, the VHAM and damping submodels have to be used in conjunction with the combustion model if one wishes to use the data gathered on the Mascotte testbed for validation.

5.7.1 Comparison - Acoustics solved with coupling tool

Here, the coupling tool is used to solve the acoustic modes, therefore the geometry is simplified (see section 5.2.2).

5.7.1.1 Geometrical definitions and flow conditions

The geometry envisaged in this example corresponds to that presented in section 5.2.4. Resonant frequencies and eigenmodes are calculated for two different sets of flow conditions. The first to evaluate the damping, using cold flow experiments, and the second to evaluate the combustion model response, which will be compared to hot fire experiments eventually. The experimental reference conditions are those of operating point OP1, described in chapter 2 and of operating point PF2 (chapter 3). These two operating points have been chosen because they share some essential features. The total mass flow rate injected is very close (methane has been replaced by nitrogen), and the injectors used (inner LOx injectors and outer coaxial gas injectors) are identical, which yield momentum flux ratios of the same order of magnitude.

The data needed to compute eigenmodes are compiled in table 5.3.
Modes for PF2 and for the MIC geometry are computed in section 5.2.4. It is only necessary to compute modes with OP1 conditions. The coupling tool is used for the same geometry but for cold flow conditions. Finally, $\Psi_m(\boldsymbol{x})^{cold}$ and $\Psi_m(\boldsymbol{x})^{hot}$ and their respective eigenfrequencies (see table 5.4) are obtained.
Once again, for this simplified geometry, resonant frequency estimates are above the experimental values. This is explained in section 5.2.6 and does not modify

OP	p (bar)	c (m s^{-1})
OP1	7.5	360
PF2	26	1050

Table 5.3: *Parameters of cold test OP1 and hot fire test PF2. OP1 test case is used to evaluate the damping coefficients to use in the PF2 modeling.*

	1L	1T	1T1L	2L	1T2L	3L	2T
f_m^{cold} (Hz)	470	720	859	935	1180	1403	1440
f_m^{hot} (Hz)	1365	2100	2504	2727	3442	4091	4197

Table 5.4: *Resonant frequencies obtained for operating point OP1 (f_m^{cold}) and PF2 (f_m^{hot}).*

the method and may not have a great influence on the results. Comparison with a complex geometry carried out in the next section give further information on this issue.

5.7.1.2 Cold flow experiments: damping evaluation

Cold flow experiments are used to evaluate damping in the system. The damping factor is estimated with the method described in section 5.4. Now that injection conditions have been introduced and eigenmodes determined, two items need to be described to solve the system: initial conditions and external modulation procedure. One may first consider that there is no initial pressure perturbation:

$$\eta_m(0) = 0, \tag{5.85}$$

$$\dot{\eta}_m(0) = 0. \tag{5.86}$$

The system is submitted to the VHAM excitation (see section 5.3.3), and there is no combustion source term, because the system operates under cold flow injection. The dynamics is represented by the following equations:

$$\ddot{\eta}_m + 2\xi_m(\omega_m^{cold})\dot{\eta}_m + (\omega_m^{cold})^2\eta_m = \left[\frac{\dot{m}_{tot}}{2\Lambda_m^{cold}}\omega_e c^2(\Psi_m^{cold}(\mathbf{x_1}) - \Psi_m^{cold}(\mathbf{x_2}))\right]\sin(\omega_e t). \tag{5.87}$$

In these equations, $\dot{m}_{tot}$ is the total mass flow rate injected, which is in the present case:

$$\dot{m}_{tot} = 195 \text{ g s}^{-1}. \tag{5.88}$$

Eqs. 5.87 are solved for values of ω_e equal to the eigenmode resonant values. A truncated modal expansion is employed, and N =12 components are retained. This yields the field $p'(\boldsymbol{x}, t)$. One can then deduce five signals at the pressure sensor locations $p'(\boldsymbol{x}_i, t)$ and compare these signals with those recorded in the experiments.

This process may then be used to chose the damping factors ξ_m in order to obtain the closest match between experimental data and numerical signals (not reproduced here for confidentiality reasons).

This leads to the curves represented in Fig. 5.11 (b), (d) and (f) which must be compared to the experimental signals (a), (c) and (e). It is found that this method provides good approximations of the experimental signals. The order of magnitude may be considered as satisfying, even if much more precise methods should be investigated. As mentioned in section 5.4.1, these values are at least two orders of magnitude higher than the ones found using linear damping assumptions.

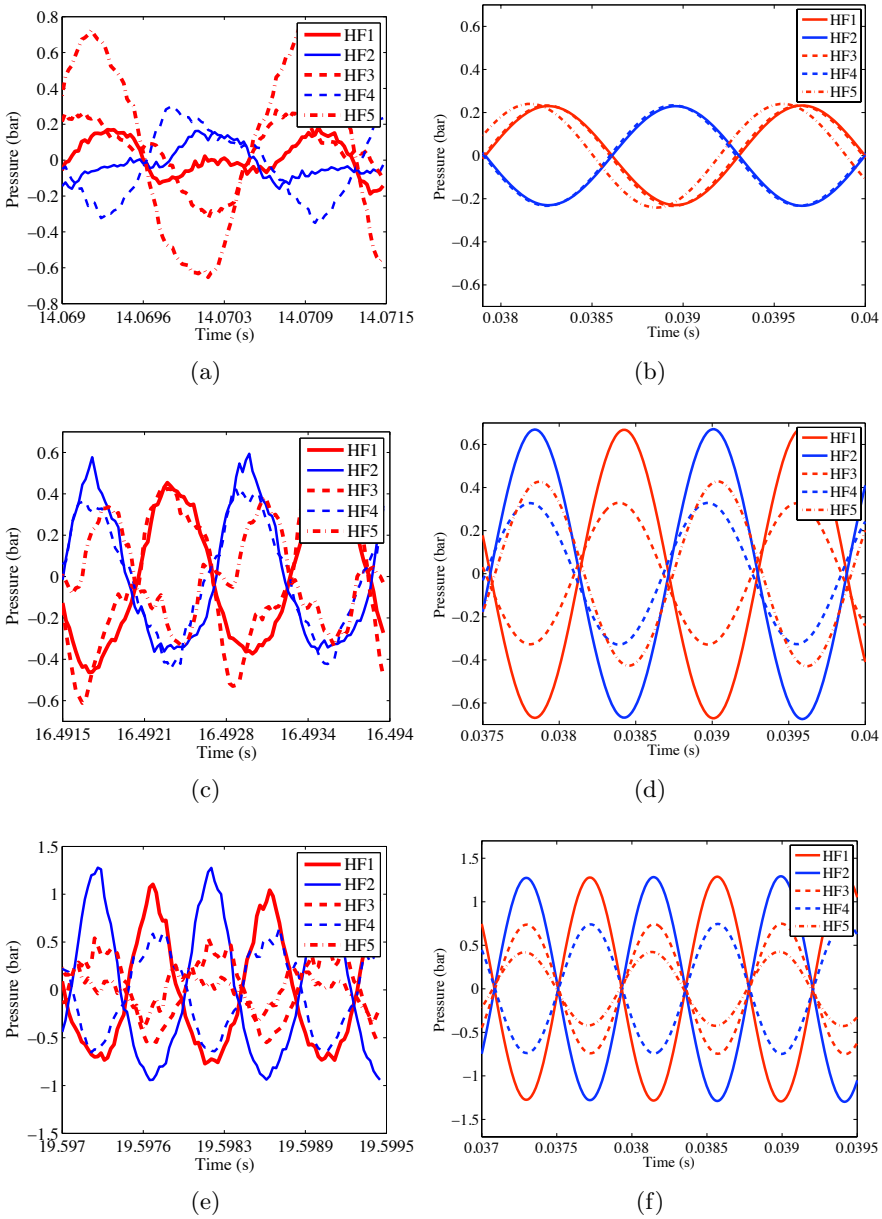

Figure 5.11: *Comparison between experimental data, HF pressure sensors for OP1 in (a), (c) and (e), and numerical results, reconstructed HF sensors in (b), (d) and (f) - (a,b) 1T mode - (c,d) 1T1L mode - (e,f) 1T2L mode.*

5.7.1.3 Hot fire comparisons

Now that the damping coefficients are estimated, the calculation is carried out under hot fire conditions, with an external modulation corresponding to the 1T2L eigenfrequency (3442 Hz). To evaluate the influence of the FAME source term, the calculation is done with and without the model to compare the amplitudes in both cases.

The dynamics is now represented by the following equations:

$$\ddot{\eta}_m + 2\xi_m(\omega_m^{hot})\dot{\eta}_m + (\omega_m^{hot})^2\eta_m = \left[\frac{\dot{m}_{tot}}{2\Lambda_m^{cold}}\omega_e c^2(\Psi_m^{hot}(\mathbf{x_1}) - \Psi_m^{hot}(\mathbf{x_2}))\right]\sin(\omega_e t) + S_{comb}. \tag{5.89}$$

In these equations, $\dot{m}_{tot}$ is the total mass flow rate injected, which is now:

$$\dot{m}_{tot} = 190 \text{ g s}^{-1}. \tag{5.90}$$

The mass flow rate is not exactly the same. For OP1, 80 g $s^{-1}$of nitrogen are injected while for PF2, 75 g $s^{-1}$of methane are injected.
The two models are tested successively.

Combustion response modeled by FAME

In Fig. 5.16, three graphs are shown. The first one reproduces the signals recorded by the pressure sensors during experiments. The second graph is the numerical result obtained without activating the model. In the last case, the model is activated.
One first notices the overall agreement in the signal amplitudes. In the experiment, pressure oscillate (for HF1 and HF2) between -4 and 6 bar approximately. Amplitude vary between -4 and 4 bar for the case without flame feedback and between -5 and 5 bar with the flame feedback, which is remarkably close to experimental result. It is necessary, though, to remember that certain parameters introduce some uncertainty in this result: (1) Damping coefficients may not be constant with frequency or amplitude, (2) It is not sure that 100% of the total mass flow rate injected is modulated by the VHAM and constitutes an acoustic source, (3) In the VHAM excitation term, two constants intervene linearly, c and ω_e. There is an uncertainty already mentioned on c, and we know that ω_e is incorrect by a couple hundred hertz (3442 Hz instead of 3200 Hz). This in turn introduces an overestimation of the modulation term.

In spite of these limitations been said, Fig. 5.16 shows a very interesting feature. There is a sensible difference of amplitude (around 20%) between the case without flame feedback and the case with the FAME model. This clearly

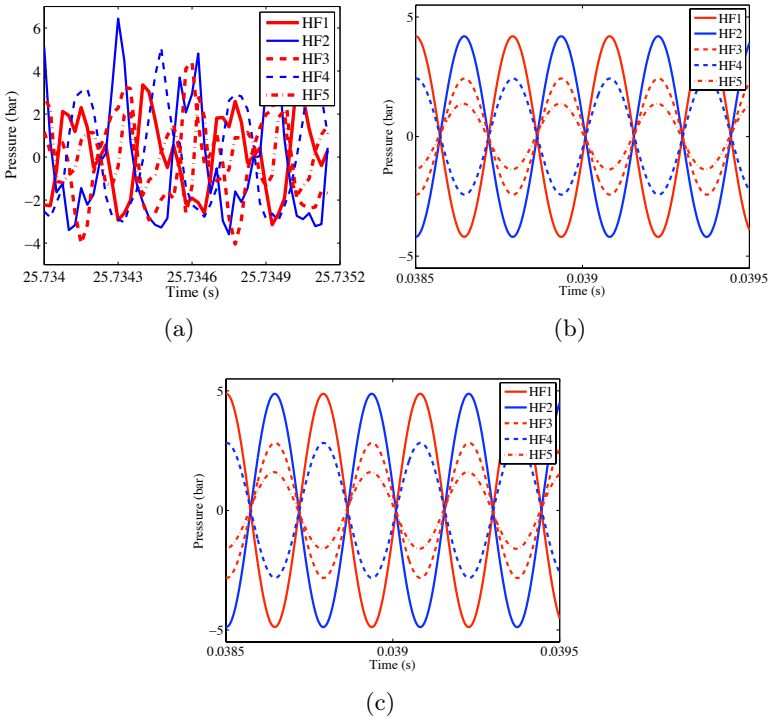

Figure 5.12: *PF2 during an excitation at the 1T2L eigenfrequency - (a) Experimental result - (b) Numerical result, without flame response - (c) Numerical result taking into account the flames feedback with the FAME model.*

demonstrates that, in the Mascotte configuration, the flame motion due to the acoustic oscillation has a non negligible impact on the amplitude of the acoustic wave. The amplitude increase is not dramatic but corresponds to the observed sensitive coupling between acoustics and combustion during the 1T2L modulation.

In the hot fire experiment, it is not possible to know what the amplitude would be in the absence of a flame response and one cannot estimate the difference in level associated with the coupling. The amplitude increase associated with the coupling is probably greater than that obtained with the model because we have not yet accounted for the asymmetry of the flame pattern and of the corresponding acoustic field. As indicated in section 4.7, this could lead to an increase of the response.

Combustion response modeled by SDM

Simulations with the SDM model requires adjustments of additional parameters as described in section 5.5. One has to specify the initial droplet size d_0 (the diameter of droplets after primary and secondary atomization without acoustic modulation) and the critical Weber number We_c. As already indicated, these parameters are not easy to evaluate precisely. These quantities are chosen in a reasonable range to illustrate the physical content of the model:

$$d_0 = 10\ \mu\mathrm{m}, \tag{5.91}$$

$$\mathrm{We}_c = 0.5. \tag{5.92}$$

Fig. 5.13 (a) shows the evolution of the fifth modal amplitude $\eta_5(t)$, corresponding to the 1T2L mode. In Fig. 5.13 (b), the variation of droplet size is indicated. When the acoustic level increases, droplet break-up is enhanced and the droplet size decreases. The droplet inertia decreases correlatively and the droplet motion is more tightly linked to the acoustic velocity field.

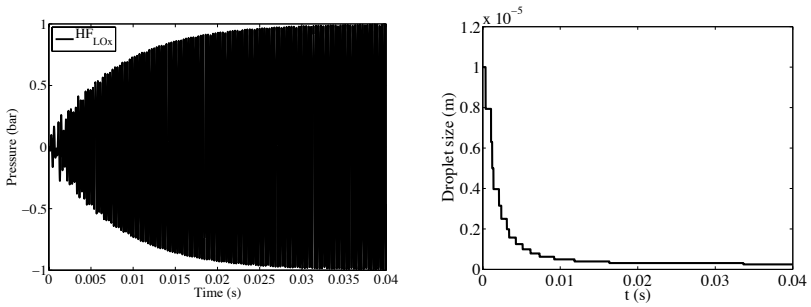

(a) (b)

Figure 5.13: *(a) Temporal evolution of the component on the 1T2L mode η_5 - (b) Evolution of the droplets size during the modulated test.*

The result of this process is shown in Fig. 5.14. The resulting acoustic field at the end of the transient regime for the FAME and SDM models is close.

5.7.2 Comparison - Acoustics solved with AVSP

It is now worth examining the model results obtained by replacing the approximate modal calculations by a more precise determination based on the AVSP Helmholtz solver.
The geometry and flow parameters are specified below for the cold flow and hot fire experiments.

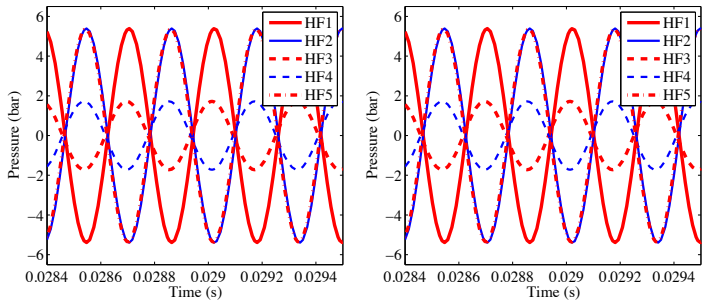

Figure 5.14: *PF2 during an excitation at the 1T2L eigenfrequency - (a) FAME model - (b) SDM model. Both models predict the same final amplitude.*

5.7.2.1 Cold flow experiments: damping evaluation

Following the procedure described previously, damping coefficients are identified.
The estimated and measured signals corresponding to cold flow experiments displayed in Fig. 5.15 are very close in this case, indicating that a precise determination of the system eigenmodes is important. The relative amplitude between the different sensors is well found and even subtle phase differences are identified.

5.7.2.2 Hot fire comparisons

Figure 5.16 shows signals obtained in the experiment and from the low order model. Here again the modeling (in this case based on FAME) provides a suitable representation of experimental observations. As noticed with the simplified geometry study, the comparison between 5.16 (a) and (b) shows that the source term predicted by the FAME model explains a significant increase of the pressure oscillation amplitude (around 20% here).

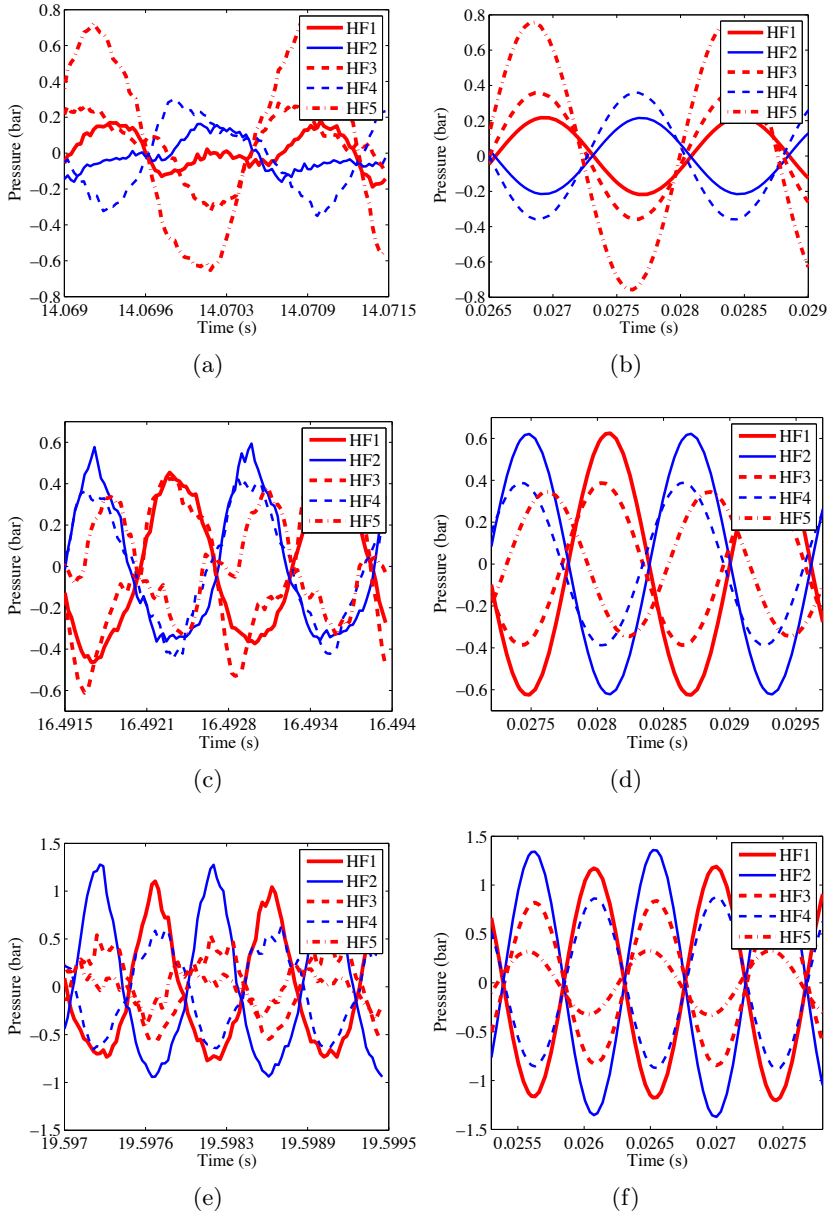

Figure 5.15: *Comparison between experimental data, HF pressure sensors for OP1 in (a), (c) and (e), and numerical results, reconstructed HF sensors in (b), (d) and (f) - (a,b) 1T mode - (c,d) 1T1L mode - (e,f) 1T2L mode.*

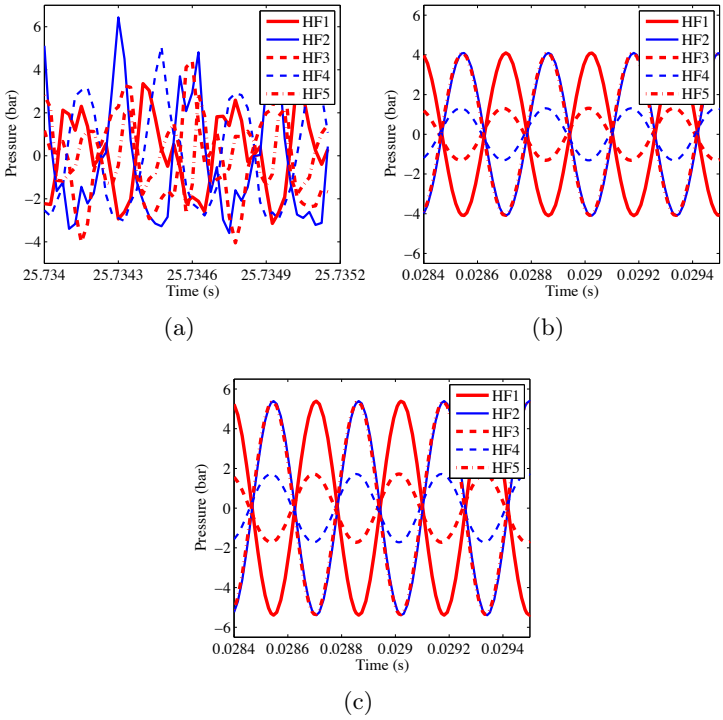

Figure 5.16: *PF2 during an excitation at the 1T2L eigenfrequency - (a) Experimental result - (b) Numerical result, without flame response - (c) Numerical result taking into account the flames feedback with the FAME model.*

5.8 Towards a realistic engine instability prediction

It is now worth applying the LOM to a stability analysis of a configuration which approximately corresponds to that of a real scale engine. The validity of the following simulation is submitted to many uncertainties. Some of them have been discussed previously: (1) information is not available on the liquid core intact length and on the spray characteristics, (2) the spray response to acoustics is not well documented and further information is needed on this process, (3) the damping characteristics of the chamber are not known. Other uncertainties are caused by the lack of precise information on real engines due to confidentiality. The geometry and flow parameters have been chosen to roughly match those found in a typical engine exemplified by the Vulcain 2 engine of Ariane 5.

5.8.1 Geometrical definition and flow parameters.

The geometry used for this computation is based on a schematic representation of the engine found in a data sheet issued by Astrium. The geometry is an approximation of that of the real engine. It comprises the main chamber, injectors and the LOX dome. In Vulcain 2, the injection plate comprises more than 500 injectors. For the sake of simplicity, this arrangement is replaced by 19 effective injectors. The injection area is conserved and the mass flow rates of the successive injection rings correspond to those found in the real engine when the backplane is subdivided in successive annular slices. The geometry and mesh are displayed in Fig. 5.17.
The mesh comprises 551731 cells and 114888 nodes. The dome and injectors are filled with liquid oxygen at $T_{LOx} = 96.7$ K, which corresponds to a sound velocity $c = 1000$ m.s^{-1}. In the chamber, the data used are gathered in table 5.5. These data can be found on Astrium website (Astrium 2009).

	T (K)	γ	c (m.s^{-1})
Dome and injectors	96.7	1.7	1000
Chamber	3500	1.2	1600

Table 5.5: *Values of some thermodynamical parameters in Vulcain 2*

5.8.2 Acoustic study

The previous set of parameters is first used to determine the system eigenmodes with AVSP. Eigenfrequencies determined in this way are gathered in table 5.6. Some of the modal pressure distributions are shown in Fig. 5.18. One first notes that for each eigenfrequency corresponding to a transverse mode, there

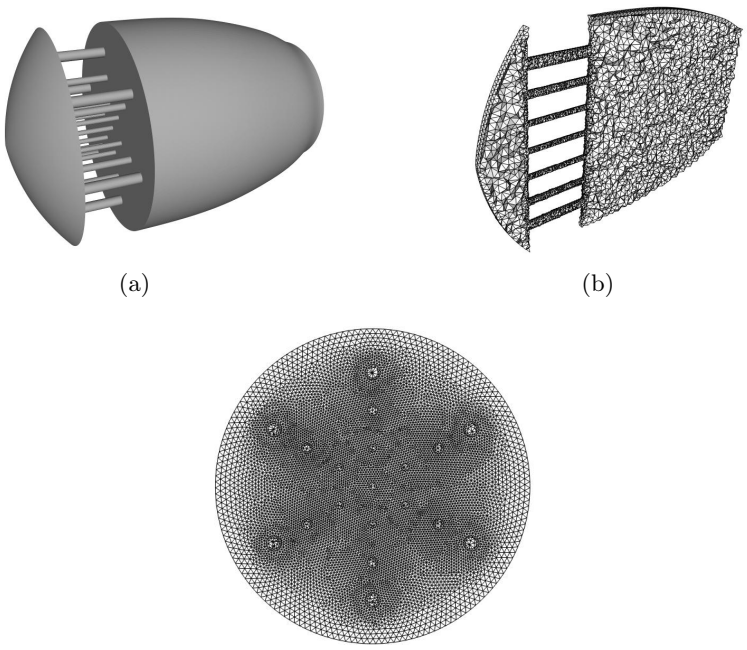

(a) (b)

(c)

Figure 5.17: *Configuration of the computation - (a) 3D domain - (b) cut of the mesh in the longitudinal direction - (c) cut of the mesh in the injection plane.*

mode	$H_{dome+ch}$	$1T_{dome}$	$1L_{ch}$	$1T_{ch}$	$2T_{dome}$	$1L_{dome}$	$1T1L_{ch}$
f (Hz)	352	1798	2045	2386	2782	3140	3395

Table 5.6: *Resonant frequencies obtained for Vulcain 2 rocket engine.*

are actually two twin modes. This is due to the cylindrical symmetry. The same azimuthal modal number m corresponds to an azimuthal structure defined by $\cos m\theta$ and by $\sin m\theta$. The combination of these two modes of equal amplitude gives rise to rotating modes. It is also interesting to see that among the first seven modes of the system given in table 5.6, four involve the dome. An accurate modeling of this element is therefore important in a detailed analysis of the system dynamics.
The spatial modal structures and frequencies obtained previously may now be used in a temporal computation. As in our previous simulations one has to specify submodels and characteristic parameters. These items are listed below:

- The combustion model,
- The damping coefficients ξ_m,

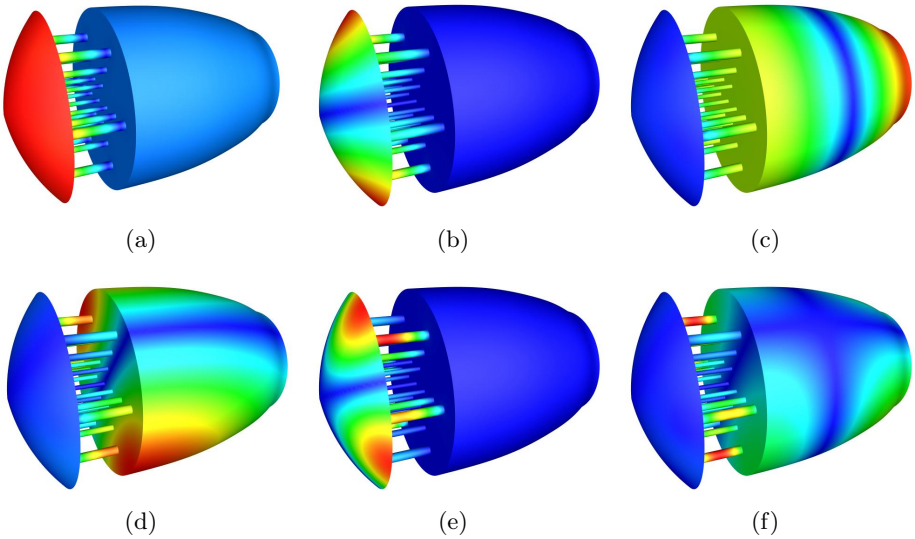

Figure 5.18: *Pressure amplitude for 6 modes computed with AVSP - (a) Coupled dome-chamber longitudinal mode - (b) 1T mode in the injection dome - (c) 1L mode in the chamber - (d) 1T mode in the chamber - (e) 2T mode in the dome - (f) 1T1L mode in the chamber.*

- The initial conditions,
- The excitation source term.

These submodels and parameters are selected in the next sections.

5.8.3 Combustion model

The *extended SDM model*, described in section 5.5 is selected because its formulation is independent of the geometry. In the absence of trustworthy information, the initial droplet size and the critical Weber number are chosen arbitrarily.

$$d_0 = 100\ \mu\text{m}, \tag{5.93}$$

$$\text{We}_c = 1. \tag{5.94}$$

5.8.4 Damping coefficients

The damping coefficients cannot be evaluated by the procedure employed in the MIC experiments. Cold flow experiments are not available and in the absence of such data, these parameters are fixed arbitrarily as well. Coefficients are chosen

by following two general rules. Longitudinal modes are damped effectively by the nozzle. Damping factors for the transverse modes must have the same order of magnitude as those found in the MIC experiments, because dimensions and frequencies are relatively close.

5.8.5 Initial conditions

It is natural to choose the simplest initial conditions for the acoustic pressure and velocity which are both set equal to zero at the beginning of the simulation. This corresponds to:

$$\eta_m(0) = 0, \tag{5.95}$$
$$\dot{\eta}_m(0) = 0. \tag{5.96}$$

5.8.6 Excitation source term

It is interesting to trigger the instability by a localized energy deposition (described in 5.3.2). The total energy, the location, and the time lapse of this disturbance can be changed and its effect on stability can be studied. One attractive feature of this scheme is that it is possible to simulate the type of data which is obtained from experiments in the form of stability maps such as the one reproduced in Fig. 5.19 from Hulka and Hutt (1995).

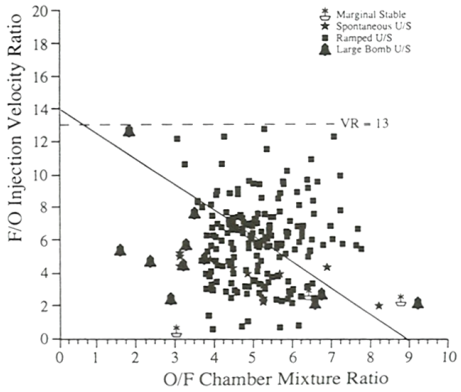

Figure 5.19: *Combustion stability mapping as a function of injection velociy ratio and chamber mixture ratio for shear-coaxial elements with impinging fuel (from Hulka and Hutt (1995)).*

In this figure, the stability of an engine depends on 3 parameters. The intensity of excitation, the mixture ratio and the injection velocity ratio. The injector shape also influences the dynamics of the system but this is taken to be fixed. Roughly, the mixture ratio change the modal characteristics (by modifying the

temperature level and distribution), the injection velocity ratio - or momentum flux ratio determines the spray characteristics for a given injector geometry. The method developed so far takes into account these parameters but in a simplified way. Some of the processes and parameters need further studies. For instance, the link between injection velocity ratio and atomization is not fully documented and the response of a spray to an acoustic field needs further analysis and modeling. The LOM tool is structured to include descriptions of these phenomena.

The current modeling level is illustrated in Fig. 5.20. The difference between the two cases shown in this figure ((a) (b) and (c) (d)) is the intensity of the energy pulse used to trigger an instability. In one case, the pulse is weak, and combustion remains stable. In the other case, the pulse triggers the instability. Fig. 5.20 (c) and (d), indicates that the pulse almost instantaneously divides by five the mean droplet size. Droplets then follow the acoustic field, which create a Rayleigh source term greater than the losses, the acoustic wave amplitude increases. The unstable loop is then operating following the mechanism identified and described in chapter 3.

The maps are obtained for a given initial droplet size d_0. This value depends on the velocity ratio. If the mean droplet diameter d_0 could be defined as a function of the velocity ratio, it would be possible to obtain the kind of map shown in Fig. 5.19. This type of correlation can be found in the literature, but their range of validity is often limited. For example Vingert et al. (1995) gives for coaxial injectors with a recess:

$$D_{32} = 127 \left(\frac{V_r}{160}\right)^{-0.93} \left(\frac{D_l}{2}\right)^{2.25} \left(\frac{D_g}{3}\right)^{-2.65} \left(\frac{R}{D_l}\right)^{-0.26}, \qquad (5.97)$$

where D_{32} is the Sauter mean diameter, $V_r = V_g - V_l$ is the relative injection velocity, D_l is the LOx post inner diameter, D_g is the annular gap outer diameter and R is the recess length. It is obtained for water and the link is not straightforward between water and liquid oxygen. As a result, the capability of constructing *a priori* stability maps for a given engine is submitted to the accurate evaluation of the droplet size distribution after atomization.

It is also subject to a refined understanding of how acoustics modifies the atomization process. In this study, an acoustic Weber number is defined, which is basically the Weber number using the maximum acoustic velocity, and then it is compared with a critic Weber number to decide whether atomization takes place or not. It is likely that this technique does not fully account for the complex phenomena which arise when a liquid stream is submitted to high frequency acoustic modes under hot fire conditions. Some of these phenomena

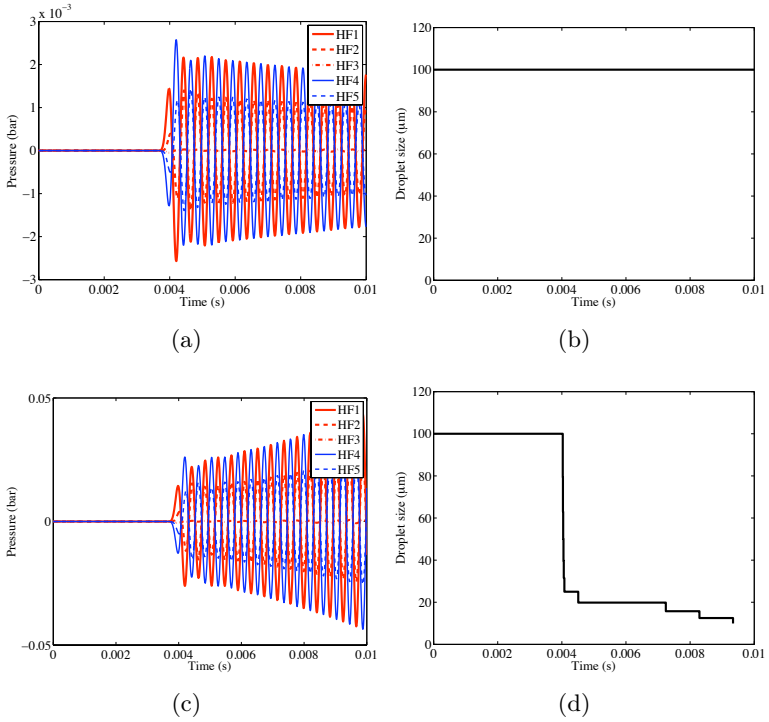

Figure 5.20: *Instability study carried out for weak (a,b) and strong (c,d) initial perturbations - (a,c) Evolution of pressure on the simulated HF sensors - (b,d) Evolution of the droplet size during the computation. When the initial perturbation is sufficient, droplets are atomized, they become smaller and follow the acoustic field more tightly. It creates an increase of the pressure response.*

are described in a recent article of Baillot et al. (2009) but more information is needed.

5.9 Conclusion

Low order modeling of combustion acoustic coupling for high frequency analysis is considered in this chapter. Simulations are based on a modal expansion method in which the pressure field is expanded in terms of the eigenmodes of the system. This is used in combination with a variety of submodels to simulate the response of various configurations. The acoustic modal analysis is first considered and treated in an approximate way using matching conditions to couple the thrust chamber with the engine dome. An exact calculation is also carried out using the AVSP Helmholtz solver. Initial conditions are examined and it is shown that an initial pulse can be expanded on a set of eigenmodes. The external excitation by the VHAM is modeled and included in the low order

tool. Damping growth rates are then determined for the MIC by comparing experiments with simulations under cold flow conditions. The modeling tool is then tested under hot fire conditions corresponding to MIC experiments. It is shown that experimental observations are reasonably well represented in this case. The low order model is finally applied to the analysis of instabilities in a configuration resembling that of the Vulcain 2 engine. This is only used to illustrate the capacity of the model to represent triggering of high frequency instabilities.

Part III

Numerical Simulation

Chapter 6

A combustion model for turbulent diffusion flames

This chapter considers the modeling of heat release for LES of turbulent diffusion flames. Existing LES equations are outlined, then a model based on the infinitely fast chemistry assumption is presented. The idea of the FER (Forward Estimate of the Reaction rate) model is to evaluate the reaction rate necessary for the reactant to be within the infinitely fast chemistry limit at each time step. It provides a simple and computationally efficient method which takes into account the particularity of cryogenic combustion. It is then embedded in the code AVBP and validated on a well documented non-premixed configuration, the "H3 flame". Velocity, mixing, species mass fractions, and temperature profiles are compared with experiments and show agreement. Finally, scatter plots are consistent with the infinitely fast chemistry hypothesis, which in turn validates the combustion model.

6.1 Introduction

The increased availability of computational resources opens new perspectives in the simulation of complex flow configurations. It is in particular possible to develop novel tools for the analysis of combustion instabilities. The general objective in this field is to establish models and computational methods allowing calculations of the combustion dynamics in model scale and more practical systems. The present research is focused on these issues and on verification and validations of models and simulation tools in well controlled situations.
It is established (see for example Richecoeur (2006)) that simulation based on the averaged Navier-Stokes equations (RANS) is not suited to study combustion instabilities (though possible in some particular conditions (Armitage et al. 2006)). The coupling between acoustics and combustion is an unsteady process

which requires Large Eddy Simulation methodologies. Because combustion is accompanied by large variations of density, it is important to account for these effects. Since the coupling involves acoustic perturbations, a compressible flow solver is needed. These different features are suitably represented in the AVBP code which is specifically developed to deal with internal flows and in particular those found in combustion applications. It is then natural to use this platform in the following developement. AVBP operates on unstructured meshes which is quite useful in the analysis of complicated geometries like those found in practical applications.
One central issue however is the modeling of turbulent combustion. This has been extensively investigated during the last period. Most of the work has concerned averaged descriptions based on RANS. Current efforts are made to develop combustion models for large eddy simulations and this topic is rapidly evolving. Most of the developments have paralleled those derived for RANS but with some modifications. This chapter begins with a general presentation of combustion models for LES. It contains an initial review of statistical descriptions based on probability density function (pdf) concepts and their application to the calculation of filtered reaction rates. The pdf can be presumed (with β-functions for example) or transported with a balance equation but this last approach is not often used in LES because of its complexity. Combustion can also be described by considering that mixing is the controlling process. This leads to some standard evaluations of the reaction rate in terms of the scalar dissipation rate ($\chi = \overline{2D(\nabla Z)^2}$). Combustion is then described using of a progress variable c or a mixture fraction Z. Another approach which has had considerable success in turbulent combustion modeling of practical configurations consists in considering that the flame is composed of reactive layers which can be identified and described in terms of local combustion rates. The amount of flame surface can be quantified algebraically or obtained from a balance equation for the surface density. In the premixed case, the treatment can also be based on a level set formulation, the G-equation. The chapter begins with a general presentation of the filtered equations. Subgrid scale modeling is considered next. These concepts are then used to treat the case of a three-dimensional jet flame called the "H3 flame". This flame is well documented and data gathered from a series of experiments will be used to validate the combustion model. The next chapter will be devoted to some preliminary calculations of the interaction between the H3 flame and transverse acoustic waves.

6.2 Basic filtered equations

The mass, momentum and species balance equations are treated with a density weighted filtering scheme. This yields the following set of equations (Poinsot and Veynante 2001):

- Mass

$$\frac{\partial \overline{\rho}}{\partial t} + \frac{\partial}{\partial x_i}(\overline{\rho}\tilde{v}_i) = 0 \tag{6.1}$$

- Momentum

$$\frac{\partial \overline{\rho}\tilde{v}_i}{\partial t} + \frac{\partial}{\partial x_j}(\overline{\rho}\tilde{v}_i\tilde{v}_j) = -\frac{\partial}{\partial x_j}[\overline{p}\delta_{ij} - \overline{\tau_{ij}} - \overline{\tau_{ij}}^t] \tag{6.2}$$

- Chemical species

$$\frac{\partial \overline{\rho}\tilde{Y}_k}{\partial t} + \frac{\partial}{\partial x_j}(\overline{\rho}\tilde{Y}_k\tilde{v}_j) = -\frac{\partial}{\partial x_j}[\overline{J_{j,k}} + \overline{J_{j,k}}^t] + \overline{\rho}\widetilde{\dot{\omega}}_k \qquad k = 1, N \tag{6.3}$$

- Energy

$$\frac{\partial \overline{\rho}\tilde{E}}{\partial t} + \frac{\partial}{\partial x_j}(\overline{\rho}\tilde{E}\tilde{v}_j) = -\frac{\partial}{\partial x_j}\left[\overline{v_i(P\delta_{ij} - \tau_{ij})} + \overline{q_j} + \overline{q_j}^t\right] + \overline{\dot{\omega}}_T + \overline{Q_r} \tag{6.4}$$

where ρ is the density, v_i the i^{th} component of velocity, p the pressure, τ_{ij} the shear stress tensor, $\overline{\tau_{ij}}^t$ the Reynolds stress tensor, Y_k the mass fraction of species k, $J_{i,k}$ the ith component of species k diffusive flux, $\dot{\omega}_k$ the production rate of species k, $\overline{J_{i,k}}^t$ the ith component of species k turbulent diffusive flux, E the total energy (the sum of internal and kinetic energies), q_i the ith component of the heat flux, $\overline{q_i}^t$ the ith component of the turbulent heat flux, Q_r is the radiative energy and finally $\dot{\omega}_T$ is the heat release rate.

Fluxes and tensors are given by the following equations:

$$\tau_{ij} = 2\mu(S_{ij} - \frac{1}{3}\delta_{ij}S_{ll}) \tag{6.5}$$

with

$$S_{ij} = \frac{1}{2}\left(\frac{\partial v_i}{\partial x_j} + \frac{\partial v_j}{\partial x_i}\right) \tag{6.6}$$

$$\overline{\tau_{ij}}^t = -\overline{\rho}(\widetilde{v_i v_j} - \tilde{v}_i\tilde{v}_j) \tag{6.7}$$

$$J_{i,k} = -\rho V_{k,i}Y_k = -\rho\left(D_k\frac{W_k}{W}\frac{\partial X_k}{\partial x_i} - Y_k V_i^c\right) \tag{6.8}$$

$$\overline{J_{i,k}}^t = \overline{\rho}(\widetilde{v_i Y_k} - \tilde{v}_i\tilde{Y}_k) \tag{6.9}$$

$$q_i = -\lambda\frac{\partial T}{\partial x_i} + \sum_{k=1}^{N} J_{i,k}h_{s,k} \tag{6.10}$$

$$\overline{q_i}^t = \overline{\rho}(\widetilde{v_i E} - \tilde{v}_i \tilde{E}) \tag{6.11}$$

where μ is the dynamic viscosity, S_{ij} the strain rate tensor, $V_{k,i}$ the ith component of the diffusion velocity vector of species k, D_k the diffusion coefficient of species k, W_k the molar mass of species k, W the mixture molar mass, X_k the molar fraction of species k, V_i^c the correction diffusion term and $h_{s,k}$ the sensible enthalpy of species k.
These expressions involve subgrid scale fluxes of momentum, species and sensible enthalpy ($\widetilde{v_i v_j} - \tilde{v}_i \tilde{v}_j$, $\widetilde{v_i Y_k} - \tilde{v}_i \tilde{Y}_k$, $\widetilde{v_i h_s} - \tilde{v}_i \tilde{h}_s$, ...) and require subgrid scale models to close the filtered set of equations (Poinsot and Veynante 2001).

6.3 State of the art of non-premixed flame modeling

While Large Eddy Simulation (LES) in combustion is a relatively recent research area, it is progressively becoming a mature field and there are already remarkable demonstrations of the predictive capacities of LES based models in simple or more complex configurations. We here consider particular conditions in which the reactants are injected at low temperature and high pressure. These extreme conditions must be taken into account to deal with combustion in high performance liquid rocket engines. Reactants are liquid or transcritical oxygen (LOx) and gaseous methane (gCH4) or hydrogen (gH2). Because oxygen is pure the chemistry is very fast. Pressure is high (more than 100 bar under nominal operation) and the temperature covers a wide range of values (from 100 K to 3500 K). Under these conditions injection is transcritical and combustion takes place between a transcritical fluid (oxygen) and a supercritical combustible.
The complex features of rocket engine combustion have been extensively studied at the EM2C laboratory, in a joint effort with the ONERA propulsion team. Experiments were carried out on their unique cryogenic experimental bench Mascotte (Herding et al. 1998; Juniper et al. 2000; Juniper and Candel 2003; Singla et al. 2005; Singla et al. 2006; Singla et al. 2007; Candel et al. 2006).
These experiments indicate that flames formed under these conditions are essentially of the non-premixed type. This is clearly illustrated in Fig. 6.1, obtained by Singla et al. (2007) which shows that fuel (gCH4) and oxydizer (LOx) are well separated by the flame sheet, even in the near vicinity of the coaxial injector.
It is then natural to first examine non-premixed combustion models devised during the recent years. For this it is possible to rely on the review of Pitsch (2006) which summarizes some common approaches to non-premixed flame LES modeling, from the simplest formulation of Cook and Riley (1994) relying on equilibrium assumptions (or on the infinitely fast chemistry limit), to the more complex flamelet models of Cook et al. (1997) (steady, incompressible), Cook and Riley (1998) (steady, compressible) or Pitsch et al. (1998) (unsteady). In these latter models one uses the so-called flamelet equation obtained by

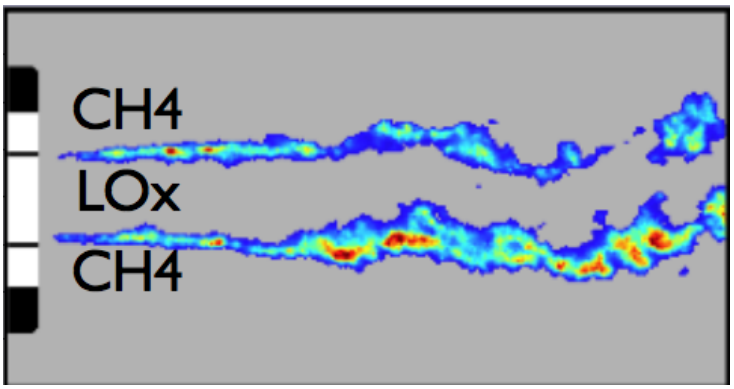

Figure 6.1: *Planar Laser Induced Fluorescence of a high pressure liquid oxygen/methane flame. In this case the flame is formed between GCH4 injected at high speed and liquid oxygen LOx injected at low speed.*

performing a change of variable of the Crocco type on the species balance and temperature equations. This process yields an equation of the form:

$$\frac{\partial Y_k}{\partial t} = \frac{1}{2}\chi\frac{\partial^2 Y_k}{\partial Z^2} + \dot{\omega}_k, \tag{6.12}$$

where $\chi = 2D(\partial Z/\partial x_\perp)^2$ represents the scalar dissipation, and $x_\perp$ is a coordinate in the direction perpendicular to the flame front. The flamelet equation describes the evolution of mass fractions in mixture fraction space. In the local flame element, the chemical species depend on scalar dissipation rate, mixture ratio, mixture fraction time, and on the chemical reaction rates through $\dot{\omega}_k$.
Equilibrium chemistry models consist in providing functions $Y_k(Z)$ and $T(Z)$. The other models quoted previously present variations around this equation. Infinitely fast chemistry models assume that the source term is a delta function centered on the stoichiometric surface $Z = Z_{st}$. In the steady flamelet models the time derivative is considered negligible while in the unsteady flamelet models this is not assumed. Steady and unsteady models are based on the tabulations of Y_k as a function of Z, χ and Z, χ, c respectively, where c is the progress variable. These tables are obtained by calculating a large number of flames using codes such as *OPP diff* or *Flamemaster*.
In Direct Numerical Simulations (DNS) the function $Y_k(Z, \chi, c)$ is sufficient to completely solve combustion. In LES, the variables' fields are spatially filtered. These filtered variables can be deduced from the instantaneous quantities by making use of a probability density function (pdf) p:

$$\tilde{Y}_k = \int Y_k(\eta)\widetilde{p}(\eta)d\eta, \tag{6.13}$$

$$\tilde{T} = \int T(\eta)\widetilde{p}(\eta)d\eta. \tag{6.14}$$

In these models, Y_k is a function of the mixture fraction Z (by assuming for example that chemistry is infinitely fast or by considering that the final state is defined by chemical equilibrium) and of the progress variable c (in unsteady models). The shape of the pdf p is usually presumed (a point which will be discussed later).

There are however two difficulties if one wishes to use the previous formulation in the present application. The first problem is of physical nature. Our objective is to accurately model combustion instabilities driven by a coupling between acoustics and combustion. This requires an explicit determination of the unsteady reaction rate. This quantity acts as a source term in the wave equation defining the pressure field in the thrust chamber and it also intervenes as a source term in the balance equation governing acoustic energy:

$$\frac{\partial e'}{\partial t} + \nabla \cdot f' = \frac{\gamma - 1}{\gamma \overline{p}} p' \dot{\omega}'_T,$$

where e', f', p' and $\dot{\omega}'_T$ are respectively the acoustic energy density, the acoustic energy flux, the acoustic pressure and the unsteady heat release. The source of acoustic energy involves the product of acoustic pressure (p') by heat release ($\dot{\omega}'_T$) fluctuations. These quantities must be predicted accurately.

The second issue is related to the presence of acoustic waves in the calculation. It turns out that methods which are based on algebraic relations for the mass fractions and temperature in terms of the mixture fraction like those used in most non-premixed flame calculations lead to numerical instabilities in a fully compressible code which is only weakly dissipative (as it should be for LES calculations). This leads us to follow a different path, which consists in calculating filtered reaction rates and obtaining the filtered mass fractions and temperature from balance equations for these variables.

One possibility is to deduce the volumetric reaction rate from the reaction rate per unit flame surface. This last quantity is obtained from the absolute value of the mixture fraction gradient. This formulation is described in Appendix B. Systematic calculations and validations carried out with T. Schmitt indicate however that this approach is less easy to generalize to transcritical combustion situations and a different track has been followed.

The general idea is to deduce first the reaction rate from the known distributions of mass fractions and from their evolution. This uses forward estimations of the mass fractions in the absence of a source term taking into account convection and diffusion. A reaction rate is then inferred by using the difference

between these estimates and the mass fractions corresponding to the infinitely fast chemistry limit. Details of this scheme are presented in the next section. The model is then exploited in section 6.5 to calculate a standard non-premixed configuration designated as the "H3 flame". The validation is carried out in the absence of an imposed acoustic field. The situation where an acoustic wave acts on the flame is considered in the next chapter.

6.4 Forward Estimation of Reaction rates (FER) for LES

In this section we show how the reaction rate can be calculated explicitly. This is first done by considering the instantaneous equations. The LES framework is considered in a second stage. In both cases one obtains the reaction rate from known mass fraction fields and from their predicted evolution after one time step. This implies a forward extrapolation of mass fractions in the absence of a chemical source term but accounting for convection and diffusion. A reaction rate is then determined from the difference between the mass fraction estimates and the values corresponding to the infinitely fast chemistry limit.

6.4.1 Derivation of the model in the laminar case

In the model presented subsequently, we focus on diffusion flames at the infinitely fast chemistry limit. To specify the method described in the previous section to obtain the source term, three quantities are transported: species mass fractions, mixture fraction, and Y_k^+, which plays the role of predictor of mass fractions without source terms.

The transport equation for species mass fractions reads:

$$\rho\frac{\partial Y_k}{\partial t} + \rho\boldsymbol{u}\cdot\boldsymbol{\nabla}Y_k = \boldsymbol{\nabla}\cdot(\rho D\boldsymbol{\nabla}Y_k) + \dot{\omega}_k, \tag{6.15}$$

The classical mixture fraction is introduced. Its transport equation is:

$$\rho\frac{\partial Z}{\partial t} + \rho\boldsymbol{u}\cdot\boldsymbol{\nabla}Z = \boldsymbol{\nabla}\cdot(\rho D\boldsymbol{\nabla}Z). \tag{6.16}$$

The mixture fraction Z is zero in the oxidizer one in the fuel. It indicates the local equivalence ratio in the combustion area.
It is convenient to split equation 6.15 and only consider the unsteady, convective and diffusive terms. This equation is solved over the time step δt. The initial condition is the distribution $Y_k(\boldsymbol{x}, t)$ calculated at the previous step. One

obtains in this way a new distribution Y_k^+ which accounts for convection and diffusion.

$$\rho \frac{Y_k^+ - Y_k}{\delta t} + \rho \boldsymbol{u} \cdot \boldsymbol{\nabla} Y_k = \boldsymbol{\nabla} \cdot (\rho D \boldsymbol{\nabla} Y_k). \tag{6.17}$$

It is next possible to integrate the mixture fraction equation 6.16 and determine the values of the mass fractions by assuming that chemistry is infinitely fast. These mass fractions are designated as $Y_k^*(Z)$ to distinguish them from the transported variables $Y_k(\boldsymbol{x}, t)$. The mass fractions $Y_k^*(Z)$ are deduced from the mixture fraction by using algebraic relations derived in the infinitely fast chemistry limit (see for example Poinsot and Veynante (2001)) for a single reaction:

$$Y_F^*(Z) = \begin{cases} 0 \text{ if } Z \leqslant Z_{st} \\ Y_F^0 \dfrac{Z - Z_{st}}{1 - Z_{st}} \text{ if } Z \geqslant Z_{st} \end{cases}$$

$$Y_O^*(Z) = \begin{cases} Y_O^0 (1 - \dfrac{Z}{Z_{st}}) \text{ if } Z \leqslant Z_{st} \\ 0 \text{ if } Z \geqslant Z_{st} \end{cases}$$

$$Y_P^*(Z) = \begin{cases} Y_P^{st} \dfrac{Z}{Z_{st}} \text{ if } Z \leqslant Z_{st} \\ Y_P^{st} \dfrac{1 - Z}{1 - Z_{st}} \text{ if } Z \geqslant Z_{st} \end{cases}$$

where $Y_P^{st} = Y_O^0 + (Y_O^0 - Y_F^0) Z_{st}$ and Z_{st} is the mixture fraction at the flame sheet, Y_F^0 and Y_O^0 are the mass fraction of fuel and oxidizer in injected streams. Mass fractions Y_k^* are deduced from the mixture fraction using the infinitely fast chemistry assumption.

The previous variables are used to obtain the reaction rate. Subtracting Eq. 6.15 from eq. 6.17 yields:

$$\dot{\omega}_k = \rho\frac{\partial Y_k}{\partial t} - \rho\frac{Y_k^+(\boldsymbol{x},t) - Y_k(\boldsymbol{x},t)}{\delta t}. \tag{6.18}$$

$$= \rho\frac{Y_k(Z(\boldsymbol{x},t+\delta t)) - Y_k(\boldsymbol{x},t)}{\delta t} - \rho\frac{Y_k^+(\boldsymbol{x},t) - Y_k(\boldsymbol{x},t)}{\delta t}. \tag{6.19}$$

$$= \rho\frac{Y_k(Z(\boldsymbol{x},t+\delta t)) - Y_k^+(\boldsymbol{x},t)}{\delta t}. \tag{6.20}$$

To determine $\dot{\omega}_k$ it is necessary to estimate the species mass fraction at time $t+\delta t$. This can be achieved by making use of the infinitely fast chemistry assumption and replacing $Y_k(\boldsymbol{x},t+\delta t)$ in the previous expression by $Y_k^*[Z(\boldsymbol{x},t+\delta t)]$:

$$\dot{\omega}_k = \rho\frac{Y_k^*(Z(\boldsymbol{x},t+\delta t)) - Y_k^+(\boldsymbol{x},t)}{\delta t} \tag{6.21}$$

It is possible to use the previous expression by making use of the mixture fraction calculated at time $t+\delta t$. Another possibility is to use a linear approximation of Z:

$$Z(\boldsymbol{x},t+\delta t) = Z(\boldsymbol{x},t) + \delta Z, \tag{6.22}$$

$$= Z(\boldsymbol{x},t) + \frac{\partial Z}{\partial t}\delta t, \tag{6.23}$$

This can be used to estimate $Y_k^*[Z(\boldsymbol{x},t+\delta t)]$:

$$Y_k^*(Z(\boldsymbol{x},t+\delta Z)) = Y_k^*(Z+\delta Z), \tag{6.24}$$

$$= Y_k^*(Z) + \frac{\partial Y_k^*}{\partial Z}\delta Z, \tag{6.25}$$

$$= Y_k^*(Z(\boldsymbol{x},t)) + \frac{\partial Y_k^*}{\partial Z}\frac{\partial Z}{\partial t}\delta t. \tag{6.26}$$

Finally, eq. 6.21 becomes

$$\dot{\omega}_k = \rho\frac{Y_k^*(Z(\boldsymbol{x},t)) - Y_k^+(\boldsymbol{x},t)}{\delta t} + \rho\frac{\partial Y_k^*}{\partial Z}\frac{\partial Z}{\partial t}. \tag{6.27}$$

Numerically, the scheme consists in computing first $Y_k^+(\boldsymbol{x},t)$ (which corresponds basically to the determination of convection and diffusion effects on Y_k) and $\partial Z/\partial t$. $Y_k^*(Z(\boldsymbol{x},t))$ and $\partial Y_k^*/\partial Z$ are known exactly from the analytical functions given previously. The time δt corresponds to the computation time step.

6.4.2 Derivation of spatially filtered reaction rates

The same reasoning is followed to obtain the subgrid scale model in the case of turbulent combustion. Once again, the objective is to model the filtered reaction rate $\widetilde{\dot{\omega}}_k$.
The transported equation for LES are, for species mass fraction:

$$\overline{\rho}\frac{\partial \widetilde{Y_k}}{\partial t} + \overline{\rho}\widetilde{\boldsymbol{u}} \cdot \boldsymbol{\nabla}\widetilde{Y_k} = \boldsymbol{\nabla} \cdot (\overline{\rho}(D + D_t)\boldsymbol{\nabla}\widetilde{Y_k}) + \widetilde{\dot{\omega}}_k, \tag{6.28}$$

$$\overline{\rho}\frac{\partial \widetilde{Z}}{\partial t} + \overline{\rho}\boldsymbol{u} \cdot \boldsymbol{\nabla}\widetilde{Z} = \boldsymbol{\nabla} \cdot (\overline{\rho}(D + D_t)\boldsymbol{\nabla}\widetilde{Z}), \tag{6.29}$$

$$\overline{\rho}\frac{\widetilde{Y_k^+} - \widetilde{Y_k}}{\delta t} + \overline{\rho}\widetilde{\boldsymbol{u}} \cdot \boldsymbol{\nabla}\widetilde{Y_k} = \boldsymbol{\nabla} \cdot (\overline{\rho}(D + D_t)\boldsymbol{\nabla}\widetilde{Y_k}). \tag{6.30}$$

The main difference compared to the laminar framework is that there are no analytical solutions for the filtered mass fractions Y_k^*, which depend on $\widetilde{Z}$ and $\widetilde{Z''^2}$, where $\widetilde{Z''^2}$ is the subgrid scale variance of Z.

$$\widetilde{Y_k^*}(\widetilde{Z}, \widetilde{Z''^2}) = \int_0^1 Y_k^*(\boldsymbol{x}, t)\widetilde{p}(Z^*)dZ^*. \tag{6.31}$$

This requires a specification of the probability density function. This can be presumed by making use of a beta-shape which is adjusted with respect to the mean $\widetilde{Z}$ and the subgrid scale variance $\widetilde{Z''^2}$ of the mixture fraction. It is also necessary to specify a method allowing the estimation of $\widetilde{Z''^2}$. It is in practice convenient to tabulate $\widetilde{Y_k^*}(\widetilde{Z}(\boldsymbol{x}, t), \widetilde{Z''^2}(\boldsymbol{x}, t))$ with respect to $\widetilde{Z}$ ans $\widetilde{Z''^2}$ before integration in the 3D simulation $\widetilde{Y_k^*}$. (one may refer to Peters (2001) for details or to Appendix B.3.3.1 for some elements).
To obtain $\widetilde{Z''^2}$ in the computation, several methods are available. One possibility could be to use a scale similarity assumption introduced by Cook and Riley (1994).

$$\widetilde{Z''^2} = \widetilde{(Z - \widetilde{Z})^2} = C_z(\widehat{(\widetilde{Z}^2)} - (\widehat{\widetilde{Z}})^2) \tag{6.32}$$

where $\widehat{f}$ denotes a test filter larger than the LES filter. C_z is a model parameter to be estimated. Unfortunately, in AVBP, filtering this type of quantities is not an easy task. To avoid the problem, the variance of $\widetilde{Z}$ could be transported (as in RANS simulations). Both methods require heavy modifications of the code. To test the combustion model, a simpler technique is envisaged here.
The easiest way to close this term is to express the variance in terms of Z and the gradient of Z. This is carried out by using the model of Pierce and

Moin (1998), who applied the dynamic procedure to derive an expression for the variance.

$$\widetilde{Z''^2} = C\Delta^2 |\nabla \widetilde{Z}|^2, \tag{6.33}$$

where Δ is the local filter size. In the following computations, the value of C is not obtained by the dynamic procedure, it is assumed constant and ($C = 0.15$). It is shown that this approximation has little effect on the present simulations. In this framework, the filtered reaction rate reads:

$$\widetilde{\dot{\omega}}_k = \overline{\rho} \frac{\widetilde{Y_k^*}\left(\widetilde{Z}(\boldsymbol{x}, t+\delta t), \widetilde{Z''^2}(\boldsymbol{x}, t+\delta t)\right) - \widetilde{Y_k^+}(\boldsymbol{x}, t)}{\delta t} \tag{6.34}$$

It is possible to use this expression by integrating the filtered mixture fraction equation and estimating the filtered variance of the mixture fraction at time $t + \delta t$. It is also possible to use linear approximations for $\widetilde{Z}$, $\widetilde{Z''^2}$ and on $\widetilde{Y_k^*}$ by writing Taylor expansions for these variables:

$$\begin{aligned}
\widetilde{Y_k^*}\left(\widetilde{Z}(\boldsymbol{x}, t+\delta t), \widetilde{Z''^2}(\boldsymbol{x}, t+\delta t)\right) &= \widetilde{Y_k^*}(\widetilde{Z} + d\widetilde{Z}, \widetilde{Z''^2} + d\widetilde{Z''^2}), && (6.35)\\
&= \widetilde{Y_k^*}(\widetilde{Z}, \widetilde{Z''^2}) + \frac{\partial \widetilde{Y_k^*}}{\partial \widetilde{Z}} \delta \widetilde{Z} \\
&\quad + \frac{\partial \widetilde{Y_k^*}}{\partial \widetilde{Z''^2}} \delta \widetilde{Z''^2}, && (6.36)\\
&= \widetilde{Y_k^*}(\widetilde{Z}, \widetilde{Z''^2}) + \frac{\partial \widetilde{Y_k^*}}{\partial \widetilde{Z}} \frac{\partial \widetilde{Z}}{\partial t} \delta t \\
&\quad + \frac{\partial \widetilde{Y_k^*}}{\partial \widetilde{Z''^2}} \frac{\partial \widetilde{Z''^2}}{\partial t} \delta t. && (6.37)
\end{aligned}$$

The filtered reaction rate takes the final form:

$$\widetilde{\dot{\omega}}_k = \overline{\rho} \frac{\widetilde{Y_k^*}(\widetilde{Z}, \widetilde{Z''^2}) - \widetilde{Y_k^+}(\boldsymbol{x}, t)}{\delta t} + \overline{\rho} \frac{\partial \widetilde{Y_k^*}}{\partial \widetilde{Z}} \frac{\partial \widetilde{Z}}{\partial t} + \overline{\rho} \frac{\partial \widetilde{Y_k^*}}{\partial \widetilde{Z''^2}} \frac{\partial \widetilde{Z''^2}}{\partial t}. \tag{6.38}$$

First and second terms are similar to the ones obtained in the laminar model. Tabulation gives $\widetilde{Y_k^*}(\widetilde{Z}, \widetilde{Z''^2})$ and their partial derivative as a function of $\widetilde{Z}$ and $\widetilde{Z''^2}$. The subgrid variance $\widetilde{Z''^2}$ is estimated using the simple gradient model and all other quantities are calculated.

6.5 Validation of the turbulent combustion model

As we are interested in the numerical description of non-premixed jet flames, it is natural to use the model in a typical free jet flame geometry. Results can be

compared in this case with experimental data. One can then use the model to examine the effect of coupling between the jet flame and a transverse acoustic mode.

6.5.1 Experimental configuration

A simple and well documented flame is now considered. The "H3 flame" is selected for comparison, because it shares some common characteristics with the cryogenic jet flames considered in this study. In both cases one may consider that chemistry is infinitely fast. This flame has been investigated experimentally and simulated during the second TNF[1] workshop. This constitutes a standard test case for non-premixed flame modeling. The data gathered by Robert Barlow and Andreas Dreizler are contained in the following articles: Cheng et al. (1995), Pfuderer et al. (1996) and Renfro et al. (2004). This case has also been used to validate large eddy simulations (see for example Pitsch et al. (1998)).
A volumetric mixture of hydrogen and nitrogen (50%/50% vol.), is injected through a nozzle with a diameter of 8 mm and a maximum centerline velocity of 42.3 m.s^{-1}. The radial fuel velocity distribution is assumed to follow the 1/7-power law, the mean fuel velocity is thus 34.8 m/s and the Reynolds number is Re=10,000. The fuel jet is surrounded by a large air stream injected through a nozzle with a diameter of 140 mm and a velocity of 0.2 m.s^{-1}. Fig. 6.2 (a) shows the experimental setup.

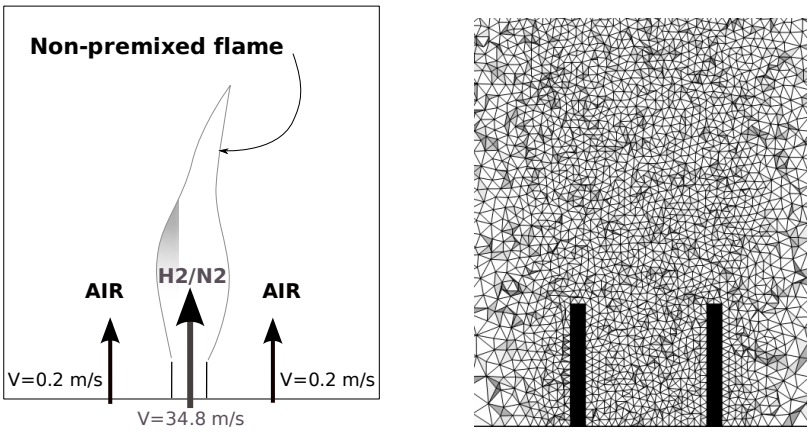

(a) (b)

Figure 6.2: *(a) H3 flame injection parameters - (b) Cut of the mesh in the inlet nozzle area.*

[1]Turbulent Non-premixed Flames

6.5.2 Three-dimensional jet flame calculations

Three-dimensional jet flame computations are now examined. Conditions adopted for these simulations are these of the H3 flame. Fig. 6.2 (b) shows a part of the mesh. The total mesh comprises 1,500,000 cells. In the diameter of the injector, 13 cells suitably describe upstream turbulence and injection velocity profile. Navier-Stokes Characteristic Boundary Conditions (NSCBC) to specify all boundary conditions (Poinsot and Lele 1992). Uniform velocity, is imposed in the main jet ($v = 34.8$ m.s^{-1}) and in the coflow ($v = 0.2$ m.s^{-1}), for the sake of simplicity. Pressure outlet is imposed at atmospheric pressure. Lateral walls are treated as slipping walls. The numerical scheme used is TTG4A and the turbulence subgrid model is WALE. These parameters are gathered in table 6.1.

Number of cells	1,500,000
Numerical scheme	TTG4A
Turbulence model	WALE
Boundary conditions	NSCBC

Table 6.1: *Parameters of the computation.*

6.5.2.1 Visualization

Fig. 6.3 (a) and (b) show instantaneous distributions of mixture fraction, temperature and heat release. An isosurface of temperature (T=1800 K) colored by velocity is represented in Fig. 6.3 (c). The flame shape is qualitatively satisfactory. We can see clearly the turbulent structures that destabilize the jet.

6.5.3 Comparison between experiments and simulation

Validation is divided into three steps. First, velocity fields are compared along the centerline and perpendicular to the jet at different locations. This step validates the jet aerodynamics. Then, predicted species mass fractions are compared with experiments to check mixing characteristics. Finally, temperature distributions are compared to evaluate the combustion model accuracy. To complete this study, scatter plots of the different species and temperature are presented to check if they are consistent with the main hypothesis of the model - infinitely fast chemistry.

6.5.3.1 Velocity profiles

Experimental and numerical velocity profiles are shown in Fig. 6.4. Beginning of Fig. 6.4 (a) highlights one difficulty of the computations presented here. For

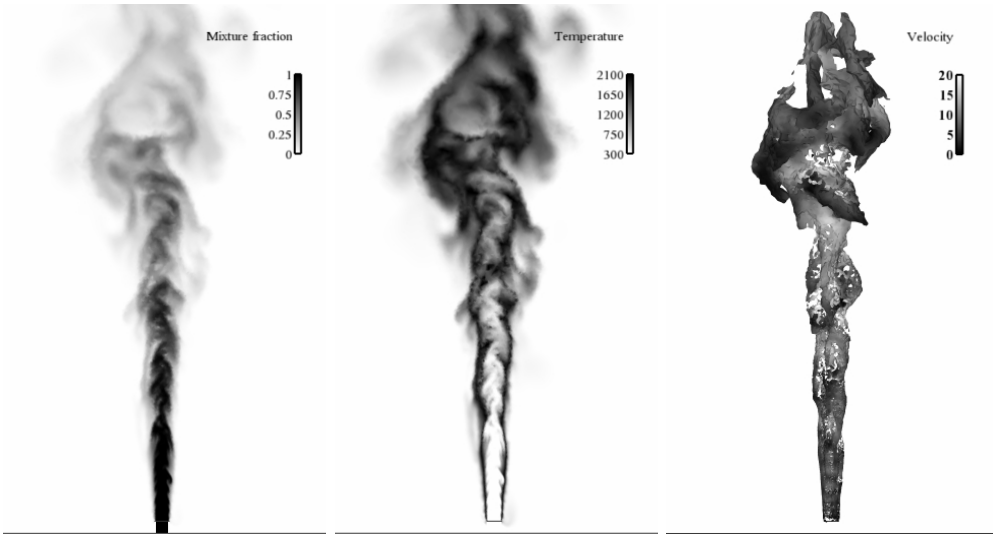

(a) (b) (c)

Figure 6.3: *Visualization of instantaneous fields for the H3 flame of (a) Mixture fraction - (b) Temperature. - (c) Isosurface of temperature (T=1800 K) colored by velocity.*

the sake of simplicity, the H_2/N_2 mixture is injected with a uniform velocity, instead of the 1/7-power law. This introduces an error in the initial region in the jet, i.e. from 0 to 10 diameters in Fig. 6.4 (a). Experimental data and numerical results slightly differ in the initial jet flow, but a good agreement is reached after 10 diameters. The rms levels and shapes are also close along the centerline (Fig. 6.4 (a)) and in the radial direction (Fig. 6.4 (b) and (c) at 20 and 40 diameters).

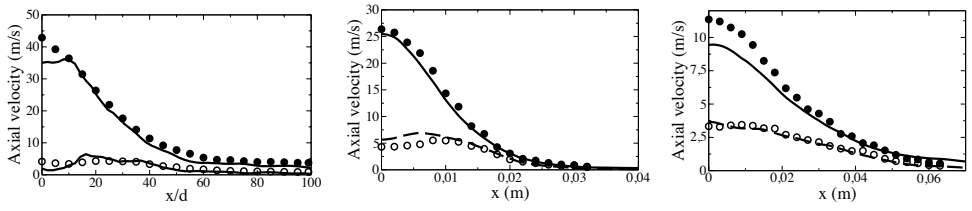

(a) (b) (c)

Figure 6.4: *Velocity profiles - (a) Centerline profiles - (b) Radial profiles at 20 injector diameters - (c) Radial profiles at 40 injector diameters [• exp (mean values), ◦ exp (rms values), — num (mean values), –– num (rms values)].*

The jet aerodynamics is modeled correctly by the code.

6.5.3.2 Species mass fraction distributions

Mass fractions of oxygen and hydrogen are shown in Fig. 6.5. Fig. 6.5 (a) and (d) display mass fraction distribution along the centerline. For both species, there is a good agreement between experiment and simulation for mean values and rms quantities. Fig. 6.5 (b,e) and (c,f) respectively show radial cuts at 20 and 40 diameters. For oxygen, results are satisfactory. The numerical simulation slightly overestimates hydrogen mass fractions. This conclusion must be moderated by the levels considered. At 40 injector diameters, little hydrogen remains, which explains the differences with experimental data.
In conclusion, simulations of mixing yield mass fraction fields which are close to those obtained experimentally.

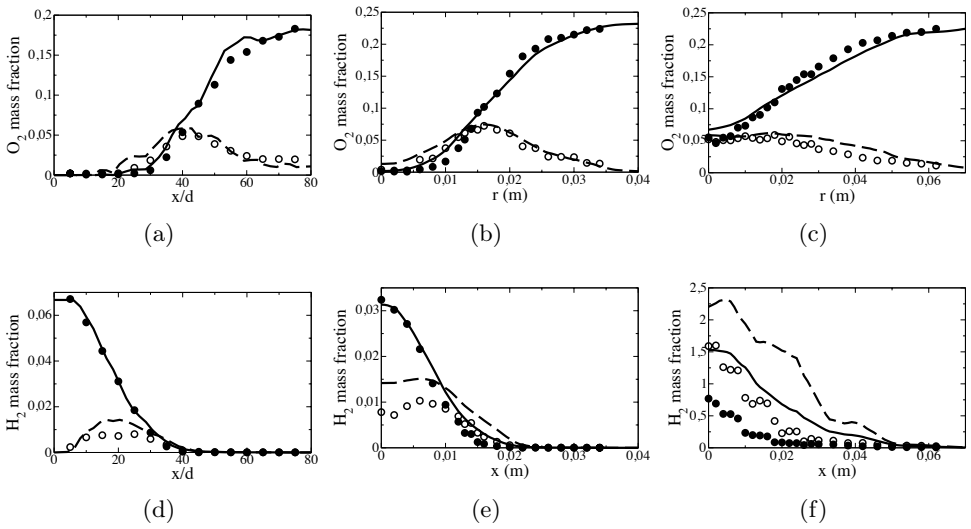

Figure 6.5: *Oxygen (top) and hydrogen (bottom) profiles - (a,d) Centerline profiles - (b,e) Radial profile at 20 injector diameters - (c,f) Radial profile at 40 injector diameters [● exp (mean values), ○ exp (rms values), — num (mean values), –– num (rms values)].*

6.5.3.3 Temperature field

The temperature distribution is displayed in Fig. 6.6. Figure 6.6 (a), indicates that the prediction along the centerline is in agreement with experiments. The flame length is found, and the shape of the rms profile fits experimental data. In particular, the two bumps before and after the flame tip are well reproduced. The radial profile at 20 diameters (Fig. 6.6 (b)) shows that the temperature is underestimated in the flame, by about 200 K. This can be caused by the model, but it is more likely due to the mesh. It is relatively coarse in this area,

and the flame is possibly filtered. Despite this problem, we note that the flame location and thickness, as well as the rms level and shape, are close to those found in the experiments. Near the end of the flame, at 40 injector diameters (Fig. 6.6 (c)), results are also satisfactory.

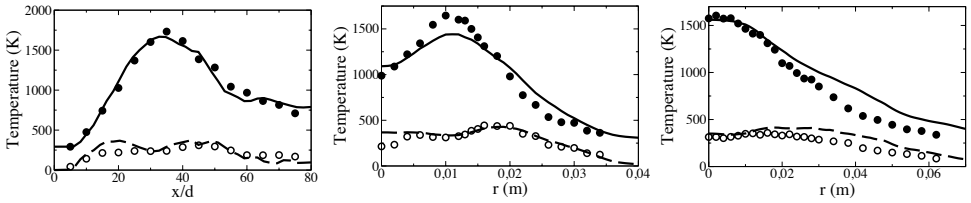

(a) (b) (c)

Figure 6.6: *Temperature profiles - (a) Centerline profile - (b) Radial profiles at 20 injector diameters - (c) Radial profiles at 40 injector diameters [• exp (mean values), ◦ exp (rms values), — num (mean values), –– num (rms values)].*

6.5.3.4 Infinitely fast chemistry assumption

The model is based on an infinitely fast chemistry assumption. Fig. 6.7 shows scatter plots of H_2, O_2 and H_2O mass fractions respectively as a function of the mixture fraction. Points are close to the infinitely fast chemistry lines, which is in agreement with the hypothesis. Near the stoichiometric mixture fraction ($Z_{st} = 0.31$), points are not exactly on the lines because of the subgrid combustion model ($\widetilde{Y_k}$ are filtered).

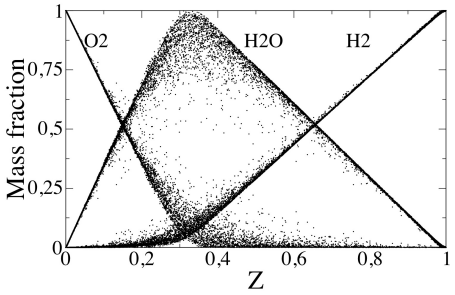

Figure 6.7: *Scatter plots as a function of the mixture fraction for H_2, O_2 and H_2O.*

6.6 Conclusion

In this chapter, a subgrid model for turbulent non-premixed flames is developed. It uses a predictor to estimate the heat release necessary to stay in the

infinitely fast chemistry limit, a baseline hypothesis of the model. This model is embedded in the numerical code AVBP and validated on the "H3 flame", for which full experimental data exist in the literature.
The model gives satisfactory results. Velocity profiles, distribution of species mass fractions and the temperature field provide acceptable comparisons with experiments. Scatter plots obtained in the computation are in agreement with the infinitely fast chemistry assumption. This study validates the combustion model, and allows to focus on the problem of flame/acoustics interaction.

Chapter 7

Simulation of flame acoustic interactions

In this chapter, the LES simulation of an acoustically modulated flame is carried out. The subgrid model for diffusion flames, FER, is used. The H3 flame, the validation test case presented in the previous chapter, is excited by a transverse acoustic wave at a frequency of 400 Hz. It is illustrated that the flame structure is modified by the velocity field. The flame shortens and oscillates in the transverse direction, reminiscent of what was observed during the Mascotte experiments. The Rayleigh source term is extracted from computation and compared to predictions given by the FAME theory. The same order of magnitude is found, although it seems the FAME model underestimates the acoustic source term. Several elements are provided in order to explain this discrepancy.

7.1 Introduction

The model developed and validated in chapter 6 is used in the case of a flame submitted to a transverse acoustic wave. This calculation is carried out in the H3 flame configuration. No experimental data is available for comparison in this case under transverse acoustic modulations. It is however possible to use the low order theoretical model developed in chapter 4 and compare its results with those obtained from simulation. The comparison between the theoretical formulation and a 3D simulation is found to be quite promising. Validation of the numerical code carried out previously already indicated that the flame could be reliably simulated and that results could be considered with some confidence. The theoretical low order model was also tested in various situations and this provided information on the source term appearing in the acoustic energy balance. It is then possible to use simulation and modeling to determine the source term and compare the two methods in the H3 configuration. This

gives access to an analysis of assumptions used to establish the theoretical source term model.

7.2 Interaction calculations

Computations presented in the following sections are carried out with the AVBP code, described in the previous chapter. As already mentioned, the following calculations are carried out in the H3 flame configuration. The essential modification is that a transverse acoustic wave is injected in the computational domain. To generate this wave, an acoustic oscillation is imposed on the lateral sides of the domain. This technique has been developed by Rey et al. (2005) and used, among others, by Richecoeur et al. (2010).

7.2.1 Configuration

A schematic diagram of the geometry of the problem is shown in Fig. 7.2.

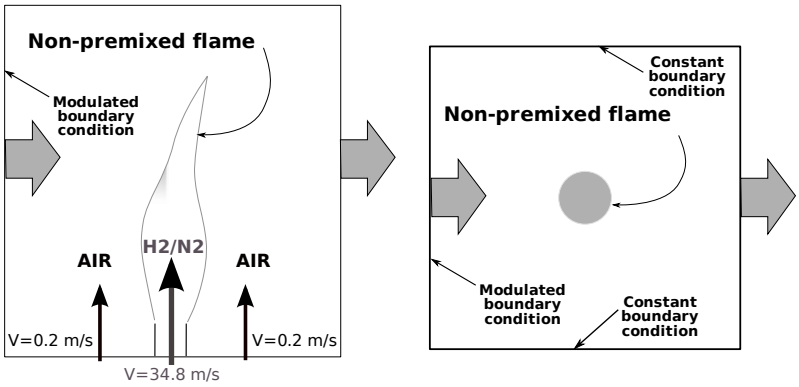

Figure 7.1: *Configuration of the modulated H3 flame - (a) front view - (b) top view.*

The boundary condition is imposed on the lateral sides of the computational domain with the form:

$$v(t) = v_0 \sin(2\pi f t).$$

Parameters used for the calculations are gathered in table 7.1.

v_0 (m.s^{-1})	f (Hz)
10	400

Table 7.1: *Acoustic modulation parameters of the lateral boundaries.*

7.2.2 Results and analysis

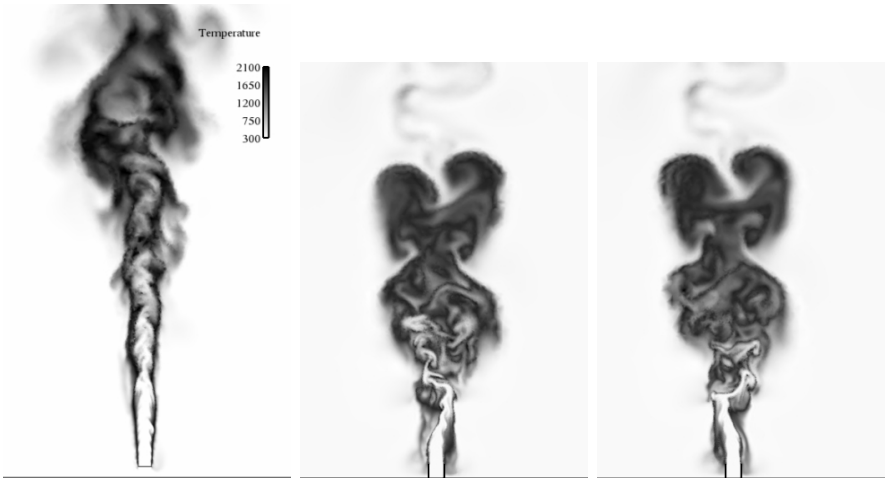

(a) (b) (c)

Figure 7.2: *Cut of the temperature field - (a) Without excitation - (b) With excitation:* $\phi = 0$ *- (c) With excitation:* $\phi = \pi$.

Figure 7.2 shows the temperature field corresponding to the computation carried out in this study. The strong effect of the acoustic field is noteworthy. The flame oscillates in response to the incident velocity field. The distribution of the mixture fraction is not symmetrical, "puffs" of hot gases are shed from one side and the other side of the jet axis. The external modulation induces this alternate pattern of reaction. Heat is released on the two sides of the centerline, acting as a source for acoustic energy. It would be of interest to change the excitation amplitude v_0, evaluate the response of the flame and tabulate it as a function of frequency f and transverse velocity amplitude v_0. This is not done here because of limitations in computational resources. At a fixed frequency, it is found however that the alternate flame pattern induced by the transverse field is more pronounced as the velocity v_0 is augmented.

7.3 Theoretical evaluation of the acoustic energy source term

The previous calculations may be used to evaluate the acoustic source term (the Rayleigh term) and compare the result with an estimate obtained from the FAME model. The problem may be first simplified by noting that there is no growth in the amplitude of oscillation. This is what is observed in the simulation, and it is also what is predicted by the low order model. The H3 flame heat release is relatively low compared to the jet flames formed in the

MIC. As discussed previously, even with five intense flames, the growth rate is small. Here, it is reasonable to assume that the energy brought by the flame will be damped by the system.
Then, the acoustic pressure corresponding to the 1T mode can be written: $p'(\boldsymbol{x},t) = p_0 \cos(\pi y/l)\cos(\omega_1 t)$, and the acoustic energy density reads:

$$\langle \mathcal{E}_1 \rangle = \frac{hlL}{4\overline{p}\gamma} p_0^2. \tag{7.1}$$

It is also possible to assume that $p_0/\overline{p}$ is small, which is also well verified in the numerical simulation. The growth factor associated with the FAME model then reads:

$$\alpha_{FAME} = \frac{\gamma-1}{\gamma\overline{p}} \frac{\mathcal{Q}}{lLh} \sin^2(\frac{\pi}{2}), \tag{7.2}$$

$$\alpha_{FAME} = \frac{\gamma-1}{\gamma\overline{p}} \frac{\mathcal{Q}}{lLh}, \tag{7.3}$$

$$\tag{7.4}$$

This growth factor may also be deduced from the ratio of the volume average Rayleigh source term to the volume average of the energy density:

$$\alpha_{FAME} = \frac{1}{2} \frac{\langle S \rangle}{\langle \mathcal{E}_1 \rangle}, \tag{7.5}$$

This can be used to express the average Rayleigh source term:

$$\langle S \rangle = \frac{\gamma-1}{2} \mathcal{Q} \left(\frac{p_0}{\gamma\overline{p}} \right)^2 \tag{7.6}$$

7.3.1 Numerical evaluation of the Rayleigh source term in the H3 flame case

The value of $\mathcal{Q}$, the power released by the flame, is deduced from the formation enthalpy for water:

$$\mathcal{Q} = -\left(\frac{W_{H_2O}\nu_{H_2O}}{W_{H_2}\nu_{H_2}} \Delta h_{H_2O} \right) \dot{m}_{H_2}, \tag{7.7}$$

where ν_{H_2} and ν_{H_2O} are the stoichiometric coefficients of species H_2 and H_2O respectively in the balance chemical equation:

$$2H_2 + O_2 \rightarrow 2H_2O. \tag{7.8}$$

The mass flow rate of hydrogen $\dot{m}_{H_2}$ is given by:

$$\dot{m}_{H_2} = \dot{m} Y_{H_2} \tag{7.9}$$

$$= v \frac{\pi D^2}{4} \rho Y_{H_2} \tag{7.10}$$

where $D = 0.008$ m is the pipe diameter, ρ is the density of the H_2/N_2 mixture, and $v = 34.8$ m.s^{-1}is the mean injection velocity. The density is obtained by taking $\rho = p/(rT)$ with $p = 101326$ Pa, $T = 293$ K and $r = R/W$. To evaluate this last quantity, we need the perfect gas constant $R = 8.314$ J.K^{-1}.mol^{-1}and the expression: $1/W = \sum Y_k/W_k$. Since $Y_{H_2} = 0.0667$ and $Y_{N_2} = 0.9333$ (which corresponds to a 50/50 distribution in volume). This yields:

$$W = 15 \text{ g.mol}^{-1}, \tag{7.11}$$

$$r = 554.4 \text{ J.K}^{-1}\text{.g}^{-1}, \tag{7.12}$$

$$\rho = 0.623 \text{ kg.m}^{-3}, \tag{7.13}$$

$$\dot{m} = 1.091.10^{-3} \text{ kg.s}^{-1}, \tag{7.14}$$

$$\dot{m}_{H_2} = 72.8.10^{-6} \text{ kg.s}^{-1}, \tag{7.15}$$

$$\mathcal{Q} = 8800 \text{ W}. \tag{7.16}$$

The heat released by the flame in the simulation, slightly fluctuates around the calculated value. This may be due to the fluctuations associated with the turbulent flow. To check the validity of the theoretical expression 7.6, it is more relevant to use the value of $\mathcal{Q}$ extracted from the simulation. The value of p_0 is also extracted from the calculation.

7.3.2 Acoustic energy source term evaluation in the simulation

In the simulation, the term which is calculated at each time step to account for the energy brought by the flame according to the following expression:

$$\mathcal{R}(t) = \frac{\gamma - 1}{\gamma \overline{p}} \int_V p'(\boldsymbol{x}, t) \dot{q}'(\boldsymbol{x}, t) dV. \tag{7.17}$$

The calculation is carried out over 16 periods of oscillation. Fig. 7.3 (a) shows $\mathcal{R}(t)$ (in black). After a transient regime which lasts approximately 8 periods of oscillation and is terminated at $t = 0.84$ s, the permanent regime is established. During the transient regime, $\mathcal{R}(t)$ takes relatively high values corresponding to the rapid modification of the flame structure. In the permanent regime, the heat release region is more compact.
Examining Fig. 7.3 (b), one finds that the Rayleigh term from the 3D simulation and the one evaluated with the FAME model are of the same order of

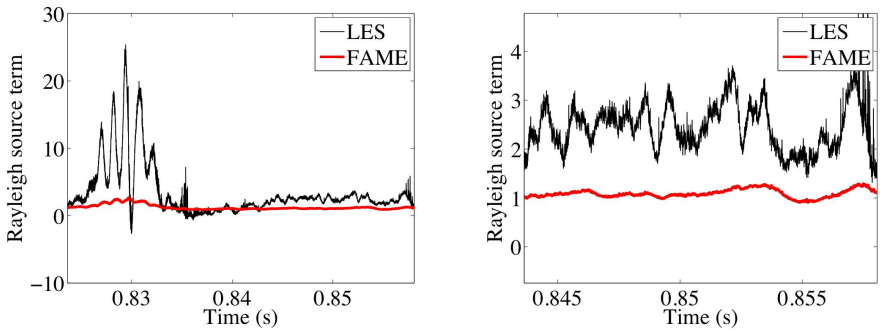

Figure 7.3: *(a) Evolution of the Rayleigh source term computed from the LES simulation and with the FAME theoretical model - (b) Close-up on the stationary period.*

magnitude. However there is a factor of about two between the value deduced from the model and that obtained from the simulation.
Several hypotheses can be proposed to explain this difference. First, the computation may not have been carried out for enough time, and the transient regime may not be completely over. The second explanation is that the main mechanism responsible for the Rayleigh source term may not be taken into account in the FAME formulation. This would mean that another phenomenon responsible for heat release fluctuations has to be modeled. However, in this simulation, the level of Rayleigh source term is very weak, and it is delicate to conclude on this comparison. The effect of turbulent structures on the Rayleigh term may be of the same order of magnitude as the one created by the jet transverse motion. Another study, with a more powerful flame or/and a more intense acoustic field, is necessary.
This example illustrates the valuable contribution that LES can bring to instability studies, in particular for the study of transient regimes, in which simple low order models will probably fail.

7.4 Conclusion

This chapter is concerned with the analysis of the response of a non-premixed flame interacting with a transverse acoustic mode. The H3 flame is considered in this investigation. This flame is set into a transverse motion by an external acoustic perturbation. The simulation is used to obtain the acoustic energy (Rayleigh) source term. This source term is also estimated by making use of the FAME model. The numerical estimate and theoretical model have the same order of magnitude but differ by a factor of about two. This confirms the validity of the modeling assumptions but also indicates that it might be

useful to calibrate the model with respect to other simulations.The computation also allows an analysis of transient regimes which are difficult to access with theoretical models.

Conclusion

This investigation addresses problems of combustion instability in rocket engines. Among the many different types of dynamical phenomena which appear in such devices this research is focused on high frequency oscillations coupled by transverse acoustic modes. This choice is made because the low frequency oscillations, generally associated with a coupling between the propellant feed manifold and the thrust chamber can be avoided in most cases by decoupling these elements by assuring head losses of 10 to 15% of the chamber pressure in the injection units. It is less easy to explain high frequency instabilities and also more difficult to suppress these oscillations when they occur. Instabilities coupled by transverse acoustic modes are specifically dangerous. Transverse modes operate in planes perpendicular to the general flow direction in the chamber and the damping by the nozzle is less effective. As a consequence the level of oscillation may reach values of the order of 20% of the chamber pressure inducing very large heat fluxes at the chamber walls and leading in some cases to the the melting of injectors and destruction of the engine. High frequency instabilities are most critical as demonstrated in the past by their destructive effects. They are also less predictable because of a lack of fundamental knowledge on the driving processes. This is still the case despite the large scale research effort developed for example during the development of the Saturn 5 main engine (F1). The so-called “instability crisis" was only resolved by a very large hot fire test program on full scale engines. The SP-194 report (Harrje and Reardon 1972), compiled after this intense period gives an account of the state of the art at that time. Progress on this problem has continued but at a slower pace (see for example Yang and Anderson (1995)). When the HF program was initiated in the year 2000, it appeared that advances could be made by developing fundamental research on the mechanisms involved in HF instabilities. It was concluded that progress made in the understanding of cryogenic combustion, model scale test facilities, optical diagnostics and in simulation methods could help unravel the underlying processes and that this could lead to improvements of engineering design methods.

The general objective of the present research is to contribute to the development of a framework that will assist engineers in the design of inherently stable propulsion systems. This needs to be preferably achieved without having to

add acoustic dampers, such as baffles, quarter wave cavities or resonators, to reduce the acoustic response because such devices add complexity and weight to the engine. An understanding of the governing mechanisms and of the coupling processes is clearly necessary if one wishes to predict stability margins of an engine. To bring forth new elements, this research effort addresses the problem on three different levels:

- Experiments are carried out under realistic conditions allowing a detailed analysis of the interaction between transverse modes and cryogenic combustion.
- Theoretical modeling is developed to define a low order description of the processes identified in the experiments. A tool is constructed which integrates knowledge in a comprehensive framework.
- Large eddy simulations are developed to gather further information on the coupling process and to advance the state of the art in the numerical description of combustion dynamics in rocket engines.

On the experimental side, it was concluded from previous doctoral work carried out by Rey (2004) and Richecoeur (2006) that further data could be made gathered from cold flow and hot fire tests on the Multiple Injector Combustor mounted on the Mascotte facility at ONERA. This pressurized combustion chamber equipped with 5 injectors represents to some extent the multiple injector systems found in real engines. Previous experiments indicated that the MIC did not exhibit self-sustained oscillations and that the coupling between acoustics and combustion could only be examined by external excitation of the resonant modes. This was initially achieved with a lateral nozzle periodically blocked by a toothed wheel. Transverse modes could be generated in this way but their level did not exceed about 8% of the chamber pressure which was too weak to reproduce conditions prevailing under self-sustained oscillations in rocket engines.

The first step in the experimental work has been to validate a novel actuator concept allowing a stronger level of modulation. The modulator designated as VHAM was specified and preliminary heat transfer calculations were carried out to make sure that it was mechanically feasible. The initial application of the VHAM is covered in the first chapter of this document, where the principle is outlined. The configuration is a simple transparent pressurized cavity. It is demonstrated that when a VHAM modulating the total mass flow rate of fluid injected in this cavity yields to relatively high acoustic amplitudes. The detailed properties of the acoustic field are investigated, and the spatial structure of the associated velocity distribution is obtained through high speed PIV measurements. This is then compared with numerical simulations obtained with

an acoustic solver (AVSP), and consistency is demonstrated. Pressure signals recorded at various places in the cavity indicate that the link between velocity and pressure fields is that predicted by numerical simulation. The mean flow is not influenced by the presence of the VHAM and is not taken into account during the calculation. The VHAM is also used to examine the influence of a transverse acoustic field on the jet of gas injected in the cavity.

The VHAM is then mounted on the MIC for cold flow experiments. Low and high pressure experiments at 7.5 bar and 55 bar are successively investigated. Fluids are liquid/transcritical oxygen and gaseous nitrogen, while injectors are coaxial. In the first step, the modal resonant frequencies and spatial structures are calculated with a numerical Helmholtz solver. Next, a linear frequency modulation is used to identify the eigenfrequencies, and the phase difference between the pressure transducers located in the chamber lateral walls providing the spatial distribution of pressure. Continuous wave modulation is carried out to examine the flow response to the first transverse mode. Data obtained with two high speed cameras, one focusing on the full accessible domain in the chamber and the other focusing on the central jet, yield complementary results. Under excitation by the VHAM, the first camera shows significantly smaller dense cores, an indication that primary atomization is enhanced by the strong acoustic field. It also features an important coherent oscillation of the jets in the transverse direction of the chamber. The disturbances are convected by the flow and by the transverse acoustic velocity. This modifies the distribution of liquid oxygen in the chamber. The nonuniform oxygen distribution resulting from this process intervenes in the mechanism of combustion instability. The second camera, which focuses on the central jet, shows smaller droplets ejected from the liquid core under resonant condition, in comparison with the liquid inclusions observed in the absence of excitation. The transverse acoustic mode clearly influences secondary atomization.

Hot fire tests reported in this document are carried out in the same multiple injector combustor mounted on the Mascotte facility. The procedure followed to predict and identify the resonant modes and frequencies is the same as that outlined previously. Five operating points are investigated, which correspond to three nominal pressures (10, 26 and 60 bar). Some runs correspond to the same chamber pressure but differ by their momentum flux ratio. Flames are submitted to a very high amplitude acoustic field and they respond in different ways depending on applied operating point and frequency excitation. These tests provide fundamental understanding on acoustic/combustion coupling, which is quite independent of the operating point. The modification of atomization, demonstrated with cold flow experiments, has different effects on the flame structure. When the acoustic mode amplitude reaches its largest values near

the backplane (1T mode), only secondary atomization is modified. The flames expansion angle increases and the combustion process is more intense. If the acoustic mode amplitude is important near the injection plane (like for the 1T2L mode), primary atomization is strongly modified as well. This yields very short flames and a dramatic increase of pressure oscillations. In most of the responding cases (at 26 bar), the pressure amplitude in the bottom of the chambers reaches more than 7 bar, almost 30% of the mean pressure in the chamber. Pressure oscillations in the top and bottom of the chamber are in phase with the corresponding photomultiplers, an indication that pressure oscillations and heat release are in phase, both of which are characteristic of a positive Rayleigh source term in the balance equation of acoustic energy. In parallel, the temperature measured at the bottom wall of the chamber increases rapidly from 400 K to 850 K. During a 6 second continuous wave modulation, the acoustic amplitude grows and flames get shorter. These phenomena indicate that the situation is close to what is observed when an actual rocket engine becomes unstable. High speed imaging provides an additional and valuable piece of information. Besides the effect of acoustics on the liquid phase, the acoustic velocity field moves flames in the transverse direction. Streak films constructed using high speed images demonstrate that flames are oscillating in the transverse direction and that their motion is important.
Another unusual feature is the asymmetry of the flame pattern observed during sensitive test cases for the 1T2L mode. This is shown to be linked to an asymmetry of the acoustic field. The cause of this asymmetry is probably related to a modification of the injected mass flow rates which cease to be uniform. The non-uniformity is enhanced by a complex coupling with the transverse acoustic field. It is argued that when acoustic levels become important, non-linear effects arise inducing an injection inhomogeneity giving rise to temperature non-uniformity in the chamber. It is also possible that a force associated to radiation pressure is acting to curve the flames toward the pressure node, which is no longer in the center of the chamber.

The second part of the study concerns low order modeling and the design of a simple tool based on the experimental findings. In a first step (chapter 4), two models are developed to represent unsteady heat release as a function of the acoustic field. The objective is to devise models which would not rely on the standard sensitive time lag description to account for the effect of acoustics on the unsteady heat release. It is known that the sensitive time lag representation is less well justified in the case of transverse instabilities and is also too phenomenological. It is shown that, in the case of the MIC equipped with the VHAM, the principle cause of heat release fluctuations between the upper and lower sides of the chamber the flame motion induced by the transverse mode. In the first model, it is assumed that the flames rigorously follow the acoustic field

(FAME model). This yields an expression of the heat release as a function of the mean heat release in the flames and of the acoustic amplitude. To account for the complete mechanism, obtained during experiments, it is necessary to introduce the liquid phase and the effect of acoustics on atomization and spray dynamics. Another constraint is to keep the computational costs relatively low. To achieve this goal, the second model (SDM) assumes that the spray can be described in terms of a single droplet diameter and follows the acoustic field with a time lag depending on momentum relaxation between the gaseous and liquid phases. The time lag then depends on the square of the droplet diameter. Combustion is assumed to take place instantaneously after vaporization. The sensitivity of droplets to the acoustic field is obtained by comparing their acoustic Weber number, based on the acoustic velocity to a critical Weber number. When the acoustic Weber number is greater than this critical value, the droplets are split in two. The inertia of the smaller droplets is reduced, and the spray follows the acoustic field more closely. This model provides a rough approximation of a more complex process but accounts for many observations made during the experimental campaign as it is able to retrieve some of the mechanisms identified experimentally.

The unsteady combustion models are introduced in a unified framework established for the low order modeling of combustion instabilities. The software tool is designed to carry out non-linear instability studies of complex geometries, taking into account cavity coupling, damping, localized source terms, non-trivial boundary conditions, modulation by external actuators like the VHAM, response of injectors to pressure perturbations and combustion response to acoustic oscillations. This integration is made possible by the modal expansion method introduced initially by Lores and Zinn (1973) and Culick (1976). In this treatment eigenmodes are first determined and one calculates the time evolution of the modal amplitudes by integrating a system of differential equations. First, the different submodels included in the tool are successively described. In a second stage, the VHAM experiments are used to evaluate the different models and validate this approach. It is shown that the source terms obtained with FAME and SDM models provide substantial increases of the limit cycle amplitudes (around 20% in the case of the 1T2L mode). In the final stage, we demonstrate the applicability of the method to a real scale engine. The mechanism identified during the VHAM experiments is reproduced. Sample calculations are carried out for a chosen set of damping coefficients, mean droplet sizes, critical Weber number, etc. The intensity of the initial perturbation imposed to the system is shown to be of primary importance. A threshold is identified: below a certain level oscillations are damped, while above this value they grow exponentially. Parameters used in this sample calculation would have to be carefully evaluated *a priori* in the case of an engine design program.

The last part of this research describes advances in multi-dimensional simulations of acoustic flame interactions using large eddy simulation (LES). LES is a useful tool to understand instabilities because it can in principle take into account the governing processes and gives access to a large amount of information which cannot be deduced from experiments. The drawback of this method is its computational cost. A few years ago, a compressible computation of five transcritical flames was considered to be out of reach. With the increase of computational resources and with advances in parallel computing, it has become possible to examine such problems. The present study makes a step in this direction. It focuses on the simulation of non-premixed flame combustion modeling for LES. It is found that models do exist for this mode of combustion but they are usually based on assumptions which are not-compatible with full compressible codes, and in particular may be difficult to use to analyze the coupling between acoustics and combustion. This issue motivates the present work. A new framework is devised in collaboration with T. Schmitt. This is based on the infinitely fast chemistry assumption but provides an explicit representation of the reaction rate. The infinitely fast chemistry limit is a reasonable hypothesis in the case of rocket engine combustion. The model is validated in a well documented non-premixed configuration known as the “H3 flame". Results obtained are quite encouraging.

In a second stage, this flame is submitted to a transverse acoustic wave. The flame is drastically shortened and it is made to oscillate in the transverse direction. The Rayleigh source term created in this situation is calculated and compared to the one obtained with the theoretical model FAME developed in chapter 4. Since the flame power is small, the corresponding Rayleigh source term is in turn small and limits the impact of a comparison. Nevertheless, the theoretical and numerical values are of the same order of magnitude. In the numerical result, one finds that during the transient regime, the Rayleigh source term takes large values. These calculations show that numerical simulations can be used to analyze the driving processes involved in combustion instability in order to complement experiments and extend the analysis to more more complex situations.

Conclusion (français)

Cette étude traite des problèmes d'instabilité de combustion dans les moteurs-fusée. Parmi les nombreux types de phénomènes dynamiques qui apparaissent dans ces dispositifs, l'analyse est axée sur les oscillations à haute fréquence couplés par des modes acoustiques transverses. Ce choix est fait car les oscillations basse fréquence, généralement associées à un couplage entre le dôme d'alimentation en ergols et la chambre peut être évité dans la plupart des cas par le découplage de ces éléments. On assure à cet effet une perte de charge de 10 à 15 % de la pression de chambre dans les éléments d'injection. Il est moins facile de prévoir les instabilités haute fréquence et aussi plus difficile de supprimer ces oscillations quand elles apparaissent. Les instabilités couplées par des modes acoustiques transverses sont les plus dangereuses. Ces modes opèrent dans un plan perpendiculaire au sens de l'écoulement dans la chambre et l'amortissement par la tuyère est moins efficace. Le niveau d'oscillation peut atteindre des valeurs de l'ordre de 20 % de la pression chambre induisant des flux de chaleur très importants à la paroi, ce qui conduit dans certains cas à la destruction des injecteurs et du moteur. Les instabilités haute fréquence sont les plus critiques et leurs effets ont été particulièrement destructeurs par le passé. Ces instabilités sont également les moins prévisibles en raison d'un manque de connaissances fondamentales sur les processus qui pilotent le phénomène. Cette situation n'a pas vraiment changé malgré l'effort de recherche de grande envergure mis en oeuvre par exemple lors du développement du moteur principal (F1) de la fusée Saturn 5. La "crise d'instabilité" n'avait alors pu être résolue que par un programme très lourd d'essais à feu sur les moteurs à taille réelle. Le rapport SP-194 (Harrje and Reardon 1972), rédigé après cette période intense rend compte de l'état de l'art à cette époque. Des progrès ont été faits par la suite, mais à un rythme plus lent (voir par exemple (Yang and Anderson 1995)). Lorsque le programme sur les instabilités haute fréquence a été lancé en l'an 2000, il est apparu que des avancées pouvaient être faites en développant des recherches fondamentales sur les mécanismes impliquées dans ces oscillations. Il a était conclu que les progrès réalisés dans la compréhension de la combustion cryotechnique, l'expérimentation sur des installations d'essai à échelle réduite, les diagnostics optiques et les méthodes de simulation pouvaient aider à mieux

identifier les processus sous-jacents. Les travaux pourraient ainsi conduire à des améliorations des méthodes de conception.
L'objectif général de ce travail de recherche est de contribuer à l'élaboration de moyens permettant la conception de systèmes de propulsion naturellement stables. L'objectif étant d'obtenir ce résultat sans avoir à recourir à des amortisseurs acoustiques, comme des baffles, des cavités quart d'onde ou des résonateurs, afin de réduire la réponse acoustique, tous ces dispositifs augmentant la complexité et le poids du moteur. Une compréhension des mécanismes générateurs et du couplage des processus est évidemment nécessaire si l'on veut prévoir les marges de stabilité d'un moteur. Pour obtenir ces éléments, cette étude aborde le problème à trois niveaux différents :

- L'expérimentation est effectuée dans des conditions réalistes permettant une analyse détaillée de l'interaction entre les modes transverses et la combustion cryotechnique.

- La modélisation théorique est élaborée pour définir une description d'ordre réduit des processus identifiés dans les expériences. Un outil est construit, qui intègre les connaissances dans un cadre unifié.

- Des simulations aux grandes échelles (LES) sont mises en place afin de recueillir des informations sur le processus de couplage et de faire progresser l'état de l'art dans la description numérique de la dynamique de la combustion dans les moteurs de fusée.

Au niveau expérimental, les travaux font suite à ceux réalisés par C. Rey et F. Richecoeur. Il s'agit de recueillir des données supplémentaires dans des conditions d'écoulements froids et dans des essais à feu sur le foyer à injection multiple ("Multiple Injector Combustor" ou MIC) monté sur le banc Mascotte de l'ONERA. Cette chambre pressurisée équipée de 5 injecteurs représente dans une certaine mesure les systèmes d'injection multiple utilisés dans les moteurs fusées actuels. Les expériences déjà réalisées indiquent que le MIC ne présente pas d'oscillations auto-entretenues et que le couplage entre l'acoustique et la combustion ne peut être examiné que par une excitation externe des modes de résonance. Dans les essais effectués précédemment, la modulation était réalisée au moyen d'une tuyère latérale bloquée périodiquement par une roue dentée tournant à grande vitesse. Des modes transverses peuvent être générés ainsi mais le niveau de fluctuation n'avait pas dépassé environ 8 % de la pression de la chambre. Cette fluctuation était trop faible pour reproduire les conditions établies par oscillations auto-entretenues dans les moteurs de fusée.
La première étape du travail expérimental a été de valider un nouveau concept d'actionneur permettant d'atteindre des niveaux de modulation plus élevés. Le modulateur "Very High Amplitude Modulator" ou VHAM a été spécifié et des calculs préliminaires de transfert de chaleur ont été effectués pour s'assurer qu'il

était mécaniquement faisable. La première utilisation du VHAM est présentée dans le premier chapitre de ce document, où le principe du système est résumé. La configuration étudiée est celle d'une cavité transparente pressurisée par un injecteur unique. Il est démontré que, quand le VHAM module le débit massique total de fluide injecté dans la cavité, on obtient des modes acoustiques transverses caractérisés par des amplitudes élevées. Les propriétés du champ acoustique sont étudiées, et la structure spatiale de la distribution de vitesse est obtenue par PIV à grande vitesse. Ce champ est ensuite comparé à des simulations numériques issues d'un solveur acoustique (AVSP), et la cohérence entre les deux approches est démontrée. Les signaux de pression enregistrés en divers endroits dans la cavité indiquent que le lien entre la vitesse et le champ de pression est celui prédit par la simulation numérique. Le débit moyen n'est pas influencé par la présence du VHAM et n'est pas pris en compte lors du calcul. Le VHAM est également utilisé pour étudier l'influence d'un champ acoustique transverse sur le jet de gaz injecté dans la cavité.

Le VHAM est ensuite monté sur le MIC pour des expériences d'écoulement à froid. On étudie successivement des écoulements à basse et haute pression à 7.5 et 55 bar. Les injecteurs coaxiaux sont alimentés en oxygène liquide transcritique et azote gazeux. Dans un premier temps, les fréquences de résonance et les structures modales sont calculées avec un solveur de Helmholtz. Une modulation linéaire de fréquence est utilisée pour identifier les fréquences propres, et déterminer la différence de phase entre les capteurs de pression situés sur les parois latérales de la chambre. Ceci permet de remonter à la distribution spatiale de pression. Une modulation à fréquence fixe permet ensuite d'examiner la réponse de l'écoulement aux modes transverses. Les données sont obtenues avec deux caméras à grande vitesse, l'une observant la totalité du domaine accessible et l'autre focalisée sur le jet central. Lorsque le VHAM fonctionne, les images indiquent que le noyau dense des jets d'oxygène présente une taille réduite correspondant à une atomisation primaire renforcée par le champ acoustique intense. Les jets sont également mis en oscillation cohérente de grande amplitude dans le sens transversal et les perturbations sont convectées par l'écoulement. Une modification de la répartition de l'oxygène liquide dans la chambre est ainsi induite. Il en résulte une distribution non uniforme de l'oxygène qui peut intervenir dans le mécanisme d'instabilité de combustion. La caméra, focalisée sur le jet central, montre que les gouttelettes éjectées à partir du noyau liquide dans des conditions de résonance sont beaucoup plus petites que les inclusions liquides crées en l'absence d'excitation. Le mode acoustique transverse influence clairement l'atomisation secondaire.

Les essais à feu décrits dans ce document sont réalisés dans la chambre de combustion à injection multiple montée sur le banc Mascotte. La procédure

suivie pour prévoir et identifier les modes et les fréquences de résonance est la même que celle décrite précédemment. Cinq points de fonctionnement sont analysés, à trois pressions nominales (1, 2.6 et 6.0 MPa). Plusieurs points de fonctionnement correspondant à la même pression chambre sont différenciés par le rapport des débits de quantité de mouvement. Les flammes sont soumises à un champ acoustique de grande amplitude et elles réagissent de façon différente selon le point de fonctionnement et la fréquence d'excitation.

Ces essais fournissent des renseignements sur le couplage acoustique/combustion. La modification de l'atomisation, démontrée dans les expériences à froid, a plusieurs effets sur la structure des flammes. Lorsque l'amplitude du mode acoustique atteint ses plus grandes valeurs en sortie de chambre (comme dans le cas du mode 1T), seule l' atomisation secondaire est modifiée. Il en résulte une augmentation de l'angle d'épanouissement de la flamme, et le processus de combustion est plus intense. Si l'amplitude du mode acoustique est importante à proximité du plan d'injection (comme pour le mode 1T2L), l'atomisation primaire est fortement influencée. Cela conduit à des flammes très courtes et à une augmentation spectaculaire des oscillations de pression. Dans les expériences réalisées à 2.6 MPa, l'amplitude des fluctuations de pression dans la partie inférieure de la chambre atteint plus de 7 bar, soit près de 30 % de la pression moyenne dans la chambre. Les variations de pression dans les parties supérieure et inférieure de la chambre sont en phase avec les signaux des photomultiplicateurs correspondants. Dans ces conditions, les oscillations de pression et de dégagement de chaleur sont en phase, et il en résulte un terme source positif dans l'équation du bilan d'énergie acoustique. On observe dans cette même situation une augmentation rapide de la température mesurée à la paroi inférieure de la chambre qui passe rapidement de 400 à 850 K. Au cours d'une modulation continue de 6 secondes, l'amplitude croît et les flammes se raccourcissent. Ces phénomènes indiquent que la situation étudiée est proche de celle qui prévaut quand un moteur fusée devient instable. L'imagerie grande vitesse donne des informations supplémentaires sur le mécanisme d'interaction. Au delà de l'effet de l'acoustique sur la phase liquide, le champ de vitesse acoustique déplace les flammes dans le sens transversal. Des films en mode “streak" construits à partir des images à grande vitesse démontrent que les flammes oscillent dans le sens transversal et que leur mouvement est important.

Une autre caractéristique observée dans les essais à amplitude élevée est l'asymétrie de la structure de la zone de combustion. Ce phénomène est notamment observé dans le cas d'une modulation par le mode 1T2L et il est lié à une asymétrie du champ acoustique. L' asymétrie est probablement liée à une modification des débits de masse injectés, dont la distribution cesse d'être uniforme. La non-uniformité est renforcée par un couplage complexe entre la combustion et le champ acoustique transverse. Lorsque les niveaux acoustiques deviennent importants, des effets non linéaires apparaissent induisant l'inhomogénéité

d'injection et la distribution de température cesse d'être uniforme dans la chambre. Il est également possible qu'une force associée à la pression de radiation agisse dans cette situation pour courber les flammes vers le noeud de pression, qui n'est plus au centre de la chambre.

La deuxième partie de l'étude porte sur la modélisation d'ordre réduit et la conception d'un outil simple exploitant les résultats expérimentaux. Dans un premier temps, deux modèles sont développés pour représenter le dégagement de chaleur instationnaire en fonction du champ acoustique. L'objectif est de concevoir une modélisation qui ne fait pas recours à la théorie du délai sensible pour représenter l'effet de l'acoustique sur le dégagement de chaleur instationnaire. On sait en effet que la théorie du délai sensible est moins bien justifiée dans le cas d'instabilités transverses. On montre ici que, dans le cas du MIC modulé par le VHAM, la cause principale des fluctuations du dégagement de chaleur a pour origine le déplacement des flammes induit par le mode transverse. Dans un premier modèle, on suppose que les flammes suivent rigoureusement la vitesse imposée par le champ acoustique (modèle FAME). On déduit ainsi une expression du dégagement de chaleur instationnaire en fonction du dégagement de chaleur moyen dans les flammes et de l'amplitude acoustique. Pour tenir compte du mécanisme complet, observé expérimentalement, il faut tenir compte de la phase liquide et des effets du champ acoustique sur la rupture du jet liquide et sur l'atomisation tout en gardant des coûts de calcul réduits. Pour cela, le second modèle (SDM) suppose que le spray peut être décrit en supposant que les gouttelettes ont un diamètre unique et qu'il suit le champ acoustique avec un temps de retard fonction de l'échange de quantité de mouvement entre les phases gazeuse et liquide. Le temps de retard dépend du carré du diamètre des gouttelettes. La combustion est supposée s'effectuer instantanément après vaporisation. La sensibilité des gouttelettes par rapport au champ acoustique externe est obtenue en comparant le nombre de Weber basé sur la vitesse acoustique à un nombre de Weber critique. Lorsque le nombre Weber acoustique est supérieur à cette valeur critique, les gouttelettes sont divisées en deux. L'inertie des gouttelettes résultant de ce processus est ainsi réduite, et le délai entre le champ acoustique et le spray est plus réduit. Ce modèle fournit une première approximation d'un processus plus complexe, mais permet de décrire les observations expérimentales faites au cours de la campagne d'essais.

Les modèles de combustion instationnaire décrits précédemment sont introduits dans un cadre unifié établi pour la modélisation d'ordre réduit des instabilités de combustion. Le logiciel est conçu pour réaliser des études non-linéaires d'instabilité dans des géométries complexes, en tenant compte du couplage entre cavités, de l'amortissement, des termes sources localisés, des conditions aux limites variées, de la modulation par des actionneurs externes comme le VHAM,

de la réponse à la pression des injecteurs, des perturbations de la combustion en fonction des oscillations acoustiques. Cette intégration est possible par le biais de la méthode de projection modale introduite initialement par Zinn et Culick. Les modes propres sont d'abord déterminés et on calcule l'évolution temporelle des amplitudes modales en intégrant un système d'équations différentielles. Les différents sous-modèles inclus dans l'outil de calcul sont passés en revue. Les expériences réalisées avec le VHAM sont ensuite utilisées pour évaluer les modèles et valider l'approche. Il est montré que les termes sources obtenus avec les modèles FAME et SDM conduisent à une augmentations des amplitudes d'oscillation (environ 20 % dans le cas du mode de 1T2L). On démontre enfin l'applicabilité de la méthode à un moteur à échelle réelle. Le mécanisme identifié au cours des expériences VHAM est reproduit. Des calculs sont effectués à titre d'exemple après avoir fait un choix de coefficients d'amortissement, de taille moyenne des gouttelettes, de nombre de Weber critique, etc. L'intensité de la perturbation initiale imposée au système se révèle être de première importance. Un seuil est identifié en-dessous duquel les oscillations sont amorties, mais au-dessus duquel la croissance est exponentielle. Les paramètres utilisés pour ce type de calcul devront être soigneusement évalués avant application au stade de la conception moteur.

La dernière partie de cette étude décrit les progrès réalisés dans l'analyse multidimensionnelle des interactions flamme/acoustique au moyen de simulations grandes échelles (SGE). La simulation peut être utile à la compréhension des instabilités car elle peut en principe prendre en compte l'ensemble des mécanismes impliqués et elle donne accès à une grande quantité d'informations qui ne peuvent être déduites des seules expériences. L'inconvénient de cette méthode est son coût de calcul. Un calcul compressible de cinq flammes transcritiques était considéré, il y a quelques années, comme hors de portée. Avec l'augmentation des ressources de calcul et avec les progrès de l'informatique parallèle, il est devenu possible d'examiner ces problèmes. La présente étude fait un pas dans cette direction. Elle est axée sur la simulation de flammes non-prémélangées pour l'analyse des instabilités. Des modèles existent pour ce mode de combustion, mais ils sont généralement fondés sur des hypothèses qui ne sont pas compatibles avec les codes pleinement compressibles, et en particulier sont difficilement applicables à l'analyse du couplage entre l'acoustique et la combustion qui est le centre de la présente étude. Un nouveau cadre est formulé en collaboration avec T. Schmitt. On utilise l'hypothèse de chimie infiniment rapide, pour déduire une représentation explicite du taux de réaction filtré. La limite de chimie infiniment rapide est raisonnable dans le cas de la combustion dans les moteurs fusées. Le modèle est validé sur une configuration non prémélangée bien documentée connue sous le nom de flamme “H3". Les résultats obtenus sont prometteurs.

Dans une deuxième étape, la flamme H3 est soumise à une onde acoustique transverse. La zone de réaction devient plus compacte et elle est mise en oscillation dans le sens transversal. Le terme source créé dans cette situation est calculé et comparé à celui obtenu avec le modèle théorique développé précédemment. Comme le dégagement de chaleur dans la flamme est réduit, le terme source de Rayleigh correspondant est faible, ce qui limite l'intérêt de la comparaison. Néanmoins, les valeurs théoriques et numériques sont du même ordre de grandeur. Dans le résultat numérique, on constate que durant le régime transitoire, le terme source de Rayleigh prend de grandes valeurs. Ces calculs montrent que les simulations numériques peuvent être utilisées pour analyser les processus impliqués dans les instabilités de combustion et qu'elles peuvent être utilisées pour compléter les expériences et étendre l'analyse à des situations plus complexes.

References

Abramzon, B. and W. Sirignano (1989, Sep). Droplet vaporization model for spray combustion calculations. *International Journal of Heat and Mass Transfer 32*(9), 1605–1618.

Adrian, R. J. (1991). Particle-imaging techniques for experimental fluid-mechanics. *Annual Review of Fluid Mechanics 23*, 261–304.

Adrian, R. J. (2004, July). Twenty years of particle image velocimetry. In *International Symposium on Applications of Laser Techniques to Fluid Mechanics*, Lisbon.

Armitage, C. A., R. Balachandran, E. Mastorakos, and R. S. Cant (2006, AUG). Investigation of the nonlinear response of turbulent premixed flames to imposed inlet velocity oscillations. *Combustion and Flame 146*(3), 419–436.

Astrium (2009, December). http://cs.astrium.eads.net/sp/launcherpropulsion/vulcain-2-rocket-engine.html.

Baillot, F., J. Blaisot, G. Boisdron, and C. Dumouchel (2009). Behaviour of an air-assisted jet submitted to a transverse high-frequency acoustic field. *Journal of Fluid Mechanics 640*, 305–342.

Barbosa, S., P. Scouflaire, and S. Ducruix (2009). Time resolved flowfield, flame structure and acoustic characterization of a staged multi-injection burner. *Proceedings of the Combustion Institute 32*(Part 2), 2965–2972.

Barrère, M. and J. Corbeau (1963). Les instabilités de combustion dans les fusées à propergol liquide. In *Combustion and Propulsion - Fifth AGARD Colloquim*, pp. 637–692.

Barrère, M. and F. Williams (1969). Comparison of combustion instabilities found in various types of combustion chambers. *Proceedings of the Combustion Institute 12*(1), 169–181.

Birbaud, A. L., D. Durox, S. Ducruix, and S. Candel (2007, Jan). Dynamics of free jets submitted to upstream acoustic modulations. *Physics of Fluids 19*(1-013602), 1–20.

Boisdron, G., F. Baillot, C. Dumouchel, and J. Blaisot (2006). Intéraction entre un jet assisté par air et une acoustique transverse. Technical report, CORIA, 2, avenue de l'Université 76314 St Etienne du Rouvray Cedex 1, France.

Candel, S., M. Juniper, G. Singla, P. Scouflaire, and C. Rolon (2006). Structure and dynamics of cryogenic flames at supercritical pressures. *Combustion Science and Technology 178*, 161–192.

Cheng, T. C., G. Fruechel, A. Neuber, F. Lipp, E. P. Hassel, and J. Janicka (1995, Jun). Experimental data-base for numerical simulations of turbulent-diffusion flames. *Forschung Im Ingenieurwesen-Engineering research 61*(6), 165–171.

Cheuret, F. (2005). *Instabilités thermo-acoustiques de combustion haute-fréquence dans les moteurs fusées*. Ph. D. thesis, Université de Provence - Aix-Marseille I.

Cook, A., J. Riley, and G. Kosaly (1997, May). A laminar flamelet approach to subgrid-scale chemistry in turbulent flows. *Combustion and Flame 109*(3), 332–341.

Cook, A. W. and J. J. Riley (1994, Aug). A subgrid model for equilibrium chemistry in turbulent flows. *Physics of Fluids 6*(8), 2868–2870.

Cook, A. W. and J. J. Riley (1998, Mar). Subgrid-scale modeling for turbulent reacting flows. *Combustion and Flame 112*(4), 593–606.

Crocco, L. and S.-I. Cheng (1956). *Theory of combustion instability in liquid propellant rocket motors*. Butterworths Scientific Publications.

Crow, S. C. and F. H. Champagn (1971). Orderly structure in jet turbulence. *Journal of Fluid Mechanics 48*(AUG16), 547.

Culick, F. (1976). Nonlinear behavior of acoustic-waves in combustion chambers .1. *Acta Astronautica 3*(9-10), 715–734.

Culick, F. (1988). Combustion instabilities in liquid-fueled propulsion system - an overview. In *AGARD conf. proceedings*, Number 450.

Culick, F. (2006). *Unsteady Motions in Combustion Chambers for Propulsion Systems*. RTO.

Culick, F. E. C. and V. Yang (1995). *Liquid Rocket Engine Combustion Instability*, Volume 169, Chapter Overview of Combustion Instabilities in Liquid-Propellant Rocket Engines, pp. 3–37. Washington, DC: AIAA, Inc.

De Bruyn Kops, S. M., J. J. Riley, G. Kosaly, and A. W. Cook (1998). Investigation of modeling for non-premixed turbulent combustion. *Flow Turbulence and Combustion 60*(1), 105–122.

de Chaisemartin, S., F. Laurent, M. Massot, and J. Réveillon (2007, September). Evaluation of eulerian multi-fluid versus lagrangian methods for ejection of polydisperse evaporating sprays by vortices. HAL.

Dowell, E. H. (1974). *Aeroelasticity of Plates and Shells*. Leyden: Noordhoff International Publishing.

Evesque, S. and W. Polifke (2002, June). Low-order modelling for annular combustors: validation and inclusion of modal coupling. In ASME (Ed.), *ASME Turbo Expo*. ASME.

Harrje, D. T. and F. H. Reardon (1972). Liquid propellant rocket combustion instability. Technical Report SP-194, NASA.

Herding, G., R. Snyder, C. Rolon, and S. Candel (1998). Investigation of cryogenic propellant flames using computerized tomography of oh emission images. *Journal of Propulsion and Power 13*, 146–151.

Ho, C. M. and P. Huerre (1984). Perturbed free shear layers. *Annual Review of Fluid Mechanics 16*, 365–424.

Hulka, J. and J. J. Hutt (1995). *Liquid Rocket Engine Combustion Instability*, Volume 169, Chapter Instability Phenomena in Liquid Oxygen/Hydrogen Propellant Rocket Engines, pp. 39–71. Washington, DC: AIAA, Inc.

Hutt, J. J. and M. Rocker (1995). *Liquid Rocket Engine Combustion Instability*, Volume 169, Chapter High-Frequency Injection-Coupled Combustion Instability, pp. 345–355. Washington, DC: AIAA, Inc.

Janardan, B., B. Daniel, and B. Zinn (1976). Measurements of acoustic responses of gaseous propellant injectors. *Journal of Sound and Vibration 47*(4), 559–569.

Juniper, M. and S. Candel (2003). Edge diffusion flame stabilization behind a step over a liquid reactants. *Journal of Propulsion and Power 19*(3), 332–342.

Juniper, M., A. Tripathi, J. Rolon, and S. Candel (2000). Structure of cryogenic flames at elevated pressures. In *Proceedings of the Combustion Institute*, Volume 28, pp. 1103–1109.

Lacaze, G., B. Cuenot, T. Poinsot, and M. Oschwald (2009, JUN). Large eddy simulation of laser ignition and compressible reacting flow in a rocket-like configuration. *Combustion and Flame 156*(6), 1166–1180.

Lawhead, R. (1961). Photographic studies of combustion processes in liquid propellant rockets. In *Proceedings of the Combustion Institute*, Volume 8, pp. 1140–1151.

Lores, M. and B. Zinn (1973). Nonlinear longitudinal combustion instability in rocket motors. *Combustion Science and Technology 7*(6), 245–256.

Marble, F. E. and S. M. Candel (1977). Acoustic disturbance from gas non-uniformities convected through a nozzle. *Journal of Sound and Vibration 55*(2), 225–243.

Ménoret, L. and G. Searby (2010). High frequency combustion peak involving internal injector resonance. *Journal of Propulsion and Power Submitted for publication*.

Méry, Y., S. Ducruix, P. Scouflaire, and S. Candel (2007). Experimentation, modeling and simulation of high frequency acoustic coupling in rocket engines - first year report. Technical report, Laboratoire EM2C.

Méry, Y., S. Ducruix, P. Scouflaire, and S. Candel (2009). Injection coupling with high amplitude transverse modes: Experimentation and simulation. *Comptes Rendus Mecanique 337*(6-7), 426 – 437. Combustion for aerospace propulsion.

Mitchell, C. E. (1995). *Liquid Rocket Engine Combustion Instability*, Volume 169, Chapter Analytical Models for Combustion Instability, pp. 403–430. Washington, DC: AIAA, Inc.

Morse, P. M. and K. U. Ingard (1968). *Theoretical Acoustics*. New York: McGraw-Hill Book Company, Inc.

Nicoud, F., L. Benoit, C. Sensiau, and T. Poinsot (2007, Feb). Acoustic modes in combustors with complex impedances and multidimensional active flames. *AIAA Journal 45*(2), 426–441.

Oefelein, J. C. and V. Yang (1993, Sep-Oct). Comprehensive review of liquid-propellant combustion instabilities in f1 engines. *Journal of Propulsion and Power 9*(5), 657–677.

Ongoren, A. and D. Rockwell (1988, Jun). Flow structure from an oscillating cylinder .2. mode competition in the near wake. *Journal of Fluid Mechanics 191*, 225–245.

Oschwald, M., Z. Farago, G. Searby, and F. Cheuret (2008, May-Jun). Resonance frequencies and damping of a combustor acoustically coupled to an absorber. *Journal of Propulsion and Power 24*(3), 524–533.

Peters, N. (2001). *Turbulent Combustion*. Cambridge University Press.

Pfuderer, D. G., A. A. Neuber, G. Fruchtel, E. P. Hassel, and J. Janicka (1996, Aug). Turbulence modulation in jet diffusion flames: Modeling and experiments. *Combustion and Flame 106*(3), 301–317.

Pierce, C. D. and P. Moin (1998, Dec). A dynamic model for subgrid-scale variance and dissipation rate of a conserved scalar. *Physics of Fluids 10*(12), 3041–3044.

Pieringer, J., T. Sattelmayer, and F. Fassl (2005). Time-domain simulation of liquid rocket combustion instabilities. In *European Combustion Meeting*.

Pitsch, H. (2006). Large-eddy simulation of turbulent combustion. *Annual Review of Fluid Mechanics 38*, 453–482.

Pitsch, H., M. Chen, and N. Peters (1998). Unsteady flamelet modeling of turbulent hydrogen-air diffusion flames. In T. C. Institute (Ed.), *Proceedings of the Combustion Institute*, Number 27. The Combustion Institute: The Combustion Institute.

Poinsot, T. and S. Lele (1992, JUL). Boundary-consitions for direct simulations of compressible viscous flows. *Journal of Computational Physics 101*(1), 104–129.

Poinsot, T. and D. Veynante (2001). *Theoretical and Numerical Combustion*. Edwards.

Pons, L., N. Darabiha, and S. Candel (2008, JAN). Pressure effects on non-premixed strained flames. *Combustion and Flame 152*(1-2), 218–229.

Preclik, D. and P. Spagna (1988). Low frequency and high frequency combustion oscillation phenomena inside a rocket combustion chamber fed by liquid or gaseous propellants. In *AGARD conf. proceedings*. AGARD.

Renfro, M. W., A. Chaturved, G. B. King, N. M. Laurendeau, A. Kempf, A. Dreizler, and J. Janicka (2004, Oct). Comparison of oh time-series measurements and large-eddy simulations in hydrogen jet flames. *Combustion and Flame 139*(1-2), 142–151.

Rey, C. (2004). *Interactions collectives dans les instabilités de combustion haute-fréquence. Application aux moteurs fusées à ergols liquides*. Ph. D. thesis, Ecole Centrale Paris, Chatenay-Malabry.

Rey, C., S. Ducruix, and S. Candel (2002). Transverse acoustic forcing of a reacting mixing layer. In *9th International conference on numerical combustion*, Sorrento, Italy.

Rey, C., S. Ducruix, and S. Candel (2005, Feb). A method for the transverse modulation of reactive flows with application to combustion instability. *Combustion Theory and Modelling 9*(1), 5–22.

Rey, C., S. Ducruix, F. Richecoeur, P. Scouflaire, L. Vingert, and S. Candel (2004). High frequency combustion instabilities associated with collective interactions in liquid propulsion. In AIAA (Ed.), *Joint Propulsion Conference*.

Rey, C., S. Ducruix, P. Scouflaire, and S. Candel (2002, September). Analysis of high frequency instabilities associated with collective interactions. In *7th French German Colloquium on Liquid Propulsion*, Orléans.

Richecoeur, F. (2006, December). *Expérimentations et simulations numériques des intéractions entre modes acoustiques transverses et flammes cryotechniques*. Ph. D. thesis, Ecole Centrale Paris.

Richecoeur, F., S. Ducruix, P. Scouflaire, and S. Candel (2008, JAN). Experimental investigation of high-frequency combustion instabilities in liquid rocket engine. *Acta Astronautica 62*(1), 18–27.

Richecoeur, F., S. Ducruix, P. Scouflaire, and S. Candel (2009). Effect of temperature fluctuations on high frequency acoustic coupling. *Proceedings of the Combustion Institute 32*(Part 2), 1663–1670.

Richecoeur, F., Y. Mery, P. Scouflaire, S. Ducruix, and S. Candel (2010). Interactions between coaxial jets and acoustic modes: experiments and simulations. *Journal of Propulsion and Power Submitted for publication*.

Richecoeur, F., P. Scouflaire, S. Ducruix, and S. Candel (2006, JUL-AUG). High-frequency transverse acoustic coupling in a multiple-injector cryogenic combustor. *Journal of Propulsion and Power 22*(4), 790–799.

Richecoeur, F., P. Scouflaire, S. Ducruix, and S. Candel (2007, July). A velocity coupling model for high frequency instabilities. In *2nd European Conference for Aerospace Sciences (EUCASS)*, Brussels, Belgium.

Searby, G., A. Nicole, M. Habiballah, and E. Laroche (2008, May-Jun). Prediction of the efficiency of acoustic damping cavities. *Journal of Propulsion and Power 24*(3), 516–523.

Singla, G., P. Scouflaire, C. Rolon, and S. Candel (2005). Transcritical oxygen/transcritical or supercritical methane combustion. In *Proceedings of the Combustion Institute*, Volume 30, pp. 2921–2928.

Singla, G., P. Scouflaire, C. Rolon, and S. Candel (2006). Planar laser induced fluorescence of oh in high pressure cryogenic lox/gh2 jet flames. *Combustion and Flame 144*, 151–169.

Singla, G., P. Scouflaire, C. Rolon, S. Candel, and L. Vingert (2007, May-Jun). Oh plif and emission imaging in high pressure cryogenic lox/methane flames. *Journal of Propulsion and Power 23*(3), 593–602.

Sirignano, W., J.-P. Delplanque, C. Chiang, and R. Bhatia (1995). *Liquid Rocket Engine Combustion Instability*, Volume 169, Chapter Liquid-Propellant Droplet Vaporization: A rate-Controlling Process for Combustion Instability, pp. 307–343. Washington, DC: AIAA, Inc.

Tischler, A. O. and T. Male (1956). Oscillatory combustion in rocket-propulsion engines. *Gas Dynamics Symposium*, 71–81.

Tong, A. Y. and W. Sirignano (1989, May-Jun). Oscillatory vaporization of fuel droplets in an unstable combustor. *Journal of Propulsion and Power 5*(3), 257–261.

Villermaux, E. (1998, SEP-OCT). Mixing and spray formation in coaxial jets. *Journal of Propulsion and Power 14*(5), 807–817.

Vingert, L., P. Gicquel, and D. Lourme (1995). *Liquid Rocket Engine Combustion Instability*, Volume 169, Chapter Coaxial Injector Atomization, pp. 145–189. Washington, DC: AIAA, Inc.

Westerweel, J., D. Dabiri, and M. Gharib (1997, May). The effect of a discrete window offset on the accuracy of cross-correlation analysis of digital piv recordings. *Experiments in Fluids 23*(1), 20–28.

White, F. (1999). *Fluid Mechanics* (4th ed.). McGraw-Hill Book Company.

Yang, V. and W. Anderson (1995). *Liquid Rocket Engine Combustion Instability*, Volume 169. AIAA.

Yang, V., J. M. Wicker, and M. W. Yoon (1995). *Liquid Rocket Engine Combustion Instability*, Volume 169, Chapter Acoustic Waves in Combustion Chambers, pp. 357–376. Washington, DC: AIAA, Inc.

Zhou, X. Y. and S. Mahalingam (2002, Nov). A flame surface density based model for large eddy simulation of turbulent nonpremixed combustion. *Physics of Fluids 14*(11), L77–L80.

Zhou, X. Y., W. Pakdee, and S. Mahalingam (2004, Oct). Assessment of a flame surface density-based subgrid turbulent combustion model for nonpremixed flames of wood pyrolysis gas. *Physics of Fluids 16*(10), 3795–3807.

Zinn, BT, B. (1970). Theoretical study of non-linear damping by helmholtz resonators. *Journal of Sound and Vibration 13*(3), 347–&.

Appendix A

Equations for the coupling of cavity

This section aims at understanding how coupling of cavities can be modeled. First, the equations describing the acoustic of the three parts considered (injection dome, injectors, combustion chamber) are given. Then, a system is established. Eigenmodes are found by solving this system of equations.

Injection dome

$$p_1 = \sum_{m=0}^{N-1} \cos(\frac{\pi m}{L_1}(y - L_1/2))[f_1^m(x) + g_1^m(x)] \tag{A.1}$$

$$f_1^m(x) = F_1^m e^{-ik_{x_1}^m x} \tag{A.2}$$

$$g_1^m(x) = G_1^m e^{ik_{x_1}^m x} \tag{A.3}$$

$$k_{x_1}^m = \sqrt{(\frac{\omega}{c_1})^2 - (\frac{\pi m}{L_1})^2} \tag{A.4}$$

$$u_1 = \sum_{m=0}^{N-1} \frac{k_{x_1}^m}{\omega \rho_1} \cos(\frac{\pi m}{L_1}(y - L_1/2))[f_1^m(x) - g_1^m(x)] \tag{A.5}$$

$$\tag{A.6}$$

j^{th} injector

$$
\begin{aligned}
p_2^j &= f_2^j(x) + g_2^j(x) && \text{(A.7)}\\
f_2^j(x) &= F_2^j e^{-ik_{x_2}x} && \text{(A.8)}\\
g_2^j(x) &= G_2^j e^{ik_{x_2}x} && \text{(A.9)}\\
k_{x_2} &= \frac{\omega}{c_2} && \text{(A.10)}\\
u_2 &= \frac{1}{c_2\rho_2}[f_2^m(x) - g_2^m(x)] && \text{(A.11)}\\
& && \text{(A.12)}
\end{aligned}
$$

Combustion chamber

$$
\begin{aligned}
p_3 &= \sum_{m=0}^{N-1} \cos(\frac{\pi m}{L_3}(y - L_3/2))[f_3^m(x) + g_3^m(x)] && \text{(A.13)}\\
f_3^m(x) &= F_3^m e^{-ik_{x_3}^m x} && \text{(A.14)}\\
g_3^m(x) &= G_3^m e^{ik_{x_3}^m x} && \text{(A.15)}\\
k_{x_3}^m &= \sqrt{(\frac{\omega}{c_3})^2 - (\frac{\pi m}{L_3})^2} && \text{(A.16)}\\
u_3 &= \sum_{m=0}^{N-1} \frac{k_{x_3}^m}{\omega\rho_3} \cos(\frac{\pi m}{L_3}(y - L_3/2))[f_3^m(x) - g_3^m(x)] && \text{(A.17)}\\
& && \text{(A.18)}
\end{aligned}
$$

These equations are reported in Fig. A.1.
To establish the modal structure of the domain, we need to write boundary conditions for each part of the domain.
The system that must be solved can then be written as follows:

$$
\begin{aligned}
\sum_{m=0}^{N-1} \alpha_1(j,m)(F_1^m + G_1^m) &= F_2^j + G_2^j, \forall j \in [1, N_b] && \text{(A.19)}\\
\sum_{m=0}^{N-1} \alpha_2(j,m)(F_2^m - G_2^m) &= F_2^j - G_2^j, \forall j \in [1, N_b] && \text{(A.20)}\\
\sum_{m=0}^{N-1} \alpha_3(j,m)(F_3^m e^{-i\theta_3} + G_3^m e^{i\theta_3}) &= F_2^j e^{-i\theta_2} + G_2^j e^{i\theta_2}, \forall j \in [1, N_b] && \text{(A.21)}\\
\sum_{m=0}^{N-1} \alpha_4(j,m)(F_3^m e^{-i\theta_3} - G_3^m e^{i\theta_3}) &= F_2^j e^{-i\theta_2} - G_2^j e^{i\theta_2}, \forall j \in [1, N_b] && \text{(A.22)}\\
F_1^m e^{i\theta_1} - G_1^m e^{-i\theta_1} &= 0, \forall m \in [0, N-1] && \text{(A.23)}\\
F_3^m e^{-i\theta_4} - G_3^m e^{i\theta_4} &= 0, \forall m \in [0, N-1] && \text{(A.24)}
\end{aligned}
$$

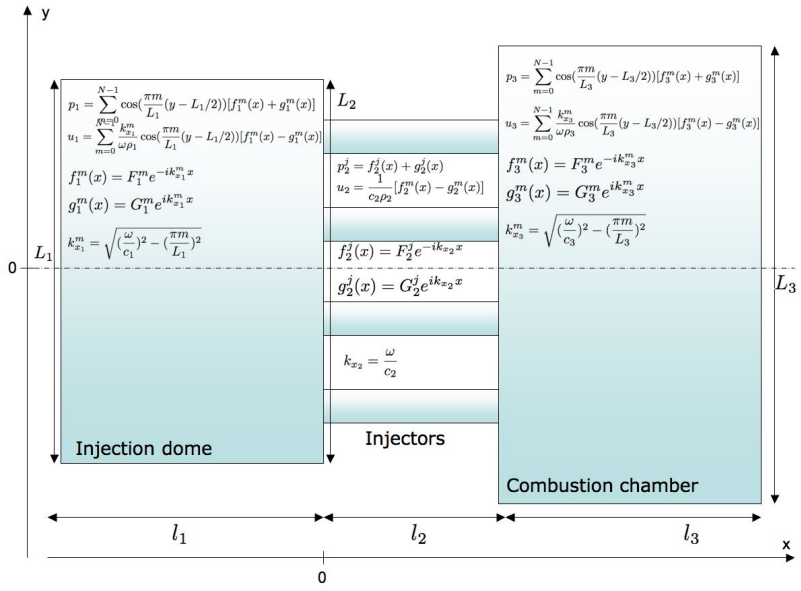

Figure A.1: *Geometry, reference frame of the coupling case with acoustic equations in each domain.*

With:

$$\alpha_1(j,m) = \cos(\frac{\pi m}{L1}(y_j - \frac{L_1}{2})), \tag{A.25}$$

$$\alpha_2(j,m) = \frac{c_2\rho_2}{\pi r^2}(lL_1)(\frac{2}{m\pi})(\frac{k_{x1}^m}{\omega\rho_1})\cos(\frac{\pi m}{L1}(y_j - \frac{L_1}{2}))\sin(\frac{\pi m}{L_1}\frac{L_2}{2N_b}), \tag{A.26}$$

$$\alpha_3(j,m) = \cos(\frac{\pi m}{L_3}(y_j - \frac{L_3}{2})), \tag{A.27}$$

$$\alpha_4(j,m) = \frac{c_2\rho_2}{\pi r^2}(lL_3)(\frac{2}{m\pi})(\frac{k_{x3}^m}{\omega\rho_3})\cos(\frac{\pi m}{L3}(y_j - \frac{L_3}{2}))\sin(\frac{\pi m}{L_3}\frac{L_2}{2N_b}), \tag{A.28}$$

$$\theta_1 = k_{x_1}^m l_1, \tag{A.29}$$

$$\theta_2 = \frac{\omega}{c_2} l_2, \tag{A.30}$$

$$\theta_3 = k_{x_3}^m l_2, \tag{A.31}$$

$$\theta_4 = k_{x_3}^m l_3 \tag{A.32}$$

This system can be written as a matrix operation: $A(\omega) = 0$. ω for which $\det(A(\omega)) = 0$ define the eigenfrequencies. When ω corresponds to an eigenfrequency, $Ker(A(\omega))$ defines the eigenmode, i.e. the spatial structure of the pressure and velocity fields.

Appendix B

A combustion model based on flame surface density

B.1 Introduction

The flame surface density concept has been developed and used most notably to study premixed flame. The strength of this formulation is that it is based on a simple and sensible assumption: the local heat release is written as the product of a local consumption rate by the flame surface density. Here, a model based on a infinitely fast chemistry assumption is developed. Probability density function formalism is used to find relationships written by (Zhou and Mahalingam 2002) in terms of flame surface density. Then, each term are examined and modeled successively.

B.2 Model derivation

The filtered reaction rate reads:

$$\widetilde{\dot{\omega}_k} = \int_0^\infty \int_0^1 \dot{\omega}_k(Z, \chi_{st}) \widetilde{p}(Z, \chi_{st}) dZ d\chi_{st} \tag{B.1}$$

$$\widetilde{\dot{\omega}_k} = \int_0^\infty \int_0^1 \dot{\omega}_k(Z, \chi_{st}) \widetilde{p}(Z) p(\chi_{st}) dZ d\chi_{st} \tag{B.2}$$

It is assumed that the probability density function for the stoechiometric scalar dissipation rate is a Dirac distribution centered on $\widetilde{\chi_{st}}$.

$$\widetilde{\dot{\omega}_k} = \int_0^1 \dot{\omega}_k(Z, \widetilde{\chi_{st}}) \widetilde{p}(Z) dZ, \tag{B.3}$$

$$\widetilde{\dot{\omega}_k} = \int_0^1 \frac{\dot{\omega}_k(Z, \widetilde{\chi_{st}})}{|\nabla Z|} |\nabla Z| \widetilde{p}(Z) dZ \tag{B.4}$$

The strong hypothesis of the model is that chemistry is infinitely fast, i.e. $\dot{\omega}_k$ is also a Dirac distribution centered on $Z = Z_{st}$. This leads to

$$\widetilde{\dot{\omega}_k} = \frac{\dot{\omega}_k(Z_{st}, \widetilde{\chi_{st}})}{\overline{|\nabla Z|}_{Z_{st}}} \overline{|\nabla Z|}_{Z_{st}} \widetilde{p}(Z_{st}). \tag{B.5}$$

In this formulation, $\overline{|\nabla Z|}_{Z_{st}}$ is the conditional average of $\overline{|\nabla Z|}$ for $Z = Z_{st}$. Let's define the source term obtained by integrating a one-dimensional flamelet:

$$\dot{\Omega}_k(\widetilde{\chi_{st}}) = \int_{-\infty}^{\infty} \dot{\omega}_k(x, \widetilde{\chi_{st}}) dx. \tag{B.6}$$

A change of variable leads to

$$\dot{\Omega}_k(\widetilde{\chi_{st}}) = \int_0^1 \frac{\dot{\omega}_k(Z, \widetilde{\chi_{st}})}{|\nabla Z|} dZ, \tag{B.7}$$

and if the same assumption is made:

$$\dot{\Omega}_k(\widetilde{\chi_{st}}) = \frac{\dot{\omega}_k(Z_{st}, \widetilde{\chi_{st}})}{\overline{|\nabla Z|}_{Z_{st}}}. \tag{B.8}$$

The model for the combustion source term reads

$$\widetilde{\dot{\omega}_k} = \dot{\Omega}_k(\widetilde{\chi_{st}}) \overline{|\nabla Z|}_{Z_{st}} \widetilde{p}(Z_{st}). \tag{B.9}$$

In this expression, the product between the quantity $\dot{\Omega}_k(\widetilde{\chi_{st}})$, the local consumption rate of a strained diffusion flame, and $\overline{|\nabla Z|}_{Z_{st}} p(Z_{st})$ appears.

Remark
A geometrical interpretation exists for this equation. The term $\overline{|\nabla Z|}_{Z_{st}} \widetilde{p}(Z_{st})$ has the dimension of a flame surface density, while $\dot{\Omega}_k(\widetilde{\chi_{st}})$ is the local consumption rate. The same kind of model is developed in the flame surface density formalism in the articles (Zhou and Mahalingam 2002) and (Zhou et al. 2004).

B.3 Mathematical modeling

In the expression for the filtered heat release $\widetilde{\dot{\omega}_k}$, three terms have to be modeled: $\dot{\Omega}_k(\widetilde{\chi_{st}})$, $\overline{|\nabla Z|}_{Z_{st}}$, $\widetilde{p}(Z_{st})$ and $\widetilde{\chi_{st}}$.

B.3.1 Modeling of the local consumption rate $\dot{\Omega}_f$

The modeling of the local reaction rate can be based on various assumptions. The simplest possible treatment is to consider that the local flame element is a strained diffusion flame and that the reaction rate is infinitely fast. This yields

simple algebraic expressions for the reaction rate. One may also consider that the chemical kinetics is finite and that the reactive element is again a strained diffusion flame. These two types of formulations are successively considered in what follows.

Strained flame elements with infinitely fast chemistry

The local consumption rate per unit flame surface may be obtained by considering that the reactive elements are formed by non-premixed reactants and that chemistry is infintely fast. This last assumption is quite suitable for the highly reactive propellants considered in the present investigation. The reaction can be written:

$$sF + O \rightarrow (1+s)P \tag{B.10}$$

The analysis follows that described for example by Poinsot and Veynante (2001). To carry out the analytic study, the density ρ is assumed to be constant. The infinitely thin reactive layer extends from x_- to x_+:

$$\dot{\Omega}_k = -\left[D\frac{\partial Y_k}{\partial x}\right]_{x_-}^{x_+} = D\left[\frac{\partial Y_k}{\partial x}\right]_{x_-} \tag{B.11}$$

$$= D\left[\frac{\partial Y_k}{\partial Z}\right]_{Z_-}\left[\frac{\partial Z}{\partial x}\right]_{x_-} = D\left[\frac{\partial Y_k}{\partial Z}\right]_{Z_-}\nabla Z(Z_{st}). \tag{B.12}$$

This leads, for the fuel, to:

$$\dot{\Omega}_F = -\frac{Y_F^0}{1-Z_{st}}\sqrt{\frac{aD}{2\pi}}e^{-\eta_f^2} \tag{B.13}$$

where $\eta_f = \mathrm{erf}^{-1}\left((\phi-1)/(\phi+1)\right)$ is a reduced normal coordinate defining the flame location, $\phi = sY_F^0/Y_O^0$ designates the global mixture ratio. In the last expression s is the mass stoichiometric coefficient of the single step reaction defining the chemical conversion in the flame. Note that the relation between local consumption rate of fuel and oxidizer. It is possible to show that for steady strain flames, the strain rate a appearing in the previous relation can be expressed in terms of the scalar dissipation at the flame χ_{st} using the equation:

$$\chi_{st} = \frac{a}{\pi}\exp\left[-2\eta_f^2\right], \tag{B.14}$$

and one obtains finally:

$$\dot{\Omega}_F = -\frac{Y_F^0}{1-Z_{st}}\sqrt{\frac{D}{2}}\sqrt{\chi_{st}}. \tag{B.15}$$

Strained flame elements with finite rate chemistry

The assumption of infinitely fast chemistry is strong, and future evolution of this model may need to consider more precisely the multiple reactions taking place in the combustion process. Following equations show that there is no theoretical problem in considering complex chemistry to deduce the local value of the consumption rate. This is achieved by integrating the volumetric consumption rate across the flame.

$$\dot{\Omega}_k(\chi_{st}) = \int_{-\infty}^{\infty} \dot{\omega}_k(x, \chi_{st}) dx \tag{B.16}$$

One may then use a detailed chemistry code to calculate counterflow strained laminar flames and deduce $\dot{\Omega}_F(\chi_{st})$ from the calculated values. The previous expression still requires a model for $\widetilde{\chi}_{st}$ which can be deduced from the available flow variables as explained in what follows. This approach was chosen by Zhou, Pakdee, and Mahalingam (2004).

B.3.2 Extracting the scalar dissipation $\widetilde{\chi_{st}}$ from the available fields

Both finite rate and infinitely fast chemistry local consumption rate models depend on a same variable $\widetilde{\chi_{st}}$ which is the scalar dissipation rate taken at its stoechiometric value. It is a very important physical term in non-premixed combustion since it is directly related to the strain of the flame. If one considers steady flamelets, the time dependent terms disappear from eq. 6.12 and one has:

$$\dot{\omega}_k = -\frac{1}{2}\chi \frac{\partial^2 Y_k}{\partial Z^2} \tag{B.17}$$

For a steady one-dimensional strained diffusion flame, it is possible to write a relation between χ and Z (see for example (Poinsot and Veynante 2001)):

$$\chi = \chi_0 F(Z) = \chi_0 \exp(-2[\mathrm{erf}^{-1}(1-2Z)]^2) \tag{B.18}$$

$$\chi = \chi_{st} \frac{F(Z)}{F(Z_{st})} \tag{B.19}$$

where $F(Z) = \exp(-2[\mathrm{erf}^{-1}(1-2Z)]^2)$. Accordingly, the scalar dissipation may be cast in the general form $\chi = \chi(Z, \chi_{st})$.
The mass averaged spatially filtered scalar dissipation can be related to the

value of the scalar dissipation on the stoichiometric surface:

$$\widetilde{\chi} = \int_Z \int_\chi \chi(Z, \chi_{st}) p(\chi_{st}) \widetilde{p}(Z) d\chi_{st} dZ \tag{B.20}$$

$$= \widetilde{\chi_{st}} \int_0^1 \frac{F(Z)}{F(Z_{st})} \widetilde{p}(Z) dZ \tag{B.21}$$

$$\widetilde{\chi_{st}} = \frac{\widetilde{\chi} F(Z_{st})}{\int_0^1 F(Z) \widetilde{p}(Z) dZ} \tag{B.22}$$

The last formula provides an expression for the spatial average of the scalar dissipation at the flame. Once again, the Dirac distribution for χ_{st} is assumed. One still has to provide a rule for calculating the spatial average of the scalar dissipation. This is accomplished for example by adopting the model proposed by De Bruyn Kops et al. (1998). The unconditioned filtered average $\widetilde{\chi}$ is expressed as:

$$\widetilde{\chi} = 2 \left(\frac{\mu}{\rho Sc} + \frac{\mu_t}{\rho Sc_t} \right) |\nabla \widetilde{Z}|^2 \tag{B.23}$$

B.3.3 Extracting $\overline{|\nabla Z|}_{Z_{st}}$ from the available fields

The expression of the averaged mixture fraction gradient conditioned at Z_{st} is obtained by writing the definition of $\widetilde{\chi}_{st}$ and considering that the distribution of χ_{st} is a Dirac:

$$\widetilde{\chi}_{st} = \int \chi_{st} p(\chi_{st}) d\chi_{st} \tag{B.24}$$

$$= \int 2D \overline{|\nabla Z|}^2_{Z_{st}} p(\chi_{st}) d\chi_{st} \tag{B.25}$$

$$= 2D \overline{|\nabla Z|}^2_{Z_{st}} \tag{B.26}$$

This leads to:

$$\overline{|\nabla Z|}_{Z_{st}} = \sqrt{\frac{\widetilde{\chi}_{st}}{2D}} \tag{B.27}$$

B.3.3.1 Presumed PDF to model $p(Z_{st})$

It is convenient to presume the shape of this PDF and use for that purpose a β-function.

$$p(Z) = \frac{1}{B(a,b)} Z^{a-1} (1 - Z)^{b-1} \tag{B.28}$$

where $B(a,b)$ is such that the sum of $p(Z)$ over all values of Z is equal to unity, and a and b are calculated from $\widetilde{Z}$ and its variance.

$$a = \widetilde{Z}\left[\frac{\widetilde{Z}(1-\widetilde{Z})}{\widetilde{Z''^2}} - 1\right] \tag{B.29}$$

$$b = \frac{a}{\widetilde{Z}} - a \tag{B.30}$$

$$\widetilde{Z''^2} = \widetilde{Z^2} - \widetilde{Z}^2 \tag{B.31}$$

where $\widetilde{Z''^2}$ is the subgrid scale variance of Z. Method for determining $\widetilde{Z''^2}$ are discussed in section6.

B.4 Summary

Table B.1 gathers formulas that have been implemented in the AVBP code. Results presented in the following are based on these set of equations.

Term to be modeled	Expression
$\widetilde{\dot{\omega}_k}$	$\dot{\Omega}_k(\widetilde{\chi}_{st})\overline{\lvert\nabla Z\rvert}_{Z_{st}}\widetilde{p}(Z_{st})$
$\dot{\Omega}_F(\chi_{st})$	$-\frac{Y_F^0}{1-Z_{st}}\sqrt{\frac{D}{2}}\sqrt{\chi_{st}}$
$\widetilde{\chi}_{st}$	$\frac{\widetilde{\chi}F(Z_{st})}{\int_0^1 F(Z^*)p(Z^*)dZ^*}$
$F(Z)$	$\exp(-2[\mathrm{erf}^{-1}(1-2Z)]^2)$
$\widetilde{\chi}$	$2\left(\frac{\mu}{\rho Sc}+\frac{\mu_t}{\rho Sc_t}\right)\lvert\nabla\widetilde{Z}\rvert^2$
$\overline{\lvert\nabla Z\rvert}_{Z_{st}}$	$\sqrt{\frac{\widetilde{\chi}_{st}}{2D}}$
$\widetilde{p}(Z)$	$\frac{1}{B(a,b)}Z^{a-1}(1-Z)^{b-1}$
a	$\widetilde{Z}\left[\frac{\widetilde{Z}(1-\widetilde{Z})}{\widetilde{Z''^2}}-1\right]$
b	$\frac{a}{\widetilde{Z}}-a$
$\widetilde{Z''^2}$	$C\Delta^2\lvert\nabla\widetilde{Z}\rvert^2$

Table B.1: *Equations of the model.*